Ultrasound Matrix Transducers for High Frame Rate 3D Medical Imaging

Shabanimotlagh, Maysam

DOI
10.4233/uuid:7ce26659-91fa-45a0-bfdf-7223375fed69

Publication date
2018

Document Version
Final published version

Citation (APA)
Shabanimotlagh, M. (2018). *Ultrasound Matrix Transducers for High Frame Rate 3D Medical Imaging*. [Dissertation (TU Delft), Delft University of Technology]. https://doi.org/10.4233/uuid:7ce26659-91fa-45a0-bfdf-7223375fed69

Ultrasound Matrix Transducers for High Frame Rate 3D Medical Imaging

Dissertation

for the purpose of obtaining the degree of doctor
at Delft University of Technology
by the authority of the Rector Magnificus, Prof.dr.ir. T.H.J.J. van der Hagen
chair of the Board for Doctorates
to be defended publicly on
Wednesday 12 September 2018 at 10:00 o'clock

by

Maysam SHABANIMOTLAGH

Master of Science in Mechanical Engineering,
at Iran University of Science and Technology, Iran
born in Tehran, Iran

This dissertation has been approved by the promotors:

Prof.dr.ir. N. de Jong
Dr.ir. M.D. Verweij

Composition of the doctoral committee:

Rector Magnificus,	chairperson
Prof.dr.ir. N. de Jong	Delft University of Technology, promotor
Dr.ir. M.D. Verweij	Delft University of Technology, promotor

Independent members:

Prof.dr. A. van der Lugt	Erasmus MC
Dr.ir. M.A.P. Pertijs	Delft University of Technology
Dr. F.M. Vos	Delft University of Technology
Prof.dr. J. Dankelman	Delft University of Technology
Prof.dr.ir. W.A. Serdijn	Delft University of Technology, reserve member

This research is part of the PUMA project (project number 13154), and is supported by the Dutch Technology Foundation STW, which is part of the Netherlands Organisation for Scientific Research (NWO), and which is partly funded by the Ministry of Economic Affairs.

ISBN 978-94-6375-077-6

Printed by: Ridderprint BV, www.ridderprint.nl

Summary

This thesis describes the design, fabrication, and characterization of a Lead-Zirconate-Titanate (PZT) matrix transducer integrated on an Application Specific Integrated Circuit (ASIC) for medical ultrasound imaging application. The focus in this thesis is on the mechanical design of the transducer elements, as well as the acoustical performance of the whole matrix transducer together with the electronics. The developed technology can be used for the next generation of ultrasound devices that allow for a real-time, three-dimensional visualization of various organs. Two specific applications are considered in this thesis: carotid artery imaging and miniaturized transesophageal echocardiography (TEE). By integrating the ASIC in the probe itself, it is possible to interact with more than 1000 transducer elements despite a limited number of electrical connections (256 connections for most of the ultrasound machines). There are several challenges from design to implementation of such a probe. These challenges are discussed and practical solutions are proposed, tested and verified extensively in different chapters of this thesis. A brief explanation of the chapter are provided in this summary as follows:

An introduction to ultrasound imaging is provided in **Chapter 1**. The technology of the ultrasound probes are described and the demand for improvements are explained. For this purpose, a review of the available approaches for three-dimensional imaging is provided, and the aim of this research project is presented.

The basis of a properly performing ultrasound transducer is a well-designed geometry of the transducer element. For optimal vibration of an element, a uniform surface motion is required. This can be achieved by selecting a small width with respect to the thickness of the element. However, a large element width is needed to obtain a high radiation power. To solve this contradiction we have applied subdicing on the width of the element in **Chapter 2**. We have systematically examined the effect of subdicing on the radiation impedance, the time and

frequency responses, and the directivity pattern of an element in a 1D linear array. The simulation results show that subdicing improves the acoustical performance of the elements when their width is larger than 60% of the wavelength in water. In this case, the transmit pressure is increased, the sidelobes and ringing time are reduced, and the resulting bandwidth is increased. Furthermore, we show that a subdicing depth of 70% of the total element thickness is enough to achieve these improvements.

To image a specific organ using a forward-looking matrix transducer, the transducer should be designed such that it covers the whole imaging area. This implies a large number of transducer elements. To restrict the number of transducer elements the size of elements should be made as large as possible. However, increasing the width-to-thickness ratio of an element lead to the occurrence of unwanted lateral modes which degrades the acoustical performance. In this situation, subdicing can be applied to remove these lateral modes. In **Chapter 3** we explain the design of an ultrasound matrix transducer for high frame rate carotid artery imaging application. For such a transducer, an element width larger than a wavelength is required, where we employ subdicing as a solution and with simulations and measurements we analyze the subdicing effect on the performance of the transducer element. We fabricate a matrix transducer and applied zero, one, or two subdicing cuts on different elements. Experimental measurements in a water tank agree qualitatively well to the simulations for all the three subdicing cases. The results show that subdicing shifts the lateral resonance peaks outside the frequency band of interest, and increases the bandwidth of the transducer. For the considered application we conclude that the transducer element with one subdicing cut shows the best performance.

In **Chapter 4**, we analyzed the effect of a silicon backing on the acoustical performance of a matrix transducer mounted on an ASIC. Since the ASIC is based on silicon and is mounted directly behind the transducer elements, it can be regarded as a rigid plate that can sustain traveling waves. These waves lead to acoustical cross-talk between the elements and result in extra peaks in the directivity pattern. We have proposed two solutions to this problem. One approach is to reduce the thickness of the silicon and use an absorbing material behind the ASIC to absorb the acoustic energy by a proper backing material. Another solution is to disturb the generated waves inside the silicon plate by sub-dicing on the back-side of the ASIC. The simulation results show that both solutions can be used to smoothen the directivity pattern.

We have designed a dedicated probe with piezoelectric matrix transducer on top of an ASIC suitable for three dimensional (3D) imaging of carotid arteries. The ASIC is designed for a matrix array of 24 × 40 transducer elements with 150 μm pitch. The geometry is designed with the possibility of tiling multiple of these ASICs to generate a larger aperture. All 960 elements are connected to the mainframe using only 24 transmit and 24 receive channels on each row. For each element, reconfigurable switches are designed to enable any arbitrary selection of transmit and receive aperture patterns. On the receiving path of each row, a cable driver and an LNA with 20 dB gain are designed, which could be activated in case of low measured signals or bypassed in case of high input signal. An electrical sample is made to characterize the electrical performance of the ASIC. In **Chapter 5** the electrical chain, which consists of three daughterboards and one motherboard, is described. They are designed to connect the ASIC to the ultrasound machine. For a proper interpretation of the received signals, the electrical performance of all components in the receiving chain, and the

entire electrical chain are electrically characterized. Furthermore, the saturation level of the chip for the two cases with LNA on and LNA bypassed are obtained. In **Chapter 6** we demonstrate the mechanical design, fabrication and acoustical characterization of the transducer. The performance of the transducer prototype is acoustically characterized in a series of water tank measurements. The reconfigurability of the transducer is tested by measuring the transmit beam from different element selections by a hydrophone. The results are in good agreement with the simulations. In a pulse-echo measurement, 87% of the working elements show sensitivity variation within -6 dB range. The transducer has a central frequency of 7.3 MHz, with 45% bandwidth. The overall received dynamic range is 83 dB and the minimum detectable pressure is 10 Pa. The results show the potential of the design to make a large matrix array suitable for 3D real-time imaging of carotid arteries.

Chapter 7 presents a prototype PZT matrix transducer with integrated ASIC, as a proof of concept for a miniature 3D TEE probe. The prototype consists of a matrix array of 9×12 piezoelectric elements. The ASIC includes front-end amplifiers with adjustable gains and micro-beamformer circuits that locally process and combine echo signals received by the elements of each 3×3 sub-array. Thus, a nine-fold reduction in the number of receive channels is achieved. The prototype has been acoustically characterized in a water tank. The ASIC allows the array to be pre-steered in 25 directions while achieving an overall dynamic range of 77 dB. Both the measured characteristics of the individual transducer elements and the performance of the ASIC are in good agreement with expectations, demonstrating the effectiveness of the proposed techniques for 3D TEE applications.

Chapter 8 presents the design, fabrication, and characterization of a miniature matrix transducer for real-time pediatric 3D TEE imaging. This 3D TEE probe consists of a 32×32 array of PZT elements integrated on top of an ASIC. A partitioned transmit/receive array architecture is designed where the 8×8 transmitter elements, located at the center of the array, are directly wired out and the remaining receive elements are grouped into 96 sub-arrays of 3×3 elements. The echoes received by these sub-groups are locally processed by micro-beamformer circuits in the ASIC that allow pre-steering up to ±37º. The transducer has been characterized acoustically and has a center frequency of 5.8 MHz, -6 dB bandwidth of 67%, a transmit efficiency of 6 kPa/V at 30 mm, and a receive dynamic range of 85 dB with minimum and maximum detectable pressures of 5 Pa and 84 kPa respectively. The properties are very suitable for the described application.

An overview of the achievements in this thesis is provided in **Chapter 9**. Other potential applications and some recommendations for the future works are given in this chapter.

Samenvatting

Dit proefschrift beschrijft het ontwerp, de fabricage en de karakterisering van een matrix-transducer voor het maken van medische afbeeldingen,die bestaat uit een piezoelektrisch (lood-zirconaat-titanaat; PZT) matrix array op een geïntegreerd circuit (ASIC; Application Specific Integrated Circuit). De focus ligt op het mechanische ontwerp van de transducerelementen en de akoestische prestaties van de gehele matrix-transducer samen met de elektronica. De ontwikkelde technologie kan worden gebruikt voor een volgende generatie ultrasoundapparaten die een real-time, driedimensionale visualisatie van verschillende organen mogelijk maken. In dit proefschrift worden twee specifieke toepassingen beschouwd: beeldvorming van de halsslagader en geminiaturiseerde transesofageale echocardiografie (TEE). Door de ASIC in de probe te integreren, is het mogelijk om gebruik te maken van meer dan 1000 transducerelementen, ondanks een beperkt aantal elektrische verbindingen (256 verbindingen voor de meeste ultrageluidmachines). Er zijn verschillende uitdagingen in het ontwerp en de implementatie van een dergelijke probe. In de afzonderlijke hoofdstukken van dit proefschrift worden praktische oplossingen voor deze uitdagingen voorgesteld, getest en geverifieerd.

In **Hoofdstuk 1** wordt de basis van echografie uitgelegd. Daarnaast wordt de werking en de tekortkomingen van de huidige transducers beschreven. Om deze tekortkomingen uit te leggen wordt een overzicht gegeven van de huidige benaderingen voor driedimensionale beeldvorming. Als laatste wordt het doel van dit onderzoek gepresenteerd.

De basis van een goed werkende transducer is een goed ontworpen transducer element. In het best mogelijke geval vibreert het transduceroppervlak uniform. Dit kan bewerkstelligd worden door de breedte van het element klein te maken ten opzichte van de dikte. Het nadeel van een kleine elementbreedte is dat het uitgestraalde vermogen laag is. Om dit op te lossen delen we in **Hoofstuk 2** de elementen op in kleinere subelementen. Het effect van het opleden

van de elementen is systematisch onderzocht door te kijken naar de stralingsimpedantie, het tijdsignaal, het frequentiespectrum en het stralingspatroon van een element in een 1D transducer. Simulaties laten zien dat het opdelen van een element zorgt voor betere prestaties indien de breedte van het hele element groter is dan 60% van de golflengte. Het opdelen heeft een positief effect op de uitgezonden druk, de zijlobben, de trillingstijd en de bandbreedte. We laten ook zien dat de elementen slechts over 70% van de dikte ingesneden hoeven te worden om een verbetering te zien in de prestaties.

Een mogelijke manier om een bepaald orgaan af te beelden is om de transducer zo groot te maken dat het oppervlak het hele orgaan omvat. Hiervoor zijn enorm veel elementen nodig. Door de elementen zo groot mogelijk te maken kan het het aantal elementen engigszins gereduceerd worden. Indien echter de breedte-dikte verhouding te groot wordt treden laterale bewegingen op in het element die een negatief effect hebben op de akoestische prestaties. Om geen last te hebben van deze laterale bewegingen kan het element worden opgedeeld in subelementen. In **Hoofdstuk 3** bekijken we door middel van simulaties en metingen opnieuw welk effect het opdelen van elementen heeft, maar nu specifiek met het doel om een transducer te ontwerpen voor het afbeelden van de halsslagader. Voor dit onderzoek is een matrix-transducer gemaakt met elementen groter dan een golflengte, die opgedeeld zijn in een, twee of drie subelemeten. Metingen met deze transducer in een watertank komen voor alle type elementen kwalitiatief goed overeen met simulaties. De resultaten laten zien dat indien de elementen worden opgedeeld, de frequenties van de laterale bewegingen buiten de gewenste bandbreedte vallen en dat de bandbreedte toeneemt. Voor de genoemde toepassing blijkt uit deze resultaten dat het het beste is om een element op te delen in twee subelementen.

Bij een matrix-transducer die is gebouwd op een ASIC, fungeert de ASIC ook als backing. In **Hoofdstuk 4** wordt het effect van deze backing onderzocht. De ASIC wordt beschouwd als een rigide siliciumplaat waarin golven kunnen propageren. Deze golven zorgen voor akoestische overspraak tussen de elementen, hetgeen het stralingspatroon negatief beinvloedt. In dit hoofdstuk presenteren we twee oplossingen voor dit probleem. Een mogelijke oplossing is om het silicium dunner te maken en een absorberend materiaal achter de ASIC te plaatsen waarin de golven geabsorbeerd worden. Een andere oplossing is om zaagsnedes in te achterkant van het ASIC te maken die de golven verstoren. Simulaties laten zien data beide voorgestelde oplossingen gebruikt kunnen worden om het stralingspatroon te verbeteren.

Voor het driedimensionaal afbeelden van de halsslagader hebben we een piëzo-electrische matrix-transducer op een ASIC ontwikkeld. De ASIC is ontworpen voor 24 × 40 elementen van elk 150 μm groot. De ASICs zijn zo gebouwd dat er meerdere naast elkaar geplaatst kunnen worden om daarmee een grotere matrix-transducer te maken. De in totaal 960 elementen zijn met 24 zend- en 24 ontvangstkanalen verbonden met het mainframe. Elk element heeft een set schakelaars waarmee ze onafhankelijk van elkaar aan en uit kunnen worden gezet in zend- en ontvangstmodus. Elke rij van 40 elementen heeft een ruisarme versterker (LNA) met een versterking van 20 dB die afhankelijk van het ontvangen signaal aan of uit geschakeld kan worden. Het elektrische gedrag van de ASIC is onderzocht door middel van een testexemplaar zonder elementen. In **Hoofdstuk 5** wordt alle achterliggende electronica besproken. Deze bestaat, naast de ASIC, uit een moederbord en drie besturingsprintplaten. Het moederbord en de besturingsprintplaten zorgen ervoor dat de ASIC

verbonden kan worden met het mainframe. Om de ontvangen signalen goed te interpreteren moet duidelijk zijn hoe elk individuele component en de gehele ontvangstketen werkt. In dit hoofdstuk wordt deze keten geanalyseerd. Daarnaast wordt het verzadigingsniveau van de chip, met zowel LNA aan en uit, gemeten. In **Hoofdstuk 6** wordt het ontwerp, de fabricage en de karakterisatie van de transducer besproken. De herconfigureerbaarheid van de chip wordt getest door in een waterbak met een hydrofoon het uigezonden veld te meten telkens nadat verschillende patronen van elementen aan of uit zijn gezet. De gemeten velden komen goed overeen met de verwachting. Puls-echo metingen laten zien dat van 87% van de werkende elementen de variatie binnen 6 dB ligt. De transducer heeft een frequentiespectrum gecentreerd rond 7.3 MHz met een -6 dB bandbreedte van 45%. Het dynamisch bereik in ontvangst is 83 dB en de minimaal meetbare druk is 10 Pa. Deze resultaten laten zien dat dit ontwerp geschikt is voor een grote matrix-transducer voor het in real-time driedimensionaal afbeelden van de halsslagader.

In **Hoofdstuk 7** wordt een prototype PZT matrix-transducer met een geintegreerde ASIC beschreven die als proof of concept dient voor een miniatuur 3D TEE transducer. Dit prototype bevat 9 × 12 piëzo-electrische elementen. In de ASIC zijn versterkers geintegreerd met een variable versterking. Daarnaast bevat de ASIC micro-bundelvormers. Een micro-bundelvormer verwerkt de ontvangen echo's van een subgroep van 3 × 3 elementen tot een enkel signaal. Dit reduceert het aantal benodigde ontvangstkanalen met een factor 9. De akoestische prestaties van het prototype zijn getest in een watertank. Door middel van de ASIC konden de subgroepen gestuurd worden in 25 verschillende richtingen en dynamisch bereik van het prototype bleek 77 dB te zijn. De meetresultaten kwamen goed overeen met de verwachtingen voor de prestaties van de induviduele elementen en de verwachte functionaliteit van de ASIC. Dit toont aan dat de getoonde technieken in dit protype geschikt zijn voor gebruik in een 3D TEE toepassing.

Hoofdstuk 8 beschrijft het ontwerp, fabricage en karaktarisatie van een miniatuur matrix-transducer voor het maken van real-time pediatrische 3D TEE afbeeldingen. Deze transducer bestaat uit 32 × 32 PZT elementen bovenop een ASIC. De transducer bevat een apart zend- en ontvangstgedeelte. Het zendgedeelte bestaat uit 8 × 8 elementen in het midden van de transducer, die direct verbonden zijn met het mainframe. De overige elementen zijn gegroepeerd in 96 subgroepen met elk 3 × 3 elementen. De ontvangen echo's op deze subgroepen worden lokaal bewerkt tot een enkel signaal door de micro-bundelvormer. Hiermee kan een bundelsturing van ±37º bereikt worden. De transducer heeft een frequentiespectrum gecentreerd rond 5.8 MHz met een -6 dB bandbreedte van 67%. Daarnaast is de zendefficiëntie 6 kPa/V op een afstand van 30 mm en is het dynamisch bereik in ontvangst 85 dB, waarbij de druk meetbaar is tussen 5 Pa en 84 kPa. Deze eigenschappen zijn zeer geschikt voor de beschreven toepassing.

Een overzicht van de behaalde resultaten in dit proefschrift wordt gegeven in **Hoofdstuk 9**. Aan het eind van dit hoofdstuk worden ook andere potentiele toepassingen besproken en aanbevelingen voor toekomsitg onderzoek gegeven.

Table of Contents

CHAPTER 1

Introduction

1.1. Medical ultrasound imaging

The term ‘ultrasound’ refers to the usage of sound waves with frequencies above the audible frequency limit (~ 20 Hz to 20 kHz). Medical ultrasound imaging is a diagnostic tool which utilizes acoustic waves with frequencies > 1 MHz to gather structural (e.g. anatomy of an organ) and physiological (e.g. blood flow in an artery) information of biological media and visualizes them. Compared to the other imaging techniques, such as computed tomography (CT) or magnetic resonance imaging (MRI), ultrasound has several advantages: it is safe (no radiation exposure), real-time, cost-effective and portable. The resolution depends on the size of the active aperture, the central frequency, the bandwidth of the transducer and the selected focal depth, but in general, the ultrasound image resolution is comparable with other imaging modalities. However, at greater depths and especially for the soft tissues, it is not easy to obtain ultrasound images with high quality. With technological developments over time, the ultrasound devices have become smaller, and the quality of the images has improved. Also, by employing microbubble contrast agents, the image contrast is significantly enhanced [1, 2]. Since the 1960s, ultrasound imaging systems have been widely used (more than billion examinations per year) in practice around the world. All pregnant women are examined with ultrasound in some countries in Europe (e.g. in Germany, Norway, Iceland, and Austria) [3].

For the imaging of different parts of the body, transducers with different frequencies, sizes and shapes have been developed. A transducer generates an acoustic wave, which propagates to the human body through a coupling material (e.g. acoustic gel). When the sound reaches a scatterer, part of the energy reflects back, and part of the energy transmits. The reflected echoes are measured with the same transducer, and the position of the scatterer is determined based on the arrival time. With one transmission line, the locations of the scatterers within the transmit beam are detected. Conventionally, multiple lines at different positions or angles are

needed to create a full image. After acquiring the receiving signals, the data are processed by the computer to construct an image. Different processing techniques are developed to improve the image quality and resolution.

The developments in the field of ultrasound imaging are based on some important inventions during the 19th and 20th centuries. The concept of "phase shifting" was first introduced by Thomas Young in 1801 in relation to the light waves, and it is the basic principle in ultrasound phased array systems to control the interference patterns and image construction [4]. The 'Doppler effect' was discovered in 1842 by Christian Doppler to investigate the motion of stars. This is now the basic principle for the blood flow measurements [4]. The first demonstration of the 'piezoelectricity' effect was made in 1880 by the Curie brothers by combining their knowledge of pyroelectricity with crystal structures, to predict the performance of a quartz plate [5]. The piezoelectric materials are used in ultrasound transducers to generate and receive ultrasound waves in the Mega-Hertz frequency range. In 1912, one month after the ship Titanic sank, Lewis Fry Richardson patented the first sonar echolocation for iceberg detection [6]. This invention was followed by introducing the first ultrasound submarine detector using the pulse-echo test in 1917 by Paul Langevin, who was the PhD student of Pierre Curie. The detector consisted of a transducer to generate a pressure pulse, and a hydrophone to detect the returned echo [6]. An important advance was made during the 1920s and 1930s, by applying the pulse-echo system to electromagnetic radio waves and developing the radar (radio detection and ranging) systems for detecting the submarines and aircraft from far away. The method for displaying the data and beam steering in radar systems were later employed in ultrasound imaging to produce two-dimensional (2D) images [3, 4].

The idea of using ultrasound in medical diagnostics goes back to the early 1940s, and the first useful images of biological structures were reported in the 1950s. Karl Theodore Dussik, an Austrian neurologist, was the first to use medical ultrasound for diagnosis. In 1947 he developed an apparatus to make images of the brain and ventricles using heat sensitive papers to record the echoes of the ultrasonic transmissions [7]. Later in 1949, George Ludwig used reflective pulse-echo ultrasound waves for diagnosing gallstones in animals [4]. The first real-time echography was made in 1953 by John J. Wild and John M. Reid for detecting cancerous growth on a breast [3]. In parallel to the progress made in the United States, on the other side of the world, in 1955, Shigeo Satomura employed the Doppler shift techniques to monitor the pulsation of the heart and peripheral blood vessels. These early findings were the most important reason for the application of ultrasound in medicine. After establishing the American Institute of Ultrasound in Medicine (AIUM) in 1952, a lot of research was conducted in the field of medical ultrasound. One of the pioneering papers in ultrasonography was written by Ian Donald's team in 1958, in which the physics of scanning techniques, experiments, and images of pregnancy were explained, and a detailed discussion on the strengths, weaknesses, and the potentials of the new technique were discussed [8]. During the next decades, several machines were designed by different research groups and companies to image static objects. A revolution toward real-time imaging was made in the late 1970's when the multi-element linear/phased arrays together with integrated circuit technology were developed. These advances resulted in small and portable and less expensive ultrasound

scanning systems [4]. Since then, advancement in transducer design, materials, electronics, and processing have dramatically improved the quality of the medical ultrasound images.

In the past two decades, medical ultrasound has been among the most active research areas. Various medical ultrasound related topics have been introduced, such as elastography, contrast enhanced imaging, super resolution imaging, 3D imaging, drug delivery, high intensity focused ultrasound (HIFU), photo-acoustics, etc. These show the interest and progress in both diagnostic and therapeutic ultrasound applications [9].

1.2. Ultrasound transducers

The ultrasound machine is composed of an ultrasonic transducer that transmits and/or receives the ultrasound beam, and an imaging system which controls the transducer and constructs the image from the received data. The images can be in two-dimensional (2D) or three-dimensional (3D), depending on the transducer type and the imaging system. Progress made in computer technology, electronics integration, data acquisition and signal processing, all have improved the quality of the ultrasound machines. However, many of these enhancements are due to the developments in the design and fabrication of the transducers [10]. Various types of transducers with different size, shape, frequency, and field of view are designed for different applications, depending on the location and properties of the object. Figure 1.1 shows a photograph of different types of medical ultrasound transducers.

Most of the ultrasound transducers in medical applications are based on piezoelectric materials. Piezoelectricity allows the conversion of the electrical energy to the mechanical energy, and vice versa [5]. This effect is the nature of the piezoelectric materials, which have made them attractive for a variety of applications. The efficiency of conversion depends on the resonance frequency of the transducer, and the excitation frequency. The resonance frequency of a slab of piezoelectric material is the preferential frequency at which the highest conversion of energy occurs. The transmit transfer function for a transducer is defined to evaluate the conversion of electrical energy into mechanical, and is expressed in kPa/V. Similarly, the received transfer function is defined based on the conversion of acoustical energy into electrical and is expressed in μV/Pa [2]. The bandwidth of an ultrasonic transducer is defined with half power frequency band around the operational resonance frequency. For high intensity applications, the transducer is designed to operate in a small frequency range (a narrow-band transducer), but for sensing applications such as ultrasound imaging, the transducers are designed for operation over a wide frequency range [5]. A transducer with high bandwidth can generate a short pulse in time, that guarantees high axial resolution of the image [11].

The majority of the ultrasound probes which are currently used in medical imaging are made from one-dimensional (1D) array of transducer elements to generate 2D images. Depending on the imaging scheme, transducers in three different categories are manufactured: linear arrays, convex arrays, and phased arrays, as shown in figure 1.2. In linear arrays, a group of piezoelectric transducer elements are chosen to generate a beam scan line. With this approach, rectangular images are constructed by combining the scanning lines from a sequence of these groups (figure 1.2a). Linear arrays are usually used for imaging with high

resolution, where high frequencies and low imaging depths are intended. In convex arrays, the piezoelectric elements are designed on a curved surface to generate a sectorial image (figure 1.2b). The imaging method is similar to the linear arrays, but a wide and deep ultrasound image is obtained with the cost of lower resolution. In the phased arrays, the excitation of the elements is electronically steered and/or focused to generate the scan line (figure 1.2c). Depending on the application, phased arrays could be made in straight or convex forms. Phased arrays are normally used when the access to the target is limited and narrow, such as a heart behind the ribs, when imaging with linear or convex arrays are difficult.

As shown in figure 1.3, a typical 1D array transducer includes an active layer with or without kerfs in between, one or two acoustic matching layers, a backing material, an acoustic lens, a ground electrode, and a flexible printed circuit board (FPCB) to connect the elements to the outside world [10]. The active layer is usually made of a piezoelectric material to generate an acoustic wave with an electrical excitation and to receive the reflected echo pulses. Since there is a high acoustic impedance mismatch between the piezoelectric material and the media, matching layers are designed to optimize the energy transfer between the active layer and the human body. This layer significantly increases the bandwidth of the transducer [12]. The backing material has high damping properties to absorb the generated energy by the active layer to the back side of the transducer. Since both backing and matching materials affect the acoustical performance of the elements, they are carefully designed to maximize the bandwidth of the transducer [2]. An acoustic lens, preferably with low attenuation, protects the transducer array from exterior damages, and focuses the ultrasound beam to a specified depth [3, 13]. The kerfs are made to isolate the transducer elements acoustically and electronically from each other, and to reduce the crosstalk [14]. Sometimes the transducer elements are subdiced, in order to subtract the spurious modes and increase the efficiency [15].

Figure 1.1. Photograph of ultrasound transducers [16]

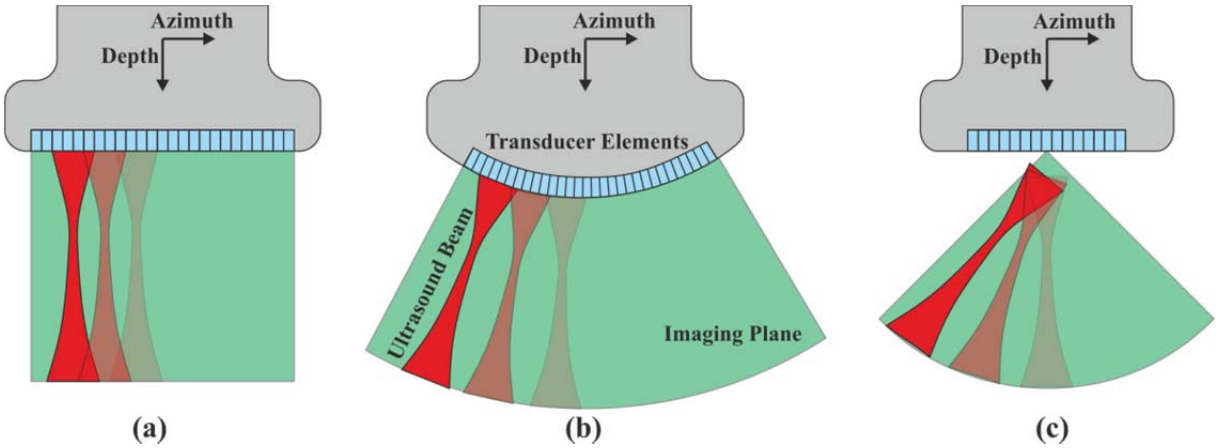

Figure 1.2. Schematics of one-dimensional transducer arrays: **(a)** a linear array, **(b)** a convex array, and **(c)** a phased array transducer.

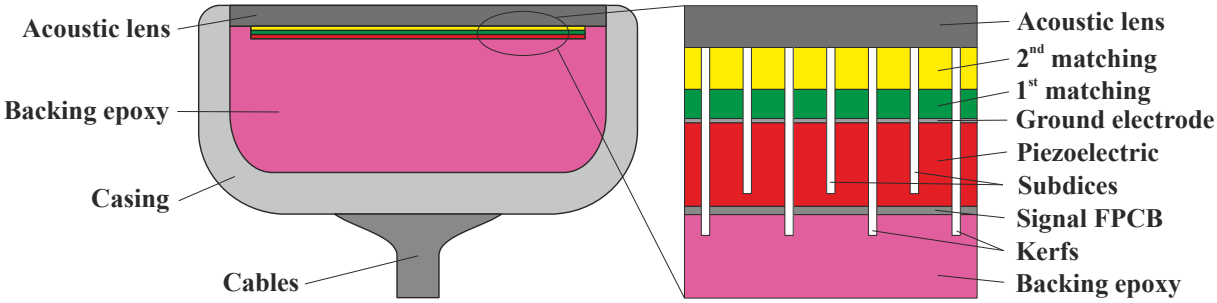

Figure 1.3. Schematics structure of a 1D array

1.3. Three-dimensional ultrasound

Conventional 2D ultrasound imaging is widely used in clinical applications, since it can dynamically display a cross-section of the region of interest in real-time. However, this technique has some limitations. Since the organs or the structures of interest are three dimensional, the sonographer should acquire multiple 2D images at different planes to understand the whole anatomy and pathology. Understanding a 3D structure from several 2D images is time-consuming, inefficient and, more importantly, variable and subjective. With conventional ultrasound, the volume of a plaque is usually estimated based on an idealized (e.g. ellipsoidal) shape, which is calculated from simple measurements of height, width, and length in two orthogonal views. However, in reality, they can have a complicated structure, and accurate estimation of the shape and the volume is not possible with 2D techniques. On the other hand, 2D imaging is not optimal for monitoring the therapeutic procedure in follow-up studies, because it is difficult to locate the transducer on the imaging plane similar to the previous examinations. Moreover, some imaging planes are sometimes impossible to achieve, due to the restrictions imposed by the patient's anatomy or position. Due to all of these restrictions, 2D ultrasound can be inaccurate and variable, it depends strongly on the skills and experiences of the sonographer, and can lead to incorrect decisions in diagnosis [17, 18]. In order to address the aforesaid problems, 3D ultrasound was developed to give a better overview for diagnosis. The main goal in 3D ultrasound imaging is to provide a user-friendly representation of the anatomical volume with real-time capabilities. In this way, the

interpretation of the images becomes much simpler because the spatial location and properties of the volume of the organ could be intuitively and correctly demonstrated. This facilitates a more accurate diagnosis, especially for abnormal anatomies such as congenital defects or distortions caused by disease [3]. The probability of finding abnormality with 3D ultrasound is higher than with 2D scanning. Furthermore, by having 3D information of the anatomy, any arbitrary 2D cross-section at any orientation could be generated [19]. Therefore, 3D ultrasound imaging promises to overcome the limitations of 2D ultrasound imaging described above.

Over the past two decades, clinical studies have shown a high interest in 3D ultrasound imaging [17-19]. Going from 2D ultrasound imaging to 3D is challenging and specific limitations are imposed depending on the application. Figure 1.4 shows different ways of data acquisition for 3D imaging. Three main approaches are introduced to acquire volumetric images: (1) mechanical sweeping transducers, (2) freehand scanning systems, (3) 2D matrix transducers.

One approach is to mechanically sweep (tilt, rotate or linearly translate) the conventional 1D linear/phased array transducer by a motorized system to acquire 3D dataset over the entire volume, as shown in figures 1.4a and 1.4b [20-22]. Since the scanning method is defined in advance, both the position and orientation of the 2D images are accurately known. For these transducers, the scanning mechanism can be designed in the housing of the transducer, or externally hold the transducer with fixtures [19]. Due to the extra hardware in mechanical sweeping transducers, the ultrasound system in this technique is usually heavy and bulky, and that makes it inconvenient to use. With this approach, large errors occur due to the motion artifact [17].

With freehand scanning systems, the position and/or orientation is measured with a sensor attached to the conventional 1D array transducer. While the transducer is manipulated, the trajectory and orientation are recorded together with acquired 2D images and stored in a computer. This information is later processed to reconstruct the 3D image [19, 23, 24]. Since the relative locations of the acquired 2D images are not predefined, the operator must ensure that the spatial sampling is appropriate and the set of images has no significant gap [17]. Different types of sensors such as optical positioner, magnetic sensors, acoustic positioner, and arm positioners have been employed in this method [17, 24-27]. In practice, the freehand scanners need special and temporal calibration each time before use, and the probe should be moved on a suitable path and speed over the skin surface to avoid artifacts [19]. Figure 1.4c shows a schematic of the freehand scanning technique for 3D imaging.

In both motorized scanning, and free-hand scanning an optimal 1D array transducer are utilized. Since the fabrication technology for 1D arrays has matured, these two techniques provide high image quality. In contrast, the poor spatial resolution between imaging plan and slow scanning time, limit the usage of these techniques for applications such as echocardiography, where the vessel/cardiac motion needs to be tracked [18].

Another approach for 3D imaging is to make a 2D matrix array in both elevation and azimuthal directions, and construct the image with 3D volumetric data, as shown in figure 1.4d. With a 2D array, the transducer could remain stationary, and electronic scanning could be used to sweep the ultrasound beam over the entire volume under examination, while both

lateral and azimuthal resolution remain the same [17]. This technique has several advantages compared to other 3D approaches, such as electronic steering and beamforming, 3D focusing and aperture shifting, which overcome the speed limitation for high volume rates in other approaches. However, the fabrication and implementation of 2D arrays are difficult [28]. There are three major challenges when fabricating 2D array transducers: large number of transducer elements; making electrical connections; high electrical impedance of the elements; and low sensitivity of the small elements [29].

Since the size of the elements in the 2D array is small, this results in high electrical impedance (~2 kΩ for 7 MHz transducers) for the transducer elements. Due to the impedance mismatch between the elements and connecting coaxial cables, the transducer element cannot efficiently drive the coaxial cable that connects the array to the ultrasound scanner [29].

In order to avoid the grating lobes in a 2D array transducer, the element pitch should be kept below the half of the wavelength in both lateral and azimuthal directions [3]. In contrast, the aperture should be large for high lateral resolution [17]. Therefore the number of elements in the 2D matrix array will be too large (i.e. >1000 transducer elements). Manufacturing such a matrix transducer is possible; however, making the electrical connections to all elements is challenging [30]. Due to hardware limitations on most ultrasound machines, a maximum of 256 transmit, and 256 receiving channels can be connected to the mainframe. Several researchers have proposed different selection of transmit and receive elements in the 2D array, such as Mills cross, random and sparse arrays, to overcome the hardware limitation [28, 29, 31-33]. These devices are capable of high frame rate 3D imaging, but the image quality is limited by the number of connected elements [34]. To increase the image resolution, contrast and SNR, or in general to improve the image quality more elements should be employed, and therefore the matrix should be fully populated [35].

To keep the fully populated matrix transducer while having reduced the number of channels, different approaches have been used to interface the matrix transducer. The signal from a sub-aperture set of the receiving elements can be locally beam-formed into one output signal [34, 36, 37]. With a row-column approach, it is possible to focus the transmit beam in one direction and the received beam in the orthogonal direction. The number of channels required in this approach is reduced from $N \times N$ to $2 \times N$, where N is the number of elements on each direction in the matrix array [38-40]. Switch matrices are proposed to connect a selection of elements in transmit and receive [41]. Annular rings are designed to connect to the elements of the 2D matrix transducer with a limited number of delay lines [41-43]. Channel multiplexing is also another approach to combine the received data from several elements with one output line simultaneously, the costs of which is a reduction in the imaging frame rate [44]. All of these techniques have their own pros and cons.

An efficient approach to making a 2D matrix transducer is to build the array of transducer elements directly on top of an Application Specific Integrated Circuit (ASIC). The ASIC can perform amplification to improve the signal quality directly under the piezoelectric elements, implement per-element processing, switching, impedance matching, multiplexing and/or signal combination to achieve the channel count reduction for connecting the large number of elements in the 2D array to 256 or less, which can be accommodated by commonly used

ultrasound systems [45]. With the improvements in the ASIC technology, the per-element circuitry occupies a small size, such that the matrix of transducer array can be built directly on top of the ASIC [34, 36].

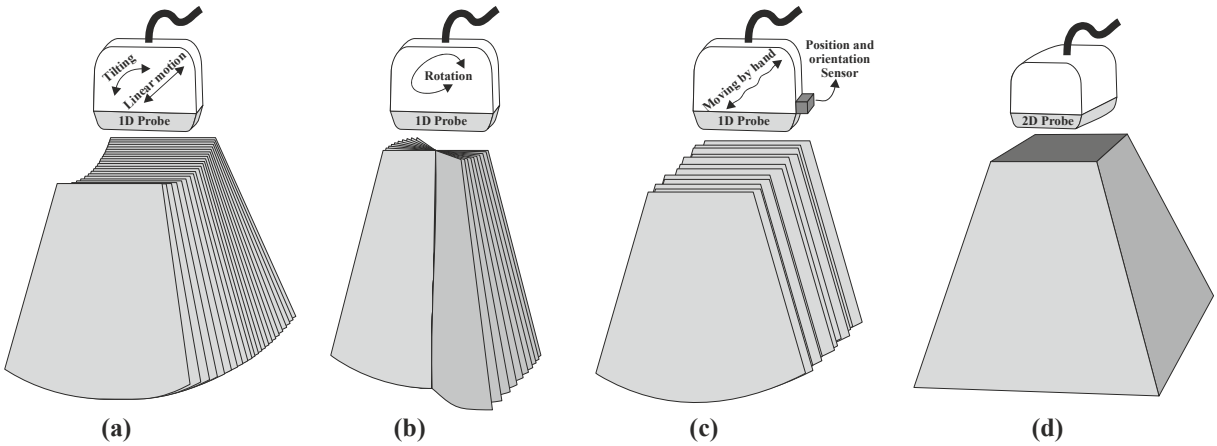

Figure 1.4. Different forms of data acquisition for 3D ultrasound imaging, **(a)** mechanically sweeping a 1D probe using a motorized system, **(b)** rotation of a 1D probe using a motorized system, **(c)** freehand method by adding a position and orientation sensor to a 1D probe and manually moving the probe through a trajectory by the sonographer, and **(d)** using a 2D matrix probe to acquire 3D data set for pyramidal scan.

1.4. Clinical applications

In this thesis, we have two specific clinical applications in mind: carotid artery imaging, and transesophageal echocardiography. The state of the art of the current technologies for these two applications, and the demand for improvement are explained below.

1.4.1. Carotid artery imaging

Stroke is among the five leading causes of mortality in the United States. In 2013, stroke approximately caused one out of twenty deaths. Each year, around 795,000 people experience a new or a recurrent stroke in the United States, which means an average rate of one person every 40 seconds [46]. The mortality rate is 30%, and many of the surviving patients experience permanent disabilities [47]. Therefore prevention is very important.

Ischemic stroke, which occurs as a result of blocked blood vessels to the brain, accounts for 90% of all strokes [48]. One of the main reasons for ischemic strokes is atherosclerosis with stenosis, which is the narrowing of the carotid arteries due to the accumulation of plaque inside the artery [49]. Atherosclerosis is a disease in which the inside of an artery narrows with plaque accumulation, and it can lead to serious problems, including heart attack and stroke. These plaques are made from fat, cholesterol, calcium, and other substances found in the blood, which are accumulated within the artery, causing an arterial lesion with inflammation and thickening of the vessel walls. These atherosclerotic lesions can grow and change over time, and thereby become evident, but they are not always symptomatic and many of them disappear. Atherosclerotic lesions of the carotid arteries may begin in infancy, but the arterial response that initiates atherosclerosis has not definitively been identified [50]. The vascular burden of atherosclerosis increases in volume and extent over time, remaining

clinically ‘silent’, while progressing through stages of development, with changes in the morphology and composition of lesions. Advanced lesions are associated with intimal disorganization and thickening, deformity of the arterial wall, and are often associated with complications such as fissure, hematoma, and thrombosis. Advanced lesions may produce symptoms, but the lesions that precede them are silent [51].

Atherosclerosis is considered a generalized disease that affects the entire vascular system, including cardiac performance. In a clinical research project on patients with chest pain, it was shown that for patients with the impaired left ventricular systolic performance the presence of carotid disease reflects the presence of severe coronary artery disease, whereas in patients with normal ejection fraction the absence of carotid disease reflects the absence of severe coronary artery disease. Thus carotid artery disease can be used as a marker for the presence of severe coronary artery disease [52, 53]. Since the carotid arteries can be assessed much more readily than the coronary arteries of the heart, this opens new ways of early screening for risk factors, diagnosis, and treatment of cardiovascular diseases. Detection of atherosclerotic plaque is critical for preventing future cardiovascular events [54].

Currently, four diagnostic modalities are used to image the carotid artery: digital subtraction angiography (DSA), duplex ultrasound (DUS), computed tomography angiography (CTA), and magnetic resonance angiography (MRA). DSA provides a radiographic visualization of the carotids vessels with a minimal view of the background tissues. Two images are taken before and after the injection of a contrast medium, and the first picture is subtracted from the second one. DSA is considered as the “gold standard” in carotid stenosis assessment, however, in comparison with MRA or carotid ultrasound it is more expensive and it carries a significant risk of stroke or death due to the invasive nature of the examination [55]. Carotid DUS is a non-invasive, safe, and inexpensive technique, which allows the direct visualization of morphology and flow measurement. However the accuracy of this technique depends on the expertise of the sonographer and the patient habitus, and variations in the patient’s anatomical situation may cause difficulties in detection. Acquisition of CT images is fast and relatively operator independent, and the main disadvantages are the use of iodine contrast medium intravenously and radiation. MRA produces 3D images of the whole artery with good sensitivity for the detection of carotid stenosis. It is less operator dependent compared to DUS and there is no radiation in comparison to DSA and CT, however, MRA is more expensive and is less readily available. The choice of the imaging method for carotid artery examination mainly depends on the clinical indications for imaging and the availability and expertise at individual center. The general approach to the patients with suspected carotid stenosis is to first perform DUS and then follow up with other non-invasive methods such as CTA or MRA [56].

1.4.2. Transoesophageal Echocardiography

Cardiovascular disease is a term that describes a range of diseases related to the heart and the blood vessels, such as atherosclerosis, congenital heart diseases, valvular heart diseases, rheumatic heart diseases and arrhythmias [57]. Atherosclerosis is a condition where plaques are built up in the arterial walls obstructing the blood flow. Atherosclerosis is linked to

coronary artery disease, which may lead to heart attack, cerebrovascular disease leading to stroke, diseases of the aorta and arteries, and peripheral vascular disease [57]. We will pay specific attention to two clinical cardiac conditions in which transesophageal echocardiography (TEE) imaging is especially important: atrial fibrillation and congenital heart diseases.

Atrial fibrillation is caused by rapid and irregular heart rate due to abnormal contraction of the atria; therefore the myocardial tissues cannot relax properly between contractions. This can lead to insufficient blood circulation in the atria and the formation of blood clots, causing a high risk of stroke. Atrial fibrillation is currently the most prevalent arrhythmia across the world. It is estimated that more than 2.5 million American adults and 4.5 million people in Europe are suffering from this disease [58]. Approximately one-third of hospitalizations for cardiac rhythm disturbances in both the USA and the EU are related to this problem [58]. Therefore, atrial fibrillation has become a considerable challenge to the modern health care system. It can be diagnosed either with an electrocardiogram (ECG) or by checking a patient's pulse. Currently, TEE plays an important role in treating patients with atrial fibrillation [59]. TEE also offers opportunities to guide catheter-based interventions. 3D TEE provides additional geometrical information, and in lengthy interventions or monitoring applications, a smaller-sized transducer is beneficial.

Congenital Heart Disease (CHD) is a problem of the heart's structure that is present at the time of birth. Every year, more than 32,000 children in the USA and approximately 36,000 children in the EU are born with CHD [60, 61]. Therefore, an improvement in CHD diagnosis and treatment procedure will have a significant impact on the healthcare system and wellbeing of the patients. Patients with CHD may need medication, surgery, or cardiac catheterization to reduce the effects of and/or repair the defects. In CHD patients, TEE has shown to be very useful for assessment of the often very complex, abnormal 3D anatomy prior to and during cardiac surgery [59]. Since these surgeries often need to be performed at a very young age or even directly after birth, pediatric TEE probes are smaller in size than adult TEE probes.

Typically, there are two types of echocardiography routinely performed in the clinic: transthoracic echocardiography (TTE) and transesophageal echocardiography (TEE). In TTE, an ultrasound transducer is placed on the chest wall and the imaging of the heart is performed through the acoustic window in between the ribs. Images produced by TTE have poor quality because of the limited acoustic window, reflections from the ribs, and high attenuation due to the large distance between the heart and the skin. Unlike TTE, in TEE, a transducer is mounted on the tip of a gastroscopic tube and inserted via the mouth into the patient's esophagus to image the heart. Images produced by TEE are not degraded by the skin, fat, or ribs. Moreover, as the esophagus is located only a few millimeters away from the heart, there is little attenuation and the received ultrasound signals in TEE are stronger than those in TTE. Since the traveling distance is low in TEE, higher frequencies can be used, and consequently, the axial resolution is higher. TEE, therefore, produces a superior image quality to TTE, especially for cardiac structures such as the aorta, pulmonary artery, valves, atria, atrial septum, appendages and even the coronary arteries.

Recently Oldelft Ultrasound has introduced the microMulti TEE transducer (μTEE) primarily for neonatal and pediatric patients. The μTEE probe has a phased array including 32

transducer elements and can produce 2D images. The probe has proven to be very useful in pediatric patients mainly because of the small size and excellent images [62-64]. Furthermore, this probe has been used for monitoring adults undergoing minimally-invasive interventions [65, 66]. Additionally, the μTEE probe is useful for diagnosing hemodynamically unstable patients both in routine preoperative cases and in postoperative critical care [67].

For 3D TEE in adults, there are a number of commercially available matrix array TEE probes (X7-2t from Philips Ultrasound, Bothell, WA [68], V5M TEE from Siemens Healthcare GmbH, Erlangen, Germany [69], and 6VT-D from General Electric Healthcare, Amersham, U.K. [70]). These matrix TEE probes are capable of real-time acquisition and live 3D display. However, they are much larger than the μTEE probes and therefore cannot be used for pediatric patients. Also in adults, due to patient discomfort, they are not suitable for long-term monitoring without full anesthesia. In contrast, a transnasal insertion of the μTEE probe has shown to be tolerated by patients for up to 24 hours [71, 72].

Several studies have shown that real-time 3D imaging is more beneficial than 2D imaging in most cardiac conditions [73, 74] because of its superior visualization of different 3D structures in the heart. Even though the μTEE probe is very useful for real-time 2D imaging, it is not capable of performing real-time 3D imaging on the heart. It should be noted that it is possible to reconstruct a 3D image from 2D TEE images (also for the μTEE probe) by rotating the imaging plane and recording over many heart cycles, but that procedure requires offline processing of sequential acquisitions gated to ECG [75]. These lengthy acquisitions and the post-processing of the acquired data increase the duration of the examination and also suffer from radial artifacts [76]. Therefore, it does not meet the need for real-time 3D imaging.

One goal in this thesis is to develop a matrix TEE transducer with the size of the μTEE probe and imaging capabilities of a 3D TEE probe. The results in Chapters 7 and 8 explains the design, fabrication, and characterization of two prototypes of miniaturized matrix transducer suitable for 3D TEE in pediatric patients as well as for transnasal use in adults for long-term monitoring. The prototype transducer consists of a receive aperture with an effective aperture area similar to the μTEE (5×5 mm^2) and a very small central transmitter (1.2×1.2 mm^2) capable of producing wide transmit beams. It is integrated on an ASIC for applying micro-beamforming to pre-steer the receive beams in 3D space. Thus, the micro-beamformers help in connecting the required elements (~1000) using a limited number of cables (~130) that can fit in the gastroscopic tube and can be connected to any ultrasound system.

1.5. The aim of the PhD project

Accurate assessment of carotid artery disease by measuring blood flow, plaque deformation and pulse wave velocity requires 3D information. The volume rates also should be high enough (> 1 kHz) to display the transient behavior along the arterial wall [77]. Building a transducer that is capable of providing 3D ultrasound image at such volume rates is challenging, especially when considering a large aperture (> 20 mm), and relatively high frequency (> 5 MHz) that is normally desired for carotid artery imaging.

In this thesis, we demonstrate a dedicated 2D matrix ultrasound transducer together with an ASIC, for real-time 3D echography of carotid arteries. We have designed a new configurable and tileable transducer, containing a matrix of 24×40 (rows $\times$ columns) PZT transducer elements, which are directly mounted on an ASIC. The ASIC contains transmit and receive switches, and control logic for each element. Through the row level transmit and receive buses, electrical connections between different combinations of elements and the ultrasound machine can be made. This enables fast programmable switching between various elements configurations. Furthermore, to improve the image quality it is possible to use compressive sensing by steering the transmit beam at different angles, and also use the on-chip memories to load up to nine different patterns and quickly switch between different patterns with a single clock. The design allows for tiling several of these arrays together to make a larger matrix array suitable for carotid imaging applications. The final goal is to tile an array of 10×2 of these ASICs to make a transducer with ~ 20,000 transducer elements in an aperture with $12\ \text{mm} \times 36\ \text{mm}$ for plane wave imaging of carotid arteries. This probe is capable of generating high volume rate images (up to 1000 volumes/s). It can be used to measure 3D vessel wall properties, including plaques and 3D blood-flow profiles. We think that this probe opens new ways of early screening for risk factors, diagnosis, and treatment of cardiovascular diseases.

For 3D transesophageal echocardiography, in this thesis we demonstrate the design, fabrication and characterization of a miniature PZT-on-CMOS matrix transducer. The main goal is to miniaturize the TEE probe while having the 3D signal acquisition and processing in real-time. This probe consists of a 32 × 32 array of PZT elements integrated on top of an Application Specific Integrated Circuit (ASIC). A partitioned transmit/receive array architecture is proposed where the 8 × 8 transmitter elements, located at the center of the array, and the remaining receive elements are grouped into 96 sub-arrays of 3 × 3 elements. The echoes received by these sub-groups are locally processed by micro-beamformer circuits in the ASIC that allows pre-steering up to ±37º. The probe is fully characterized in a series of water-tank measurements and the properties are very suitable for a miniature pediatric real-time 3D TEE probe.

This thesis focuses on part of the research including the mechanical design, fabrication, and acoustical characterization of the probe. The electronic design and characterization are done in collaboration with Electronic Instrumentation Lab of the Technical University of Delft, and development of the imaging algorithms for diagnostic purposes was done in cooperation with Thoraxcenter in the Erasmus Medical Centre.

1.6. Outline of the thesis

With this brief introduction we obtain the general idea why this new transducer is important for medical ultrasound imaging applications. In other chapters of this thesis we discuss the various steps of designing, manufacturing and characterizing such a matrix transducer.

In **Chapter 2** the influence of subdicing on vibration performance of the ultrasound transducer element is studied. The radiation impedance is calculated from a mathematical

model, and the results are compared with the finite element simulations for a 1D transducer array. The number of subdicing cuts and the depth of the cuts are optimized to improve the acoustical performance. The results show that optimal subdicing can enhance the image resolution and contrast by improving the signal to noise ratio.

The effect of subdicing on the electromechanical performance of a transducer element is both analytically and experimentally investigated in **Chapter 3**. For this purpose a matrix transducer with elements width larger than a wavelength is considered, and zero, one, or two subdicing cuts are applied. The simulation results are compared with acoustic measurements. The results proof that subdicing improves the performance of elements, and we conclude that the transducer element with one subdicing cut shows the best performance.

The acoustical effect of a silicon backing under a transducer array is described in **Chapter 4.** The mechanism of the mechanical crosstalk and the effect on the directivity pattern is explained. Two solutions are proposed to reduce the crosstalk effect: by decreasing the silicon thickness and putting an absorbing epoxy behind, or by applying extra cuts on the backside of the ASIC to disturb the waves in silicon. The simulation results show that both solutions can be used to smooth the directivity pattern.

The design of the ultrasound matrix transducer together with an ASIC for high frame rate 3D carotid artery imaging is described in **Chapter 5**. The electrical performance of the individual components (i.e. the LNA linearity and saturation level at different settings of the ASIC, the buffer performance, and the Verasonics performance at different TGC gains) are evaluated. It is shown that for a proper interpretation of the received signals, the performance of all electrical components in the receiving chain, and the whole electrical chain should be electrically characterized.

The design, fabrication, and acoustical characterization of a prototype of piezoelectric matrix transducer with a single ASIC, as a proof of concept for a larger probe for high frame rate 3D ultrasound imaging of carotid arteries is described in **Chapter 6**. The transducer contains a matrix with 24×40 elements with 150 μm pitch, which are mounted on the ASIC. The specifications of the ASIC for programming for different transmit and receive configurations are experimentally validated. Furthermore, the acoustical performance of the individual elements in transmit and in receive are fully characterized in a series of measurements. Finally the sample is used in an imaging application on a phantom.

A prototype of a piezoelectric matrix transducer with 9×12 transducer elements which are mounted on an ASIC is described in **Chapter 7**. The prototype is designed for miniaturized 3D transesophageal echocardiography (TEE) application. The concept of micro-beamforming and adjustable gains are applied with the ASIC, and the electromechanical performance of the transducer is characterized in different measurements. Both the measured characteristics of the individual transducer elements and the performance of the ASIC are in good agreement with expectations, demonstrating the effectiveness of the proposed techniques.

Chapter 8 presents the design, fabrication and characterization of a miniature PZT-on-CMOS matrix transducer for real-time pediatric 3D transesophageal echocardiography (TEE). This probe consists of a 32×32 array of PZT elements integrated on top of an ASIC. A

partitioned transmit/receive array architecture is designed where the 8×8 transmitter elements, located at the center of the array, are directly wired out and the remaining receive elements are grouped into 96 sub-arrays of 3×3 elements. The echoes received by these sub-groups are locally processed by micro-beamformer circuits in the ASIC that allows pre-steering up to ±37º. The performance of the transducer is experimentally characterized and it is shown that the properties are very suitable for a miniature pediatric real-time 3D TEE probe.

Finally in **Chapter 9**, an overview of the achievements in this thesis is summarized. The results of this thesis are categorized in two aspects. The results in Chapters 2, 3 and 4 have contributed to the physics of ultrasound transducers. On the other hand, the results in Chapters 5 to 8 explain the developed technology for two specific applications: the carotid artery imaging, and the transesophageal echocardiography (TEE). Other potential applications and some recommendations for the future works are given in this chapter.

CHAPTER 2

Improving the Performance of a 1-D Ultrasound Transducer Array by Subdicing[1]

Abstract

In medical ultrasound transducer design, the geometry of the individual elements is crucial since it affects the vibration mode of each element and its radiation impedance. For a fixed frequency, optimal vibration (i.e., uniform surface motion) can be achieved by designing elements with very small width to thickness ratios. However, for optimal radiation impedance (i.e., highest radiated power), the width should be as large as possible. This leads to a contradiction that can be solved by subdicing wide elements. To systematically examine the effect of subdicing on the performance of a 1-D ultrasound transducer array, we applied finite-element simulations. We investigated the influence of subdicing on the radiation impedance, on the time and frequency response, and on the directivity of linear arrays with variable element widths. We also studied the effect of varying the depth of the subdicing cut. The results show that, for elements having a width greater than 0.6 times the wavelength, subdicing improves the performance compared with that of non-subdiced elements: the emitted pressure may be increased up to a factor of three, the ringing time may be reduced by up to 50%, the bandwidth increased by up to 77%, and the sidelobes reduced by up to 13 dB. Moreover, this simulation study shows that all these improvements can already be achieved by subdicing the elements to a depth of 70% of the total element thickness. Thus, subdicing can improve important transducer parameters and, therefore, help in achieving images with improved signal to noise ratio and improved resolution.

[1]This chapter has been published as:
Jovana Janjic, Maysam Shabanimotlagh[*], Gijs van Soest, Antonius F. W. van der Steen, Nico de Jong, and Martin D. Verweij; Improving the performance of a 1-D ultrasound transducer array by subdicing, IEEE Transactions on Ultrasonics, Ferroelectrics, and Frequency Control, 2016, 63, 8, pp. 1161-1171.
[*] The first and second authors equally contributed to this work.

2.1. Introduction

Most of the clinically available ultrasound imaging probes are 1-D linear transducers. They consist of small piezoelectric (PZT) elements, which are the active components of the probe. An electrical excitation is used to induce vibration of the individual elements, which in turn generates pressure waves that propagate into the medium. The pressure waves reflected from different scatterers are subsequently received by the elements and converted back into electrical signals, which are processed in the ultrasound machines to yield echo images. To create images with high resolution and high signal-to-noise ratio, the geometry of the elements plays a crucial role in transducer design. This is because the geometry affects both the element vibration and the element radiation impedance.

Regarding the element vibration, it is known that if the width-to-thickness ratio is smaller than 0.7 [78], the element will mainly vibrate along the thickness direction. Knowing that the wavelength in PZT is almost twice the wavelength in water (λ), we can also say that thickness vibration is obtained when the width of the element is well below 0.7λ. Elements with a thickness vibration have a piston-like behavior; this behavior is considered optimal because all the surface points of the element, when excited, will have the same velocity amplitude and phase, which is favorable for the transmission efficiency.

The geometry also affects the radiation impedance, which describes the acoustic coupling of the vibrating element to the medium, and is usually defined for piston motion [79]. To obtain the highest radiated power, the radiation impedance should be real and equal to the acoustic impedance of the medium. For a wavelength λ and a circular element with diameter a, the complex radiation impedance is mainly imaginary for $a < 0.5\lambda$ [79, 80]. This means that little or no energy is transmitted into the medium. A similar behavior is found for square elements with sides a and infinitely long strip elements with width a: the radiation resistance drops quickly when a assumes values below 0.7λ [81, 82]. The strip geometry is representative of 1-D ultrasound transducer arrays, where each element is many times longer than it is wide.

From what was stated in the previous paragraphs, it is clear that to design 1-D transducer arrays with piston-like behavior, elements with very small widths are preferred. However, for optimal radiation impedance, the element should be as large as possible. This leads to a contradiction when trying to achieve both optimal vibration and optimal radiation impedance. The current approach is to consider elements having a width between 0.5λ and λ. This, however, might not be the optimal solution.

The geometrical requirements for optimal vibration and optimal radiation impedance are even more crucial for high-frequency transducers. To better explain this, we can consider a linear array with a center frequency of 15 MHz and a wavelength λ of 100 μm in water. If we assume a PZT speed of sound of approximately 3000 m/s, the element thickness has to be 100 μm. Therefore, for optimal vibration and optimal radiation efficiency, the width of the element has to be about 70 μm. Such small dimensions, however, are difficult to achieve when manufacturing transducers, especially if we consider the difficulty of making electrical connections to these individual elements. A possible solution to this problem is to consider elements with a width greater than 0.7λ and perform subdicing.

Subdicing means cutting each transducer element into two or more sub-pillars while keeping the electrical connection between the elements intact [83]. Subdicing decreases the width-to-thickness ratio of the vibrating pillars and separates the lateral vibration from the thickness resonance [78, 83-86]. The depth of the subdicing cut is also important, mainly because of fabrication issues; by partially subdicing the elements, damage of the electrodes can be prevented and mechanical stability can be ensured. To date, it seems that no systematic studies have been performed that quantitatively show the effect of subdicing in itself and the influence of the subdicing depth on the transducer performances. In our opinion, such systematic studies are important to further improve the efficiency of the transducer design process.

In this paper, we systematically present the effect of subdicing by showing finite-element analysis (FEA) simulations obtained with PZFlex software (Weidlinger Associates, Los Altos, CA). We focus on the performance of linear array elements with an operational frequency of approximately 14 MHz. We analyze the influence of subdicing on the radiation impedance, the time and frequency response, and the directivity pattern. We also investigate the effect of the depth of the cut to understand if it is possible to partially subdice the elements and still achieve good transmission performance.

2.2. Simulation model and role of subdicing

In 1-D arrays the length of the elements is much larger than the width and the thickness [3]. Therefore, in this paper the elements will be considered infinitely long, which reduces our simulations to 2-D problems.

The 2-D simulation study is performed using the FEA software PZFlex, and the considered model is depicted in figure 2.1. In this study, the thicknesses of all the layers are fixed, while the width a of each of the elements is varied from 10 to 250 μm in steps of 10 μm. Only a portion of a realistic linear array is modeled, with a central active element and three neighboring passive elements on both sides. The space between the elements and in the subdicing cuts is approximately 8 μm wide and is taken to be void [87], while water is used as the medium in which the ultrasound is propagating. After subdicing, the width of the elements and the subdicing cuts may differ from the ideal values by at most ±2 μm, i.e., one grid step, due to numerical rounding. To reduce the simulation time, we assume symmetry in the plane $x = 0$. With this condition, only half of the model needs to be simulated. The domain is surrounded by absorbing boundary conditions to avoid reflections from its edges. The thicknesses and material properties of each layer of the transducer are given in table 2.1.

To validate the PZFlex model, we have compared the simulation results for the radiation impedance and for the directivity with the analytical curves. Moreover, a numerical test has been performed with a twice denser numerical grid. The obtained results showed no significant differences with the results obtained for our standard grid. This ensures the numerical accuracy of our simulations.

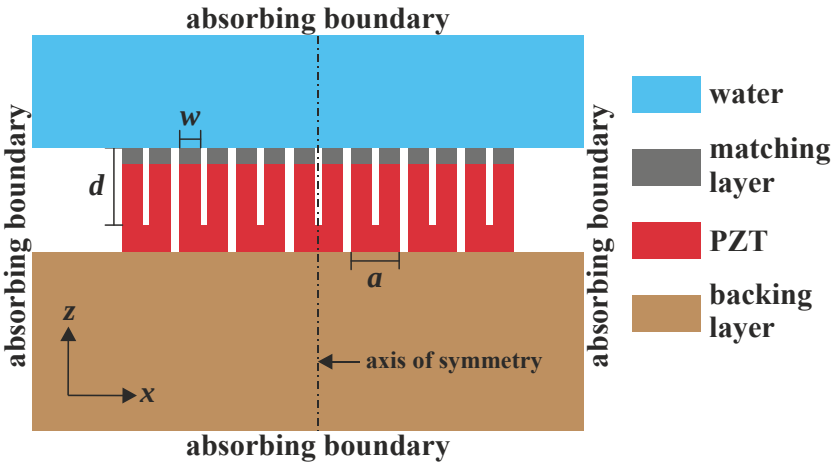

Figure 2.1. 2-D simulation model. Seven transducer elements are modeled and only the central element is electrically excited. The width of each of the elements is *a*, the width of the sub-pillars is *w*, and the depth of the cuts is *d*.

Table 2.1. The thickness and material properties used in the simulations.

Layer	Material	Thickness (μm)	Properties
PZT	Ceramic (PZT-5A)	100	$\rho = 7700\ \text{kg/m}^3$ $c_{11} = 147, c_{12} = 105, c_{13} = 93.7,$ $c_{33} = 113, c_{44} = 23, c_{66} = 21.2\ \text{MPa}$ ${}^{s}\varepsilon_{15} = 11.64,\ {}^{s}\varepsilon_{31} = -3.09,\ {}^{s}\varepsilon_{33} = 16\ \text{C/Vm}$ ${}^{s}\varepsilon_{11} = 10,\ {}^{s}\varepsilon_{33} = 8.09 \times 10^{-9}\ \text{C/Vm}$
Matching	Conductive epoxy	30	$\rho = 3350\ \text{kg/m}^3$ $Z = 6.7\ \text{MRayl}$ $c_{shear} = 1050\ \text{m/s}$
Backing	Tungsten loaded epoxy	500	$\rho = 2975\ \text{kg/m}^3$ $Z = 5.8\ \text{MRayl}$ $c_{shear} = 1960\ \text{m/s}$

The electrical impedance plot is the primary tool that we will employ to see whether an element has vibration modes with a non-uniform surface motion. To explain this, we show in figures 2.2 and 2.3 the electrical impedance versus frequency for elements in different situations.

Figure 2.2 demonstrates how the electrical impedance plot for a narrow ($a = 40\ \mu m = 0.4\lambda$) nonsubdiced element with piston-only motion is formed. The magnitude of the electrical impedance for a bare PZT element with a piston-like behavior is shown in figure 2.2(a). In the considered frequency band, a single minimum value of the electrical impedance occurs in this case at a frequency of 12.6 MHz. For this so-called resonance frequency, the corresponding mode shape is shown, confirming that the element vibrates only along the thickness direction. When a matching layer is added on top of the PZT, the electrical impedance changes, as shown in figure 2.2(b). It now has two minima and two resonance frequencies due to the presence of two different layers. For both resonance frequencies, the indicated mode shapes are still showing the typical piston-like motion.

Figure 2.3 illustrates what happens to the electrical impedance for a wide element before and after subdicing. Figure 2.3(a) shows the electrical impedance of a wide element ($a = 120\,\mu m = 1.2\lambda$) before subdicing. Multiple local minima are present, which correspond to different resonance modes. Two of the three resonance mode shapes are clearly showing an undesired nonuniform surface motion. The occurrence of the typical local minima in figure 2.3(a) is an indication that subdicing will be opportune. Figure 2.3(b) shows the electrical impedance when the same element is provided with two subdicing cuts that extend to the bottom of the PZT layer. Doing so yields an electrical impedance plot with two minima and corresponding mode shapes with a piston-like behavior. For the wide element considered, subdicing has restored the desired situation of figure 2.2(b).

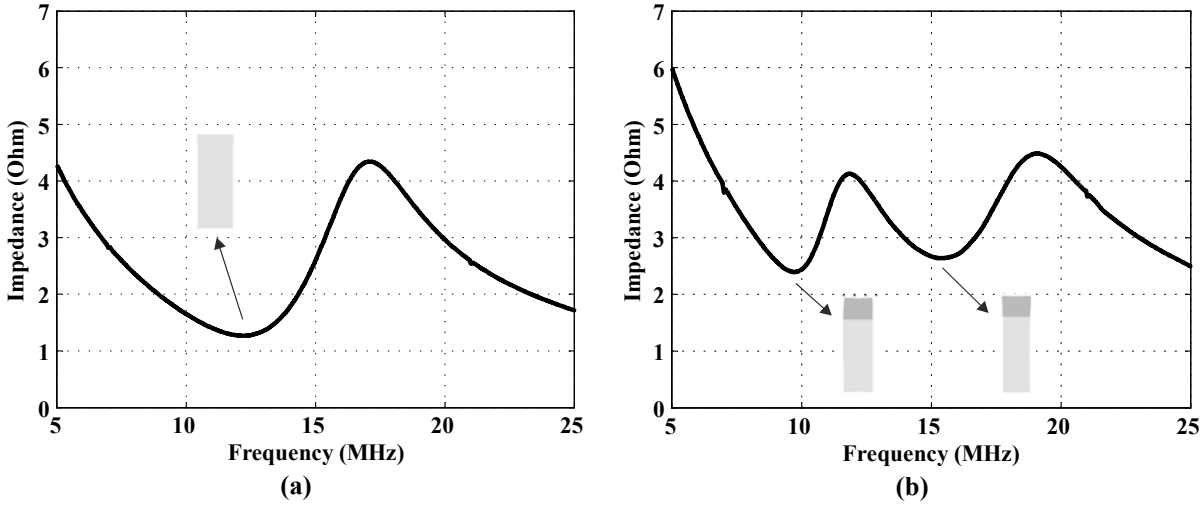

Figure 2.2. The plot of the electrical impedance per unit length for an element with a small width (a = 40 μm = 0.4λ) consisting of **(a)** bare PZT and **(b)** PZT with a matching layer. Gray insets: the mode shapes for the resonance frequencies at each minimum (light gray = PZT; dark gray = matching layer).

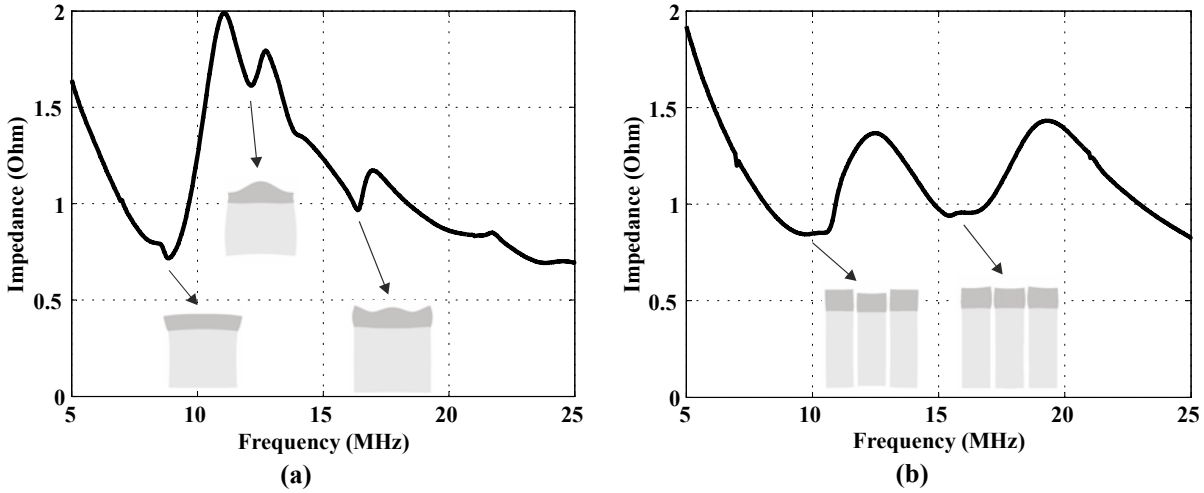

Figure 2.3. The plot of the electrical impedance per unit length for an element with a large width (a = 120 μm = 1.2λ) **(a)** before subdicing and **(b)** after subdicing with two cuts that run through the entire PZT and matching layer. Gray insets: the mode shapes for the resonance frequencies at each minimum (light gray = PZT; dark gray = matching layer).

2.3. Optimal number of subdicing cuts

We determined the optimal number of subdicing cuts for elements with widths a between 10 and 250 μm. We have defined the optimal number of cuts as the lowest n that yields $a/(n+1) \leq \lambda/2 = 50\,\mu m$. We have numerically verified that this is the number of equidistant subdicing cuts that will exclude modes with nonuniform surface motion, i.e., for obtaining the situation in figure 2.3(b). For the simulations, the central element was excited with a chirp pulse having a duration of 1 μs and a frequency sweep between 5 and 25 MHz. The chirp excitation was designed to have an even frequency content across the range of interest. The center frequency f_c of the subdiced element was obtained as the center of the −3 dB bandwidth of the average surface pressure.

In table 2.2, the optimal number of subdicing cuts n and the corresponding center frequency f_c are shown for elements with different widths a. Table 2.2 also shows the individual subpillar width w after subdicing as well as the products $k_c a$ and $k_c w$, where

$$k_c = \frac{2\pi f_c}{c} = \frac{2\pi}{\lambda_c} \tag{1}$$

with c is the speed of sound and λ_c is the wavelength at f_c, both in water.

The number of optimal subdicing cuts n varies from 0 to 4, while the sub-pillar width ranges from 26 to almost 47 μm. After subdicing, the product $k_c w$ is always close to 2 and the frequency f_c is about 14 MHz for all the widths a. This confirms that after subdicing, the dominant resonance frequency depends mainly on the thickness of the element, which is kept constant. In all the remaining simulations, the resonant frequency f_c is used as the excitation frequency for each specific width a.

Table 2.2. The optimal number of subdicing cuts, the center frequency f_c, the subpillar width w, and the product $k_c a$ and $k_c w$, for each element width a

a	n	f_c (MHz)	w (μm)	$k_c a$	$k_c w$	a	n	f_c (MHz)	w (μm)	$k_c a$	$k_c w$
10	0	17.9	10.0	0.75	0.75	140	2	13.9	42.7	8.17	2.49
20	0	15.0	20.0	1.26	1.26	150	2	13.5	46.7	8.50	2.65
30	0	14.5	30.0	1.83	1.83	160	3	14.4	35.0	9.68	2.12
40	0	13.5	40.0	2.27	2.27	170	3	14.3	38.0	10.21	2.28
50	0	12.8	50.0	2.69	2.69	180	3	14.1	40.0	10.66	2.37
60	1	14.6	26.0	3.68	1.59	190	3	13.6	38.0	10.85	2.17
70	1	14.3	32.0	4.20	1.92	200	3	13.5	45.0	11.34	2.55
80	1	14.2	36.0	4.77	2.15	210	4	14.3	37.6	12.61	2.26
90	1	13.4	42.0	5.07	2.36	220	4	14.2	39.2	13.12	2.34
100	1	13.1	46.0	5.50	2.53	230	4	14.1	41.6	16.62	2.46
110	2	14.7	33.3	6.76	2.06	240	4	13.8	43.2	13.91	2.50
120	2	14.5	36.0	7.31	2.19	250	4	13.6	45.6	14.28	2.60
130	2	14.3	40.0	7.81	2.40						

2.4. Radiation impedance

For each width a and corresponding frequency f_c, two different types of excitations have been simulated: a ten-cycle sinusoid is used to simulate a quasi-continuous excitation, and a two-cycle sinusoid is used to simulate an impulse-like excitation, which is commonly employed in imaging systems. After driving the element with either type of excitation, the average pressure and the average velocity over its surface have been computed.

In figure 2.4(a) and (b), the maximum of the envelope of the average pressure P_{max} and the maximum of the envelope of the average velocity v_{max} are plotted relative to $k_c a$, for both types of excitation and for both the nonsubdiced and optimally subdiced cases. The obtained values for P_{max} and v_{max} are also used to obtain the modulus of the radiation impedance Z. The latter quantity is defined for a piston moving in a perfectly rigid baffle as the average complex pressure amplitude divided by the real normal particle velocity amplitude [88]. Therefore, $|Z|$ may be found from figures 2.4(a) and (b) as

$$|Z| = \frac{P_{max}}{v_{max}} \tag{2}$$

Figure 2.4(c) shows the relative radiation impedance $|Z_r|$, defined as

$$|Z_r| = \frac{|Z|}{Z_{water}} \tag{3}$$

where $Z_{water} \cong 1.5$ MRayl. Moreover, in figure 2.4(c) the analytical curve for the radiation impedance of an infinitely long 2-D strip with piston-like behavior in a rigid baffle is shown for comparison. This curve is the result of the numerical computation of the following equation [82]:

$$|Z_r(\omega)| = \frac{1}{K}\int_{-K/2}^{K/2}\int_{-K/2}^{y} H_0^{(2)}(y - y')\, dy' dy \tag{4}$$

where $H_0^{(2)}$ is the Hankel function of the second kind and zero order, and $K = k_c a$.

For $k_c a > 3.5$ (or $a > 0.55\lambda_c$), the pressure and velocity after subdicing are up to three times higher than those in the nonsubdiced case for both types of excitations. This improvement in the transmit efficiency can be explained by two effects. The first effect of subdicing is the removal of modes with nonuniform surface motion, which causes an inefficient radiation into the acoustic medium. The second effect is a change in the electromechanical coupling factor of the PZT: when subdicing wide elements, the vibrational behavior of the PZT will change from plate mode to bar mode, which has a higher coupling factor [3, 89, 90].

In figure 2.4(c), for $k_c a < 2$ (or $a < 0.32\lambda_c$), the simulation results are in good agreement with the theoretical curve, confirming that for very small elements, the radiation impedance drops quickly, impairing the energy radiation into the medium.

Without subdicing, the radiation impedance for the ten-cycle excitation shows an irregularity of 40% around $k_c a = 10$, unlike the two-cycle excitation. This difference in behavior may be explained by the bandwidth of the two excitation signals. For a quasi-continuous excitation with a narrow bandwidth, most of the energy is used to excite a specific frequency, which might correspond to a mode with nonuniform surface motion. The two-cycle pulse simultaneously excites all occurring resonance frequencies, including the dominant thickness resonance. Therefore, simulations with narrow pulse excitation result in a radiation impedance that is in better agreement with the analytical derivation.

Disregarding the drop at $k_c a = 10$ that is seen for the ten-cycle excitation in the absence of subdicing, the radiation impedances obtained from the simulations assume, in general, values higher than those expected from the analytical derivation. This may be caused by the fact that the analytical curve is derived for a piston in a rigid baffle, while the simulated model is more representative of a transducer in a baffle with a finite compliance. When a compliant baffle boundary condition is assumed, the pressure at the surface of the element is higher than that for rigid baffle boundary condition [11]. Therefore, with a compliant baffle, a higher radiation impedance is expected.

Overall, for $k_c a > 5$ (or $a > 0.48\lambda_c$) and an optimal number of subdicing cuts, a dominant thickness vibration is obtained for both types of excitation, which results in a relative radiation impedance close to 1. This means that the radiation impedance is almost equal to the acoustic impedance of the medium and, therefore, almost all the power is radiated into the far field.

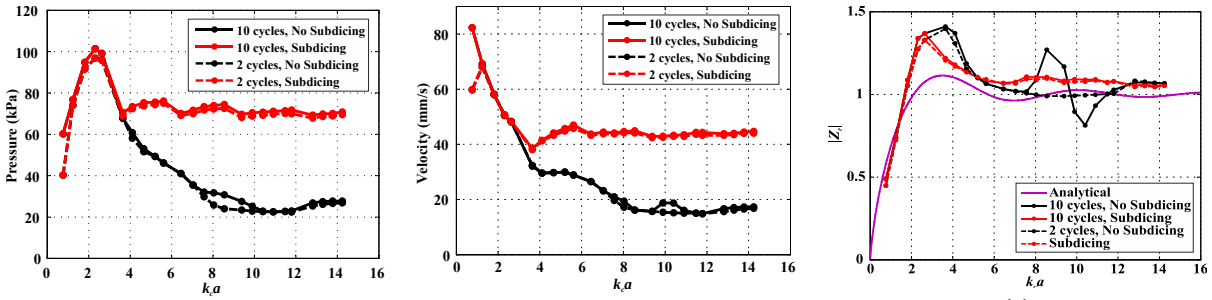

Figure 2.4. (a) Maximum average pressure, **(b)** maximum average velocity, and **(c)** relative radiation impedance for both types of excitations, plotted against $k_c a$. The width a of the elements is varying from 10 to 250 µm. For the subdiced curves, the optimal number of subdicing cuts n is indicated.

2.5. Time and frequency responses

In this section, we consider the effect of subdicing on the time and frequency responses of the elements in transmit and receive. We consider four different element widths that require a different optimal number of subdicing cuts: 1) $a = 60$ µm ($k_c a \cong 3.7$); 2) $a = 120$ µm ($k_c a \cong 7.3$); 3) $a = 180$ µm ($k_c a \cong 10.7$); and 4) $a = 240$ µm ($k_c a \cong 13.9$). For the transmit response, a two-cycle sinusoidal voltage excitation with a 1 V amplitude is defined at

the electrodes of the element, and the resulting emitted average pressure at the surface of the element is computed. For the receive response, a uniform two-cycle sinusoidal pressure excitation with a 1-Pa amplitude is defined close to the surface of the element, and the voltage at the electrodes of the element is computed.

For both the subdiced and the non-subdiced elements, the time trace of the transmitted pressures and the envelope of these signals are shown in figure2.5. For all but the smallest width, a relevant enhancement in the peak pressure amplitude is seen after subdicing, which is consistent with the results shown in figure 2.4(a). For the non-subdiced case, figure 2.5(b)–(d) shows multiple peaks in the envelopes and long ringing tails. Subdicing substantially reduces these adverse effects in the transmitted waveform.

Figure 2.6 depicts the frequency responses of the subdiced and the non-subdiced elements, both for transmit and receive. The differences between subdiced and non-subdiced elements are also apparent in the frequency domain. For non-subdiced elements, figure 2.6 shows strong spectral amplitude fluctuations in both transmit and receive spectra, which disappear after subdicing. In general, the frequency responses in transmit and receive have a similar shape after subdicing, although they are not exactly the same. The small differences are explained by the reciprocity equation [91], which relates the transmit function to the receive transfer function via the electrical impedance of the element. Another interesting observation from both the time responses and the frequency spectra is the similarity between the curves for all the different element widths after subdicing. This is because the final sub-pillar width w is almost constant (see table 2.2). This means that the time and frequency responses after subdicing have become dependent on the sub-pillar width rather than on the total element width.

To further quantify the improvement of the time response of the transmitted pressure, we define the −6 and −20 dB ringing intervals $\Delta t_{-6\,\mathrm{dB}}$ and $\Delta t_{-20\,\mathrm{dB}}$, which are the time intervals over which the amplitude of the envelope is greater than −6 and −20 dB of its corresponding maximum. In addition to that, we introduce the relative ringing amplitude, defined as the size of the second peak of the pressure envelope divided by the size of the first (main) peak. The frequency domain performance in transmit is further quantified by the relative −3 dB bandwidth ($BW_{-3\,\mathrm{dB}}$), and the maximum dip within the band (in decibel relative to the −3 dB level). Table 2.3 lists these quantities for an element of size $a = 120$ μm ($k_c a \cong 7.3$) and a number of subdicing cuts ranging from 0 to 4. For this particular element, two subdicing cuts remove the spurious modes from the electrical impedance (figure 2.3). However, it is interesting to investigate if $n = 2$ is also optimal in terms of time and frequency response. Table 2.3 shows that when *n* is increased from 0 to 2, the ringing times are shortened and the relative ringing amplitude is decreased. For $n = 2, a$ − 3 dB bandwidth of 43.2% without dips is obtained. However, no further substantial improvement is obtained for $n > 2$. Therefore, for optimal performance in both the time and frequency domains, two subdicing cuts are sufficient.

The considerations for $k_c a \cong 7.3$ can be extended to the other element widths. In table 2.4, the characteristic time and frequency domain quantities are shown for the nonsubdiced and the optimally subdiced cases. The results demonstrate that the ringing time may be shortened

by up to 50% ($\Delta t_{-20\,\mathrm{dB}}$for $k_c a \cong 13.9$) and the relative ringing amplitude may be decreased by up to 80% ($k_c a \cong 7.3$). Moreover, the maximum increase in bandwidth is 77% ($k_c a \cong 3.7$), while the maximum dip is reduced by up to around 24 dB ($k_c a \cong 7.3$).

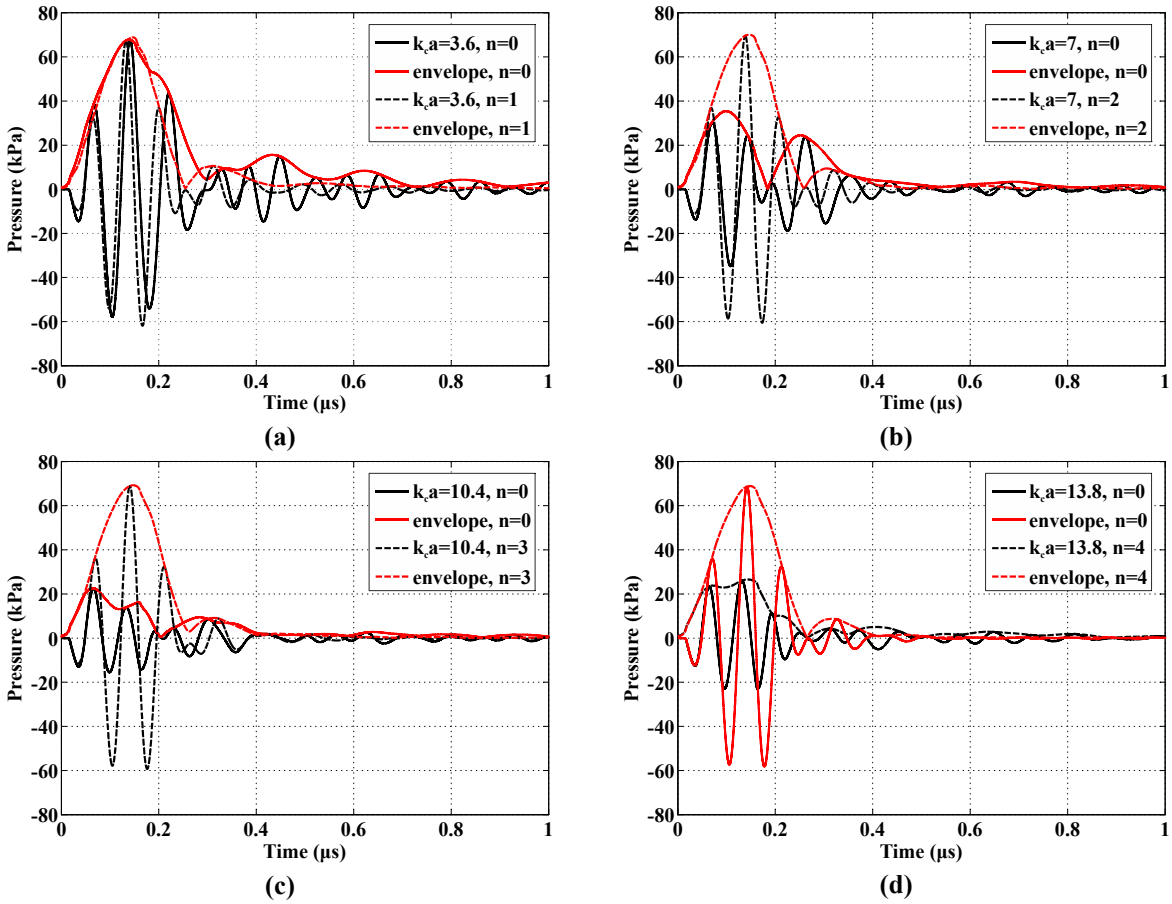

Figure 2.5. Average transmit pressure versus time for elements of size, **(a)** a = 60 μm ($k_c a \cong 3.7$), **(b)** a = 120 μm ($k_c a \cong 7.3$), **(c)** a = 180 μm ($k_c a \cong 10.7$), and **(d)** a = 240 μm ($k_c a \cong 13.9$). Plots for both the nonsubdiced (n = 0) and the optimally subdiced ($n \neq 0$) case are given, with envelopes. Excitation occurs with a two-cycle sinusoidal pulse with a 1 V amplitude.

Table 2.3. Characteristic time domain and frequency domain quantities for an element of size $a = 120$ μm ($k_c a = 7.3$) and the number of subdicing cuts n ranging from 0 to 4

	n	$\Delta t_{-6\mathrm{dB}}$ (μs)	$\Delta t_{-20\mathrm{dB}}$ (μs)	Ringing Amplitude (%)	$BW_{-3\mathrm{dB}}$ (%)	Max. dip (dB)
$a = 120$ μm $k_c a = 7.3$	0	0.25	0.42	69.0	60.2	23.7
	1	0.17	0.58	13.2	29.8	8.4
	2	0.14	0.32	13.5	43.2	0
	3	0.14	0.33	15.4	44	0
	4	0.14	0.33	15.6	45	0

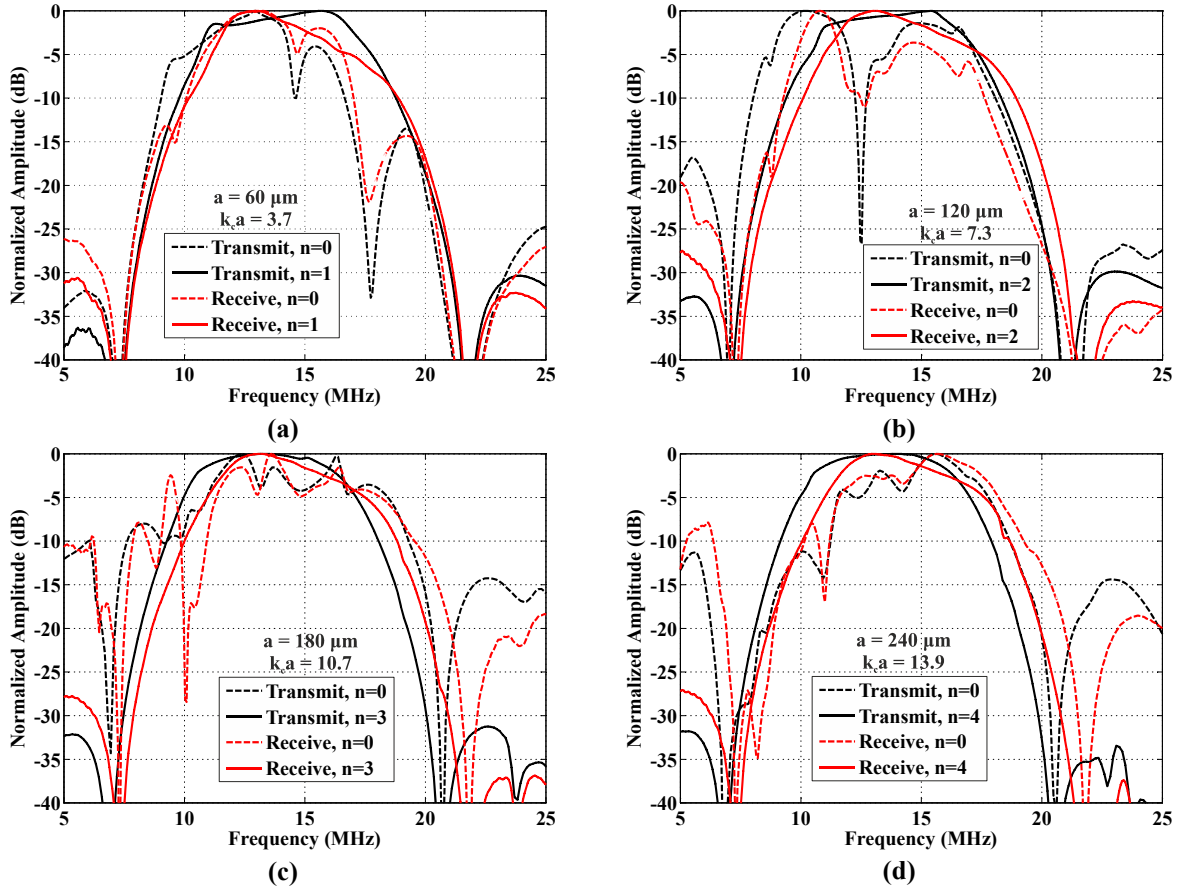

Figure 2.6. Frequency responses in transmit and receive for elements of size, **(a)** a = 60 μm ($k_c a \cong 3.7$), **(b)** a = 120 μm ($k_c a \cong 7.3$), **(c)** a = 180 μm ($k_c a \cong 10.7$), and **(d)** a = 240 μm ($k_c a \cong 13.9$). Plots for both the nonsubdiced ($n = 0$) and the optimally subdiced ($n \neq 0$) case are given.

Table 2.4. Characteristic time domain and frequency domain quantities for elements of size $a = 60$ μm ($k_c a = 3.7$), $a = 120$ μm ($k_c a = 7.3$), $a = 180$ μm ($k_c a = 10.7$), and $a = 240$ μm ($k_c a = 13.9$). Data for both the nonsubdiced ($n = 0$) and optimally subdiced ($n \neq 0$) cases are given.

	n	Δt_{-6dB} (μs)	Δt_{-20dB} (μs)	Ringing Amplitude (%)	BW_{-3dB} (%)	Max. dip (dB)
$a = 60$ μm	0	0.18	0.64	23.0	25.5	0
$k_c a = 3.7$	1	0.14	0.34	15.4	45.1	0
$a = 120$ μm	0	0.25	0.42	69.0	60.2	23.7
$k_c a = 7.3$	2	0.14	0.32	13.5	43.2	0
$a = 180$ μm	0	0.14	0.32	41.8	37.4	1.2
$k_c a = 10.7$	3	0.14	0.29	13.3	45.2	0
$a = 240$ μm	0	0.15	0.65	19.1	27.2	1.3
$k_c a = 13.9$	4	0.14	0.32	12.7	45.1	0

2.6. Directivity pattern

Directivity can be calculated in PZFlex using the extrapolation toolkit, which enables the computation of the magnitude of the transmitted pressure in the far field, assuming linear propagation. The directivity patterns for both the non-subdiced and optimally subdiced cases

are shown in figure 2.7, in which we show the analytical curve of the directivity $D(\theta)$, which follows from:

$$D(\theta) = \mathrm{sinc}\left(\frac{a\,\sin(\theta)}{\lambda}\right) \tag{5}$$

with θ being the observation angle, a the transducer width, and λ the wavelength [3]. This expression holds for an ideal piston in a rigid baffle.

For the smallest element size $a = 60$ µm ($k_c a \cong 3.7$), no sidelobes are present and no substantial difference is seen between the nonsubdiced and the subdiced cases. The other element sizes give rise to sidelobes, which are reduced by subdicing. Moreover, the directivity patterns for the subdiced elements are in good agreement with the analytical curves. This agreement further demonstrates the benefits of subdicing in achieving the ideal piston-like behavior.

It is important to mention that the directivity and, hence the choice of the element width, will depend on the specific application [11].

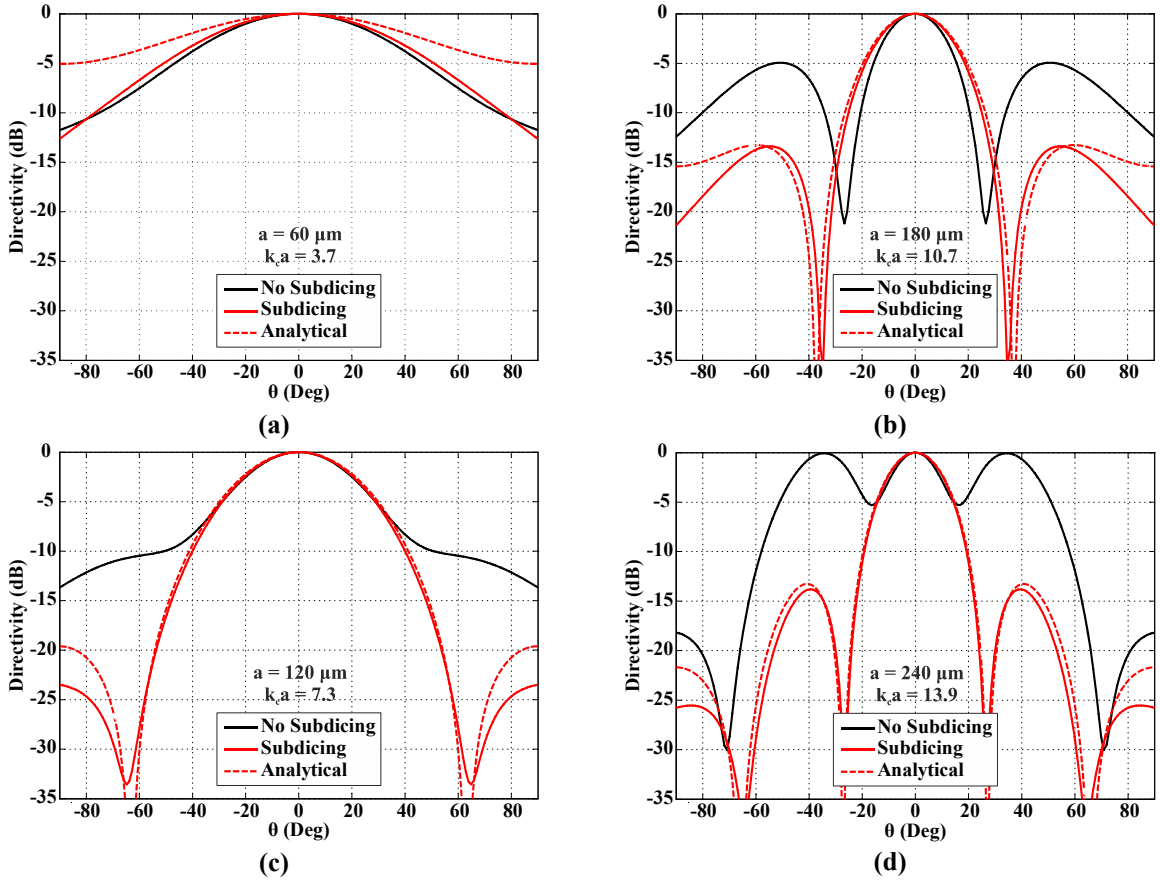

Figure 2.7. Directivity plots for elements of size, **(a)** a = 60 µm ($k_c a \cong 3.7$), **(b)** a = 120 μm ($k_c a \cong 7.3$), **(c)** a = 180 µm ($k_c a \cong 10.7$), and **(d)** a = 240 µm ($k_c a \cong 13.9$). Plots for both the nonsubdiced ($n = 0$) and the optimally subdiced ($n \neq 0$) case are given, together with the analytical curve.

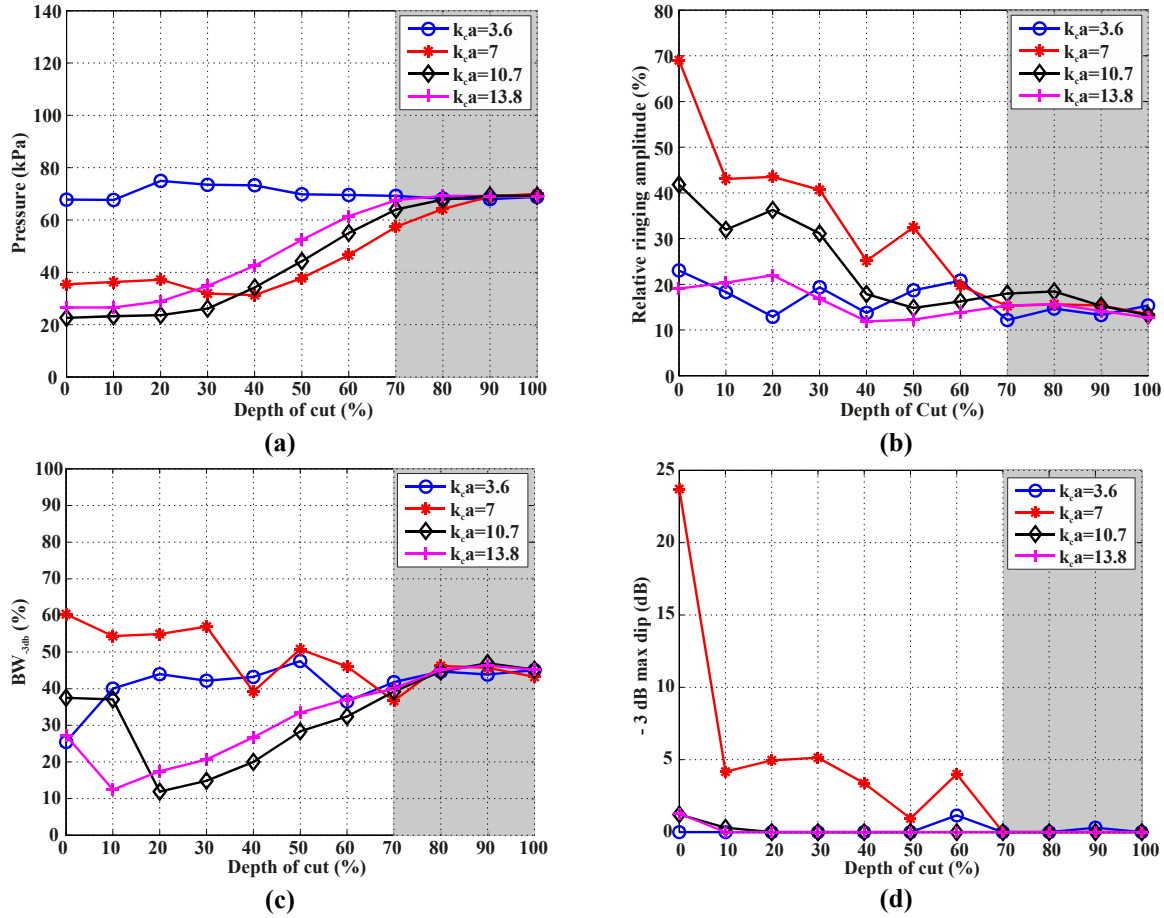

Figure 2.8. Influence of the relative depth of the subdicing cut *d*. **(a)** Maximum average surface pressure. **(b)** Relative ringing amplitude. **(c)** Relative −3 dB bandwidth in percentage. **(d)** Maximum dip in the frequency band. Data are shown for elements of size a = 60 µm ($k_ca \cong 3.7$), a = 120 μm ($k_ca \cong 7.3$), a = 180 µm ($k_ca \cong 10.7$), and a = 240 µm ($k_ca \cong 13.9$). In each case, the optimal number of subdicing cuts is applied. In the shaded area, almost no further improvements are obtained.

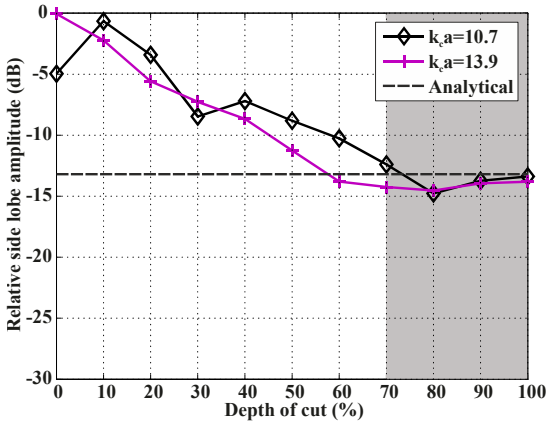

Figure 2.9. Relative sidelobe level versus the relative depth of the Subdicing cut. Data are shown for elements of size a = 180 µm ($k_ca \cong 10.7$), and a = 240 µm ($k_ca \cong 13.9$). In the shaded area, almost no further improvements are obtained. The dashed line is the analytical sidelobe level.

2.7. Subdicing depth

Because the cutting depth is an important aspect in the construction of a transducer, in this section, we consider the influence of using subdicing cuts that do not extend to the bottom of the PZT layer. The depth of the subdicing cut is varied from 0% to 100% of the total element thickness, i.e., the thickness of the PZT and the matching layer, in steps of 10%. Figure 2.8 shows the maximum of the average surface pressure, relative ringing amplitude, bandwidth, and maximum dip within the frequency band, as functions of the depth of the subdicing cut.

For $a = 60$ μm ($k_c a \cong 3.7$), both the maximum average surface pressure (figure 2.8a) and the relative ringing amplitude (figure 2.8b) are almost constant for increasing depth of cut because the element is so small that piston motion is predominant even in the nonsubdiced case. This is in agreement with the results of the previous sections. For wider elements, the increase in pressure and the decrease in relative ringing amplitude are appreciable when subdicing up to 70% of the total element thickness. The −3 dB bandwidth (figure 2.8c) and the maximum dip within the band (figure 2.8d) as functions of the depth of the cut have a less clear trend for the different element widths. Nevertheless, we can state that to have both a large bandwidth and avoid strong fluctuations within the band, the depth of the cut should be between 70% and 100%, irrespective of the width of the element. In this range also the emitted pressure and the relative ringing amplitude are almost constant and assume the highest and lowest value, respectively. Figure 2.9 shows the relative sidelobe levels for single elements of size $a = 180$ μm ($k_c a \cong 10.7$) and $a = 240$ μm ($k_c a \cong 13.9$) as functions of the depth of the cut. For increased subdicing depth, the sidelobes are reduced and, similar to the other characteristic quantities, for a depth of cut between 70% and 100%, an almost constant minimum value is reached.

2.8. Summary

In this study we have shown, through FEM simulations, that subdicing improves the performance of transducer elements having a width greater than 0.6 times the resonance wavelength in water. More precisely, subdicing improves the emitted pressure, the radiation impedance, the time response, the frequency response, and the directivity pattern.

The increase in the emitted pressure and in the radiation impedance after subdicing leads to an increase in the power radiated into the medium. High power is beneficial for improved signal-to-noise ratio during imaging. Regarding the time response, we showed that subdicing reduces the ringing time and the ringing amplitude. Ringing is an unwanted effect, which occurs when the radiation impedance of an element including a matching layer deviates from the impedance of the medium. This is the case when there is a nonuniform motion of the element surface. Subdicing restores the uniform motion at the surface and thus ringing will be avoided. A time response without ringing has a shorter pulse length, which in turn improves the axial imaging resolution. The frequency response also benefits from subdicing by obtaining a higher bandwidth and avoiding strong spectral dips.

Regarding the directivity pattern, low levels of sidelobes are necessary to avoid imaging artifacts originating from off-axis ultrasound beams. We have shown that subdicing can also reduce the sidelobe levels of wide elements.

The depth of the subdicing cut may be crucial during the fabrication process. Cutting all the way through the element can lead to mechanical instability and cause damage to the electrodes. We have demonstrated by our simulations that it is possible to achieve the most significant improvements in transducer performances by cutting to only a depth of 70% of the total element thickness.

We expect that the presented quantitative knowledge about the effect of subdicing on the transducer performances may help to improve the design of high-quality imaging transducers.

CHAPTER 3

Effect of Subdicing on Performance of an Ultrasound Matrix Transducer for Carotid Imaging: Numerical and Experimental Study[1]

Abstract

High frame rate volumetric ultrasound imaging of fast cardiovascular motion requires the use of a matrix transducer. The large amount (>1000) of transducer elements makes it necessary to reduce the number of channels inside the probe. This may be achieved by mounting the ultrasound matrix directly on a silicon chip that performs signal processing and data reduction. In addition, elements should be made as large as possible to restrict their number. However, increasing the width-to-thickness ratio of elements usually causes degradation of their performance due to the occurrence of modes with unwanted lateral vibrations. This adverse effect may be overcome by applying subdicing of the elements. To demonstrate the effect of subdicing, in this paper we consider a matrix array for carotid imaging and investigate, both numerically and experimentally, the effect of subdicing on the acoustical and electrical performance of the transducer elements. For the numerical evaluation we used the finite element package PZFlex, while for the experiments we perform water tank measurements on 7.5 MHz piezoelectric elements with zero, one, or two subdices, mounted on a silicon chip. We observe that numerical and experimental results agree qualitatively well for all the three subdicing cases. Furthermore, subdicing shifts the lateral resonance peaks outside the frequency band of interest, and increases the bandwidth of the transducer. For the considered application we conclude that the transducer element with one subdicing cut shows the best performance, with a central frequency of 7.7 MHz and a -3 dB bandwidth of 43%.

[1] This chapter is submitted for publication as:
Maysam Shabanimotlagh, Shreyas B. Raghunathan, Jovana Janjic, Verya Daeichin, Emile Noothout, Michiel A.P. Pertijs, Johan G. Bosch, Nico de Jong, Martin D. Verweij; Effect of subdicing on performance of an ultrasound matrix transducer for Carotid imaging: numerical and experimental Study, IEEE Transactions on Ultrasonics, Ferroelectrics, and Frequency Control.

3.1. Introduction

A three-dimensional (3D) ultrasound image can in principle be generated from multiple two-dimensional (2D) images obtained by mechanical translation of a linear or a phased array probe. However, this method is relatively slow and tedious, and therefore not suitable for accurate tracking of the fast cardiovascular motion of, for instance, the carotid arteries [92, 93]. In order to achieve real-time volumetric images with a high frame rate (~1000 volumes per second), 3D imaging requires the use of a matrix probe. A matrix transducer is generally composed of numerous (>1000) transducer elements, which provide data that will be processed into an image by an imaging system. Because of hardware limitations, making direct electrical connections between the matrix elements and the imaging system is not an option, and therefore processing and electronic switching should be performed inside the probe to reduce the number of channels. An efficient approach is to manufacture the elements directly on top of an Application Specific Integrated Circuit (ASIC) [45]. The ASIC can incorporate amplifiers to improve the signal quality directly under the piezoelectric elements, and perform per-element processing, switching, multiplexing and/or signal combination to achieve the channel count reduction.

The sensitivity and the bandwidth of a matrix transducer in transmission and reception play a key role in achieving a good contrast and resolution of the final image. Hence, elements with high sensitivity, sufficient bandwidth, and short ringing time are aimed when designing an ultrasound transducer. The geometry of a transducer element determines its vibration behavior [3]. According to literature, choosing the width-to-thickness (w/t) ratio of the element to be lower than 0.6-0.7 guarantees bar mode vibration with piston-like surface motion, resulting in a good radiation performance of the element; otherwise there is the risk that lateral vibrations degrade the performance of the element [78, 94]. In applications with specific design limitations, such as large apertures in combination with a limited number of channels, or in high-frequency applications, it may be difficult to meet this width-to-thickness requirement.

Subdicing of the elements can be a solution to suppress the effect of lateral modes and only retain the bar mode. In a study done by Cortes et al. [95], a semi-analytical finite element approach is utilized to investigate the wave dispersion and resonance behavior of one-dimensional (1D) piezoelectric arrays with different geometries. They have shown that subdicing plays an important role in the mode coupling behavior and the resonance performance of an ultrasound transducer array. Recently we used finite element analysis to investigate the effect of subdicing on the acoustic performance of an element and proposed an approach to find the optimal number of subdicing cuts needed for an efficient element design for a 1D ultrasound transducer array. We have shown that for applications in which the width (w) of the element is greater than 0.6 times the wavelength (λ) in water, subdicing may improve the temporal and frequency response of a transducer [15]. Usually, the wavelength in PZT is about twice the wavelength in water, and the thickness (t) of the PZT of an element is half a wavelength in PZT, i.e. equal to the wavelength in water. We may thus assume that for elements with PZT material the ratio w/λ is equal to the ratio w/t.

The principle of keeping the width-to-thickness ratio of piezo elements sufficiently low to ensure only bar mode vibration is also applied in 1-3 piezocomposites. Because these materials consist of piezoelectric pillars embedded in a polymer matrix, additional requirements on the width and pitch of the elements are necessary to avoid lateral Lamb modes [96]. In contrast, we consider piezoelectric arrays with empty kerfs that do not lead to coupling between the elements and avoid the occurrence of the associated Lamb waves.

In this paper we will consider the design of a matrix transducer for 3D carotid imaging to demonstrate the effect of subdicing on the performance of the individual elements. In current clinical practice, 2D imaging of a single cross section is used to obtain parameters such as carotid blood flow, intima-media thickness, and plaque morphology and composition [97, 98]. Although such 2D parameters have been shown to be indicative for the overall level of systemic atherosclerosis, there is a high demand to perform real-time 3D imaging for more accurate assessment of local atherosclerosis in the carotids [17, 98, 99]. This requires a large volume to be scanned at a high rate. To achieve this, our technical design is based on a large matrix array that operates in linear array mode in the *x*-direction and in plane wave imaging mode in the *y*-direction. The PZT matrix will be built directly on top of an ASIC. In the *y*-direction steering will be restricted to small angles and we take elements with a relatively high length-to-thickness ratio of 1.56. To suppress lateral vibrations in the elements, we will apply the subdicing solution from [15].

We test our design by performing simulations with a 3D Finite Element Method (FEM) and comparing the results to measurements on a prototype transducer with elements having different numbers of subdicing cuts. In section II of this paper, we further explain the layout of the matrix transducer, the FEM simulation model, the prototype preparation, and the measurement setup. Both simulation and measurement results for the electrical impedance of the elements and the transmitted pressure are presented and discussed in section III, and the main conclusions are given in section IV. The topic of this chapter is the effect of subdicing on the performance of an individual element. Analysis of the performance of the entire array is beyond the scope of the current paper.

3.2. Methodology

3.2.1. Layout of the matrix array

Figure 3.1a shows a schematic layout of the matrix transducer (12 mm × 36 mm) with 80 × 120 elements and a pitch of 150 μm × 300 μm. Each row has a transmit and a receive bus, which is connected to one channel of the ultrasound mainframe (Verasonics V1, Verasonics Inc., Kirkland, WA, USA). In transmit, all the elements in one row are shorted by the ASIC, and by applying a high voltage excitation signal to all rows, a pulsed plane acoustic wave is generated, as symbolized by the red planes in figure 3.1b. In the standard reception mode, the elements from a number of adjacent columns (e.g. 1-20) per row are combined and an image plane is generated, as symbolized by the blue planes in figure 3.1b. This acquisition cycle is repeated by shifting the selection of elements in the *x*-direction, until a full 3D image is constructed. To improve the image quality by compounding [100], transmit beam steering on

y-direction is possible. A central frequency of 7.5 MHz is chosen to achieve an imaging depth of 2-5 cm.

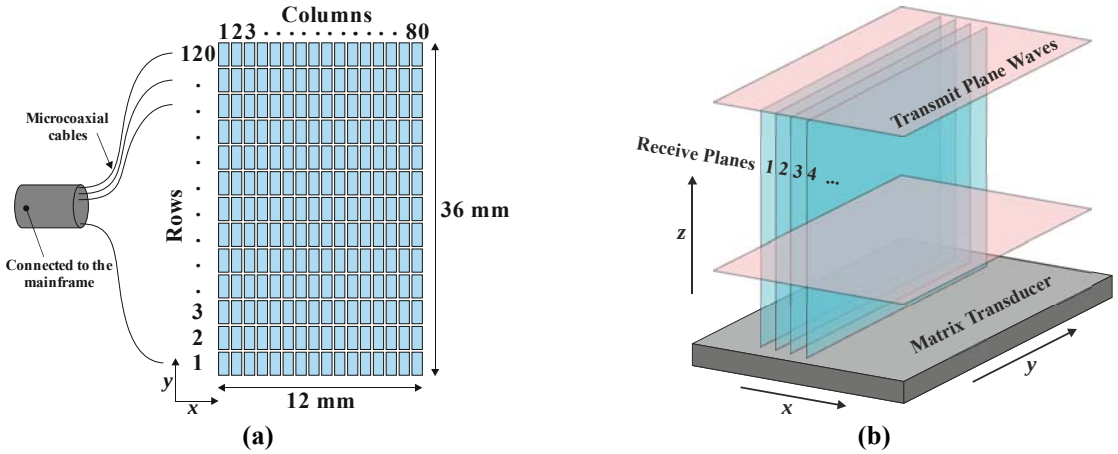

Figure 3.1. (a) The layout of the matrix transducer, **(b)** Transmit plane waves (red) and successive receive planes (blue).

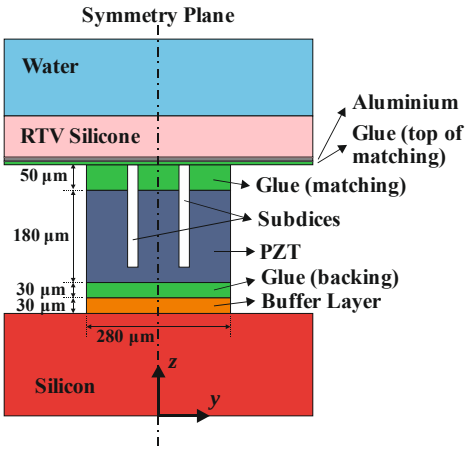

Figure 3.2. The 3D FEM model in the *yz* plane, showing an element with two subdicing cuts. The element width is 130 µm in the *x*-direction and 280 µm in the *y*-direction.

3.2.2. Simulation study

To analyze the acoustic performance of an individual element, we developed a 3D FEM simulation model in PZFlex (PZFlex LLC, Cupertino, CA, USA). Figure 3.2 shows the FEM geometry of the acoustic stack for a single element with two subdicing cuts. The element is mounted on an 800 µm thick ASIC silicon layer. A buffer layer is made from a non-conductive epoxy, filling the gap between the electrical connections on the ASIC bond-pads. Choosing a 30 µm thick buffer layer provides enough margin for the dicing procedure that is explained in the next chapter. The next layer of 30 µm conductive glue is used to paste a 180 µm thick CTS 3203 HD piezoelectric ceramic to the ASIC. On top, the piezo has a 50 µm thick matching layer made of conductive glue. An 8 µm aluminum foil is used as a ground electrode and glued on top of the matching layer using 7 µm conductive glue. The whole acoustic stack is made waterproof by a 100 µm RTV silicone rubber layer. The element is loaded with water. The material properties of all the layers in the model are given in table 3.1.

After cutting, the whole element has a width of 280 μm in the *y*-direction and 130 μm in the *x*-direction. Subdicing is applied in the *y*-direction with zero, one, and two kerfs (the kerf width is 20 μm). A subdicing cut depth of 70% of the total pillar thickness is sufficient to avoid the lateral mode, as shown by Janjic et al. [15]. A 70% cut, which has an additional advantage of improving the mechanical stability of the elements, is applied in both the simulation as well as in the realization of the elements.

The acoustic stack is excited with a half cycle of a 7.5 MHz sinusoidal pulse, which has a -3 dB bandwidth of 109% and 1 V peak amplitude. The electrical impedance is computed from the excitation voltage and the calculated current through the transducer element. Furthermore, the calculated pressure at the surface of the element is propagated into the water over an axial distance of 15 mm using the Kirchhoff extrapolation technique [101]. This is the same distance at which all the measurement were carried out.

3.2.3. Sample preparation

To assess the acoustic performance of the real transducer, we build a small prototype of the PZT matrix on top of a silicon ASIC by using PZT-on-CMOS integration [45]. The ASIC holds a representative number of elements for each subdicing type, and will provide direct electrical connections between the PZT elements and the bond pads on the periphery of the chip. After applying all layers with the above-mentioned thicknesses on top of the ASIC, we dice the acoustic stack. Two types of cuts are used. Full cuts are made to separate the PZT elements with 300 × 150 μm pitch. As shown in figure 3.3a, the full cut should be deep enough to guarantee the electrical and acoustical isolation between the elements, without damaging the chip. It may, however, partially extend into the buffer layer. On the other hand, the aim of subdicing cuts is to remove the lateral vibrations. To keep mechanical stability, the subdicing depth only extends to about 70% of the pillar thickness [15]. All the dicing/subdicing cuts are made by a 20 μm thick diamond blade, and the kerfs are air-filled to minimize the crosstalk between the elements. A rotation speed of 28.000 rpm for the dicing blade is used for optimal cutting and stability, and a dicing feed below 1 mm/s is chosen to avoid excessive stress. Since both mechanical forces and temperature contribute in depolarization of the material [102], we keep the temperature in the whole process below 70 °C by cooling with water. This temperature is well below the Curie temperature of 225 °C for the PZT material. Figure 3.3 shows a schematic drawing and a photograph of the manufactured matrix transducer with different subdicing cuts.

After dicing the transducer, the chip is mounted on a printed circuit board (PCB), and an 8 μm thick aluminum ground foil is glued to cover the matrix elements. The electrical connections from the bond pads on the periphery of the ASIC to the PCB are made by 18 μm thick aluminum wire bonds. To protect the wires, UV curing glob top epoxy is applied over the bonding wires. Finally a silicone layer is applied on top of the ground foil and the edges of the array are covered by a flexible waterproof material to protect the whole matrix transducer during the acoustic measurements. To excite or read out the elements, the PCB is connected to the main frame with commercially available micro coaxial cables (Samtec, New Albany, IN, USA).

Table 3.1. Properties and thicknesses of the materials used in the FEM model (parameter from PZFlex library).

Material	Properties	Thickness
PZT CTS 3203 HD	$\rho = 7820, \text{kg/m}^3$ $c_{11} = c_{22} = 137, c_{12} = 88, c_{13} = c_{23} = 92,$ $c_{33} = 126, c_{44} = c_{55} = 22, c_{66} = 25$ MPa $e_{15} = e_{24} = 16, e_{31} = e_{32} = 9, e_{33} = 22$ C/m^2 $\varepsilon_{11} = \varepsilon_{22} = 1306, \varepsilon_{33} = 1200$ C/Vm	180 µm
Aluminium	$\rho = 2690$ kg/m^3, $c_p = 6306$, $c_s = 3114$ m/s	8 µm
Silicon	$\rho = 2330$ kg/m^3, $c_p = 7526$, $c_s = 4346$ m/s	800 µm
RTV silicone	$\rho = 1294$ kg/m^3, $c_p = 1022$, $c_s = 125$ m/s	100 µm
Buffer epoxy	$\rho = 2975$ kg/m^3, $c_p = 1960$, $c_s = 1047$ m/s	30 µm
Conductive glue	$\rho = 3350$ kg/m^3, $c_p = 2000$, $c_s = 1050$ m/s	backing: 30 µm matching: 50 µm top of matching: 7 µm

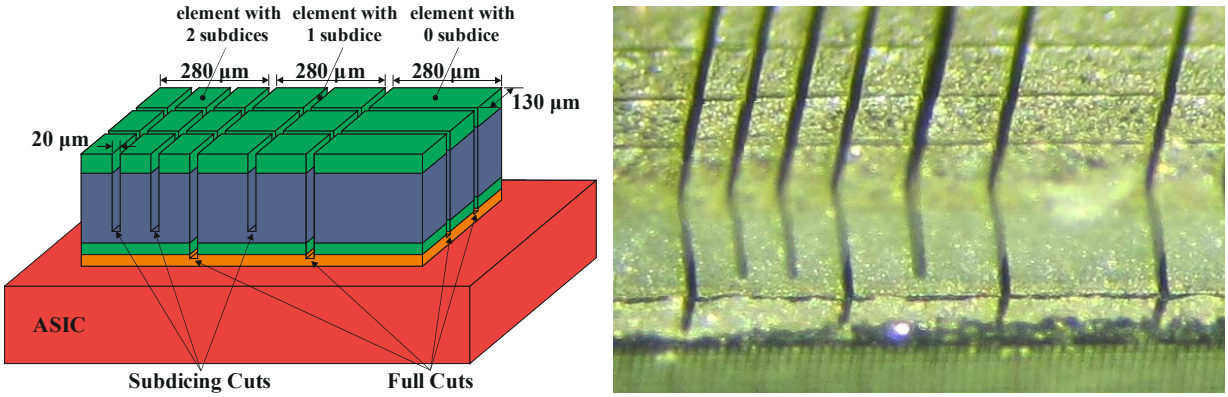

Figure 3.3. **(a)** Schematical drawing of the subdiced transducer elements (layers have the same thicknesses as in figure 3.2), **(b)** Photograph of the realized subdiced transducer elements under a microscope.

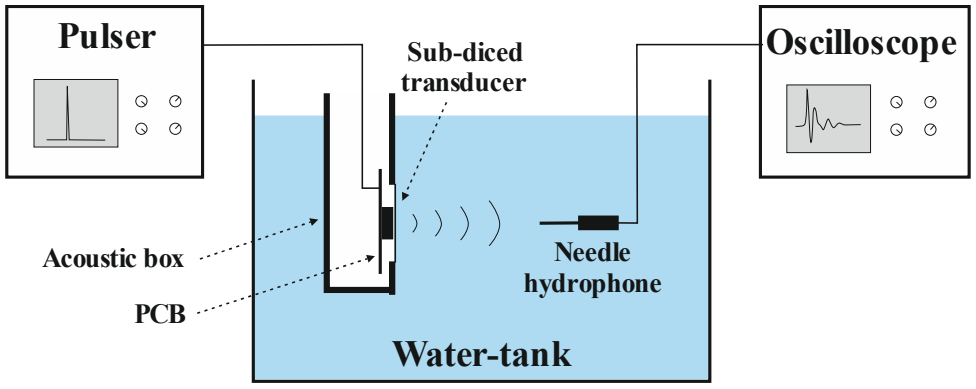

Figure 3.4. Schematical overview of the acoustic measurement setup.

3.2.4. Measurement setup

For electrical impedance measurements, a small water tank is used and the PCB with the transducer is acoustically coupled to the water through a window consisting of a 100 µm polyester membrane. We measure the electrical impedance of the individual elements on test pads that are provided on the PCB close to the ASIC. After calibrating the measurement setup

up to 50 MHz, the electrical impedance of each individual element is recorded from 1 to 20 MHz with an impedance analyzer (Agilent 4294A, Keysight Technologies, Santa Rosa, CA, USA). Since the metal traces on the PCB have different lengths for different elements and because of the unknown parasitics of the wire-bonds, it is not possible to fully de-embed the parasitics for each individual element. Therefore we calibrate the setup including the coaxial cable from the impedance analyzer to the PCB, and correct the measured data afterward by applying a -10 pF capacitance (which is estimated from a separate measurement) in parallel to each element to compensate for (i.e. subtract) the capacitive effect of the PCB traces. While the capacitance of the transducer elements cannot be determined precisely using this approach, due to element-to-element variations of the parasitics, the resonant characteristics of the impedance spectrum will still be indicative for the mechanical resonances of the transducer.

For acoustical evaluation of the transducer, the PCB is mounted in a box with an acoustically transparent window and the whole setup is submerged in a tank filled with deionized water. Figure 3.4 shows a diagram of the acoustic measurement setup. A manually controlled pulser-receiver (5072PR, Olympus Corporation, Tokyo, Japan) is used to create a short excitation pulse with a peak amplitude of 60 V, and -3 dB bandwidth of 133%, centered around 7.5 MHz. To measure the acoustic pressure, a calibrated 0.2 mm needle hydrophone (Precision Acoustics, Dorchester, U.K.) is placed at 15 mm distance from the transducer surface, and aligned with respect to the element under test. The excitation pulse is delivered to each individual element in separate measurements, and the acoustic pressure is recorded with the hydrophone. The output of the hydrophone is recorded using a digital oscilloscope (DSOX4054A, Keysight Technologies, Santa Rosa, CA, USA). To compare the measurement results with simulations, afterward we normalize the measurements to correspond to a 1 V excitation amplitude.

3.3. Results and discussions

3.3.1. Electrical impedance

From the PZFlex simulation results, the electrical impedance of a transducer element is calculated as:

$$Z(\omega) = \frac{V(\omega)}{I(\omega)}$$

where V(ω) is the Fourier transform of the excitation voltage, I(ω) is the Fourier transform of the current through the element, and Z(ω) is the complex electrical impedance. The magnitude and phase of the simulated impedance for elements with zero, one, and two subdicing cuts are compared in figures 3.5a and 3.5b. We define the resonances based on the position of the resonance/anti-resonance frequencies, which are in turn defined by the dips/peaks in the magnitude plot of figure 3.5a and correspond to the maximum positive/negative phase change in figure 3.5b. For an ideal element, we expect to have one resonance, representing the thickness mode vibration of the transducer element. In the simulation for the non-subdiced

element (the blue curves), besides the thickness resonance around 8 MHz, an extra resonance around 4.5 MHz (arrows) is observed. This is due to a mode with lateral vibration. By subdicing, the lateral mode shifts to higher frequencies, while the thickness mode does not change its frequency. We observe that this result for a matrix array element agrees quantitatively with our previous observation i.e. that for a linear array element the performance could be improved by subdicing when the element width is larger than 60% of wavelength [15]. This may be explained by the fact that for a matrix array with rectangular elements the lateral resonances in both horizontal directions are independent, and each may be avoided in the same way as for a linear array element.

The magnitude and phase of the measured impedance for the elements with zero, one and two subdicing cuts are compared in figures 3.6a and 3.6b. Again for the non-subdiced transducer, an extra resonance is observed around 6 MHz (arrows), which is removed by subdicing. This qualitatively agrees with the effects observed in the simulation results. However, a quantitative comparison between the measurement and simulation results is difficult. This is partly because the parasitic capacitances are not exactly known, as explained in the previous chapter. Other reasons are that the thickness of the fabricated layers may deviate up to ±5 μm from the design values used in the simulations, and that the material properties used in the simulations, especially for the piezoelectric material, may differ from the real values in the manufactured sample.

In figure 3.7, the simulated displacement mode shapes at the desired center frequency of 7.5 MHz are shown for the elements with zero, one, and two subdicing cuts. For the non-subdiced element, the existing lateral vibrations induce a non-uniform surface motion, thus impairing the efficiency of the transducer. With one subdicing cut, the displacement at the surface is more uniform than the non-subdiced case, whereas for the element with two subdicing cuts almost the whole surface of the element is moving in phase. This is necessary for a good radiation performance of the element [3, 79]. The mode shape at 7.5 MHz, is a weighted superposition of all resonance mode shapes, where the weight of the resonance modes that are close to the desired frequency are dominant. For optimal vibration, the element should be designed such that the lateral modes of the element are outside the frequency band of interest. In this simulation the lateral resonance frequency at 4.5 MHz for the non-subdiced element is shifted to higher frequencies and will hardly be excited for the elements with one and two subdicing cuts, resulting in an almost piston-like vibration mode at the desired center frequency.

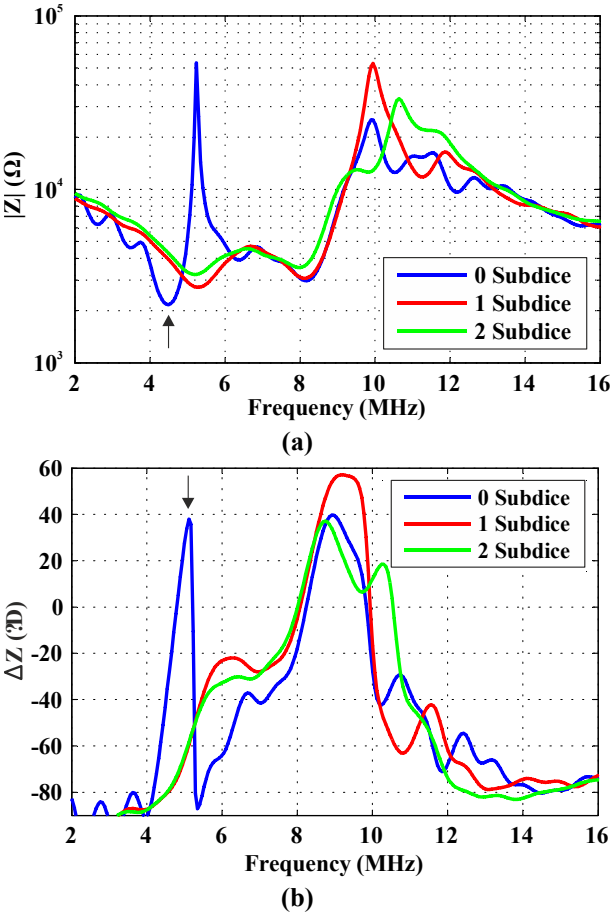

Figure 3.5. Calculated electrical impedance for the elements with zero, one, and two subdicing cuts obtained from FEM simulation, **(a)** impedance magnitude, **(b)** impedance phase

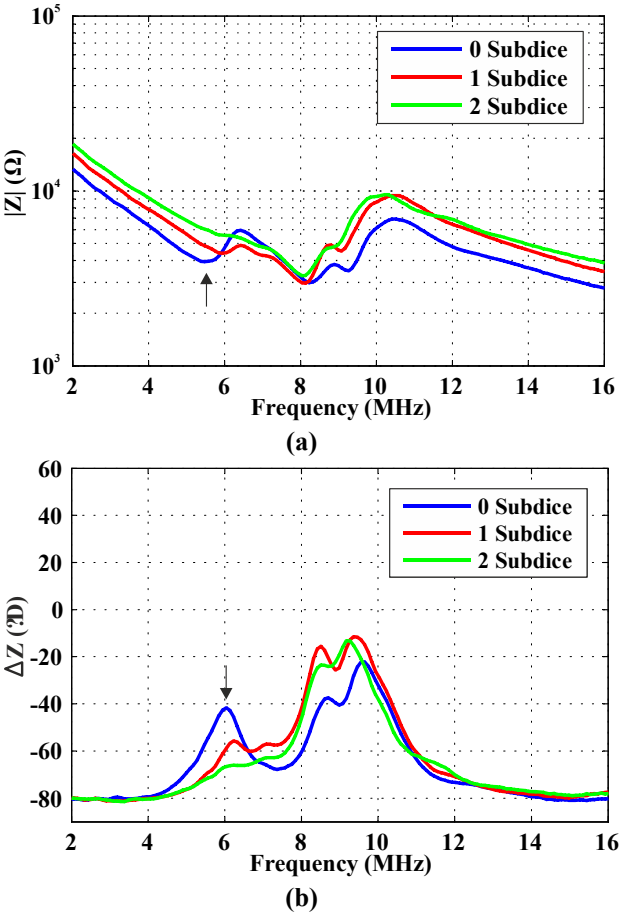

Figure 3.6. Measured electrical impedance for the elements with zero, one, and two subdicing cuts under water load condition, **(a)** impedance magnitude, **(b)** impedance phase

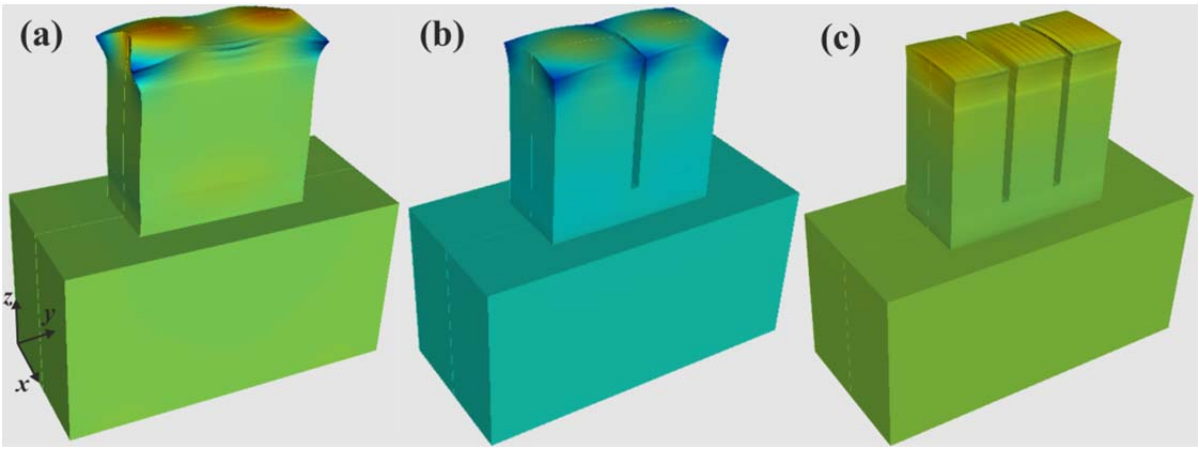

Figure 3.7. Displacement mode shape at 7.5 MHz obtained from FEM simulation results, (a) non-subdiced element, (b) element with one subdicing cut, and (c) element with two subdicing cuts.

3.3.2. Acoustic performance

Figure 3.8 shows the simulated (panel a) and measured (panel b) acoustic responses to the 1 V half cycle excitation pulse, as obtained at a distance of 15 mm from the transducer surface. Comparing the simulation results with the measured responses, the general shapes of the signal for different elements are quite similar. Even though we lose some part of the surface area by subdicing, the transmit efficiency of the subdiced elements are higher than the non-subdiced element.

The frequency spectra are obtained from the Fourier transform of the time responses of the pressure for different elements. Figure 3.9a shows the frequency responses of the signals in figure 3.8a. These responses have been normalized with respect to their own maximum, where the difference between the non-normalized maxima is at most 1.3 dB. Trailing waves (indicated by 'side reflections' in figure 3.8b) are observed in the measured pressure wave, while these are not present in the simulation results. These waves are most likely due to lateral acoustic waves in the silicon that reflect at the sides of the chip. Since we consider absorbing boundary conditions on the borders of the FEM model, we don't see this effect in the simulations. Since we cannot avoid the reflections caused by the sides of the ASIC in the measured data, and we are interested in analysing the effect of subdicing, we apply a Tukey window on the measured time trace (from 8.5 μs to 9.2 μs in figure 3.8b), and compute the Fourier transform of the remaining signal. The results are shown in figure 3.9b.

From the simulation results in figure 3.9a, we see that the non-subdiced transducer (the blue curve) shows a sharp dip in the frequency spectrum, which is due to the lateral resonance around 4.5 MHz, which reduces the bandwidth. In this case one and two subdicing cuts (the red and green curves), remove the unwanted dip from the frequency range of interest. In the measured spectra in figure 3.9b, the ripples that show up for the non-subdiced transducer (the blue curve) are removed by subdicing, resulting in a smoother frequency response. We observe that the transducer with one subdicing cut has the highest bandwidth.

To verify that the observed 'side reflections' are indeed due to lateral acoustic waves in the silicon that reflect at the sides of the chip, we performed further simulations. We considered the element with two subdicing cuts, mounted on a silicon layer with the same size as the ASIC used in the measurements. By changing the FEM boundary conditions on the edges of the ASIC from absorbing to free, the time trace changed considerably, as shown in figure 3.10a. The presence of 'side reflections' in the curve for an ASIC with free boundary justifies our assumption. To examine the effect of a time window on the frequency response, we applied the Tukey window on the simulated time trace for an ASIC with free boundary conditions. In figure 3.10b we compare the frequency response of the obtained time trace with the frequency responses of the non-windowed traces from figure 3.10a. As expected, the spectrum of the windowed time trace matches quite well with the spectrum of the non-windowed trace for the ASIC with absorbing boundary condition. Because this phenomenon deteriorates the performance of the transducer, it will need further analysis.

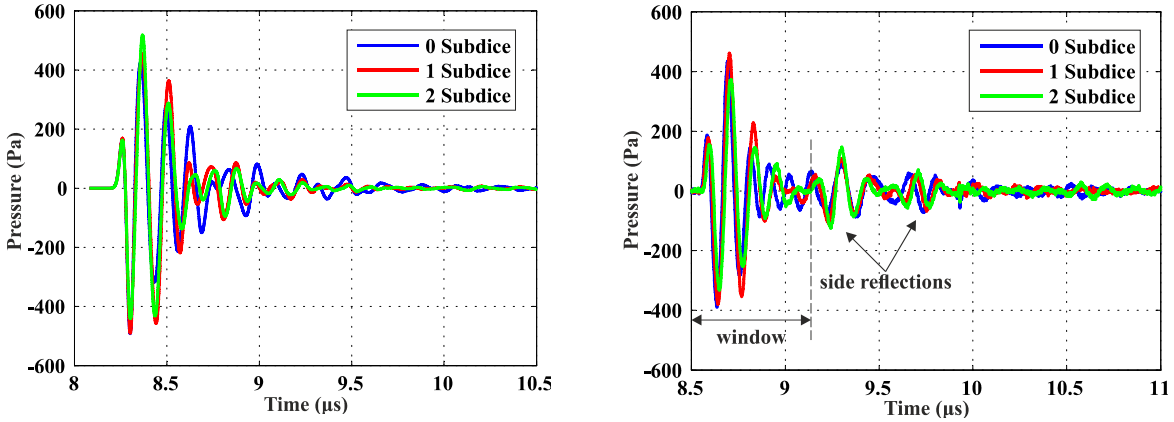

Figure 3.8. Acoustic pressure from transducer elements with zero, one and two subdicing cuts, at 15 mm distance from the transducer surface, **(a)** time response from FEM simulation**, (b)** measured time response (graphs normalized to 1 V excitation).

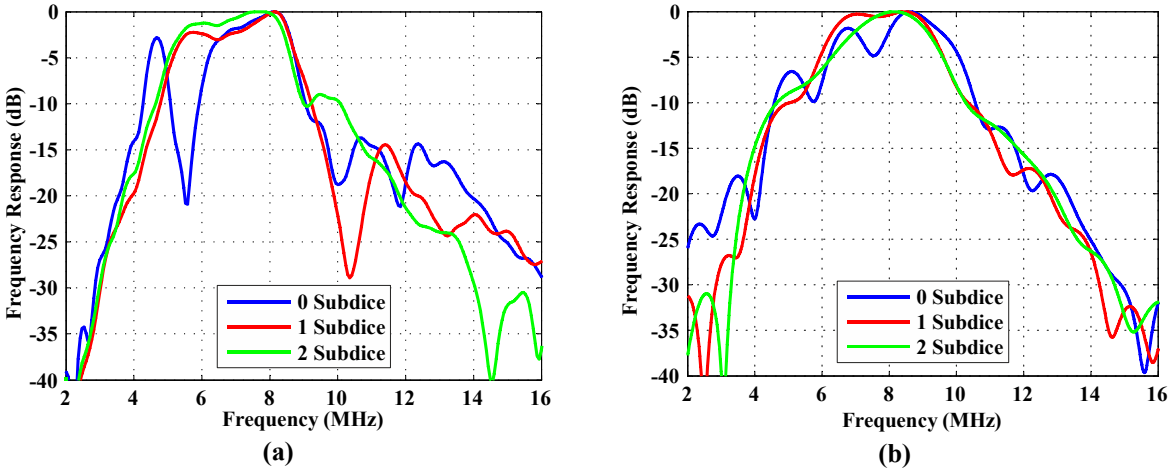

Figure 3.9. Frequency plot of the acoustic pressure from transducer elements with zero, one and two subdicing cuts, at 15 mm distance from the transducer surface, **(a)** frequency response from FEM simulation**, (b)** measured frequency response.

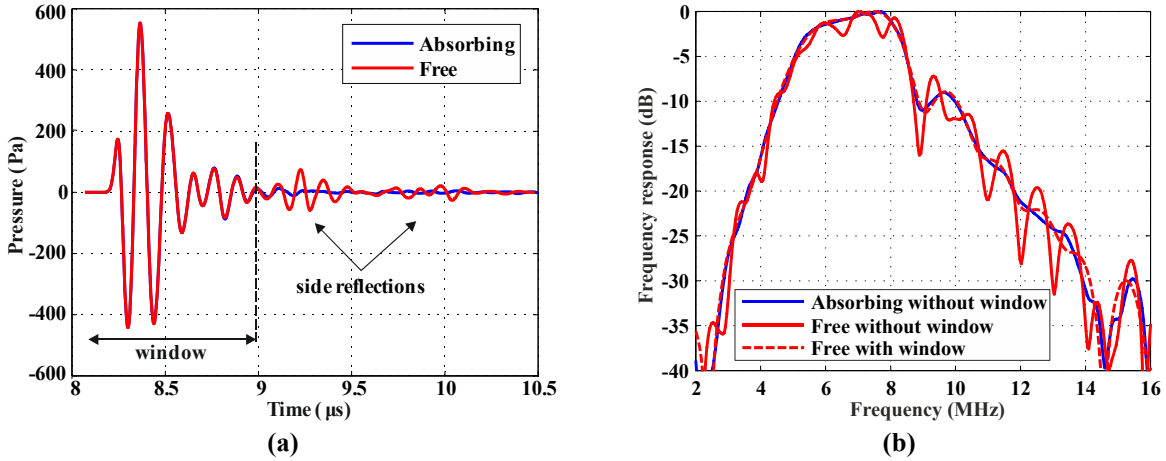

Figure 3.10. Calculated acoustic responses of a transducer element with two subdicing cuts on a 5 mm × 5 mm silicon chip with different boundary conditions on the edges, at15 mm from the transducer surface, **(a)** time responses, **(b)** frequency responses.

Table 3.2 shows the quantitative comparison of the peak to peak pressure (P_{pp}), the central frequency (f_c), and the bandwidth (BW_{-3dB}), for zero, one and two subdiced elements. The simulation results show that the transmit efficiency of the transducer and the bandwidth are both increased by subdicing. From the measurement results we conclude that the sensitivity of the transducers with one subdicing cut has increased, and the bandwidth has improved by 21% with respect to the non-subdiced element. On the other hand, both the transmit efficiency and bandwidth of the element with two subdicing cuts have decreased compared to the element with one subdicing cut. Although in the simulations we observe a minimal improvement for two subdicing cuts compared to one subdicing cut, the measurement results show better performance for the element with one subdicing cut.

Furthermore, the effect of sub-dicing on the simulated directivity pattern of a single element is shown in figure 3.11. These directivity patterns are obtained by extrapolating the time domain pressure at the surface of the element to the far field, and then taking the peak value in each direction. The results show that subdicing slightly enlarges the opening angle of the element. While the non-subdiced element has a -3 dB opening angle of ±15°, the elements with one, and two subdicing cuts have similar opening angles of ±17.5°.

Table 3.2. Quantitative comparison of simulated and measured peak pressure ($\boldsymbol{P_{pp}}$), central frequency ($\boldsymbol{f_c}$), and -3 dB bandwidth ($\boldsymbol{BW_{-3dB}}$), for transducer elements with zero, one, and two subdicing cuts.

		P_{pp} (Pa)	f_c (MHz)	BW_{-3dB} (%)
Simulation results	**0 subdices**	918	7.6	28
	1 subdice	945	7.0	47
	2 subdices	960	6.9	48
Measurement results	**0 subdices**	827	8.8	22
	1 subdice	842	7.7	43
	2 subdices	706	7.9	34

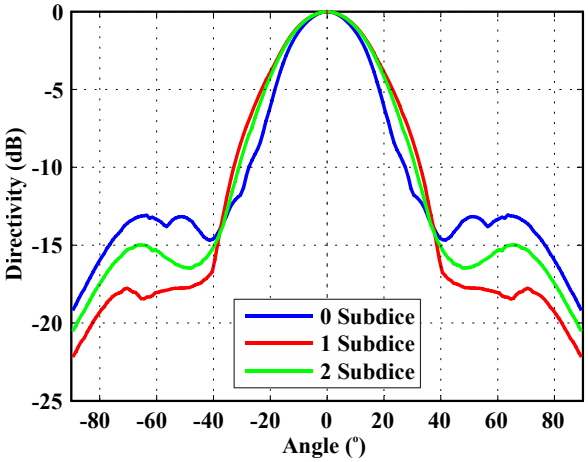

Figure 3.11. The simulated directivity pattern of a single element with zero, one, and two sub-dicing cuts. The graphs show the relative peak time domain pressure in the far field for the given direction.

3.4. Summary

In this study, the effect of subdicing on the acoustical performance of an individual element of a piezoelectric matrix transducer mounted on an ASIC is investigated using simulations and measurements. The electrical impedance plots show that the modes with lateral vibrations, which reduce the performance of the element, are shifted to higher out-of-band frequencies by subdicing. The unwanted dip in the frequency spectrum of the non-subdiced element can therefore be removed from the frequency response by subdicing, resulting in a higher bandwidth. Although in the simulations we observe a marginal improvement when going from one to two subdicing cuts, in practice the element with one subdicing cut is expected to perform better because it suffers less from deterioration by the subdicing process. From the measurement results, in the presented case the best performance is obtained for an element with one subdice, yielding a central frequency of 7.7 MHz and a -3 dB bandwidth of 43%.

CHAPTER 4

Optimizing the Directivity of Piezoelectric Matrix Transducer Elements Mounted on an ASIC[1]

Abstract

Over the last decade, clinical studies show a strong interest in real-time 3D imaging. This calls for ultrasound probes with high-element-count 2D matrix transducer array, interfaced to an imaging system using an in-probe Application Specific Integrated Circuit (ASIC) that takes care of element selection, signal amplification, sub-array beamforming, etc. Since the ASIC is based on silicon and is mounted directly behind the transducer elements, it can be regarded as a rigid plate that can sustain traveling waves. These waves lead to acoustical cross-talk between the elements, and results in extra peaks in the directivity pattern. We propose two solutions to such a problem based on our numerical investigation. One approach is to decrease the wave speed in the silicon by reducing the silicon thickness, absorb the energy by a proper backing material. Another solution is to disturb the waves inside the silicon plate by sub-dicing the back-side of the ASIC. We conclude that both solutions can be used to smoothen the directivity pattern.

[1] This chapter has been published as:
Maysam Shabanimotlagh, Verya Daeichin, Shreyas B. Raghunathan, Pieter Kruizinga, Hendrik J. Vos, Johannes G. Bosch, Michiel Pertijs, Nico de Jong, Martin Verweij; Optimizing the directivity of piezoelectric matrix transducer elements mounted on an ASIC, IEEE International Ultrasonics Symposium, IUS, 2017, 8091752.

4.1. Introduction

Over the past decade, there was a large interest in 3D ultrasound imaging. A comprehensive study on the recent developments for real-time 3D ultrasound imaging technology is reported in [19]. A common approach is developing a matrix ultrasound array with a large number of elements (>1000). Then the sub-aperture beamforming is implemented in an application specific integrated circuits (ASICs), inside the probe. In this way, the ASIC reduces the required channels for connecting a large number of elements in the 2D array to less than 256 channels provided by commonly used ultrasound systems [34]. With the improvements in the ASIC technology, the per-element circuitry occupies such a small size that allows the transducer matrix to be built directly on top of the ASIC [34, 36].

Although mounting the transducer elements directly on top of the ASIC has a lot of advantages, but the ASIC is not an ideal backing material for the transducer array. The ASIC is based on silicon, which is a hard material with very low attenuation, sustaining traveling waves. By exciting an element, different waves generate, and propagate through the silicon layer. These waves effectively lead to acoustical cross-talk between the elements in the matrix array [103]. Furthermore, some portion of the acoustical energy in the backing, bounce back to the front side of the transducer, and produce acoustic pressure in water. Since the source of generated pressure in water is wave propagation in the ASIC, they can be coherent over a certain angle, and consequently affect the directivity pattern of a single element in the array.

In an array of transducer elements, crosstalk is basically defined by the excitation of one element for contiguous elements, and it can be electrical or mechanical [103, 104]. The mechanical crosstalk has two sources: crosstalk through the water, and crosstalk through the backing. In this paper we study the crosstalk through the backing, and we focus on the performance of a silicon backing. In the next chapter we explain the simulation model. In the results section, we first explain the physics behind the acoustical crosstalk through the silicon backing, and show how it affects the directivity pattern. Then we propose two solutions to reduce the crosstalk and improve the directivity profile.

4.2. Simulation model

To analyze the acoustical effect of a silicon ASIC behind the transducer elements, finite element simulation is done in PZFlex. The geometry of the transducer model is shown in figure 4.1. The transducer is composed of 41 elements on both x and y directions, and has a central frequency of 7.5 MHz, with a bandwidth of 43%. The element pitch is 100 μm and the void kerf width is 20 μm. The transducer elements are designed on a silicon ASIC, and a backing material with high attenuation is used behind the silicon. In some cases, additional cuts up-to a certain depth level are considered into the bottom side of the silicon. The element pillar is composed of a 180 μm PZT ceramic and 40 μm matching layer, which is glued on top of a 20 μm buffer layer. On top of the elements an 8 μm layer of Aluminium and a 40 μm RTV silicone rubber is considered, and the whole transducer is loaded with water. The material properties of different layers are given in table 4.1. In order to avoid reflections from the sides of the model, absorbing boundary condition is applied on the edges. Also To reduce

the simulation time we assume symmetric boundary in the middle. Since the geometry on both directions is similar, we only analyze the performance along the *x*-direction.

Usually the ASIC silicon has a thickness in the order of hundreds of micrometers. Similar to our fabricated ASICs, we assume a 500 μm thick silicon, and a damped backing material (i.e. Tungsten loaded epoxy with 25% volume fraction) layer underneath.

A two-sided Gaussian function with 40 ns time width, with -3dB bandwidth from 3.5 to 13 MHz, is used to excite the central element. To calculate the directivity pattern for the overall frequency band, we calculate the acoustic pressure over an extrapolation plane, which is defined at 100 μm away from the transducer surface in water. Then using the extrapolation toolkit, the Kirchhoff method is utilized to calculate the transmitted pressure at 100 mm away from the transducer, and at angles from -90° to 90°. The beam pattern is obtained based on the peak of the envelope of the pressure over different angles.

4.3. Problem statement

The directivity pattern of the model explained in the previous chapter is shown in figure 4.2. In the directivity plot, two extra peaks occur at ±22°, as shown by the arrows in figure 4.2. We hypothesize that these peaks are due to a wave traveling in the ASIC and bouncing back into the water from the crosstalk through the neighboring elements.

To verify this, we look at the wave propagation in the silicon, and at the surface of the transducer. By exciting the middle element, Lamb waves are also generated in the ASIC. We track the propagation of these waves by calculating the average acoustic pressure in the top surface (water) and in the bottom surface (silicon) over time for all elements. The propagation of these waves for each element is shown in figure 4.3. Figure 4.3a shows the wave propagation in the silicon, and figure 4.3b shows the wave propagation in water. In both figures, the first curve from below represents the calculated pressure for the first neighbor of the excitation element. The second curve shows the pressure for the second neighboring element, and subsequently the last (top) curve shows the pressure for the 20th element away from the excitation element.

In figure 4.3a, two dominant waves are observed. The propagation speeds of these waves are close to the velocity of the zero order symmetric and anti-symmetric Lamb waves in silicon. Furthermore, the anti-symmetric mode has a higher amplitude than the symmetric mode. In figure 4.3b, three dominant waves are observed. The fast wave is caused by the waves traveling in the ASIC with higher velocities than the wave speed in water. Next are the waves with velocities similar to the speed of sound in water. And the third waves with a very low velocity but high amplitude are generated due to the traveling waves in the front layers (i.e. the aluminum and RTV rubber materials). Since these waves have velocities much lower than the speed of sound in water, the will not affect the directivity pattern.

Using the Dispersion Toolkit in PZFlex, we calculate the dispersion of free Lamb waves for a silicon plate. The results are shown in figure 4.4, where the *x*-axis represents the product of the frequency and thickness of the silicon layer, and the *y*-axis is the phase velocity of the Lamb waves. At high frequencies the lamb wave velocities converge to the Rayleigh wave velocity (approximately 92% of the shear wave velocity).

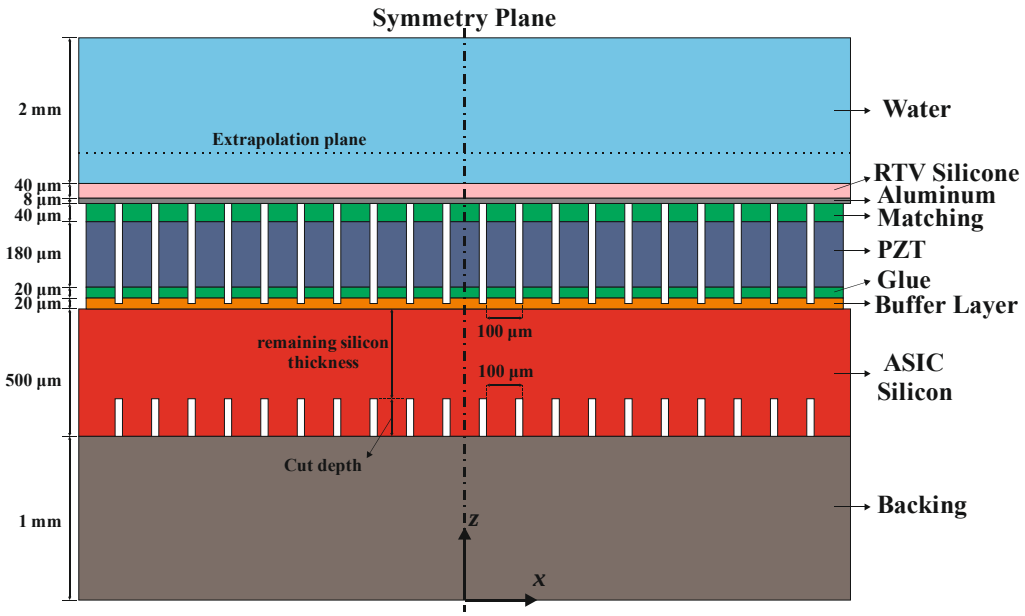

Figure 4.1. The geometry of the simulation model.

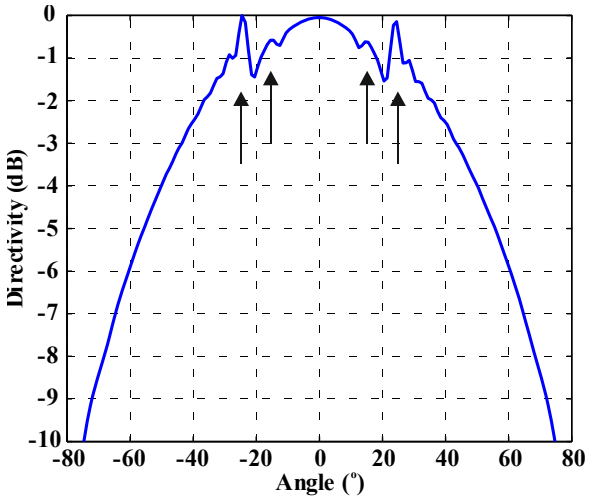

Figure 4.2. Directivity pattern of a single element excited in an array mounted on a 500 µm thick silicon ASIC (without cut) and highly damped backing material.

By propagation of the Lamb waves in silicon, part of the energy of these waves bounces back into the water medium via the neighboring elements with a certain delay. Such a time delay is related to the element pitch and the wave velocity in the silicon. Although these generated pressures in water have relatively weak amplitude, they are coherent at a specific angle, resulting in disturbance of the directivity pattern of a single element in the array.

In our study, with silicon thickness of 500 µm, and frequency of 7.5 MHz, the velocity of zero order anti-symmetric Lamb wave (A_0 wave) is 3900 m/s, and the velocity of the zero order symmetric wave (S_0 wave) is approximately 5200 m/s (figure 4.4). With these velocities the waves are coherently summed over the angles of 22° and 16° respectively. This agrees well with the extra peaks observed in figure 4.2. Among the two peaks, the one related to the S_0 mode is weaker than the peak for the A_0 mode. This is related to the particle motion of these waves. The elliptical particle motion of the A_0 mode is more perpendicular to the plane

of the plate, while that for the S_0 mode is mainly in the plane of the plate [105]. Therefore the A_0 wave can couple better to the other elements and generate a higher pressure in water. This is also observed in figure 4.3b.

Table 4.1. Material properties used in the simulation, parameters are obtained from the PZFlex library

Material	Properties
PZT (CTS 3203 HD)	$\rho = 7820$ kg/m^3 $c_{11} = c_{22} = 137$, $c_{12} = 88$ MPa $c_{13} = c_{23} = 92$, $c_{33} = 126$ MPa $c_{44} = c_{55} = 22$, $c_{66} = 25$ MPa $e_{15} = e_{24} = 16$, $e_{33} = 22$ C/m^2 $e_{31} = e_{32} = 9$ C/m^2 $\varepsilon_{11} = \varepsilon_{22} = 1306$, $\varepsilon_{33} = 1200$ C/Vm
Aluminium	$\rho = 2690$ kg/m^3, $c_p = 6306$, $c_s = 3114$ m/s
Silicon	$\rho = 2330$ kg/m^3, $c_p = 7526$, $c_s = 4346$ m/s
RTV silicone	$\rho = 1294$ kg/m^3, $c_p = 1022$, $c_s = 125$ m/s
Buffer epoxy	$\rho = 2975$ kg/m^3, $c_p = 1960$, $c_s = 1047$ m/s
Glue/matching	$\rho = 3350$ kg/m^3, $c_p = 2000$, $c_s = 1050$ m/s
Backing (Tungsten loaded Epoxy with 25% vf)	$\rho = 5700$ kg/m^3, $c_p = 1750$, $c_s = 935$ m/s Attenuation: 10 dB/cm/MHz
PCB Backing	$\rho = 1850$ kg/m^3, $c_p = 3602$, $c_s = 2396$ m/s Attenuation: 3 dB/cm/MHz

4.4. Proposed solutions

To avoid the unwanted peaks in the directivity plot, we propose two solutions. The first solution is to lap-down the silicon thickness. By reducing the thickness of the silicon, the Lamb wave speed for A_0 mode is decreased (in an ideal case to a speed lower than the speed of sound in water). The second solution is to disturb the Lamb wave propagation in silicon by sub-dicing the ASIC to avoid coherent summation of the generated wave.

To analyze the effect of the lapping, four different silicon thicknesses with 500, 300, 100, and 30 μm are considered. Furthermore, we consider two different backing materials: a highly damped Tungsten loaded backing, and a PCB backing. And to analyze the effect of cutting in the ASIC, a silicon thickness of 500 μm on Tungsten loaded epoxy material is chosen with dicing cut depths up-to 300, 100, and 30 μm. In all cases all parameters are the same, except the silicon thickness, silicon cut depth level, and the backing material. With the similar method as explained earlier, the directivity pattern of a single element is calculated, and results are compared in figure 4.5.

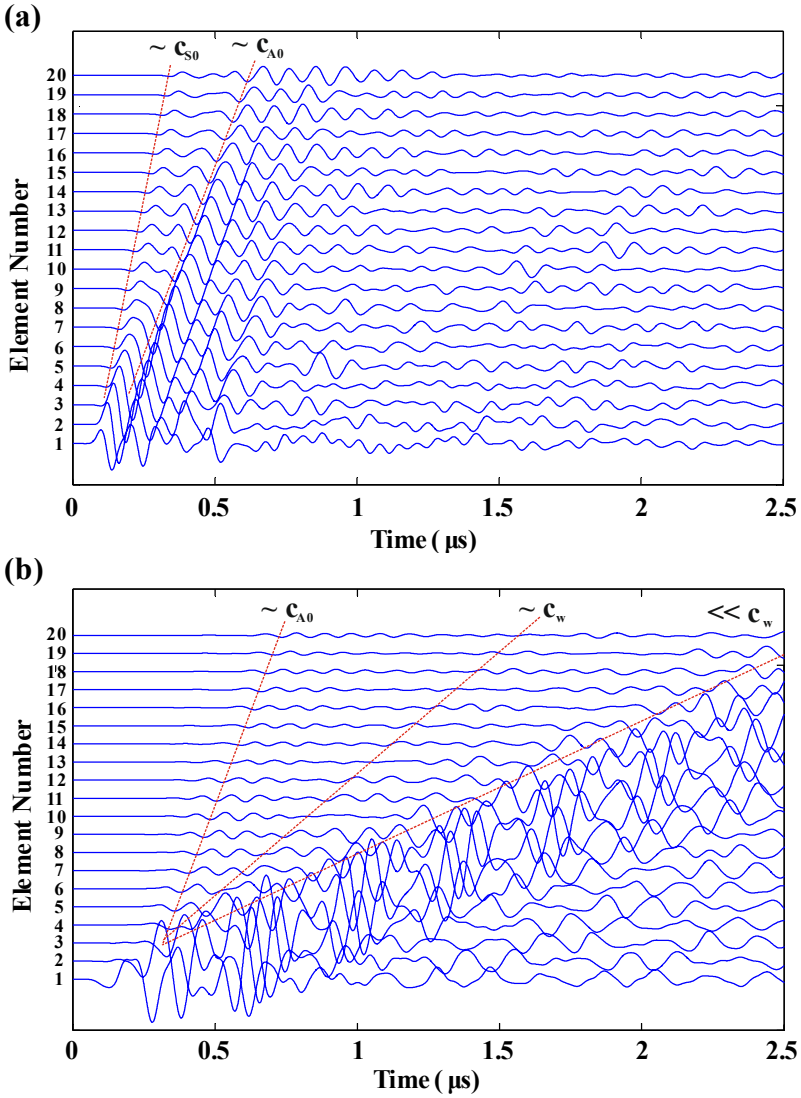

Figure 4.3. Wave propagation, calculated from the average of the acoustic pressure, **(a)** on top of the pillars, in water, and **(b)** on the bottom side of the pillars, in silicon.

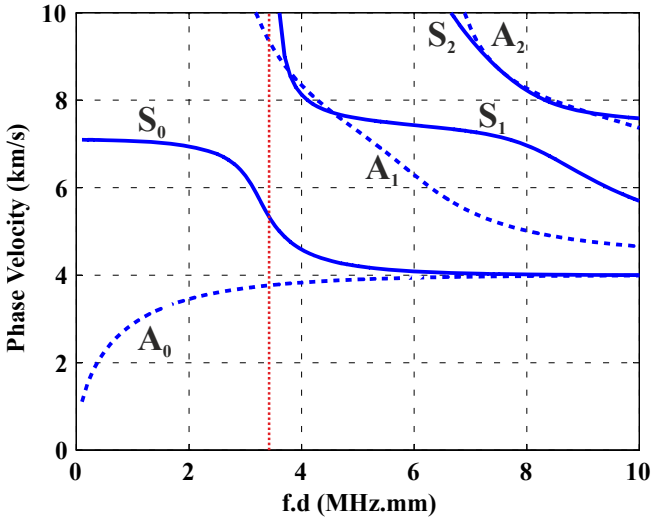

Figure 4.4. Dispersions curves of free Lamb waves for silicon material, calculated with the dispersion toolkit in PZFlex.

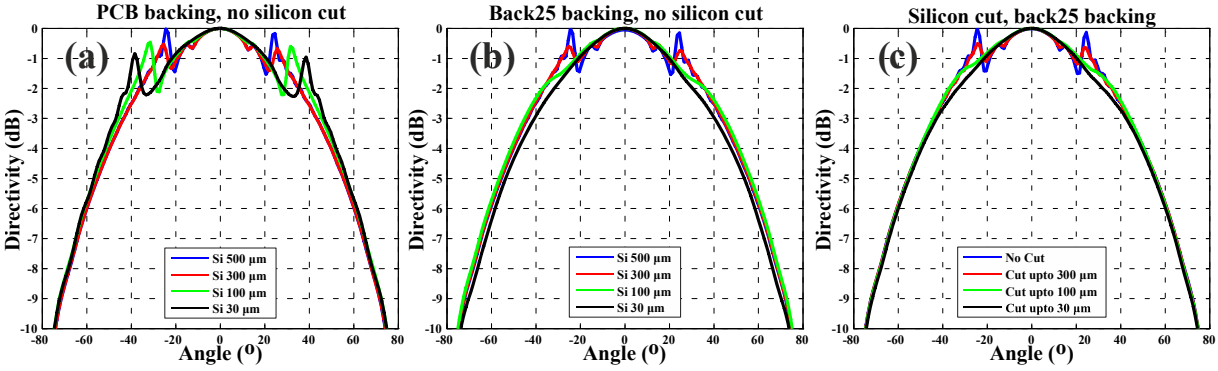

Figure 4.5. Directivity pattern of a single element, **(a)** four different silicon thicknesses are compared when a PCB backing is considered, **(b)** four different silicon thicknesses are compared when Tungsten loaded epoxy is considered, **(c)** silicon thickness of a 500 µm is considered on a Tungsten loaded epoxy, and four different cut levels on the back side of silicon are compared.

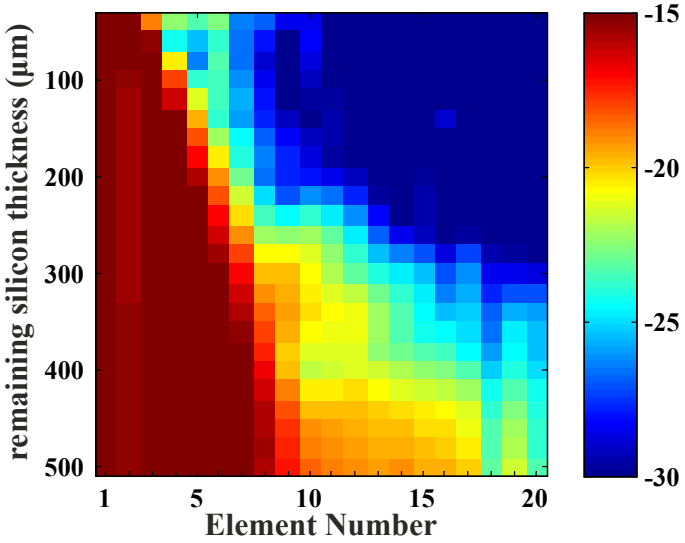

Figure 4.6. Cutting depth level optimization. The color map shows the pressure level in the silicon chip, under different elements, normalized to the pressure level under the excitation element. the *x*-axis is the element number, and element 1 is the excitation element, the *y*-axis shows the depth level of the cut in silicon..

Figure 4.5a shows the directivity of a single element when different silicon thicknesses are used on a PCB backing. By reducing the silicon thickness, the extra peak in the directivity pattern shifts to higher angles. This is due to the reduction of A_0 Lamb wave velocity for lower silicon thickness, resulting in longer time delays between the elements, and therefore a coherent summation of the waves over a higher angle.

Figure 4.5b, is the same comparison, but on a high damping backing material. In this case also by reducing the silicon thickness, the extra peak occurs at higher angles, but the effect is much weaker than for the low silicon thickness. This can be due to two effects. Compared to the PCB backing, since the acoustic impedance of Tungsten epoxy is closer to the acoustic impedance of silicon, higher transmission of energy to the backing is expected. Also since the attenuation in Tungsten epoxy is higher than the PCB, the attenuation of the energy is more efficiently done with Tungsten epoxy backing, especially in low thickness values.

Figure 4.5c show the directivity profile when the silicon is diced up-to a certain level. The results show that when the cut in silicon is deep enough, the waves in the silicon are disturbed and will not efficiently propagate into the water. This mechanism seems to be independent of the backing material. Therefore, we also modeled this situation with PCB backing, and the results are very similar to figure 4.5c.

Among the studied situations, both sub-dicing in the silicon, or lapping down the thickness of the silicon, can reduce the Lamb wave propagation in the silicon backing, and improve the directivity pattern of a single element in an array. In practice, dicing the silicon may be preferred to maintain the mechanical stability of the silicon layer.

To find the optimal silicon dicing depth, we consider a silicon thickness of 500 μm, and change the cutting depth level from 20 μm to 500 μm (no dice). For each case, the average pressure in silicon, under each element (element 1 to 20) is calculated, and the maximum pressure for that element is normalized to the maximum pressure under the excitation element (element 1), in dB scale. The results are shown in figure 4.6. Based on the figure, in general, the lower the cut level, the lower crosstalk is expected. From a manufacturing viewpoint, very low cutting depth may generate mechanical instability. In practice there is a tradeoff between the keeping the mechanical stability and reducing the crosstalk. We can tune the depth of sub-dicing cut such that the crosstalk is minimized while the mechanical stability is also maintained.

4.5. Summary

In this paper with finite element simulations, we investigate the acoustical effect of an ASIC mounted directly behind an ultrasound matrix transducer. The ASIC is based on silicon material, and acts as a rigid plate, which is prone to the propagation of waves. When an excitation occurs, Lamb waves are generated in the silicon layer, and are coupled to the water through the acoustical crosstalk with other elements in the array. The generated acoustic pressure in the water makes extra peaks in the directivity pattern of a single element. We propose two solutions to remove the peaks from the directivity plot. One approach is to shift the peaks to higher angles, by reducing the silicon thickness, and use a proper damped backing material to absorb the acoustical energy from the silicon layer. Another solution is to disturb the waves inside the silicon plate by producing cuts on the back side of the ASIC. We conclude that with a proper choice for the silicon thickness (in the first approach) or depth of cut (in the second approach), both solutions can be used to remove the extra peak from the directivity plot.

CHAPTER 5

Electrical Evaluation of the Electronic Chain for an Ultrasound Matrix Transducer Integrated on ASIC for Carotid Imaging

Abstract

In the past two decades the technology for making ultrasound matrix transducers has been developed for real-time three-dimensional (3D) imaging application. An efficient approach is to integrate a matrix transducer with >1000 elements directly on top of an Application Specific Integrated Circuit (ASIC). The ASIC employs micro-beamformers, switches, amplifiers, etc. to improve the signal quality and to reduce the number of cables needed for connecting the elements to the ultrasound machine. To implement this technology, extra circuitry is inevitable to connect the ASIC to the ultrasound machine. This circuitry includes the cable drivers, the matching networks, and the ultrasound machine, and they highly influence the overall performance of the transducer. Therefore, to characterize the performance of the transducer, we have to initially evaluate the performance of the electronic chain. In this chapter we explain an ASIC together with the extra circuitry which is developed for high frame rate 3D imaging of carotid arteries. Through a series of measurements, the performance of the Low Noise Amplifiers (LNAs) of the ASIC, the extra buffers on the transmission line, and the input-out relationship of the ultrasound machine are characterized. The results determine the operational range by defining the saturation level of the ASIC for different settings. The results of this chapter are necessary for a proper interpretation of the acoustic measurement results.

5.1. Introduction

In principle a three-dimensional (3D) ultrasound image is generated from multiple two-dimensional (2D) images at different planes or angles. These 2D images are obtained by mechanical translation or rotation of a linear or a phased array probe. However, this method is relatively slow and tedious, and therefore not suitable for accurate tracking of fast cardiovascular motion [92, 93]. In order to achieve real-time volumetric images with high frame rate (~1000 volumes per second), a 2D matrix probe is required. A matrix probe is composed of numerous (>1000) transducer elements, which provide a 3D dataset that is processed and converted into an image by an imaging system. Because of hardware limitations making direct electrical connections between all transducer elements and the imaging system is not possible. A solution is to locally process or combine the signal from a group of elements, for instance by employing a micro-beamformer or electronic switches, to reduce the number of required channels to a manageable amount. An efficient approach is to manufacture the transducer elements directly on top of an Application Specific Integrated Circuit (ASIC) [45]. With the improvements in the ASIC technology, the per-element circuitry occupies such a small size that the transducer elements could be manufactured directly on top of the ASIC bond pads [34, 106].

Mechanical behavior of a transducer plays a key role in achieving images with high contrast and resolution. Elements with high sensitivity, wide bandwidth, and short ringing time are aimed when designing an ultrasound transducer. The geometry of the transducer element determines its vibration performance [3]. Choosing the width-to-thickness (w/t) ratio of the element to be lower than 0.7 guarantees the bar mode vibration with piston-like surface motion, which results in an efficient radiation performance; otherwise the lateral vibrations degrade the performance of the transducer [78, 94]. For the carotid imaging application a transducer with 7.5 MHz resonance frequency is required. To achieve this resonance frequency a piezoelectric with ~200 μm thickness is required. Therefore to guarantee an efficient vibration maximum acceptable width is ~140 μm, in both lateral and azimuthal directions. The capacitance of such a small transducer element is ~3 pF, with ~7 kΩ impedance. In general, most of the commercial coaxial cables has an effective capacitance of ~60-110 pF/m, and with a characteristic impedance of 50 Ω [107]. The high relative capacitance of the cable and the impedance mismatch highly influences the acoustical performance of the transducer elements. The circuitry of the ASIC compensates for the effect of the transmission cables, and by signal amplification, buffering, and impedance matching, it significantly increases the overall dynamic range of the transducer.

In order to realize the performance of the ASIC in the matrix probe, extra electrical connections are needed to control and provide the voltages and currents required for the operation of the ASIC. These may be provided via an external computer, an FPGA, or PCBs. The overall performance of the transducer depends on the acoustical performance of the elements, the electronics of the ASIC, and all other components which are designed on the electrical transmission line from the ASIC to the imaging system. Therefore, for characterization of the transducer, the performance of all the electronics chain from the ASIC to the ultrasound machine should be characterized.

Considering carotid arteries imaging in mind, we have designed an ASIC suitable for building a matrix transducer on top of it. The ASIC is controlled by an FPGA, and the transmission line is provided through a daughterboard PCB and a motherboard PCB. In this chapter we focus on the characterization of the whole electronic chain, without the PZT transducer. In section 2, we explain the design choices and the architecture of the ASIC, in addition to the design of the electronic chain, the measurement setup and the analysis method. In section 3, the measurement results for the individual components, as well as the whole electrical system are presented and discussed. And the concluding remarks are given in section 4.

5.2. Materials and methods

5.2.1. Transducer design choices

For 3D real-time imaging, during transmission all elements in the matrix of the piezoelectric transducer are simultaneously excited to generate a plane wave, as indicated by the green plane in figure 1. In reception, a subset of elements on each row is selected by programming the electronic switches in the ASIC, and the signal from the combined elements on each row is transferred to the mainframe. By processing the received data, an image in a receiving plane is obtained, as indicated by the blue planes in figure 1. In the next acquisition the selected subset of elements on each row is shifted and an image in the next receive plane is obtained. This procedure is repeated to acquire the signals for all imaging planes, and by combining the data from all receive planes a 3D image of the total volume is constructed.

To image the carotid arteries, a transducer with an aperture of 12 mm × 36 mm (x dimension × y dimension) is chosen. Since the transducer array is too large to be covered by a single ASIC, an array of 2 × 10 ASICs will be employed, as shown in figure 1. Each ASIC contains a matrix of 40 × 24 elements with 150 μm pitch, which covers a transducer area of 6 mm × 3.6 mm. The transducer is designed for a center frequency of 7.5 MHz, which is recommended for carotid imaging applications [108]. To avoid image saturation, a minimum dynamic range of 70 dB is required for the front end, as in similar applications [3]. The main focus in this paper is to verify the performance of the single chip transducer. Consequently, we have made a prototype of a PZT matrix transducer on a single ASIC, and characterized the electrical and acoustical performance of the transducer in different configurations.

The layout of the ASIC is such that all wire-bond connections are situated only on one side, and the other three sides of the chip are covered by transducer elements. This allows for tiling these ASICs in a head-to-head, and side-by-side fashion. This design choice makes it possible to up-scale the prototype to a larger matrix array.

5.2.2. ASIC design and implementation

Figure 2 shows the electronic architecture of the ASIC. Row-level circuits interface the PZT transducer array to an imaging system. Each row has 40 elements, which can be individually connected to one transmit and one receive bus. Thus the achieved channel count

reduction factor is 20. This arrangement results in a manageable number of channels (< 256 for most of the ultrasound machines) for the full matrix transducer. The element-level circuitry fits in the 150 μm × 150 μm area occupied by the transducer element, allowing the transducer array to be integrated directly on top of the ASIC.

Each row-level RX bus is wired out through a shared row-level low-noise amplifier (LNA) and cable driver. To avoid saturation for strong receive signals, the row-level LNA has a bypass option that is controlled by a vertical shift register. Each row-level TX bus receives an externally generated high-voltage transmit signal. Each transducer element has a programmable switching circuit that allows the element to be connected to the RX bus or the TX bus. The ASIC allows a rapid configuration of the selected RX and TX elements. Moreover, its architecture supports a variety of element configurations for different imaging schemes. Control logic, programmed through vertical and horizontal shift registers, determines whether an element participates to the intended configuration. The detailed design of the ASIC circuitry is presented in our earlier work [109]. The ASIC is fabricated in a 0.18 μm high-voltage BCDMOS process and can handle signals up to 30 V.

5.2.3. Electrical system

A daughterboard is designed to accommodate the piezoelectric matrix transducer sitting on top of the ASIC. The main role of this daughterboard is to transfer the transmit, receive, power and control signals from the Verasonics and the control units to the ASIC. This daughterboard consists of three Printed Circuit Boards (PCBs), which are stacked on top of each other: the TX PCB (on top) for transmitting signals; the RX PCB (in the middle) for the receive signals; the data PCB (on the bottom) for the power and control signals. The transducer is mounted on the data PCB, and the RX and TX PCBs with opening windows are mounted on top. This arrangement is chosen to accommodate all the connections to the ASIC bond-pads.

A motherboard PCB is designed to interface the signals between the daughterboard and the ultrasound machine. The motherboard is connected to the Verasonics machine (V-1, Verasonics, WA, USA) with two Canon connectors (LLC DLM5-260PW6A, ITT Corporation, NY, USA). On the transmit paths, a matching network is designed to guarantee a unipolar excitation pulse. The receive signals are buffered with unity gain operational amplifiers on the motherboard before being fed into the Verasonics. This is to compensate for the cable load effect and to minimize the losses. Commercially available micro coaxial Samtec cables (Samtec, New Albany, IN, USA) are used to transfer the TX and RX signals between the daughterboard and the motherboard. An external FPGA (Altera DE2-115, San Jose, CA, USA) is used to generate the control signals for programming the ASIC. Furthermore, an external power supply provides the voltages and currents needed for the ASIC and the buffer amplifiers. The power and control signals are transferred via a flat ribbon cable from FPGA to the motherboard and from the motherboard to the daughterboard. The computer of the imaging system controls the overall operation of the whole system. A schematics of the electrical configuration is shown in figure 5.3.

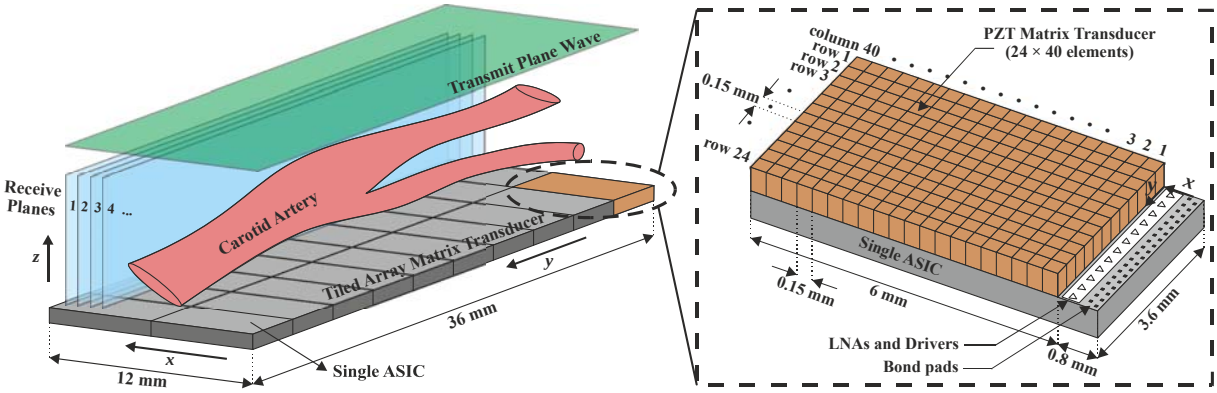

Figure 5.1. Schematic drawing of the full matrix transducer, together with a single ASIC transducer with PZT elements mounted on top.

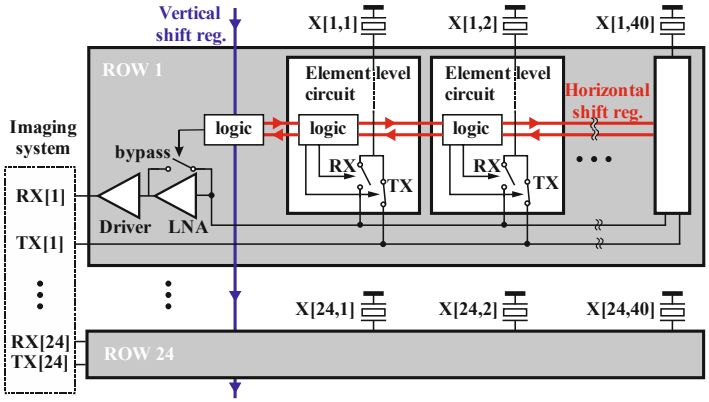

Figure 5.2. Electronic architecture of the ASIC.

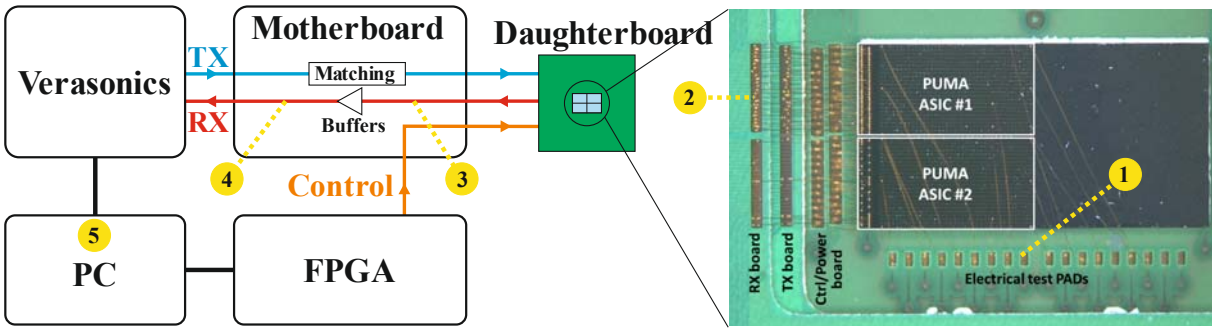

Figure 5.3. The electrical configuration of the transmit, receive and control signals between the matrix transducer and ultrasound machine. A photograph of the top view of the ASICs mounted on the daughterboard is shown on the right side. The FPGA provides the control data for the ASICs, and a PC controls the performance of the whole system. The electrical measurements are done on the test points specified with dashed yellow lines.

5.2.4. Verasonics machine

The Verasonics is a commercial system with a specification suitable for ultrasound research. The system consists of Verasonics Data Acquisition System (VDAS), connected to a desktop computer, that can provide control over the transmitting and receiving parameters for real-time acquisition on maximum 256 channels simultaneously. The reconstruction of the RF data, the signal processing and image display is done on a Graphical Processing Unit (GPU), through Matlab Executable (MEX) functions containing compiled C-Code. This makes the

image reconstruction fast enough for real-time imaging. By having all of the functionalities in Matlab environment, the user is able to build a custom acquisition sequence, and create his own processing functions. These specifications and flexibility in programming make it an appropriate candidate for a broad range of ultrasound applications [110].

The goal of our research is to connect all transmit and receive channels of our ultrasound matrix transducer to the Verasonics machine. On the other hand, for characterization of the performance of the transducer elements, the relationships between the input voltage and the acquired data with the Verasonics is crucial. We aim to measure this relationship through an independent measurement without the transducers, and then use that information to characterize the receiving performance of the matrix elements.

In this research, two different versions of the machine were used: the V1 and the Vantage systems. The V1 system can transmit on 256 channels and receive on 128 channels, while the Vantage can transmit and receive on all 256 channels. Maximum sampling frequency in receive for V1 system is 45 MHz while for the Vantage is 62.5 MHz. Also, the V1 has 12 bit A/D converter while the Vantage has a 14-bit converter. Furthermore, the Vantage has more possibilities of configuring the different parts of the acquisition chain, including the gain of the low noise amplifier (LNA), and the cutoff frequency of the anti-aliasing filters.

For accurate interpretation of a signal from a transducer, it is important to know the real input voltage level. Therefore the relationship between the input signal and the Verasonics signal level at different TGC settings are crucial. Several gain settings are available to allow the user to adjust the overall gain on the receiving signal. In this research, the effect of the TGC gain on both Verasonics machines was investigated. All other parameters on the receive settings were set to the default values.

The TGC object defines the time-gain-compensation for the receiving signal in an acquisition event in Verasonics. This is defined by specifying 8 control points which are equally spaced over the receiving acquisition interval. The TGC control points are defined between 0 to 1023, and in total it can amplify the signal between up to 40 dB range. The gain is programmed to increase by increasing the depth of acquisition to compensate for the signal attenuation. The TGC effectively starts from the time zero, and the user could define the maximum applying range (which is usually set to the end of the receiving time, and is defined by the maximum imaging depth).

In order to characterize the performance of the Verasonics an input signal with 40 cycles sinusoidal burst function with 7.5 MHz frequency was applied to one of the input pins of the Verasonics. By changing the amplitude of the input signal, the signal was acquired at different TGC settings. We considered constant TGC gains of 100, 300, 500, 700 and 900. The sampling frequency was set to the highest value (i.e. 45 MHz for V1 and 62.5 MHZ for Vantage system). The amplitude of the input signals, and the acquired signal by the Verasonics were analyzed with similar approach explained above.

5.2.5. Measurement setup

For electrical evaluation of the chip, two bare ASICs (without PZT transducer elements) are mounted on a daughterboard. A few of the element bond pads are randomly chosen to

apply a known input signal, mimicking an input from a PZT transducer. The output signal from the ASIC is used to investigate the TX-RX switches and also the performance of the receiving path with two LNA settings: LNA on and LNA off. The electrical connections from the ASIC bond pads to the daughterboard were made with a wire bonding machine, using 25 μm thick gold wires. Then epoxy was applied to cover the bond wires for protection. A photograph of the top view of two ASICs mounted on the daughterboard is shown in figure 5.3, where point 1 shows the test bond pads on the daughterboard and point 2 shows the wire bonds from the ASIC bond pads to the daughterboard.

The electrical performance of the individual units (i.e. the ASIC, the buffers on the motherboard, and the Verasonics), and the whole electrical chain were systematically characterized in a series of measurements. To characterize the ASIC, a known input signal was applied to a test pad (i.e. test point 1 in figure 5.3), and the received signal (i.e. test point 2 in figure 5.3) was recorded for two settings (LNA on and LNA off). The input signal was provided by an Acoustic Waveform Generator (AWG; Agilent 33250A from Agilent Technologies, USA), and the received signals were acquired by a digital oscilloscope (DSOX4054A, 500 MHz, 4 Channels Oscilloscope from Agilent Technologies). By changing the input voltage and observing the received signal, the linear regime and the saturation level of the ASIC were determined. In order to test the high voltage transmit switches, a known signal was applied to the TX pad at test point 2, and the transmitted signal was measured at the test point 1 for TX switch on and off. With the same approach, the buffers on the motherboard were characterized by applying a known input signal to the buffer input (test point 3 in figure 5.3), and measuring the output signal (test point 4 in figure 5.3). Furthermore, the Verasonics performance was characterized by applying a known voltage to the input pin (test point 4 in figure 5.3), and measuring the acquired signal by the Verasonics machine (point 5 in figure 5.3) at different TGC gain settings (TGC of 100, 300, 500, 700, and 900), while all other parameters were kept to the default setting. Moreover, to characterize the performance of the whole chain, an input signal was applied to the ASIC test pad (i.e test point 1 in figure 5.3), and the output signal was recorded at test points 3, 4, and 5.

5.2.6. Data Analysis

The electrical performance of the system was evaluated by comparing the output signals to the expected outputs based on the configuration of the electrical pathway. With the AWG we generated a 40 cycle sinusoidal burst as an input signal. Figure 5.4a shows three input signals with different amplitudes, applied to the Verasonics input pin. The acquired signal with the Verasonics at the constant TGC gain of 500 is shown in figure 5.4b. By increasing the input amplitude, the acquired signal with the Verasonics is clipped, which shows the saturation of the electronic circuit of the machine. Also, at the end of the signal an overshoot is observed which its amplitude is increased by increasing the amplitude of the input signal.

To compare the signal level different methods can be used to quantify the signal, such as the amplitude, the peak to peak value, the peak value, the average value, or the RMS value. The peak, or peak to peak values are highly sensitive to the noise in the signal, and the average or RMS values are dependent on the length of the recorded signal, and the DC

component of the signal. We chose to compare the amplitude of the signals. The signal amplitude is obtained based on the amplitude of the windowed signal in the Fourier domain at the transmit frequency. For this purpose a part of the signal, containing a complete 40 periods of the sinusoidal function, was cropped. In this case the Fourier transform of the windowed signal is equivalent to the Fourier coefficient and we define it as the signal amplitude. The values for the sub/super harmonics can also be used to investigate the nonlinear deformation of the signal. In figure 5.5, the Fourier transform of the signals of figure 5.4 are compared. As shown in figure 5.5a the spectrum of the signals have sharp peaks at the excitation frequency (i.e. 4 MHz on this signal), while at other frequencies the spectrum shows the noise level. On the other hand figure 5.5b shows the spectrum of the signals acquired with Verasonics, where not only the peaks at the excitation frequency (i.e. 4MHz) but also peaks at super-harmonics of the main frequency are observed. This nonlinearity occurs due to the clipping of the high voltage signals through the electronic front end of the Verasonics, and is stronger for the larger signals. To quantify the nonlinearity we calculated the ratio of the superharmonic values (up to 5^{th} harmonic) to the 1^{st} harmonic value. When the ratio of any super harmonic is higher than -30 dB, we considered a non-linear deformation of the signal. Based on this definition, the red and green curves in figure 5.5b are nonlinearly deformed signals.

5.3. Results and discussions

5.3.1. Characterization of the ASIC

To characterize the performance of the ASIC in receive mode, a 40 cycle sinusoidal burst signal with 7.5 MHz frequency was applied to the input of the ASIC, and the ASIC output was measured for two settings with LNA on and LNA off. By increasing the input voltage amplitude, nonlinear deformation at the output was observed. The generated harmonics due to the nonlinear deformation are compared for LNA off and for LNA on (figure 5.6a and figure 5.6b). The output voltage versus the input voltage is shown in figure 5.6c, and the gain of the ASIC is shown in figure 5.6d. In case of the LNA off, the 3^{rd} harmonic of the output signal exceeds -30 dB with an input signal of about 0.45 V amplitude, while in case of the LNA on, the nonlinear deformation happens at a much lower amplitude of the input signal (around 0.043 V). As shown in figure 5.6c, at higher input voltages the output signal has no longer a linear relationship with the input signal, and therefore the ASIC gain also drops. These measurements show that the maximum acceptable input voltage for linear operation of the ASIC (0.45 V with LNA off and 0.043 V with LNA on), and the saturation limit is reached for ~ 0.1 V.

In order to verify the operation of the high voltage switches of the ASIC in transmit mode, an excitation voltage of 30 V with 200 ns pulse width was applied to the TX pad (test point 2 on figure 5.3) and the output signal was measured at the ASIC output bond pad (test point 1 on figure 5.3). The input and output signals when TX-switch is on or off are compared in figure 5.7. The result verifies that the high voltage signal is successfully isolated when the switch is off.

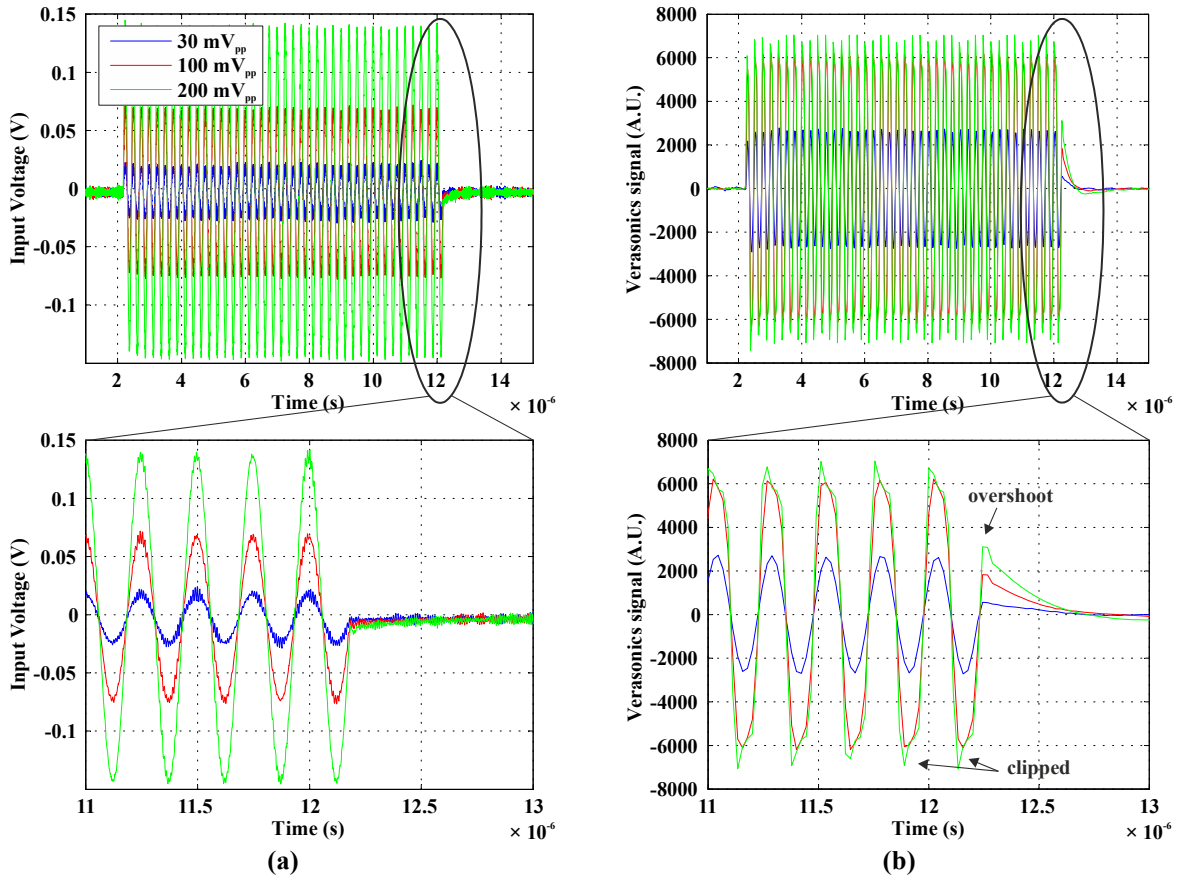

Figure 5.4. (a) Input signals to the Verasonics machine with three different amplitudes, **(b)** acquired signals with the Verasonics at TGC gain setting of 500.

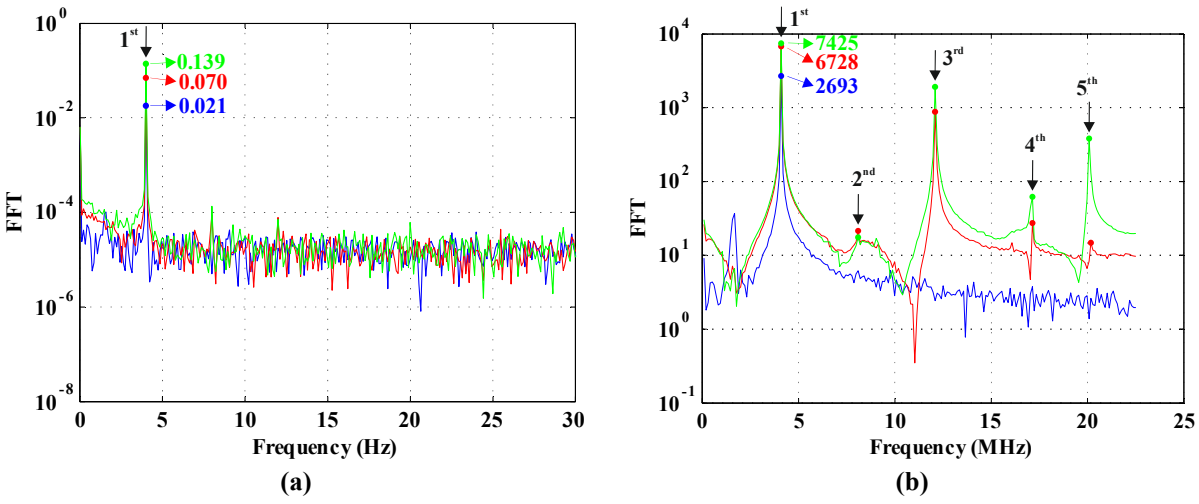

Figure 5.5. (a) The spectrum of the input signals to the Verasonics machine at three different amplitudes, **(b)** Spectrum of the signals acquired with the Verasonics at TGC gain setting of 500.

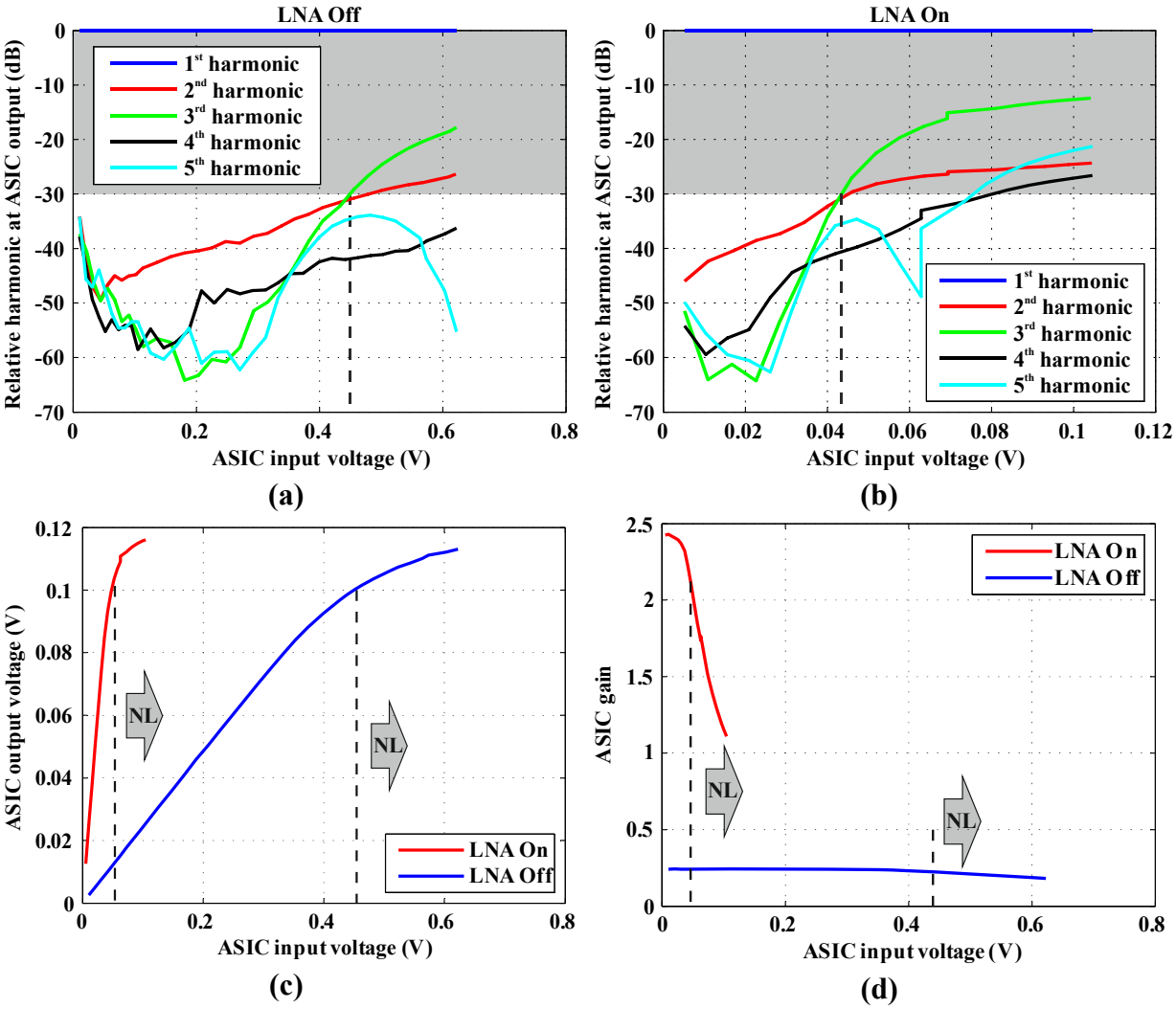

Figure 5.6. The performance ASIC for two cases of LNA on and LNA off, **(a)** the super harmonics relative to the main harmonic coefficient in case of LNA off, **(b)** the super harmonics relative to the main harmonic coefficient in case of LNA on, **(c)** the output versus the input voltages of the ASIC for two cases of LNA on and LNA off, and **(d)** The ASIC gain measured for two cases of LNA on and off.

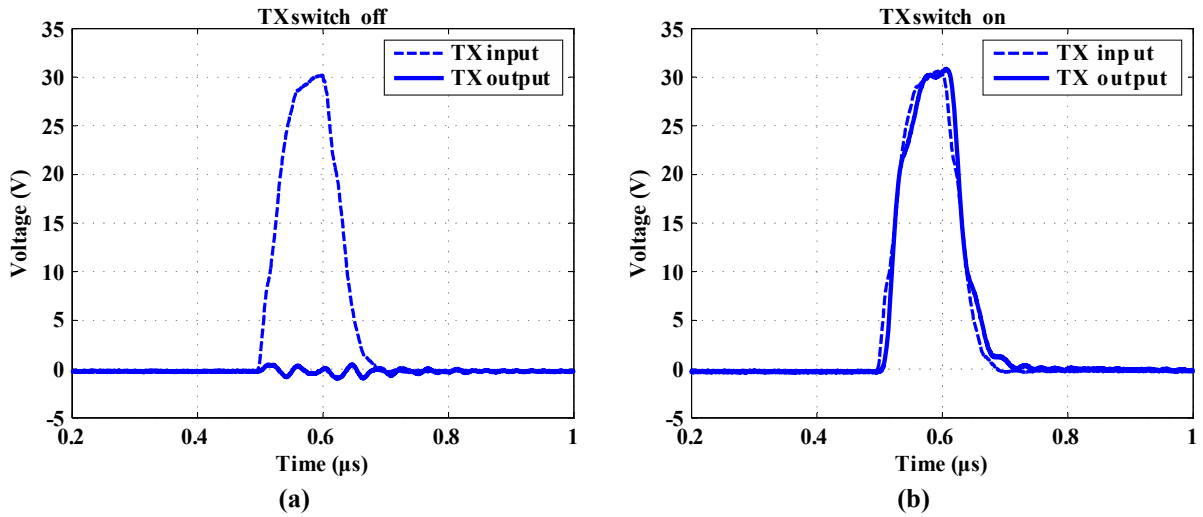

Figure 5.7. Measurement of the operation of the high-voltage TX switch, **(a)** when TX switch is off, and **(b)** when TX switch is on.

5.3.2. Characterization of the buffer

In this section, the performance of the buffers on the motherboard are explored. Figure 5.8a shows a schematics of the buffer circuit. As shown in this figure, the input signal (a 40-cycle sinusoidal burst at 7.5 MHz) was applied at probe point 1, and the output was measured at probe point 2. The resulting harmonic values for the first 5 higher harmonics are obtained and plotted in figure 5.8b. The output amplitude is compared to the input amplitudes in figure 5.8c. The measured gain is obtained by the ratio of the amplitude of the output signal to the input signal at the fundamental frequency (figure 5.8d). For the buffer, the higher harmonics exceed -30 dB level at ~1.08 V input amplitude. Since the linear regime for the buffer is at higher level than the ASIC, the buffer has an acceptable performance. The change in the slope of the curve in figure 5.8c shows the start of nonlinearities, which also corresponds to the drop in the gain.

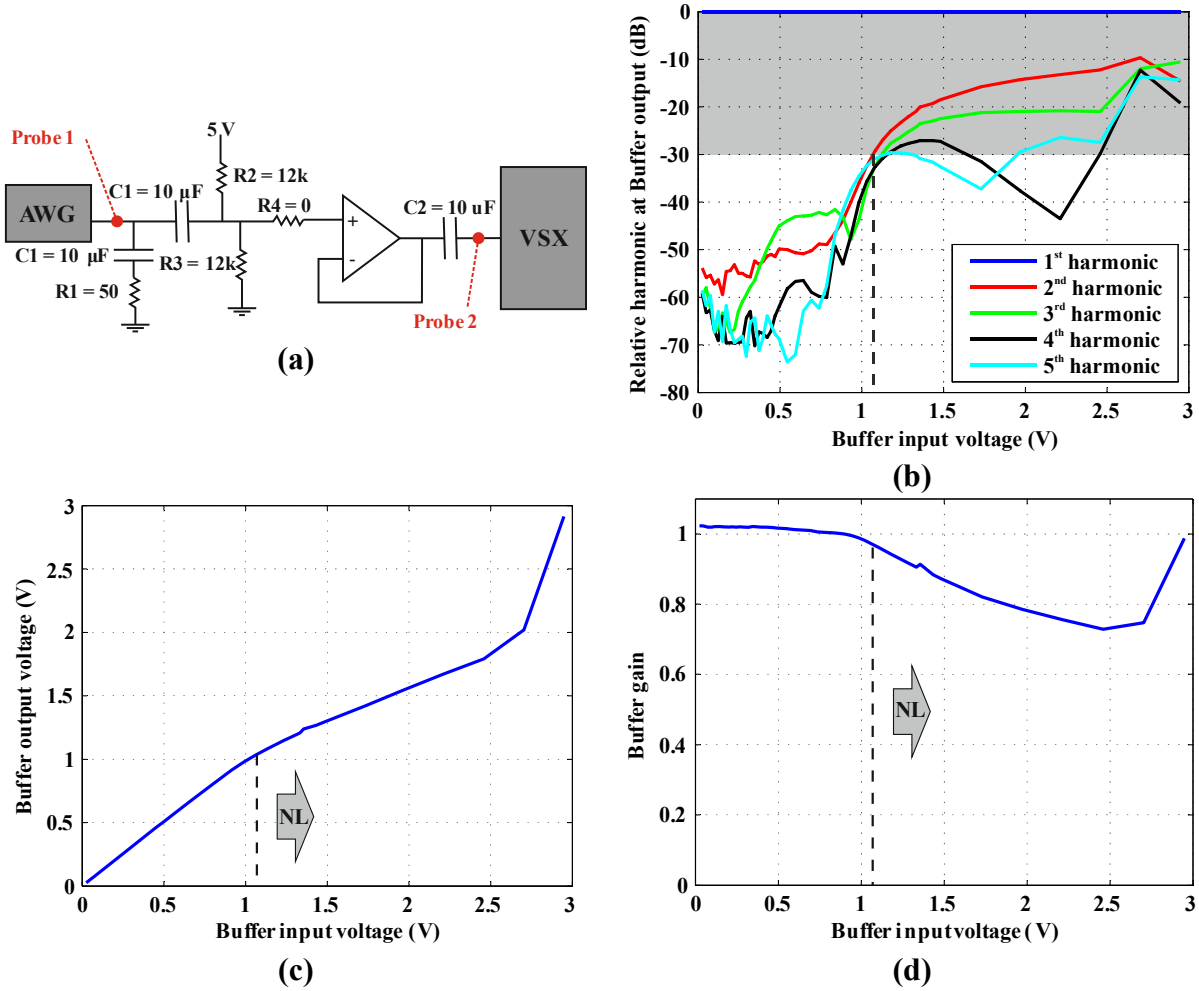

Figure 5.8. Characterization of the buffer on the motherboard, **(a)** Schematics of the measurement setup, **(b)** The higher harmonic coefficients, **(c)** The input to output relationship, and **(d)** Calculated gain based on the input to output relationships

5.3.3. Characterization of the Verasonics

Figures 5.9 and 5.10 shows the relationships between the input voltage to the acquired signal by the Verasonics machine with different TGC settings for the V1 system and the Vantage system respectively. Figures 5.9a and 5.10a, show the measured signal amplitude by Verasonics unit with respect to the input voltage, and figures 5.9b and 5.10b, show the gain. For each gain setting the saturation level is obtained when the super-harmonics amplitude exceeds -30 dB amplitude of the 1st harmonic. The saturation levels for each TGC setting are shown by the dashed lines. In case of having a linear performance the gain is constant, and the gain drops when the saturation occurs. The saturation level, the maximum acceptable input voltage, and the gain in the linear range at each TGC settings are given in table 5.1. By increasing the TGC, the Verasonics gain is increased, however the maximum acceptable input voltage in the linear regime is decreased.

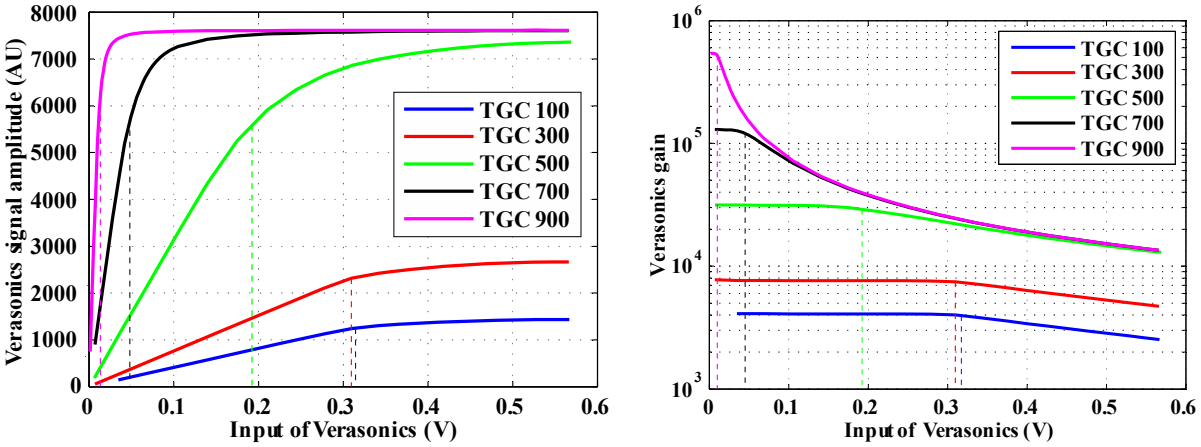

Figure 5.9. Characterization of the Verasonics V1 system at different TGC settings of 100, 300, 500, 700, and 900. **(a)** The relation between the measured signal by the Verasonics and the input voltage. **(b)** The gain (i.e. the Verasonics amplitude divided by the input voltage).

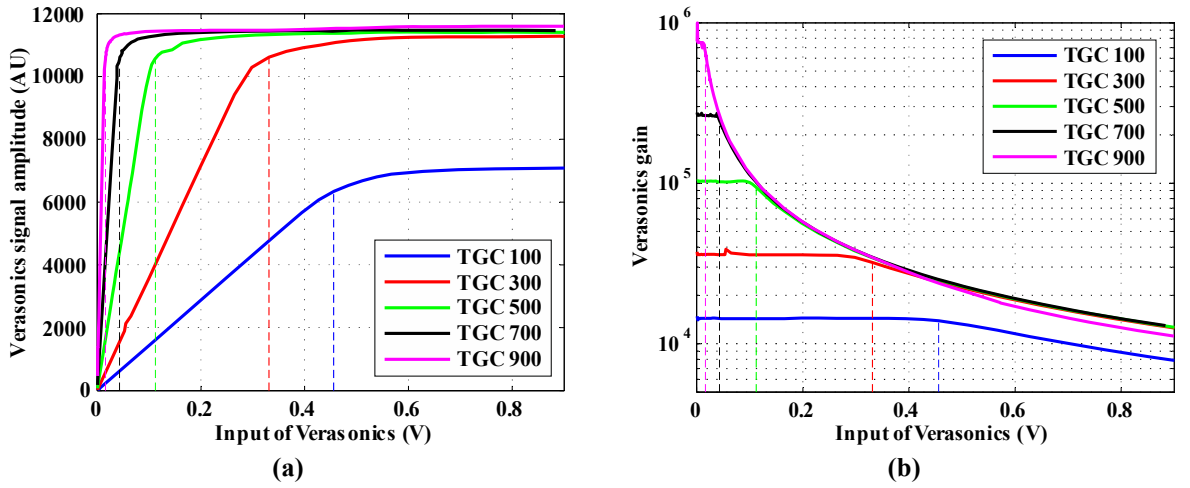

Figure 5.10. Characterization of the Verasonics Vantage system at different TGC settings of 100, 300, 500, 700, and 900. **(a)** The relation between the measured signal by the Verasonics and the input voltage. **(b)** The gain (i.e. the Verasonics amplitude divided by the input voltage).

Table 5.1. Measurement results

	V1 system			Vantage system		
	Max input (mV)	**VSX level (AU)**	**Gain (AU/mV)**	**Max input (mV)**	**VSX level (AU)**	**Gain (AU/mV)**
TGC 100	310	1245	4.1	456	6341	14.4
TGC 300	310	2315	7.6	331	10620	36.1
TGC 500	185	5497	31.4	112	10560	103.2
TGC 700	45	5514	129.3	43	10540	263.5
TGC 900	11	5602	543.3	16	10630	754.9

5.3.4. Characterization of the whole electrical chain

To characterize the performance of the whole electrical system including the ASIC, buffers, and the Verasonics system, an input signal was applied to the ASIC input (i.e. at the test pad 1 in figure 5.3) and the output signal was measured at the ASIC output, the buffer output and on the Verasonics (i.e. test point 3, 4, and 5 in figure 5.3). For this purpose, the amplitude of a 40 cycle sinusoidal burst signal with 7.5 MHZ frequency was swept with an AWG and the signals at different locations were recorded by the oscilloscope. These measurements were performed with both Verasonics V1 and Vantage systems for LNA on and LNA off, and for 5 different TGC settings (TGC of 100, 300, 500, 700, and 900). After processing, the relationships between the amplitude of the input signal and output signal at the fundamental frequency and the higher harmonics were obtained.

Figure 5.11 displays the relationship between the input signal on the ASIC to the ASIC output, the buffer output, and the acquired signal by the Verasonics at different input amplitudes. The results for the V1 system is presented in figure 5.11a, and for the Vantage system is shown in figure 5.11b. In both figures, on the first quadrant, the relationship between the input and output of the ASIC are compared. It is shown that the threshold for the ASIC output, before it reaches to the nonlinear saturation regime is around 0.08 V. This saturation level occurs when the input signal is above 0.45 V in case LNA off, and 0.045 V in case LNA on. The second quadrant shows the performance of the buffers on the motherboard. As expected, it has a linear performance in the working amplitude range of the ASIC. This is due to the saturation level of the buffer which was measured at ~1 V (obtained from figure 5.8b). The third quadrant displays the performance of the Verasonics by comparing the acquired signal with Verasonics to the Verasonics input signal. This should be compared to figure 5.9a (for the V1 system), and 5.10a (for the Vantage system).

The results of figure 5.11 are the combined results of the individual measurements presented earlier in the figures 5.6c, 5.8c, 5.9a and 5.10a. The only difference here is an extra -4 dB attenuation of the signal in the entire electrical pathway. This attenuation is caused by the transmission cables. We have used micro-coaxial cables with ~1 m length to transfer the signals from the daughterboard to the motherboard/Verasonics. The 4 dB attenuation is expected for such a long cable.

The results in figures 5.11 show that when low TGC settings (i.e. TGC settings of 100, 300, and 500) are used, the nonlinear deformation of the final acquired signal with Verasonics is dominated by the saturation of the ASIC. By increasing the TGC gains (i.e TGC settings of

700 and 900) the nonlinear deformation occurs in the front end of Verasonics. These findings are very important to determine the acceptable operational voltage range at each transmit-receive setting for performing imaging with the matrix transducer when connected to the Verasonics system.

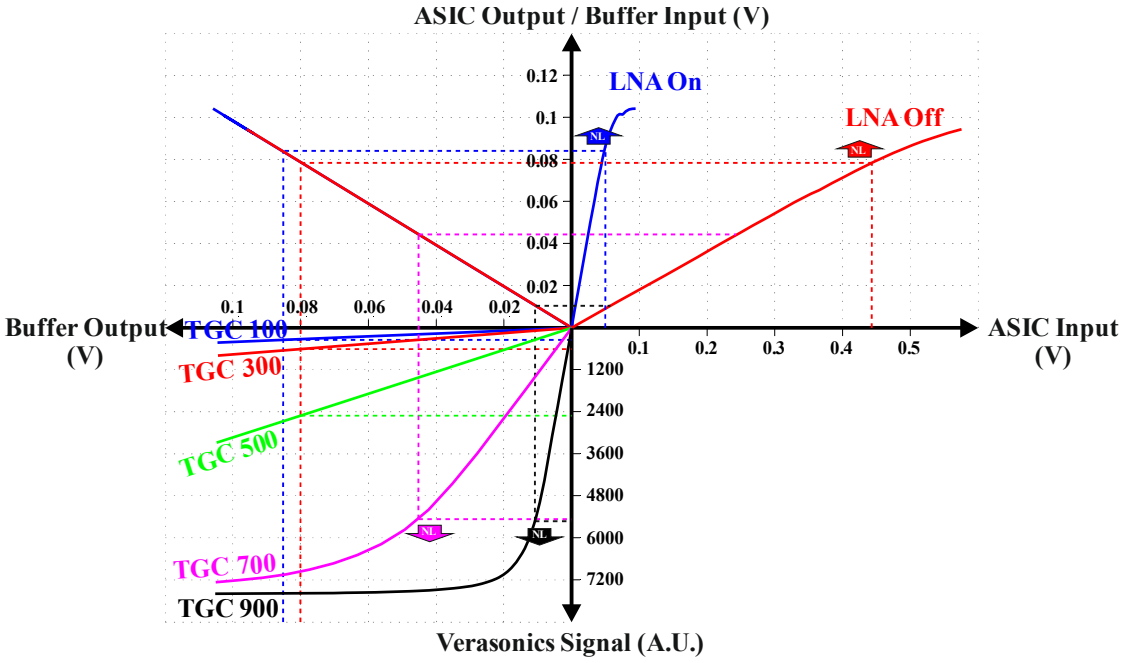

Figure 5.11. Characterization of the whole electrical chain including the ASIC, transmission cables, motherboard, and the Verasonics. The first quadrant shows the relation of the output to the input of the ASIC for LNA on and LNA off. The second quadrant shows the linear performance of the buffers on the motherboard. The third quadrant shows the acquired signal by the Verasonics with respect to the input signal, at TGC gain settings of 100, 300, 500, 700, and 900. The results with **(a)** Verasonics V1, and **(b)** Verasonics Vantage.

5.4. Summary

One efficient approach to make an ultrasound matrix transducer is with direct integration of the transducer elements on top of an ASIC. We have designed an ASIC, which is suitable for high frame rate carotid imaging application. The ASIC contains an array of 24 × 40 elements with 150 μm pitch. The elements are connected to the ultrasound machine through a row level transmit and receive scheme, and transducer elements on rows are accessed by the electronic switches under the elements. This makes the selection of different aperture possible. To connect the ASIC to the ultrasound machine, a motherboard and a daughterboard are designed. In this chapter we focused on the characterization of the whole electronic chain, including the ASIC, the motherboard, and the ultrasound machine (Verasonics V1 and Vantage systems). To characterize the performance of the ASIC, first the effect of TX-RX switch on the transmit signal was tested. Then on the receiving path, the relation between the input and output of the ASIC in two cases of LNA on and LNA off were investigated. The linearity of the buffers on the motherboard was tested in a separate measurement. The relation between the input and the acquired signal on both Verasonics systems were also measured in five different constant TGC settings. The performance of the whole electrical chain was tested and the results were compared with the measurements of the individual components. The measurement results determine the saturation level of the ASIC and the Verasonics system in different settings. It is shown that the operational range is limited by the ASIC at low TGC gains and by the Verasonics at high TGC gains. The results of this chapter are necessary for a proper interpretation of the acoustical measurements of the piezoelectric matrix transducer.

CHAPTER 6

A Programmable and Tileable PZT Matrix Transducer with Integrated Electronics for 3D Real-time Ultrasound Imaging[1]

Abstract

This paper describes the development and characterization of a prototype PZT matrix transducer, which can act as a building block of a larger matrix array for three dimensional, real-time ultrasound imaging. Although it is specifically intended for imaging of the carotid arteries, the transducer can be used for other imaging applications as well. The transducer consists of a matrix array with 24×40 piezoelectric transducer elements with 150 μm pitch, which are mounted on an Application Specific Integrated Circuit (ASIC). The ASIC connects the 960 elements to the ultrasound mainframe through only 24 transmit and 24 receive channels. The ASIC contains programmable switches under each element, by which any configuration of elements can be defined in both transmit and receive. The geometry of the transducer allows easy tiling of these ASICs. The prototype is electrically and acoustically characterized in a series of measurements. In a pulse-echo measurement, 87% of the working elements are within the -6 dB sensitivity range. The transducer has a central frequency of 7.35 MHz, with a -3 dB single path bandwidth of 45%. The overall received dynamic range is more than 83 dB and the minimum detectable pressure is 10 Pa.

[1] This chapter is submitted for publication as:
Maysam Shabanimotlagh, Eunchul Kang, Verya Daeichin, Pieter Kruizinga, Qing Ding, Emile Noothout, Zu-Yao Chang, Hans Bosch, Michiel Pertijs, Nico de Jong, Martin Verweij; A programmable and tileable PZT matrix transducer with integrated electronics for 3D real-time ultrasound imaging, Physics in medicine and biology.

6.1. Introduction

Carotid plaque is usually monitored to identify high-risk patients [111]. With conventional two-dimensional (2D) ultrasound imaging, the assessment of the plaque is based on multiple cross-sectional, two-dimensional images of the three-dimensional (3D) vessel structure. Using this approach, an accurate assessment of the plaque progress is difficult and highly dependent on the skills and experience of the sonographer [17]. This requires reproduction of the same imaging plane at later times, which is difficult and sometimes impossible due to the restrictions imposed by the patient's anatomy or position. Moreover, quantitative estimation of the plaque volume in 2D ultrasound is based on measurements of height, width and length in different orthogonal views for ideal shapes (e.g. ellipsoidal), which are prone to error [18]. 3D ultrasound has the potential for accurate quantitative comparison of the changes in plaque volume, and maybe vital for therapy assessment [98, 112-114]. In carotid artery diagnosis, measurement of blood flow and plaque surface motion are important parameters [115]. These phenomena are essentially 3D, while with 2D ultrasound these can only be measured in the imaging plane. For accurate analysis of the dynamics of the blood flow, 3D vector velocities at a high frame rate are necessary. 2D methods do not provide a realistic picture of the actual flow and do not provide information about the out of plane velocity component [116]. These 3D phenomena can only be assessed correctly with high frame rate 3D ultrasound imaging.

Going from 2D to 3D ultrasound imaging is challenging and specific limitations are imposed, depending on the application. Different approaches are used for realizing 3D ultrasound imaging. One approach is to mechanically sweep the conventional one-dimensional (1D) linear or phased array probes for 2D imaging by a motorized system to acquire a 3D dataset [19-21]. With this approach large errors can occur due to motion artifacts. Furthermore, large structures are difficult to scan, and sometimes the bulkiness and the weight of the scanning probe makes it inconvenient to use [17]. To overcome these limitations, free-hand scanning techniques have been developed, in which a position and orientation sensor is added to the conventional 1D array transducer. While the transducer is manipulated, the trajectory and orientation are recorded together with the acquired 2D images, which are afterward combined to produce a 3D image [19, 23, 117]. Since the relative locations of the acquired images are not predefined, the operator must ensure that the spatial sampling is appropriate and the set of images has no significant gaps [17]. In both motorized and free-hand scanning, an optimal 1D array transducer can be utilized. The fabrication technology for 1D arrays has matured and these two scanning techniques have high image quality in the scan planes. However, these techniques show poor spatial resolution in the direction perpendicular to the scan planes, and suffer from low frame rate. These issues limit the use of mechanical scanning for applications such as echocardiography, where motion needs to be accurately tracked [18]. Another approach for 3D imaging is to make a 2D matrix array that extends in both elevation and azimuthal directions, and to construct the image from 3D volumetric data. With a 2D array, the transducer could remain stationary, and electronic scanning could be used to sweep the ultrasound beam over the entire volume under examination, while both lateral and azimuthal resolution remain the same [17]. In addition, this approach enables electronic beamforming, 3D focusing, and aperture shifting. Electronic

scanning overcomes the frame rate limitation in other approaches. However, the fabrication and implementation of 2D matrix arrays are challenging [28].

With a 2D matrix array, the element pitch should be kept below half a wavelength in both lateral and azimuthal directions to avoid grating lobes [3]. On the other hand, to obtain high lateral resolution the total aperture should be large. The combination of small elements and a large aperture may result in a very large number of transducer elements. It is fairly well possible to make a matrix array with >1000 elements, but making electrical connections to all the elements are challenging [30]. Several dynamic switching schemes have been proposed for the selection of the transmit and receive elements, with the purpose to reduce the cable count to the amount that is available on conventional ultrasound machines [18, 19]. Sparse arrays are also proposed because these can maintain good 3D beam characteristics with a low number of elements that can be directly connected to an ultrasound machine [28, 31, 118]. Sparse arrays are capable of high volume rates, but the image quality is still limited by the number of connected elements [34]. To improve the image quality (increase image resolution, contrast and SNR), more elements should be used, and therefore the matrix should be fully populated [35].

To realize a fully populated matrix transducer that uses a reduced number of channels, different approaches have been proposed for combining the signals from multiple elements of the matrix transducer. The signals from the elements in a sub-aperture can be locally beamformed to obtain one output receive signal [34, 36, 37]. This reduces the number of receive channels by a factor that is equal to the number of elements in a subgroup. With the row-column approach it is possible to focus the transmit beam in one direction and the receive beam in the orthogonal direction. The number of channels required in this approach is reduced from N^2 to 2N, where N is the number of elements in each direction of a square matrix array [38-40]. Switching matrices are proposed to connect a selection of elements to a limited number of transmit and receive busses [41]. Annular rings are used to connect the elements of the 2D matrix transducer with a limited number of delay lines [41-43]. Channel multiplexing is also another approach to combine the data from several receive elements into one output line, at the cost of frame rate reduction [44]. All of these techniques have their own pros and cons.

An efficient approach to construct an ultrasound matrix transducer is to build the array of piezoelectric elements directly on top of an Application Specific Integrated Circuit (ASIC). The ASIC performs amplification of the receive signals right under the piezoelectric elements to improve the signal quality. Moreover, it allows to achieve per-element signal delay, switching and impedance matching, and to perform signal addition and multiplexing to achieve channel count reduction [45]. With state-of-the-art ASIC technology, the per-element circuitry only occupies a small area, such that the matrix array can be built directly on top of the ASIC [34, 36].

We intend to develop a probe for high frame rate, 3D imaging of the carotid arteries. To achieve fast volumetric scanning and limit the channel count, we will use a piezoelectric matrix array on top of an ASIC. Moreover, employing plane wave imaging will highly speed up the scanning process. However, for carotid imaging this requires a matrix transducer of

about 1.5 cm × 3.5 cm, which is too big for a single ASIC. Therefore, we propose a tiling approach by which a large matrix transducer is constructed from smaller building blocks.

We have designed a new configurable and tileable transducer, containing a matrix of 24×40 (rows × columns) PZT transducer elements, which are directly mounted on an ASIC. The ASIC contains per element transmit and receive switches, and control logic. Through the row level transmit and receive buses, electrical connections between different combinations of elements and the ultrasound machine can be made. This enables fast programmable switching between various elements configurations. The design allows for tiling several of these arrays together to make a larger matrix array suitable for carotid imaging applications. In this paper we describe the development of a prototype of the matrix transducer, together with the electrical and acoustical characterization results. Section 2 describes the design of the PZT matrix and the ASIC, the imaging capabilities of the transducer, the fabrication of the prototype, and the measurement setup for the characterization. Section 3 presents both the electrical and acoustical characterization results. Discussions of the characterization results are presented in section 4, and conclusions are given in section 5. Carotid plaque area and progression is usually monitored to identify the high-risk patients [111]. With conventional ultrasound imaging, the sonographer makes the decision based on multiple cross-section two dimensional (2D) images of a three dimensional (3D) structure. Therefore an accurate assessment of the plaque progress is difficult and it highly depends on the skills and experiences of the sonographer [17]. Also, for follow-up studies, reproducing the same imaging plane at a later time is difficult, and sometimes impossible due to the restrictions imposed by the patient's anatomy or position. Furthermore, quantitative estimation of the plaque volume in 2D ultrasound is based on measurements of height, width and length in different orthogonal views for an ideal shape (e.g. ellipsoidal), which are prone to error [18]. 3D ultrasound has the potential for accurate quantitative comparison of the changes in plaque volume, and is vital for the assessment of the therapy [98, 112-114]. On the other hand, the measurement of blood flow and plaque surface motion are important parameters in carotid artery diagnostics [115]. While these phenomena are 3D, with 2D probes they can only be measured in the imaging plane. For accurate analysis of the dynamics of the blood flow, 3D vector velocities at a high frame rate is necessary. 2D methods do not provide a realistic picture of the actual flow and do not provide information about the out of plane velocity component [116]. These 3D phenomena can only be assessed with a 3D ultrasound probe which is capable of producing real-time data.

6.2. Materials and methods

6.2.1. Transducer design choices

For 3D real-time imaging, during transmission all elements in the matrix of the piezoelectric transducer are simultaneously excited to generate a plane wave, as indicated by the green plane in figure 6.1. In reception, a subset of elements on each row is selected by programming the electronic switches in the ASIC, and the signal from the combined elements on each row is transferred to the mainframe. By processing the received data, an image in a receiving plane is obtained, as indicated by the blue planes in figure 6.1. In the next

acquisition the selected subset of elements on each row is shifted and an image in the next receive plane is obtained. This procedure is repeated to acquire the signals for all imaging planes, and by combining the data from all receive planes a 3D image of the total volume is constructed.

To image the carotid arteries, a transducer with an aperture of 12 mm × 36 mm (x dimension × y dimension) is chosen. Since the transducer array is too large to be covered by a single ASIC, an array of 2 × 10 ASICs will be employed, as shown in figure 6.1. Each ASIC contains a matrix of 40 × 24 elements with 150 µm pitch, which covers a transducer area of 6 mm × 3.6 mm. The transducer is designed for a center frequency of 7.5 MHz, which is recommended for carotid imaging applications [108]. To avoid image saturation, a minimum dynamic range of 70 dB is required for the front end, as in similar applications [3]. The main focus in this paper is to verify the performance of the single chip transducer. Consequently, we have made a prototype of a PZT matrix transducer on a single ASIC, and characterized the electrical and acoustical performance of the transducer in different configurations.

The layout of the ASIC is such that all wire-bond connections are situated only on one side, and the other three sides of the chip are covered by transducer elements. This allows for tiling these ASICs in a head-to-head, and side-by-side fashion. This design choice makes it possible to up-scale the prototype to a larger matrix array.

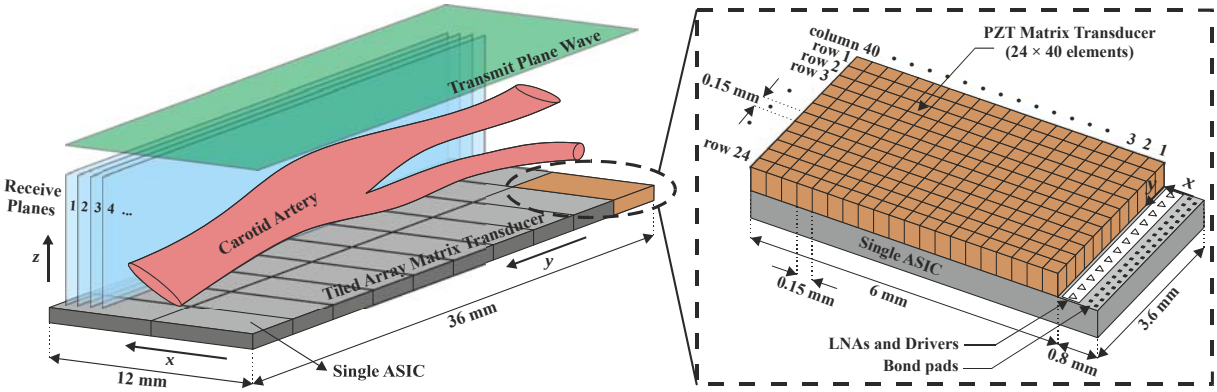

Figure 6.1. Schematic drawing of the full matrix transducer, together with a single ASIC transducer with PZT elements mounted on top.

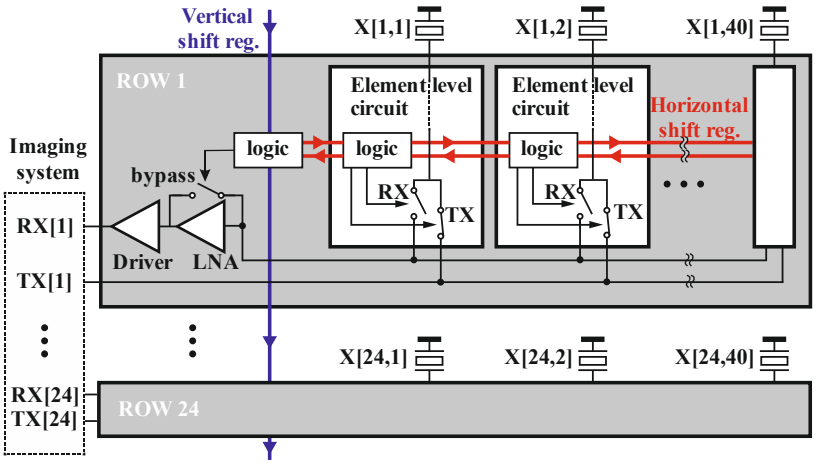

Figure 6.2. Electronic architecture of the ASIC.

6.2.2. ASIC design and implementation

Figure 6.2 shows the electronic architecture of the ASIC. Row-level circuits interface the PZT transducer array to an imaging system. Each row has 40 elements, which can be individually connected to one transmit and one receive bus. Thus the achieved channel count reduction factor is 20. This arrangement results in a manageable number of channels (< 256 for most of the ultrasound machines) for the full matrix transducer. The element-level circuitry fits in the 150 μm × 150 μm area occupied by the transducer element, allowing the transducer array to be integrated directly on top of the ASIC.

Each row-level RX bus is wired out through a shared row-level low-noise amplifier (LNA) and cable driver. To avoid saturation for strong receive signals, the row-level LNA has a bypass option that is controlled by a vertical shift register. Each row-level TX bus receives an externally generated high-voltage transmit signal. Each transducer element has a programmable switching circuit that allows the element to be connected to the RX bus or the TX bus. The ASIC allows a rapid configuration of the selected RX and TX elements. Moreover, its architecture supports a variety of element configurations for different imaging schemes. Control logic, programmed through vertical and horizontal shift registers, determines whether an element participates to the intended configuration. The detailed design of the ASIC circuitry is presented in our earlier work [119]. The ASIC is fabricated in a 0.18 μm high-voltage BCDMOS process and can handle signals up to 30 V.

6.2.3. Imaging capabilities

The main idea behind the electronic architecture of the ASIC is to activate individual elements in the matrix array by means of electronically programmable switches. With reconfigurable per-element logic, the ASIC supports different element configurations for different imaging purposes. A few examples are outlined in table 6.1. For example, for plane-wave imaging the whole aperture can be used for transmission and reception can take place column by column, while for synthetic aperture imaging column by column transmission and reception can be used. For other purposes, specific patterns, or even a pseudo-random selection are possible [120]. Each imaging scheme allows for a different trade-off between spatial and temporal resolution. For imaging of the carotid artery, this trade-off follows from the intended imaging mode: conventional B-mode requires the highest spatial resolution possible, Doppler mode needs the best temporal resolution [40, 121], and pulse wave imaging requires a bit of both [122].

For fast reconfiguration, each element has 9 memory bits, which can be pre-programmed for 9 different element configurations. The ASIC can switch between these patterns in a single clock cycle. Another capability is shifting the memory of one element to the neighboring element in the row, which can be used to shift the selected aperture/pattern to the left or right. This can be used for example to operate the matrix transducer as an electronic moving linear array.

Table 6.1. Imaging schemes determined by different transmit (TX) and receive (RX) element configurations.

	(a) Plane wave imaging	(b) Dynamic linear array	(c) Growing aperture (dynamic focusing)	(d) Random pattern imaging
Transmit aperture	Plane wave TX	TX1 TX2 TX3 ...	TX1 TX2 TX3 ...	Random 1
Receiving aperture	RX1 RX2 RX3 ...	RX1 RX2 RX3 ...	RX1 RX2 RX3 ...	Random RX 1

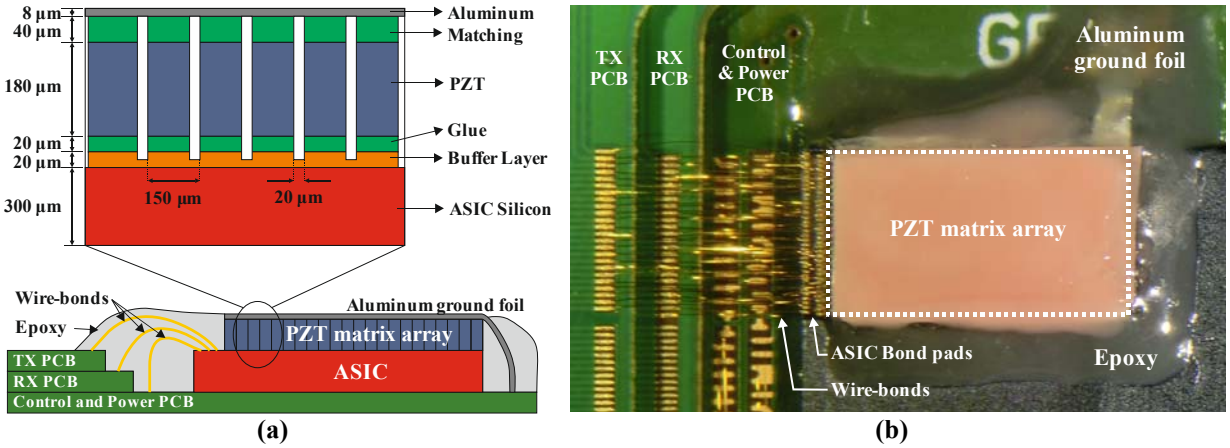

(a) (b)

Figure 6.3. (a) A schematic drawing of the side view of the transducer prototype, with materials and layer thicknesses of the acoustic stack, **(b)** a photograph of the top view of the transducer prototype, which is wire bonded to the three-stage daughterboard PCB, and covered by ground foil and epoxy.

6.2.4. Transducer fabrication

The transducer prototype was made by fabricating the piezoelectric matrix elements on top of an ASIC by using the PZT-on-CMOS integration scheme described by [45]. In figure 6.3a, a schematic drawing of the acoustic stack with information of all materials and thicknesses is shown. A buffer layer was made by gold ball bumping on top of the element bond pads of the ASIC, which have the same pitch as the transducer elements, i.e. 150 µm in both x and y directions. The gaps between these gold balls were first filled with an electrically non-conductive epoxy material, and then it was grinded down until the gold balls were again exposed. The main role of this layer was to establish a mechanical buffer layer for dicing the matrix of piezoelectric elements. This buffer layer also provides the electrical connections from the ASIC bond pads to the piezoelectric elements, while electrically isolating the neighboring elements from each other. On top of the buffer layer, a piezoelectric ceramic plate (CTS 3203 HD, CTS Corporation, Elkhart, Indiana, United States) with 180 µm thickness was stacked using an electrically conductive glue (IQ-Bond 5600) layer with an approximate thickness of 20 µm. A 40 µm thick matching layer consisting of the same

conductive glue was applied on top of the PZT ceramic. After applying all layers, the acoustical stack was diced with a dicing machine, to make the 2D matrix array. The dicing should be such to electrically separate the transducer elements, but not cut into the ASIC. For the dicing machine, a rotation speed of 28,000 rpm and a dicing feed below 1 mm/s was chosen to avoid excessive stress and achieving optimal cutting and stability. Since both mechanical forces and temperature contribute in depolarization of the PZT material, we kept the temperature in the whole process below 70 °C by cooling with water [45]. This temperature is well below the Curie temperature of 225 °C for the PZT material. The dicing kerfs were made using a 20 μm thick diamond blade, and were left unfilled to minimize the acoustical crosstalk between the elements. Finally to make the common ground electrode, an 8 μm thick aluminum foil was glued on top of the whole matrix array.

A daughterboard is designed to hold the matrix transducer, and to provide the transmit, receive, power, and control signals to the ASIC. A photograph of the top view of the final matrix transducer mounted on the daughterboard is shown in figure 6.3b. This daughterboard consists of three printed circuit boards (PCBs), which are stacked on top of each other. The TX PCB and the RX PCB provide the transmit and receive connections respectively, and the third PCB provides the power and control data to the ASIC. The matrix transducer was mounted at the center of the power and control PCB, where the RX and TX PCBs had a hole. This stacked solution was chosen because the density of the bond-pads on the ASIC was too high to be matched by a sequence of bond-pads on one PCB. The electrical connections from the ASIC bond-pads to the daughterboard bond-pads were made with a bonding machine using 18 μm thick aluminum wire-bonds. UV curing glob top epoxy was applied over the bonding wires for protection. Finally, a hard epoxy material was applied on the edges of the array to make the transducer water resistant.

A motherboard is used as an interface between the daughterboard and the ultrasound machine. The motherboard is provided with two Canon connectors (LLC DLM5-260PW6A, ITT Corporation, NY, USA) such that it can be mounted on a Verasonics machine (V-1, Verasonics, WA, USA). A matching network is provided in the transmit paths (TX) to minimize the overshoot and undershoot to guarantee the unipolar excitation generated from the Verasonics. On the other hand, to compensate for the cable load effect and to minimize the losses of the transmission line, the receive paths (RX) are buffered with unity gain operational amplifiers on the motherboard, which feed into the Verasonics. Commercially available micro coaxial Samtec cables (Samtec, New Albany, IN, USA) are used to transfer the TX and RX data between the daughterboard and the motherboard. The power and control signals are transferred via a flat ribbon cable from the motherboard to the daughterboard. An external FPGA (Altera DE2-115, San Jose, CA, USA) generates the control data to program the ASIC, and an external power supply provides the voltages and currents needed for the daughterboard and the motherboard. The computer of the imaging system controls the overall operation of the whole system. Figure 6.4 illustrates a schematic of the electrical chain in the measurement setup.

6.2.5. Measurement setup

6.2.5.1. Electrical characterization

We mounted a bare ASIC (without PZT array) on a daughterboard. This was used as a test sample to evaluate the electrical performance of the ASIC and the whole signal chain from the ASIC to the ultrasound machine, including the cables and the motherboard. A wire bond was made between a randomly selected element bond-pad on the ASIC and an externally accessible test pad on the daughterboard. The transmit, receive, power and control bond-pads on the ASIC were wire bonded to the daughterboard in the usual way. After programming the ASIC a known signal from an AWG was applied to the test bond pad and the corresponding output signal was recorded. In this way we could assess the electrical performance of the ASIC and the signal chain in different modes, e.g. with the LNA active or bypass, and with the TX and RX switches on or off.

6.2.5.2. Acoustical characterization

Figure 6.4 shows a schematic diagram of the setup for the acoustical evaluation of the transducer. For this purpose, the daughterboard was mounted in a box with an acoustically transparent window (25 µm thick polyimide) and the whole setup was submerged in a tank filled with deionized water. To test the transmit performance, the Verasonics was used to excite the matrix transducer. The produced pressure was detected by a calibrated 1 mm needle hydrophone (Precision Acoustics, Dorchester, UK), and the hydrophone output was recorded using a digital oscilloscope (DSOX4054A, Keysight Technologies, Santa Rosa, CA, USA), see option (a) in figure 6.4. To test the pulse-echo performance of the transducer, a 12 mm thick quartz plate was placed in the far field of the transducer (at 100 mm), see option (b) in figure 6.4. The transducer was excited by the Verasonics and the reflected pressure was detected by the transducer at different settings. To test the receive performance, a 0.5 inch 7.5 MHz transducer (V320, Olympus Corporation, Tokyo, Japan) was excited by an arbitrary waveform generator (33250A, Agilent Technology, Santa Clara, CA, USA), and the generated pressure was detected by the matrix transducer, this is option (c) in figure 6.4.

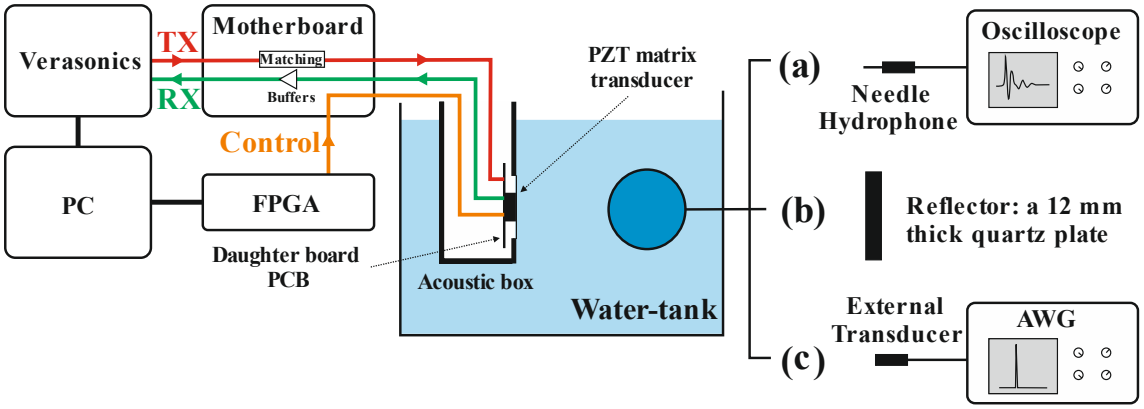

Figure 6.4. A schematic drawing of the acoustical measurement setup. **(a)** Transmit performance: a needle hydrophone is connected to a digital oscilloscope to measure the transmit pressure from the transducer. **(b)** Pulse-echo performance: a 12 mm thick flat quartz plate is used to reflect the pressure pulse back to the transducer. **(c)** Receive performance: an external transducer is excited with an arbitrary waveform generator to obtain a known incident wave on the transducer.

6.3. Results

6.3.1. Electrical characterization

To explore the linearity of the electronic system and the saturation limit of the chip, test signals were applied to the test bond pad of the daughterboard, and the resulting output signals were recorded at three different locations: (1) at the input of the buffer on the motherboard, (2) at the output of the buffer on the motherboard (i.e. at the input of the Verasonics), and (3) at the output of the analog-to-digital (A/D) converter inside the Verasonics. The measurements were performed for two ASIC settings (LNA on and LNA off) and five Verasonics settings (constant TGC gains 100, 300, 500, 700, and 900). All other receive settings of the Verasonics were kept at the default values. A 50 cycle sinusoidal signal with 7.5 MHz frequency was used as a test signal. The amplitude of the test signal was increased in steps until the output signal was saturated. The output amplitudes are obtained from the spectral peak of the windowed output signal.

The results of the electrical characterization are presented in figure 6.5. In the first quadrant, the relation between the input and output of the ASIC is given for both LNA settings. At high voltages, nonlinear deformation of the signal is observed, which is due to the saturation of the chip. The saturation level is defined here as the level where the higher harmonics rise above -20 dB (relative to the amplitude of the fundamental). The saturation input voltage for LNA on is 48 mV and for LNA off is 443 mV. Both values correspond to an output signal of approximately 80 mV. In the second quadrant, the performance of the buffer on the motherboard is analyzed. The two curves verify that the buffer is performing in the linear regime, and the buffer gain is 1. In the third quadrant, the relation between the input voltage and the A/D output signal of the Verasonics is shown for different TGC gains. The curves show that with TGC gains of 700 and 900, the signals above 5500 units are nonlinear, which is caused by saturation of the Verasonics electronic system. For the TGC gains of 100, 300, and 500, the Verasonics signal are always in the linear range, and they are limited by the saturation of the ASIC.

In a separate measurement, the frequency response of the ASIC was examined for LNA on and LNA off. For this purpose, a 50 cycle sine signal with an amplitude of 10 mVpp was applied to the test pad on the motherboard, and the frequency was swept from 0.5 MHz to 20 MHz in steps of 0.1 MHz. The output signal of the ASIC was measured with a digital oscilloscope (DSOX4054A, Keysight Technologies, Santa Rosa, CA, USA). The variations in the frequency responses for both LNA settings are within -1 dB between 1.3 MHz and 20 MHz, which means a reasonably flat frequency response in the frequency range of interest. Furthermore, a gain of 20 dB is measured for LNA on.

6.3.2. Acoustical characterization

First, through systematic measurements, the configurability of the chip, and the electromechanical performance of the elements (i.e. sensitivity, time and frequency response, directivity, and dynamic range) were examined. Then the prototype was tested in an imaging setting with a phantom.

6.3.2.1. Element configurations

To test the configurability, the FPGA was programmed to activate different patterns of transmit elements on the ASIC. In every test all 24 rows were excited in parallel with a unipolar pulse with a center frequency of 7.5 MHz and an amplitude of 25 V, generated by the Verasonics. Similar to option (a) in figure 6.4, a hydrophone was mounted on a controllable XYZ positioning stage, and used to measure the pressure in a plane parallel to the transducer at approximately 2 mm distance. To observe the pattern of active elements, the pressure was recorded in this *xy* plane, using 30 points at 0.3 mm increment in both *x* and *y* directions. After scanning, the maximum of the envelope of the pressure was calculated for all measurement points. The results are shown in figure 6.6. The dashed rectangle in the figure shows the size and approximate position of the transducer array, and the element configurations are indicated in the insets at the top-right corners.

Figures 6.6a, 6.6b, and 6.6c show the ability to electronically change the width of the aperture. Figures 6.6d, 6.6e, and 6.6f show the possibility of electronically shifting a selected aperture. In figure 6.6g, a random selection of five elements was chosen. The transmit beams from the single elements are quite similar, which implies a low sensitivity variation between these elements. Figures 6.6h and 6.6i show that we can define arbitrary selections of elements with the programmable ASIC.

The effect of aperture width on the transmit beam in the *xz* plane was also investigated by both simulation and measurement. First, the ASIC was programmed to transmit with 8, 16, 24, and 32 active columns. The hydrophone was used to scan the *xz* plane with 30 points at 0.3 mm increment in the *x*-direction and 50 points at 2 mm increment in the *z*-direction. Similar to the *xy* scan, the maximum of the envelope of the pressure is computed for each measuring point. The results are shown in figure 6.7a to 6.7d.

Second, a simulation in Field II was performed for comparison. For this purpose, a 2D matrix array with 24 rows and j columns (j=8,16,24,32) is defined, with 130 μm wide elements and 20 μm wide kerfs in both *x* and *y*-direction. A Gaussian modulated sinusoidal signal with 3 periods and 7.5 MHz center frequency was considered for the impulse response of the elements. The *xz* plane was discretized by using grid points from -4.5 mm to 4.5 mm with 0.1 mm distance in the *x*-direction, and from 1 mm to 100 mm with 1 mm distance in the *z*-direction. Again, the plots of the transmit beam were based on the maximum envelope of the pressure in the grid points. The resulting simulated beams for different aperture sizes are shown in figure 6.7e to 6.7h.

For all cases, the shape of the measured beam is qualitatively in good agreement with the simulated beam. Since the measurement is done with a 1 mm needle hydrophone, the plots of the measured beam show an averaged pressure over the aperture of the hydrophone. Therefore, as compared to the simulation, the measurement results are smoothened in the *x*-direction. By increasing the width of the aperture, the natural focus of the beam shifts to higher depths. This is observed for both the measured and the simulated results.

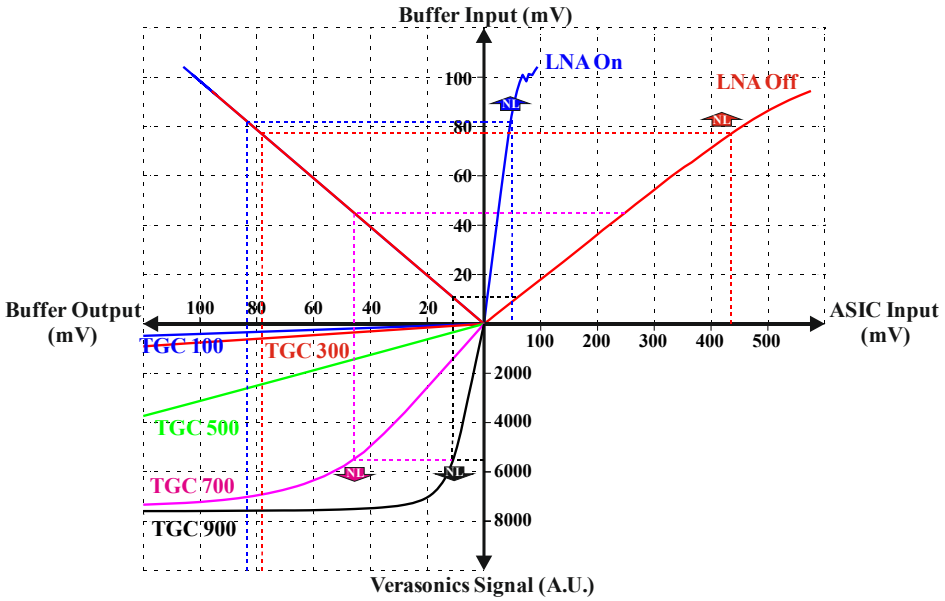

Figure 6.5. Performance of the electronics chain from ASIC input to Verasonics A/D converter output. The first quadrant shows the relation between the ASIC input and the ASIC output for LNA on and LNA off. The second quadrant shows the linear performance of the buffers. The third quadrant shows the relation between the input and the A/D converter output of the Verasonics, for several TGC gains.

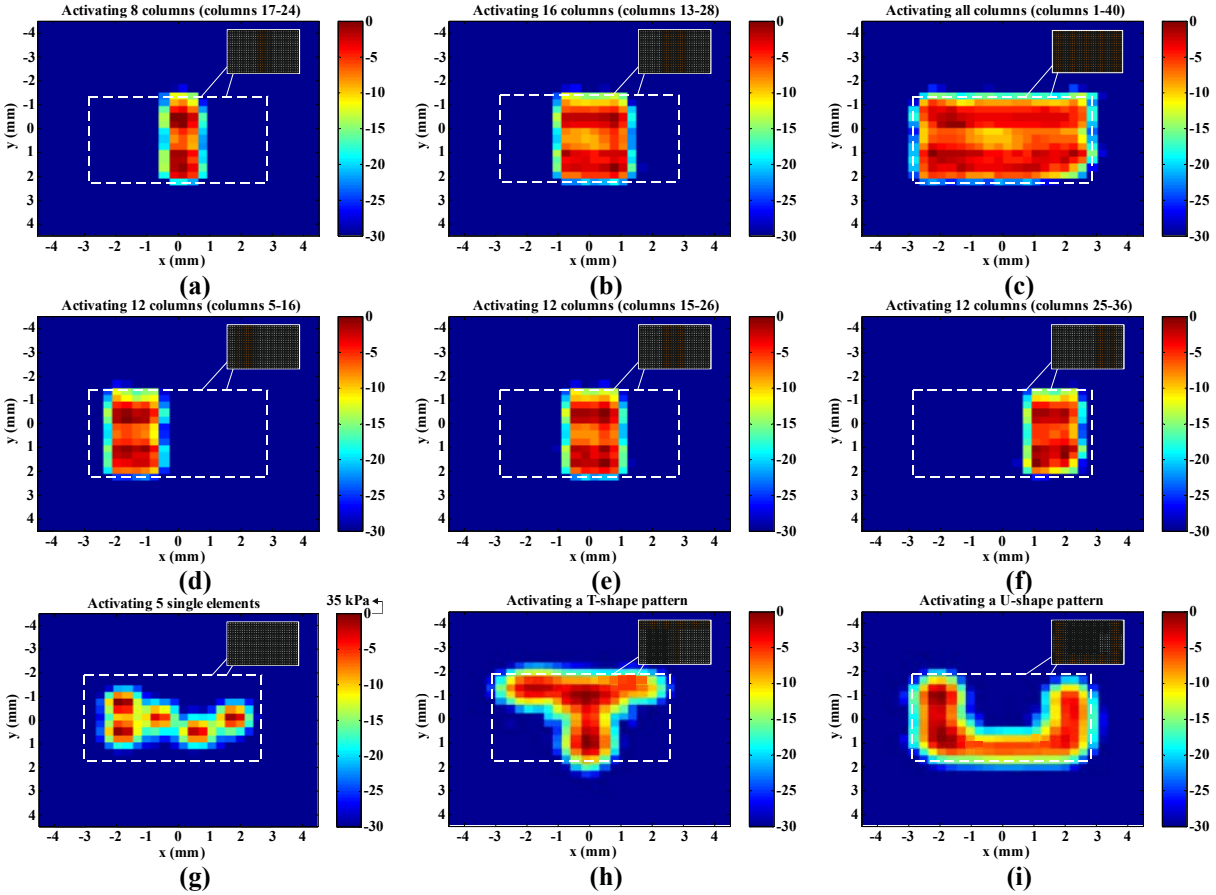

Figure 6.6. Transmit pressure measured by a hydrophone in the *xy* plane at approximately 2 mm from the transducer surface, for different element configurations, **(a)** selection of 8 columns (columns 17-24), **(b)** selection of 16 columns (columns 13-28), **(c)** selection of all columns (columns 1-40), **(d)** selection of 12 columns (columns 5-16), **(e)** selection of 12 columns (columns 15-26), **(f)** selection of 12 columns (columns 25-36), **(g)** selection of 5 elements with random location, **(h)** selectuion of a T-shape pattern, and **(i)** selection of a U-shape pattern.

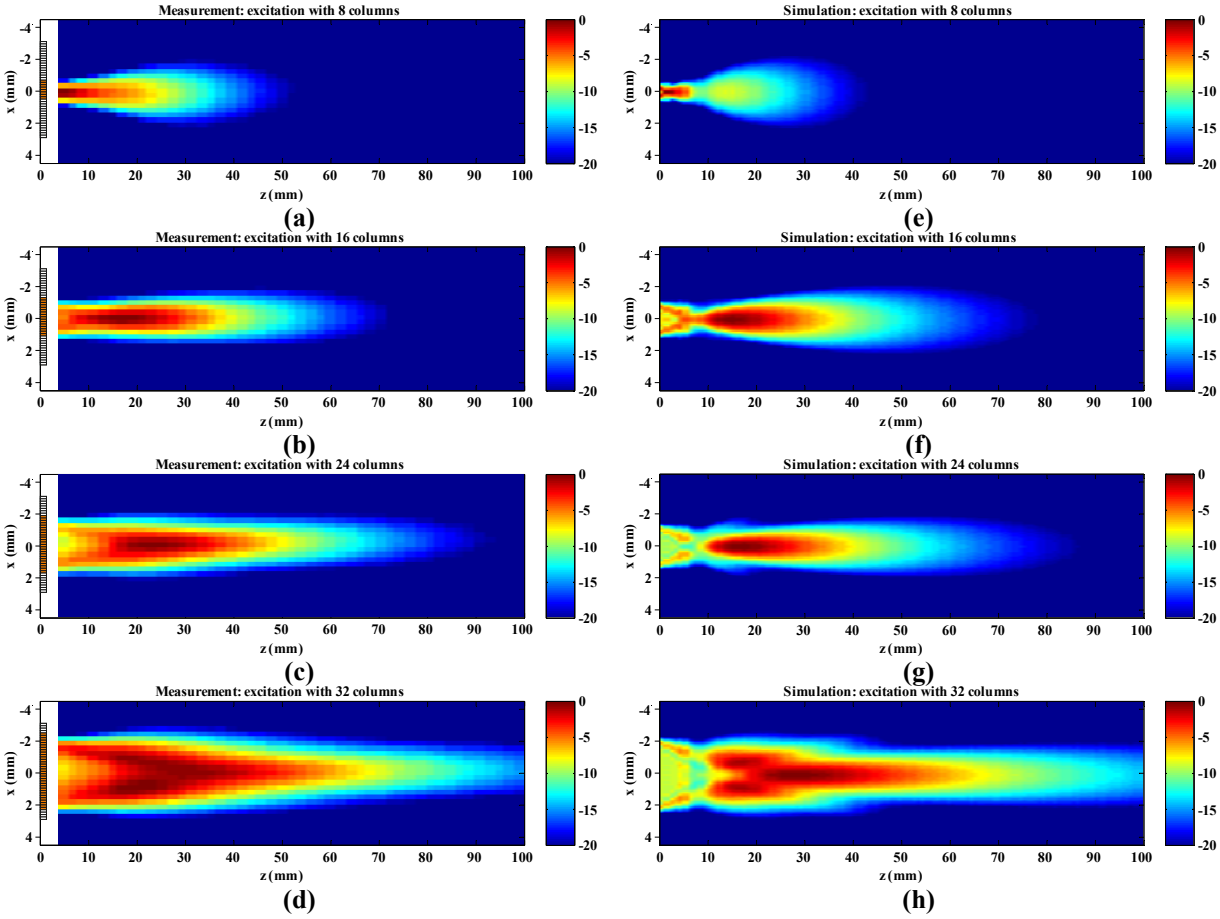

Figure 6.7. Simulation and measurement results for the transmit beam in the *xz* plane, for with different aperture widths. **(a)** measurement with 8 active columns (columns 17-24), **(b)** measurement with 16 active columns (columns 13-28), **(c)** measurement with 24 active columns (columns 9-32), **(d)** measurement with 32 active columns (columns 5-36), **(e)** simulation with 8 active columns, **(f)** simulation with 16 active columns, **(g)** simulation with 24 active columns, **(h)** simulation with 32 active columns.

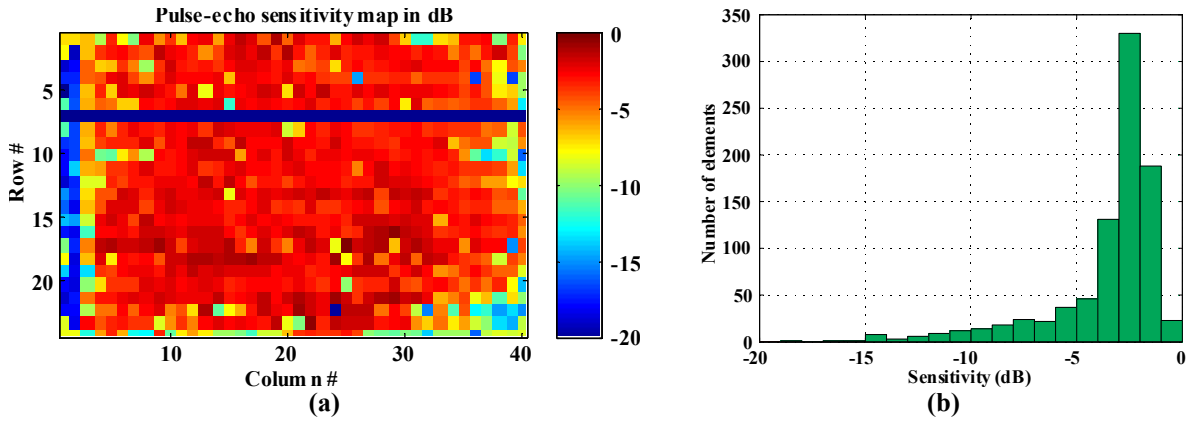

Figure 6.8. (a) Pulse-echo sensitivity map, **(b)** number of elements within different sensitivity ranges.

6.3.2.2. Sensitivity and efficiency analysis

To measure the sensitivity variations between different elements, the prototype transducer was used in a pulse-echo measurement, see option (b) in figure 6.4. An acoustic pressure wave was generated by sending a unipolar pulse with a center frequency of 7.5 MHz, and 30 V amplitude to all the elements of the transducer array. A quartz plate with 12 mm thickness

was placed at 100 mm away from the transducer. The distance of the reflector was chosen to be far enough to mimic a plane wave coming back to the transducer. The reflected echo signals from all individual elements were recorded separately by the Verasonics. The amplitude of the signal received by each element was determined from the first reflected pulse. To normalize the sensitivity of the elements, the maximum amplitude among all elements was used. The resulting sensitivity plot is given in figure 6.8a.

Row 7 suffers from a problematic wire-bond and therefore there was no meaningful output from the daughterboard for that row. The first two columns and some elements on the edges of the array have suffered some damages during the fabrication process. Figure 6.8b shows the number of elements within 1 dB sensitivity ranges. In this plot, row 7, and columns 1 and 2 have been excluded. This figure shows that the majority of the elements are within the 0 dB to -6 dB level of two-way (pulse-echo) sensitivity range.

6.3.2.3. Time and frequency response

To measure the time and frequency response in transmit, all elements of the matrix array were excited simultaneously with the positive half cycle of a 7.5 MHz, 25 V sine, and the transmit pressure was measured with the hydrophone at the natural focus of the aperture (approximately 45 mm away from the transducer). The time and frequency transmit response of the entire array are plotted in figure 6.9. Figure 6.9a shows a maximum pressure of 500 kPa, and figure 6.9b shows a -3 dB bandwidth of 45% with a central frequency of 7.35 MHz. Furthermore, the measured transmit efficiency is 20 kPa/V at 45 mm.

To perform pulse-echo measurements, the 12 mm thick quartz plate was placed at approximately 100 mm from the transducer. All elements were excited simultaneously with the pulse described above, and the reflected pressure was measured by individual elements. The resulting time and frequency responses for 10 randomly selected receive elements are plotted in figure 6.10. The measured responses for the elements are similar.

6.3.2.4. Directivity pattern

The directivity of a single element was measured and compared with finite element simulations in PZFlex. As schematically indicated by option (c) in figure 6.4, an external transducer was placed at approximately 100 mm from the matrix array, and excited by two cycles of a 7.5 MHz sine, generated by an AWG. This produces a plane, pulsed wave at the array surface. The matrix array was then rotated from -60^{o} to 60^{o} with steps of 1^{o}, and the pressure was recorded by all transducer elements and averaged. The directivity pattern was obtained from the peak of received signals at each angle, and normalized to the value at zero degrees. The resulting directivity pattern is the blue curve in figure 6.11.

Also, a finite element model similar to figure 6.3a was constructed in PZFlex to analyze the directivity of a single element in the matrix array. Two cases were considered for the simulation study: (1) loading the transducer elements directly with water, and (2) considering an intermediate layer (25 μm thick polyester sheet, mimicking the acoustically transparent window in the acoustic box) between the transducer elements and the water. The obtained

directivity patterns for case 1 and case 2 are indicated by the green and red curves, respectively, in figure 6.11.

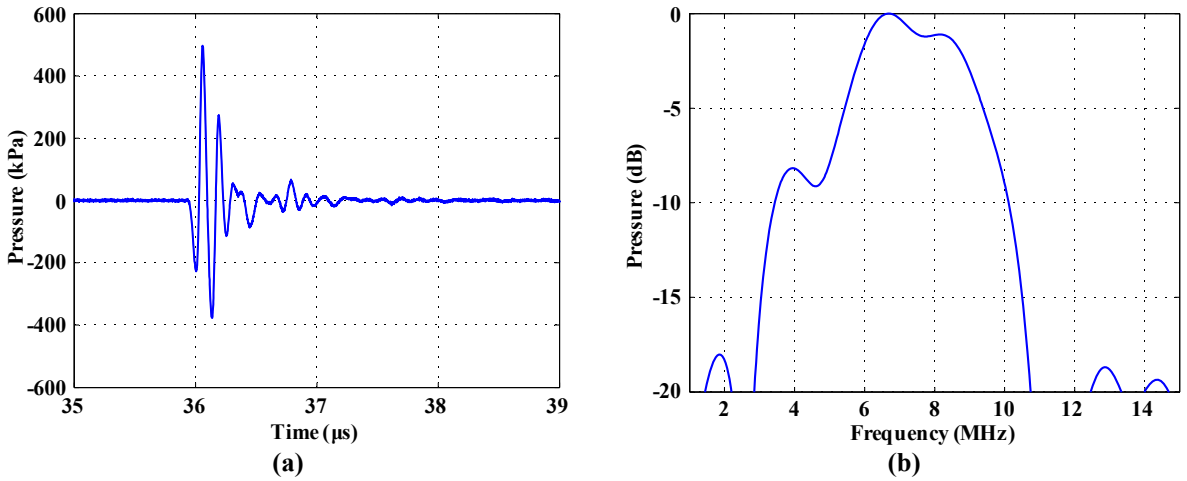

Figure 6.9. Transmit pressure from the simultaneous excitation of all the elements, measured with a hydrophone at approximately 45 mm distance, **(a)** time response, **(b)** frequency response.

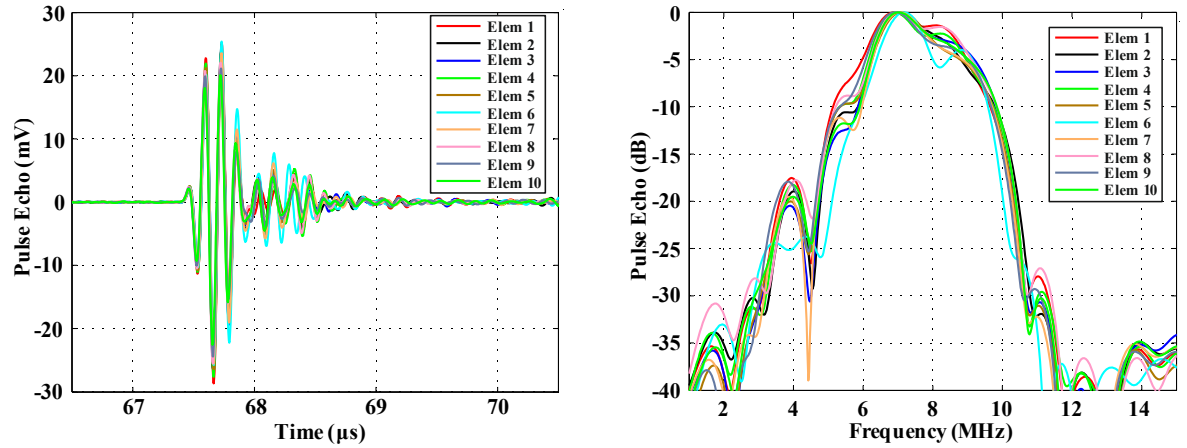

Figure 6.10. Receive pressure from the pulse-echo measurement, measured by 10 randomly selected individual elements, **(a)** time response, **(b)** frequency response.

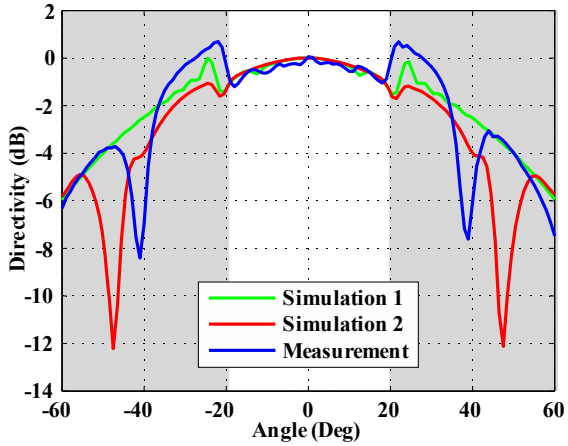

Figure 6.11. Directivity pattern of elements from measurement results and PZFlex simulations for 2 cases: simulation 1 involves water loading of the transducer element, and simulation 2 includes an additional 25 µm thick polyester layer between the transducer elements and the water.

6.3.2.5. Dynamic range

The dynamic range is defined as the difference between the highest and the lowest detectable pressures. To measure the overall dynamic range, we transmitted a wave with a known pressure with a well-defined external transducer and used the matrix transducer in receive mode. For this purpose, a single-element transducer with 1 mm aperture size (PA865, Precision Acoustics, Dorchester, UK) was placed in the water-tank at 150 mm from the matrix transducer. Using excitation voltages from 2 mV to 150 V, we first performed hydrophone measurements of the amplitude of the transmitted pressure wave at the intended location of the matrix transducer. Moreover, we measured the linearity and the width of the transmitted beam. Then we replaced the hydrophone with the matrix transducer and recorded the received voltages in the Verasonics, both with LNA on and LNA off. With this described excitation approach we could increase the pressure from 1.8 Pa to 136 kPa at the surface of the matrix transducer. Since the noise floor and the saturation levels of the Verasonics varies at different TGC gain settings, we repeated the measurements for TGC settings 500, 700, and 900. The received signal amplitudes at different TGC gain settings were then translated back to the output voltage of the ASIC using the plot in figure 6.5. The relation between the pressure at the matrix elements and the recorded voltage at the output of the ASIC is plotted in figure 6.12.

The different noise levels of the Verasonics at different TGC gains are visible in the curves for LNA off. The noise level for LNA on, is higher than the Verasonics noise level, and is similar for all the three gain setting. This is the ASIC noise level for LNA on. The minimum detectable pressure is approximately 10 Pa, which is limited by the noise floor level for LNA on. On the other hand, the maximum pressure is about 136 kPa, which is the saturation level of the signal of the ASIC for LNA off. In this case the maximum pressure is still in the linear regime of the ASIC, but we stopped generating higher pressures to avoid damage due to high voltage on the transmitting transducer. Thus, the overall dynamic range is measured to be more than 83 dB. The difference between the two curves for LNA on and off shows the expected 20 dB gain effect of the LNA. Furthermore, an overall receive sensitivity of 0.5 μV/Pa for LNA off and 5 μV/Pa for LNA on is measured.

6.3.3. Imaging

We tested the single tile matrix array in an imaging experiment using the setup shown in figure 6.13. We imaged four static needles in water by applying plane waves in transmission and column-by-column read-out as illustrated by the plane wave imaging scheme in table 6.1. Every transmit-receive acquisition took 100 μs, which yields a volume-rate of 250 Hz for this 40 column matrix array. The volume reconstruction involving 321 × 481 × 801 (X × Y × Z), isotropic voxels of 50 μm), was done using a conventional delay-and-sum algorithm implemented on a GPU using CUDA and MATLAB software. Figure 6.13 shows a 3D rendering of the needles in water, and 3 orthogonal mean intensity projections of the reconstructed volume in water.

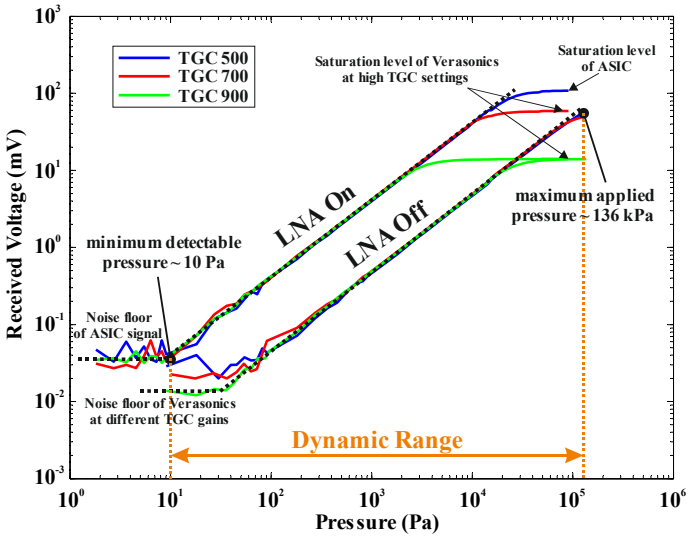

Figure 6.12. The relation between the pressure at the matrix elements and the recorded voltage at the output of the ASIC, for LNA on and LNA off. The difference between the lowest and the highest measurable pressure is the dynamic range of the matrix transducer.

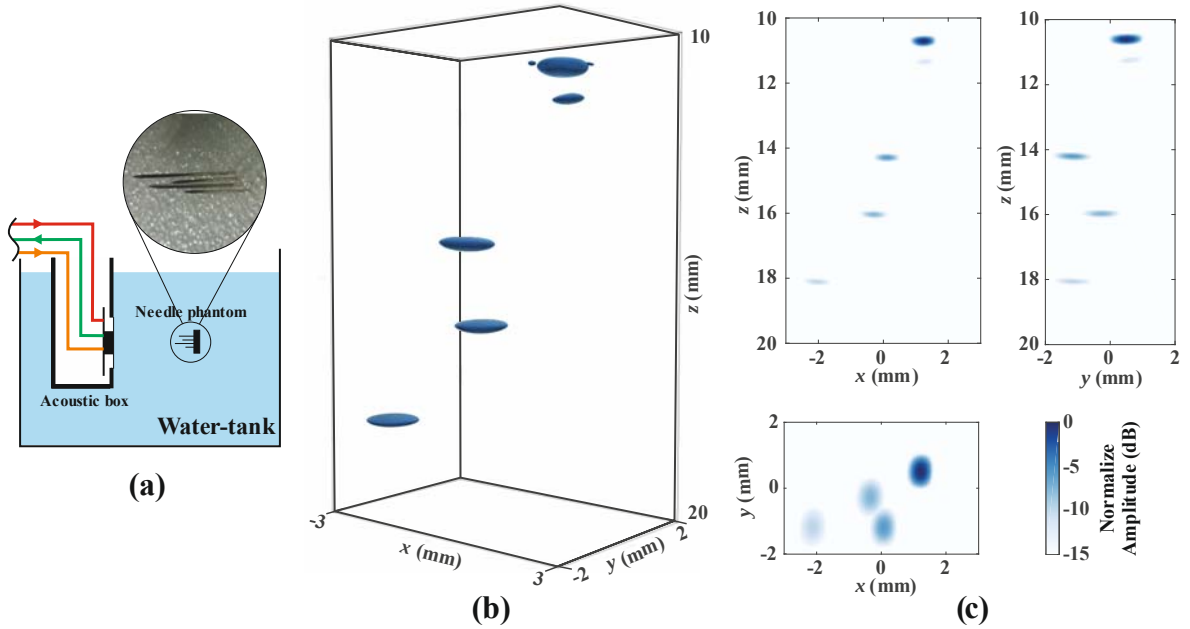

Figure 6.13. Volume reconstruction of needles in water: **(a)** the imaging phantom composed of four needles in space, **(b)** 3D rendering, **(c)** maximum projections on three orthogonal planes.

6.4. Discussions

6.4.1. Electrical aspects

The saturation level, the LNA gain, and the frequency response of the ASIC circuitry were explored in electrical measurements, by injecting a signal at an element bond pad on the ASIC. In case of a strong input signal, the LNA can be bypassed, while for weak signal values the LNA with 20 dB gain can be employed. We have found that the transfer functions of the circuitry with LNA on and LNA off have both a flat frequency spectrum between 1.3 MHz and 20 MHz. Thus, apart from providing the elements with a constant load impedance, the electronic circuit does not seem to affect the frequency response of the elements. Knowing the

saturation levels at different settings are important for selecting the operational settings of the system. When the output signal of the ASIC exceeds approximately 80 mV peak, it starts to behave non-linearly. However, at high TGC gain settings (700 and 900), the electronics inside the Verasonics are limiting the linear range of the system.

6.4.2. Acoustical aspects

The blood flow in the cardiovascular system, and especially in the carotid artery is a complex 3D phenomenon. In the areas close to the bifurcation, short vortices happen within 100-200 ms. For an accurate assessment of the dynamics of the blood flow, 3D velocity data at hundreds of volumes per second is required [116, 123]. The presented matrix transducer is in principle capable of acquiring 3D data with such a high frame rate when it is programmed in plane wave imaging mode, as shown in table 6.1a, and figures 6.6d to 6.6f. Considering an imaging depth up to 50 mm, the acquisition time for collecting one full volumetric dataset with image planes that are stepped over one element is approximately 2 ms, resulting in 3D images with 500 Hz volume rate. This volume rate is much higher than the state of the art approaches [19]. Still, to increase the frame rate, we can electronically step the imaging planes over two or more elements in receive, at the cost of resolution in the *x*-direction. On the other hand, to improve the image quality through compounding, there is potential for steering the plane wave up-to $\pm 20°$ in the *y*-direction, since the rows can be individually excited by the ultrasound machine. However, this will reduce the frame rate [124].

Our probe has the potential to be programmed for imaging at different focal depths. By generating element configurations with different aperture size and combining the data, we can generate high image resolution at larger depths. This is achieved with the growing aperture mode, as shown in table 6.1c, and figure 6.6a, 6.6b and 6.7. This approach, for example, can be used in the assessment of carotid plaque growth with high resolution volumetric image. For this purpose, the plaque burden could be quantified by predicting the total plaque volume from the 3D ultrasound image, which is a more accurate approach than using the total plaque area from 2D ultrasound [125].

In applications where both frame rate and image quality are important, the dynamic linear array mode can be used, see table 6.1b and figures 6.6d to 6.6f. For example, multiple 3D images with high resolution within a heart cycle are required to track the plaque deformation and to find the mechanical forces caused by the blood flow [115].

One of the operational modes of our prototype transducer is the configuration of random element patterns. This mode can be utilized to generate different sparse arrays for 3D imaging. Usually, static sparse array transducers are designed to overcome the cable count limit imposed by ultrasound machines, while still having a 2D matrix array with a large aperture [19, 28, 31]. However, in our case we can also dynamically generate a set of known sparse arrays. This yields the electronic version of a recent approach using a single element transducer with a coded mask [126]. With this technique, the number of measurements required to reconstruct a volumetric image can be drastically reduced.

In figure 6.8, the majority of the elements are within the -4 dB to -1 dB sensitivity range. In total 764 elements out of 874 working elements (87% of the working elements) have a

sensitivity above -6 dB. This variation is acceptable and demonstrates an appropriate dicing and assembly of the matrix array. Looking at the sensitivity map, most of the elements with lower sensitivity are located at the edges of the array. This is partly due to possible damages caused during the manufacturing, and partly due to none uniform plane wave hitting the transducer surface.

Figure 6.10 shows that in the pulse-echo mode the time and frequency response of different elements are similar. From this observation and the low sensitivity variation between different elements, we infer that the mechanical performance of elements is also similar. The measured -6 dB bandwidth in pulse-echo mode is 45%. This corresponds to the -3 dB single-way bandwidth, and is adequate for carotid imaging, since there is no need for harmonic imaging. The bandwidth is comparable with other reported transducers with a similar design [36, 45].

In the measured directivity pattern (the blue curve in figure 6.11), two bumps at approximately $\pm 22^{o}$ and two dips at approximately $\pm 40^{o}$ are observed. The bumps at $\pm 22^{o}$ are due to the acoustical crosstalk between the elements, due to the ASIC. The ASIC is made from silicon and is directly mounted behind the transducer elements. Acoustically, this layer performs as a rigid plate which carries traveling waves. Silicon is a rigid material with low damping, which is not an ideal backing material for the transducer elements. Considering the pitch of the elements, and the speed of the Lamb waves in the silicon plate, constructive interference is indeed expected at $\pm 22^{o}$. We have extensively explained this physical phenomenon in a separate paper [127]. On the other hand, two dips at $\pm 40^{o}$ are observed in the measurement and the simulation results in case of an acoustically transparent window (simulation 2; red curve). The other simulation (simulation 1, green curve) shows that this dip can be removed by excluding the intermediate window. This shows that the dip is an artifact from the measurement setup and not the transducer itself, and in order to fix it we have to find another approach to waterproof the whole matrix transducer for water tank measurements. Also, since this prototype is made for applications with low steering angles (up to $\pm 20^{o}$), extra artifacts at higher steering angles (the gray areas in figure 6.11) are considered not important.

The minimum detectable pressure of 10 Pa is limited by the noise floor of the LNA. By measuring the root mean square (RMS) value of the noise and compensating for the LNA gain and the losses, an input referred noise of ~15.1 μVrms is obtained for the ASIC. This is in reasonable agreement with the Johnson-Nyquist noise associated with the resistive part of the transducer's impedance, which corresponds to 13.6 μVrms. The total dynamic range of the receive signal is more than 83 dB, which is sufficient for carotid imaging applications [3]. Furthermore, the measured receive sensitivity of individual elements is about 5 μV/Pa for LNA on and 0.5 μV/Pa for LNA off. These values are comparable with similar designs [36, 45].

The performance of the prototype transducer was tested by imaging a phantom made from 4 needles as shown in figure 6.13. The figure proofs the applicability of the prototype for plane wave 3D imaging, however further evaluation of beamforming image quality in standard phantoms will be the focus of our future work.

6.5. Summary

We have demonstrated and characterized a prototype of an ultrasound matrix transducer with integrated electronics. This can act as a building block for a large transducer for 3D real-time carotid imaging. The prototype contains a matrix of 24×40 piezoelectric elements, which are mounted on an ASIC. The ASIC employs programmable electronic switches that allow each of the 40 elements on a row to be connected with row-level transmit and receive buses. This architecture reduces the channel count with a factor of 20, and enables fast switching between predefined element configurations.

The promising measurement results obtained from the characterization of the prototype matrix transducer encourage us to pursue further up-scaling by fabricating a larger PZT matrix transducer on 2×10 tiled ASICs. In this way we expect to realize a fully populated matrix involving about 20,000 transducer elements in the near future.

CHAPTER 7

A Prototype PZT Matrix Transducer with Low-Power Integrated Receive ASIC for 3D Transesophageal Echocardiography[1]

Abstract

This chapter presents the design, fabrication and experimental evaluation of a prototype PZT matrix transducer with an integrated receive ASIC, as a proof of concept for a miniature 3D transesophageal echocardiography (TEE) probe. It consists of an array of 9 × 12 piezoelectric elements mounted on the ASIC via an integration scheme that involves direct electrical connections between a bond-pad array on the ASIC and the transducer elements. The ASIC addresses the critical challenge of reducing cable count, and includes front-end amplifiers with adjustable gains and micro-beamformer circuits that locally process and combine echo signals received by the elements of each 3 × 3 sub-array. Thus, an order-of-magnitude reduction in the number of receive channels is achieved. Dedicated circuit techniques are employed to meet the strict space and power constraints of TEE probes. The ASIC has been fabricated in a standard 0.18 μm CMOS process and consumes only 0.44 mW/channel. The prototype has been acoustically characterized in a water tank. The ASIC allows the array to be pre-steered across ±37° while achieving an overall dynamic range of 77 dB. Both the measured characteristics of the individual transducer elements and the performance of the ASIC are in good agreement with expectations, demonstrating the effectiveness of the proposed techniques.

[1] This chapter has been published as:
Chao Chen, Shreyas B. Raghunathan, Zili Yu, Maysam Shabanimotlagh, Zhao Chen, Zu-yao Chang, Sandra Blaak, Christian Prins, Jacco Ponte, Emile Noothout, Hendrik J. Vos, Johan G. Bosch, Martin D. Verweij, Nico de Jong, and Michiel A. P. Pertijs; A prototype PZT matrix transducer with low-power integrated receive ASIC for 3D transesophageal echocardiography, IEEE Transactions on Ultrasonics, Ferroelectrics, and Frequency Control, 2016, 63, 1, pp. 47 - 59.

7.1. Introduction

Echocardiography is a popular cardiac imaging tool used for accurate diagnosis of cardiovascular diseases and for guiding interventional procedures. Its advantages over alternative imaging techniques include its low-cost, its non-invasive character and its capability of producing real-time images. Transesophageal echocardiography (TEE) has been developed to complement the more standard transthoracic echocardiography (TTE). As its name suggests, TEE uses the esophagus as the imaging window to the heart and thus eliminates the reflections from the lungs and ribs, which limit the image quality in TTE [128]. Conventional TEE probes employ a one-dimensional (1D) ultrasound array to obtain fan-shaped two-dimensional (2D) cross-sectional images of the heart. The array can be mechanically rotated around the image axis to obtain images within a conical volume. However, 2D imaging falls short in the case of complicated interventions, since cardiac morphology, leakage of valves and function of the outflow tracts are all 3D phenomena that are difficult to interpret from 2D images in a non-standard 3D anatomy. Therefore, there is a clear clinical need for TEE probes that are capable of providing real-time 3D images [129].

Commercially-available 3D TEE probes (X7-2t, Philips Ultrasound, Bothell, WA and Vivid E9 BT12, General Electric Healthcare, Amersham, UK) have a large head volume (~ 10 cm^3) and are intended for procedures in adults only. Unfortunately, a TEE procedure involving such a large probe is associated with intolerance in about 1% of cases and high levels of patient discomfort in around 35% of cases [130, 131]. Procedures in non-anesthetized patients are generally limited to less than about 20 minutes [130] to minimize this. Consequently, a 3D TEE probe of a significantly smaller size that is suitable for sustained monitoring and for children becomes compelling. The target of our work presented in this paper is to demonstrate and assess technologies that enable the implementation of a miniature 3D TEE probe with a head volume < 1 cm^3. Such a small probe will enable the use of 3D TEE for monitoring of cardiac procedures in adults and make real-time 3D TEE imaging feasible in newborns and children.

Several challenges exist in the design of a miniature 3D TEE probe. In conventional 2D TEE probes, the 1D phased array is mounted at the tip of a specialized gastroscopic tube, through which all piezo-electric transducer elements are individually connected to a bed-side ultrasound system via micro-coaxial cables with a typical outer diameter of 300 μm. Typically, for an imaging depth of 6 cm to 12 cm, an array consisting of 32 to 128 elements, operating between 5 MHz and 10 MHz, is used to obtain a field of view of ±45˚ to ±60˚ in the azimuthal direction. In 3D probes, however, the field of view extends in both azimuthal and elevation directions, calling for a 2D matrix transducer with several thousand of independent elements [129]. For such a large array, it is not feasible for the gastroscopic tube to accommodate the corresponding number of coaxial cables while remaining flexible [132]. Moreover, the density of the elements makes their individual wiring very intricate. Moving signal processing modules into the probe is an efficient way to reduce the number of fan-out cables. However, the limited volume of the probe tip precludes the possibility to accommodate commercial ultrasound front-end integrated circuits (e.g. AD9271, Analog Devices, Norwood, MA) or multi-chip systems [132, 133] within the probe. Therefore, an

application specific integrated circuit (ASIC) that could be closely integrated with the 2D transducer matrix is desired for a 3D TEE probe [129]. This integrated approach also provides an effective way to make connections with all individual elements.

An additional challenge is that the in-probe power dissipation of a 3D TEE probe, either caused by the transducers or electronics, should comply with FDA regulations [134] to prevent excessive tissue temperature rise. This requirement sets an upper bound to both the largest transmit power and the self-heating power associated with the in-probe electronics. For comparison, the heat dissipation of pulse transmission in a standard 2D TEE probe without electronics was estimated at 1.0 W. 3D TEE probes have to operate within a comparable overall power budget. To ensure that the in-probe integrated circuit does not contribute a significant increase to self-heating, its total power consumption should be limited to about 0.5 W, which is equivalent to 0.5 mW/channel in a 1000-element array. This is beyond the state-of-the-art of front-end ultrasound ASICs reported in open literature, which consumes several milliwatts per channel [135, 136]. Within this strict power budget, a dedicated circuit design that fully optimizes the power efficiency of each ASIC building block is certainly called for.

Moreover, from an acoustic point of view, a particular challenge is to avoid ringing and crosstalk of the piezoelectric elements. In conventional 1D arrays, the elements are backed by a relatively thick slab of damping material, to avoid reflections from the back side of the piezo elements and to minimize lateral waves that may couple into neighboring elements. In the integrated design, the opposite would be achieved when the 2D piezo array is in direct mechanical contact with the silicon of the ASIC, which is a thin slab of material with negligible damping. To minimize ringing and crosstalk in the integrated design, a specially designed interconnect layer should be applied in between the piezo array and the ASIC.

To demonstrate and assess the technologies that will be used in a full-blown miniature 3D TEE probe, we present a prototype with a reduced number of elements in this paper. The prototype consists of a 9 × 12 element PZT matrix that is integrated with a receive ASIC. This ASIC is capable of providing the required order-of-magnitude cable reduction by applying sub-array signal processing, while being sufficiently compact and power-efficient for in-probe integration. The prototype has been experimentally evaluated, both electrically and acoustically.

The proposed concepts can be later applied to realize a full >1000-element miniature 3D TEE probe. Figure 7.1 illustrates the physical architecture of the envisioned full probe. A lead zirconium titanate (PZT) transducer matrix with 1024 elements (32 × 32) is directly mounted on top of the ASIC. As proposed in [132], a split-array design is adopted, in which a small directly-wired sub-array is used to transmit a wide beam, while the major part of the array is dedicated to receiving the resulting echoes through the ASIC. The transmit sub-array will be optimized to enable parallel beamforming in reception and to guarantee a sufficiently high volume frame rate. A specialized flex-circuit acts as the bonding substrate of the ASIC, and provides the electrical connection between the ASIC and solder pads for micro-coaxial cables. These cables are accommodated in a flexible gastroscope tube with a length of 1 m ~ 2 m and a diameter of about 5 mm and connected to the probe handle, which connects via a thicker

cable to the external imaging system. Thanks to the channel reduction performed by the ASIC, the number of cables required by the proposed 3D TEE probe is comparable to what is currently used in miniature 2D TEE probes.

In this chapter, the design of the prototype PZT matrix and the integrated receive ASIC are presented. Section II describes the design of the PZT matrix and the signal processing method utilized in the ASIC, as well as the PZT-on-CMOS integration approach. The circuit implementation details of the ASIC are described in Section III. Section IV presents the experimental setup and both electrical and acoustic measurement results. Conclusions are given in Section V.

7.2. Methods

7.2.1. Transducer matrix on CMOS

A schematic diagram of the prototype is depicted in figure 7.2. It is constructed by mounting a 9 × 12 PZT matrix on top of an ASIC. Commercially-available CTS 3203 HD is used as the piezo-ceramic and the acoustical stack is optimized using PZFlex (Weidlinger Associates Inc., Mountain View, CA) for a center receive frequency of 5 MHz and a 50% bandwidth, which is adequate for the fundamental imaging typically used in TEE applications. The entire array measures 1.8 mm × 2.4 mm with an element pitch of 200 μm and a dicing kerf of 30 μm. An array consisting of 9 × 9 elements is directly interfaced to the pre-amplifiers in the ASIC. The remaining 9 × 3 elements are wired out through metal interconnections in the ASIC and are used for the characterization of single elements without electronics.

Given the limited space in a miniature TEE probe, the PZT matrix must be directly stacked on top of the ASIC, requiring a high-density interconnect scheme to provide the large number of electrical connections between the transducer elements and the ASIC. Several design constraints apply here. First of all, the assembly process for PZT transducers requires a working temperature well below the Curie point of the piezo-material to prevent depolarization. In our design, the Curie temperature of the chosen material is 225˚C. To keep a proper margin, the integration process temperature should be controlled below 110˚C. Another challenge comes from the construction of the PZT matrix, which is cut from a PZT slab after it has been mounted on the ASIC. When dicing the piezoelectric ceramic, the cut must be deep enough to guarantee mechanical and electrical separation of the individual transducer elements, without damaging the ASIC. Therefore, there is a need for an isolation layer that is sufficiently thick to act as a dicing buffer between the PZT matrix and the ASIC.

PZT-on-CMOS integration solutions that have been reported so far all rely on intermediate connectors. In [137], a custom-designed interconnection block based on anisotropic elastomers is utilized as an intermediate connector between multiple ASICs and the PZT matrix. The volume of such interconnection block, however, exceeds the space available in a miniature TEE probe. The flip-chip bonding technology, which is widely used in the semiconductor industry, has been applied to the direct integration of capacitive micro-machined ultrasonic transducers (CMUT) and the associated front-end ICs [136, 138]. However, direct flip-chip bonding of a PZT matrix to an IC is generally not applicable,

because of both the lack of a dicing buffer layer and the minimum temperature requirement of the flip-chip bonding process [139].

In this work, we apply a direct PZT-on-CMOS integration scheme as illustrated in figure 7.3. A metallic interconnection layer is applied on top of the transducer bond-pads of a CMOS ASIC, which are arranged in a matrix pattern with the same pitch as the transducer array. A non-conductive epoxy layer is then deposited, filling the gaps between the metal. The epoxy is then grinded down to expose the metal and form electrical contacts, allowing the epoxy to act as an electrical isolation layer as well as a mechanical dicing buffer. On top of the grinded epoxy layer the PZT matrix is constructed. The electrical connection between the contacts and the electrode on the back-side of the piezoelectric ceramic is created by a layer of electrically conductive glue. This layer also has the acoustical function of minimizing ringing and crosstalk of the elements. For the purpose of acoustic matching, a conductive matching layer is applied on top of the piezoelectric layer. After that, the stack is diced to create the 2D array. The dicing kerfs extend into the epoxy layer for approximately 10 μm, which guarantees the electrical separation of the transducer elements. The dicing kerfs are air-filled to minimize the crosstalk between elements. A ground foil is then glued on top of the matching layer to create a common counter electrode for all elements.

This integration scheme is particularly suited for prototyping and small-volume production. Alternatively, similar direct integration of PZT on CMOS can be achieved using cleanroom post-processing to form a dicing buffer layer on top of a CMOS chip [140].

7.2.2. Micro-beamforming

To reduce the number of output signal channels, the sub-array beamforming scheme [137], also referred to as “micro-beamforming” or “pre-steering” [141], is adopted in this work. This approach is depicted in figure 7.4. The transducer matrix is divided into sub-arrays of 3 × 3 elements, the receive signals of which are combined by a local micro-beamformer circuit in the ASIC to reduce the number of channels by a factor of 9. The delay applied to the received signals is divided into a coarse delay, which is common for all elements within one sub-array, and a fine delay for each individual element. The fine delays are applied locally in the micro-beamformer, while the coarse delays are applied in the imaging system that further processes the output signals of the micro-beamformers.

To simplify the control of the beamforming electronics, all 3 × 3 sub-arrays are given the same fine delay pattern. As such, the fine delays tilt all beam axes of the sub-arrays to a certain angle, thus effectively changing the beam direction of the entire array [141]. Compared to the situation in which all elements have the ideal time delay, this pre-steering approach comes at the cost of a slightly degraded beam profile [132]. A delay depth of 280 ns, corresponding to 7 delay steps with a step size of 40 ns, is required for each element to ensure that the each 3 × 3 sub-array can cover a pre-steering range of –37° to 37°.

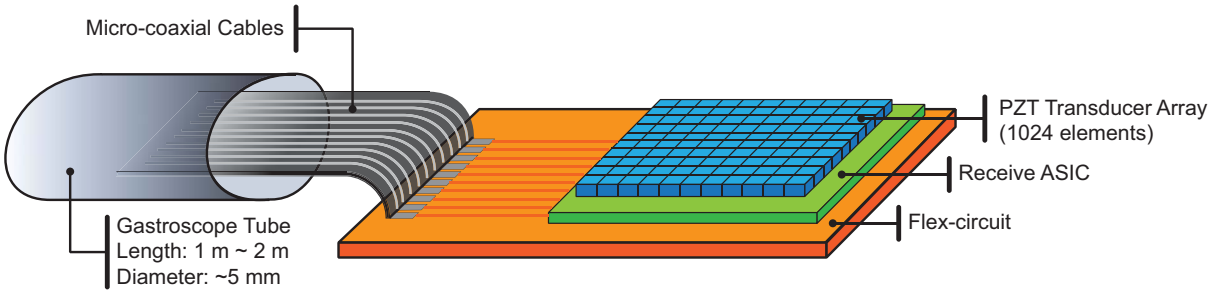

Figure 7.1. Schematic diagram of the envisioned full TEE probe.

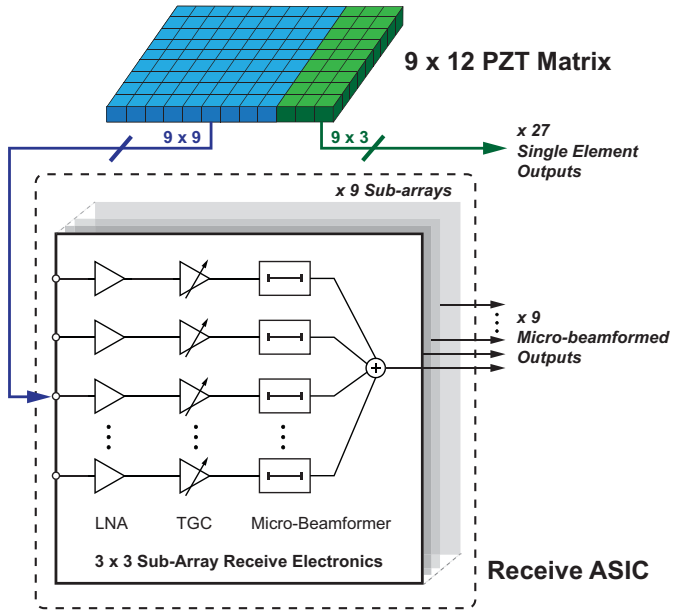

Figure 7.2. The architecture of the prototype matrix transducer.

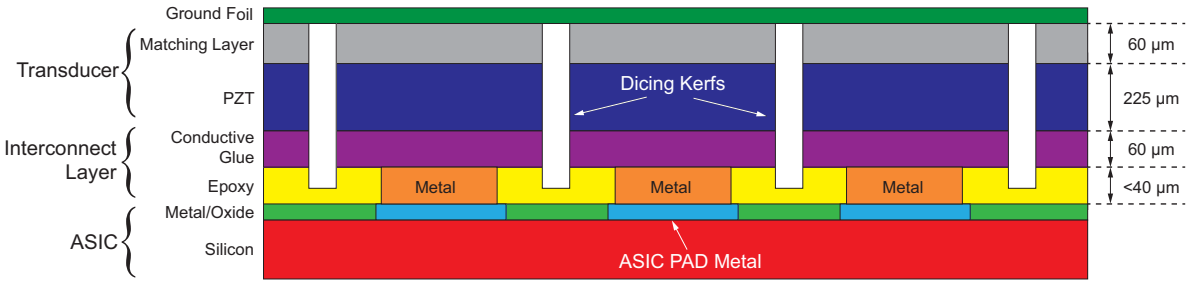

Figure 7.3. PZT-on-CMOS integration scheme with labeled layer thicknesses.

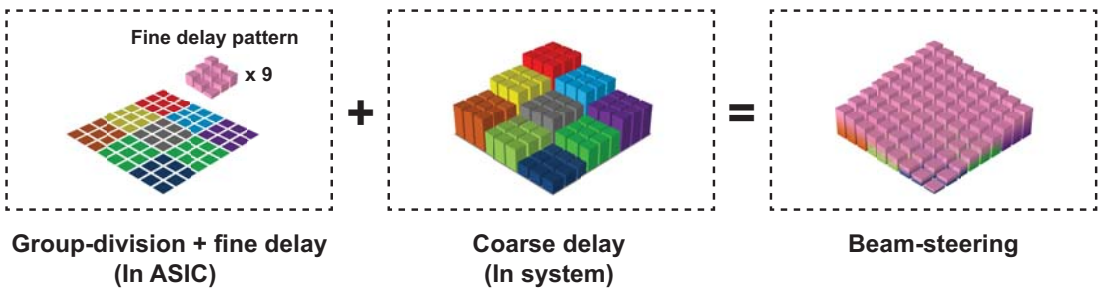

Figure 7.4. The operation principle of micro-beamforming; the height of each bar represents the time delay applied to the signal received by the corresponding element of the array.

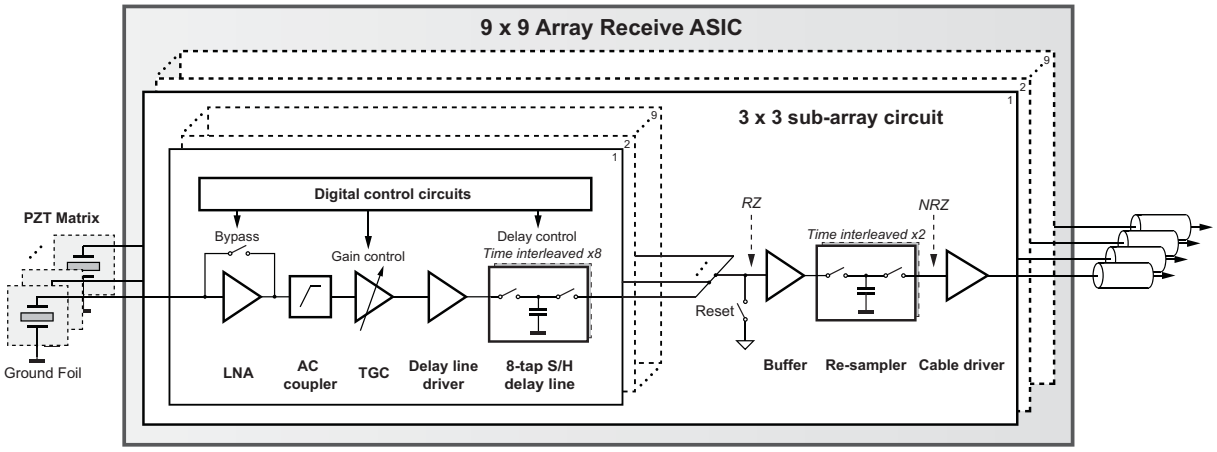

Figure 7.5. Block diagram of the 9 × 9 array receive ASIC.

7.3. Implementation of the received ASIC

This section describes the implementation details of the receive ASIC. The ASIC processes the echo signals received by the transducer elements in two steps: front-end signal conditioning, including pre-amplification and time-gain compensation (TGC), and micro-beamforming. Figure 7.5 shows a block diagram of the ASIC. It contains 81 input channels, each being interfaced to one transducer element in the 9 × 9 matrix. The channels are divided into 9 sub-arrays; signals from the 9 elements of each sub-array are first amplified, then aligned in time using sample-and-hold (S/H) delay lines and summed up by charge redistribution among the outputs of 9 delay lines to implement the micro-beamforming. The output signal of each sub-array is transmitted to the external imaging system via a 1 m ~ 2 m micro-coaxial cable; an on-chip cable driver provides the required output drive capability.

In the following, the design considerations for the front-end amplifiers, the micro-beamformers and auxiliary circuits will be discussed. A brief overview of the silicon realization will also be given.

7.3.1. Front-end amplifier

The front-end signal conditioning in each channel is performed by a low-noise amplifier (LNA) and a TGC amplifier, as shown in figure 7.5. The LNA provides a fixed gain of 20 dB to increase the signal level, thus reducing the impact of the electrical noise generated by subsequent stages. In order to achieve an input-referred noise level that is small compared to the transducer's noise, the majority of the power in the receive circuitry is consumed by the LNA. To meet the strict power constraint, we use a single-ended common-source amplifier with a resistive load, as illustrated in figure 7.6. The gate of the input transistor (M1) is directly connected to the PZT element. As such, the LNA has a high input impedance and senses the voltage across the transducer. The input bias voltage of the LNA is defined by a diode-connected transistor (MB1) and a current source (IB) via a large resistor (RB). Two ESD protection diodes are added to the input node to prevent the circuits from being damaged by an electrostatic discharge when integrating the ASIC with the transducer matrix.

A PZT transducer element is essentially a bi-electrode device; one electrode is connected

to the matching layer and the ground foil shared by other elements in the array, while the signal generated on the other electrode is fed to the input of the LNA. However, a conventional common-source amplifier is inherently single-ended and only senses the voltage difference between the input node and the supply rail. As a result, any interference that appears on the ground foil or the supply rail will also be amplified. To address this problem, an NMOS transistor M2 is added in series with M1, and correspondingly MB2 is added to the bias network. Both transistors are built in deep N-wells such that their substrate can be connected to the ground foil, while their gates are connected to the ESD supply (VESD), which is AC coupled to the ground foil with an external capacitor. In this way, any voltage fluctuation on the ground foil will also appear at the source of the PMOS input transistor M1, so that the gate-source voltage of M1 tracks the differential voltage across the transducer element and thus the effect of the ground foil interference is (partially) compensated for. By including M2 and MB2, the power-supply rejection ratio (PSRR) of the LNA is also improved.

When compared with its closed-loop counterparts [142, 143], the usage of the simple open-loop topology comes at the cost of large gain errors and poor linearity [144]. As a design choice, we allocate the majority of the gain-error budget (+/- 2dB) to the LNA. The gain accuracy of the subsequent circuits, mainly the TGC amplifiers, can be well controlled by using closed-loop topologies; they are much less power hungry than the LNA due to the relaxed noise requirements. Moreover, the linearity requirement is relieved by including a bypass path in parallel with the LNA, as shown in figure 7.5. At the high input-signal levels associated with near-field echoes, the LNA is bypassed to prevent saturation or distortion at the output of the LNA, hence enhancing the dynamic range of the received signal. Since the signal amplitudes in the near field are much higher than the noise level of the subsequent circuitry, the absence of the LNA in this situation does not affect the detection limit of the ASIC.

A TGC amplifier with four gain steps (0 dB, 12 dB, 26 dB and 40dB) follows the LNA to further enhance the dynamic range by compensating the propagation attenuation of echo signals. In addition, it helps to relax the linearity requirements of the subsequent circuits, especially the micro-beamformer. While operating, the gain of the TGC amplifier is increased with time linearly in decibels. A differential cascaded-flipped-voltage-follower with switchable degeneration-resistor network, as proposed in [132] and [145], is utilized to perform the time-gain compensation. Discrete gain levels are chosen to simplify the implementation of the amplifier [132].

The LNA and the TGC amplifier are AC coupled by an RC network to reject offset and low-frequency noise and to independently set the input DC bias condition of the TGC amplifier. The corner frequency of this RC network is 2.4 MHz, well below the lower cut-off frequency of the PZT transducer, i.e. 4 MHz.

7.3.2. Micro-beamformer

As discussed in Section II, the operation principle of micro-beamforming is to apply relative delays to the echo signals received by different transducer elements in such a way that

for a specific incident angle they are properly aligned in time and add up coherently. When implemented in circuits, the relative delays can be realized in the analog or the digital domain. While a digital delay line is able to offer a higher delay resolution and accuracy, the power required for the digitization of the output signal of each element is far beyond the sub-mW power budget per channel [146]. Therefore, in this design, a programmable analog delay line with pipeline-operated sample/hold (S/H) stages [132, 147] is used to construct the micro-beamforming cell. It consists of 8 memory cells operating in a time-interleaved fashion at a sampling rate of 25 MHz, which leads to a tunable delay range from 40 ns to 320 ns with a delay resolution of 40 ns.

The circuit implementation and the timing diagram of the proposed micro-beamformer are depicted in figure 7.7. The micro-beamformer consists of 9 delay lines. In each delay line, the output voltage of the corresponding TGC amplifier is cyclically sampled and held on capacitors C1 to C8 under the control of non-overlapping sampling clocks S1 to S8, while readout clocks R1 to R8 sequentially release the voltages stored on the capacitors to the output node. Thus, the signal delay can be determined by the time shift between the falling edges of the acquisition and the readout clocks. In [132], we presented a similar analog beamformer circuit that employs current-domain signal summation. It requires extra building blocks to perform the voltage-to-current conversion, which degrades the power efficiency. In this work, instead, the choice is made to sum up the signals in the charge domain [147]. As illustrated in figure 7.7, the outputs of all 9 delay lines are joined together, causing the sampled charge to be averaged among the capacitors that are connected to the output node. This effectively adds the delayed signals with low circuit complexity and high power efficiency.

In order to eliminate errors due to the residual charge stored on the parasitic capacitance associated with the switches and the interconnect, the charge summing node is periodically reset by a switch before each summation cycle, leading to a return-to-zero (RZ) waveform at the output of the micro-beamformer. To recover this signal, a ping-pong S/H circuit is implemented following the micro-beamformer (figure 7.5), which re-samples the signal at its non-zero phase at a rate of 25 MHz.

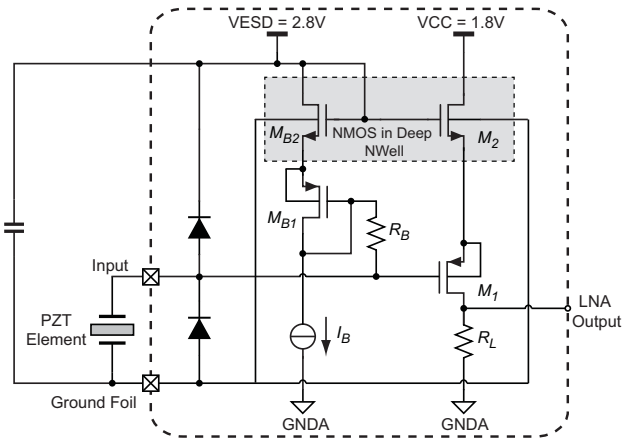

Figure 7.6. Circuit diagram of the front-end low-noise amplifier.

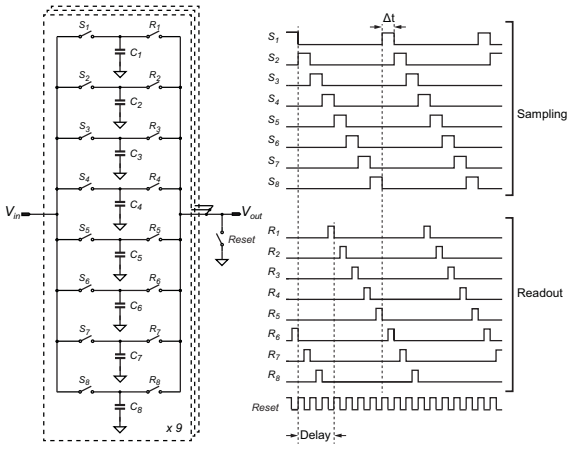

Figure 7.7. Circuit diagram of the front-end low-noise amplifier.

7.3.3. Auxiliary circuits

Custom-designed digital circuits are included to generate the delay-control clock pattern for the delay lines. There are two 8-bit shift registers in every receive channel, which are used for the generation of acquisition and readout clocks. During the configuration phase of the ASIC, each shift register can be connected in series with its counterparts in adjacent channels of the same 3 × 3 sub-array, forming a daisy-chain that allows the ASIC to be programmed via a serial interface. Thus, the delay patterns can be loaded into the shift registers. Upon the start of the beamforming phase, each 8-bit shift register is re-configured as a circular shift register by feeding back its output to its input. As such, the delay patterns loaded during the configuration phase will re-circulate as long as clocks are applied. Before being connected to the S/H switches in the delay line, the parallel outputs of the shift registers are further processed by logic gates to ensure that the switches are driven by non-overlapping signals.

As mentioned earlier, the ASIC is directly loaded by the micro-coaxial cables. For the given cable length (1 m ~ 2 m) and working frequency (around 5 MHz), the combination of a cable and a characteristic load can be modeled as a lumped RC network with a resistance of 50 Ω ~ 100 Ω and a parallel capacitance of 100 pF ~ 200 pF. To drive such a heavy load, a cable driver with high power efficiency is required. In this design, we choose a class-AB super source follower [148] as the output voltage buffer, which is capable of providing both a high slew-rate and low standby power consumption.

7.3.4. Silicon realization

The ASIC has been fabricated in a standard 0.18 μm CMOS process with a supply voltage of 1.8 V for both analog and digital circuits, except for the ESD protection and bias circuits of the LNAs, which use a 2.8 V supply (from which very little current is drawn). Figure 7.8 illustrates the layout and the microphotograph of the ASIC. The dimensions of the ASIC are 3.2 mm × 3.8 mm. It consists of the 9 × 9 receive channels, each of which consists of an LNA, a TGC amplifier, an AC coupler, an 8-memory-cell delay line and the associated digital control circuits. All circuits in an individual channel are laid out within a square area of 200 μm × 200 μm, as illustrated in figure 7.8(c). A bond-pad with a size of 60 μm × 60 μm is implemented in the top metal layer on top of the LNA for creating the connection to the corresponding transducer element. The cable drivers are laid out beside the center array and close to the I/O bond pads.

Table 7.1 lists a power consumption breakdown of all circuits blocks. While operating, the receive ASIC consumes only 35.5 mW, corresponding to 0.44 mW for each channel. In a full 1000-element miniature TEE probe, this would translate to about 440 mW, which is within the power budget for TEE probes.

7.4. Experimental results

7.4.1. Fabricated prototype

Figure 7.9(a) shows a photograph of the fabricated PZT matrix that is mounted on a receive ASIC using the integration solution described in Section II. To facilitate water-tank measurements, the prototype device has been bonded on a PCB, as shown in figure 7.9(b), and has subsequently been encapsulated in non-conductive silicone rubber.

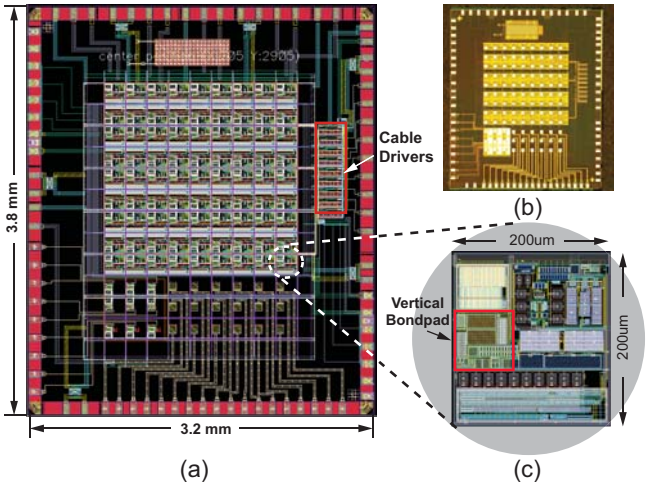

Figure 7.8. Circuit diagram of the front-end low-noise amplifier.

Table 7.1. Power Consumption Breakdown of the Receive ASIC

Circuit block	Power consumption (μW/channel)	Proportion (%)
LNA	155.7	35.5
TGC	51.5	11.6
Micro-beamformer	9.9*	2.2
Cable driver	91.8**	20.8
Biasing	13	2.9
Digital control	120.6	27.3
Total	442.5	100

* The power consumption of a single delay line;
** 1/9 of the power consumption of a single cable driver.

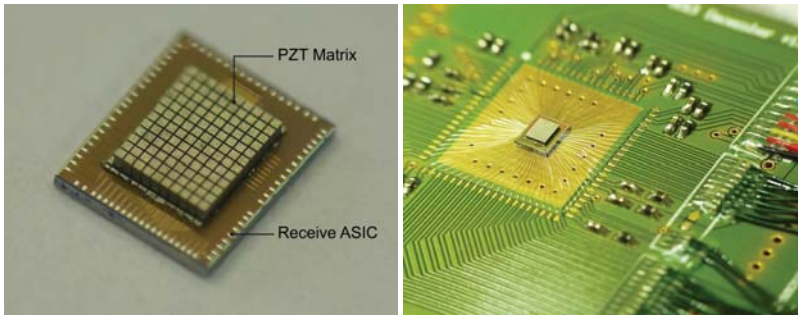

Figure 7.9. (a) Fabricated prototype; (b) the prototype bonded on a daughter PCB for water-tank measurements (before applying ground foil and silicone rubber).

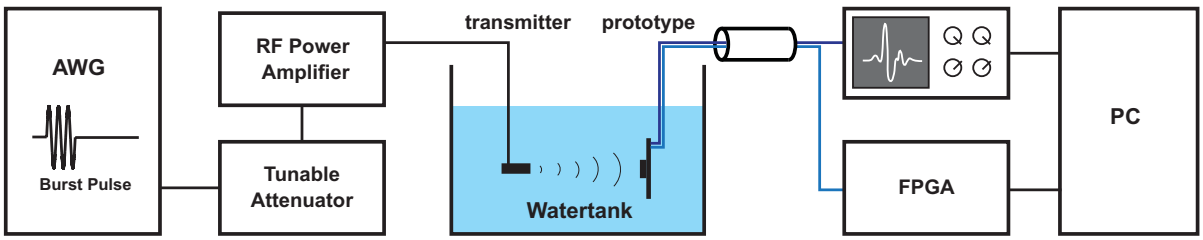

Figure 7.10. Schematic diagram of the acoustical experimental setup.

7.4.2. Acoustic measurement setup

To evaluate the acoustical performance of the prototype, the encapsulated PCB was immersed in a water tank in front of a 5-MHz, 0.5-inch single-element transmit transducer (V309, Olympus Scientific Solutions, Waltham, MA) that was used to generate acoustic test signals, as shown in figure 7.10. The prototype was placed at the focus of the transmit transducer, which is 10 cm away from the transducer's surface. In order to emulate echoes arriving at different angles, the prototype was mounted on a rotational stage capable of sweeping its angle relative to the axis of the transmit transducer between –90° to +90° in steps of 0.1° (see the inset of figure 7.14). Periodic test pulses with varying frequency, duration and amplitude were generated using an arbitrary waveform generator (AWG) (33250A, Keysight Technologies, Santa Clara, CA) and delivered to the transmit transducer via a benchtop attenuator (50BR-036, JFW Industries, Indianapolis, IN) with tunable attenuation from 0 dB to 110 dB, and a RF power amplifier (403LA, Electronics & Innovation, Rochester, NY) with a fixed gain of 37 dB. The output signals of the ASIC were captured using a digital oscilloscope (DSOX4054A, Keysight Technologies, Santa Clara, CA). The ASIC was programmed using an FPGA on a custom-designed mother PCB.

To calibrate the pressure generated by the transmit transducer, a 0.2 mm needle hydrophone with integrated pre-amplifier (Precision Acoustics, Dorchester, UK) was placed at the position of the prototype prior to the experiments. Using the AWG, the transmit transducer was driven with a 20-cycle sine wave, the frequency of which was swept from 2 MHz to 8 MHz in steps of 50 kHz. The resulting acoustic pressure was recorded using the hydrophone to derive the transfer function of the transmit transducer, which was found to have a bandwidth of 80%, a center frequency of around 5.8 MHz, and an efficiency of 0.56 kPa/V at focus for 5 MHz.

7.4.3. Single element characterization

In order to determine the transfer function of the individual elements of the prototype, the transmit transducer was driven in the same way as during the hydrophone calibration, while the voltage signals induced across the individual elements of the prototype array, oriented at 0° relative to the transmit transducer, were recorded successively using the oscilloscope. After correcting for the transfer function of the transmit transducer, these measurements were used to determine the frequency response of the individual elements. However, it should be noted that the capacitive loading of the measurement cable and the measurement equipment have not been compensated for, which leads to a large attenuation of the measured signal owing to the impedance mismatch between the single element and measurement equipment. Given that the attenuation increases with frequency, this influences the measured transfer function.

In figure 7.11, the measured frequency response of 9 individual piezo-electric elements is plotted as a function of frequency. The differences between the individual transfer functions are less than 3 dB within the frequency range from 3.5 MHz to 6.7 MHz, showing a good reproducibility of the manufacturing process. The elements have a center frequency of 5.5 MHz, a -3 dB bandwidth of 40%, and a sensitivity of 0.2 μV/Pa. The bandwidth is quite

limited but adequate for TEE imaging, where harmonic imaging is less important since there is no clutter from the skin, ribs, fat layers, etc. The measured element sensitivity appears very low due to the attenuation of the signal by the capacitive loading of the coaxial cables connected to the elements. The capacitance of a single piezoelectric element is approximately 1 pF, while the length of the coaxial cables used in the experiment is 1 m, corresponding to a capacitive load of about 100 pF. Thus, the measured single-element sensitivity is about 40 dB lower than the unloaded sensitivity.

7.4.4. Micro-beamforming: frequency response

The transfer function of the signal-conditioning and beamforming circuits on the ASIC was first measured electrically by applying a sinusoidal test voltage to an ASIC without transducer matrix, of which all transducer bond-pads of a 3 × 3 sub-array have been wire-bonded for electrical testing. The frequency of the test signal was swept from 0.38 MHz to 10 MHz while the output voltage of the corresponding sub-array circuit of the ASIC was captured using the oscilloscope. No beam steering was applied to the micro-beamformer. The resulting frequency response is shown in figure 7.12, where Gain 1-7 represent various combinations of gain settings of the ASIC's signal-conditioning circuits (LNAs and TGCs). The measured gain at 5 MHz varies from -11 dB to 34 dB, corresponding to a 45 dB gain range. The measured gain steps are in good agreement with the design values. The absolute gain levels are approximately 10 dB lower than what would be expected based on the combined gain of the LNA and the TGC. This difference can be attributed to the small attenuation associated with several source followers in the ASIC that act as signal buffers and with the parasitic capacitance at the charge summing node of the micro-beamformer. It has no significant impact on the functionality of the ASIC.

To determine the transfer function from an acoustical input signal to a micro-beamformed electrical output, a similar approach was used as for the single-element characterization. The LNA and TGC were configured to the lowest gain setting (Gain 1 in figure 7.12), and the micro-beamformer was configured to pre-steer at 0°. The results are shown in figure 7.13. All the 9 micro-beamformed sub-arrays in the prototype have a similar response, with a variation of less than 3 dB among the micro-beamformers. Since the bandwidth of the ASIC exceeds that of the transducer elements, the center frequency of 5.5 MHz and a -3 dB bandwidth of 40% are virtually identical to those found for the individual elements.

However, compared with the frequency response of individual elements as given in figure 7.11, a notable difference is found in the spectrum around 7 MHz, where a second resonance peak is present in the frequency response of the micro-beamformed outputs of the sub-arrays. A similar resonance peak is found using PZFlex simulations of an individual transducer element, but cannot be observed in the measured frequency response of the individual elements. Simulations using a KLM model [149] of a transducer element show that the absence of this peak can be qualitatively explained by the fact that the single elements in subsection III.C are loaded by a coaxial cable, which causes an attenuation that increases with frequency and thus masks the resonance peak. The elements connected to the circuitry of the ASIC, in contrast, are only loaded by the relatively small input capacitance of the LNA. Their

output signal is therefore much less attenuated and reveals the second resonance peak.

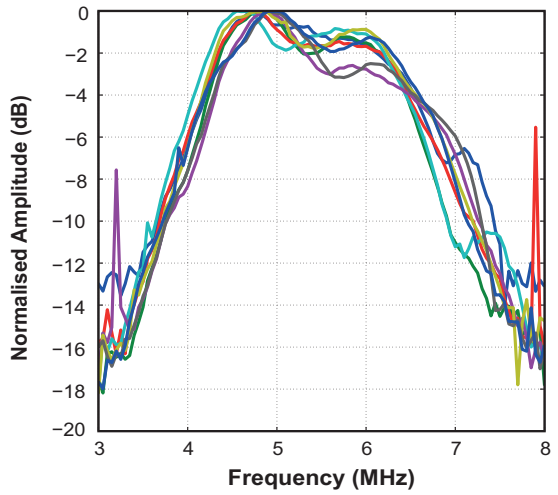

Figure 7.11. The measured frequency response of 9 individual elements.

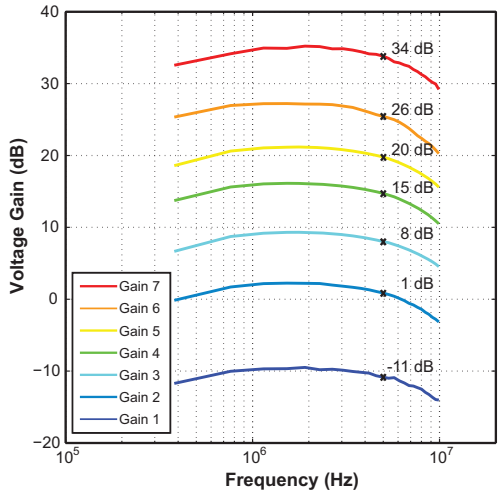

Figure 7.12. The measured transfer function of a single 3 × 3 beamformer of the ASIC for various gain settings.

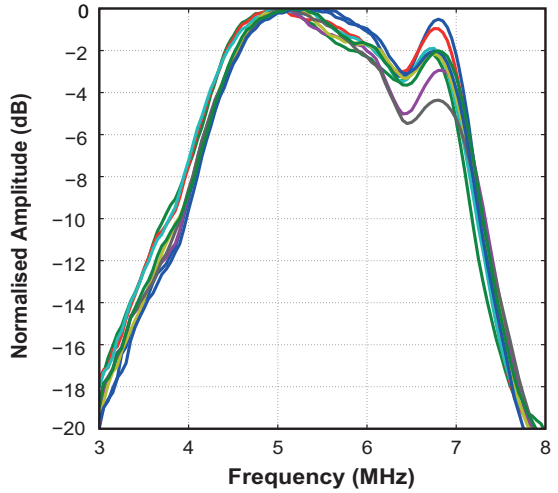

Figure 7.13. The measured frequency response of the 3 × 3 micro-beamformed sub-arrays.

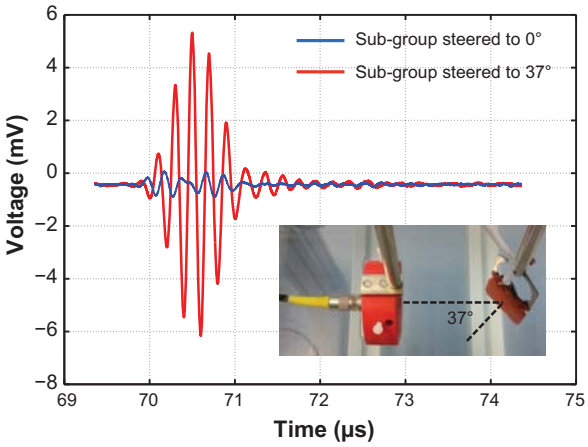

Figure 7.14. Voltage traces recorded at the output of the micro-beamformer for different steering angles (averaging of 32 traces was applied in the oscilloscope). The prototype has an angle of 37° to the transmitter.

7.4.5. Micro-beamforming: steering response

To characterize the ASIC's micro-beamforming function, three different delay patterns were programmed: with equal delays, 40 ns delay steps, and 80 ns delay steps between adjacent elements, corresponding to pre-steering angles of 0°, 17° and 37°, respectively. In this way, the possible beams of the 3 × 3 sub-arrays will have a sufficient overlap to cover the whole region of interest. The effect of micro-beamforming is illustrated in figure 7.14 by recording the micro-beamformer output for two different delay patterns when the prototype is positioned at an angle of 37° to the transmitter. The micro-beamformed output corresponding to a delay equivalent to 37° steering is significantly higher than the output corresponding to

0°, demonstrating that the micro-beamformer works well.

In order to obtain the beam profile, the transmit transducer was driven using a 20-cycle sinusoidal pulse of 5 MHz, while the angle of the prototype relative to the transmit transducer was swept from –90° to +90° using the rotational stage. The micro-beamformer output voltage of the central sub-array was recorded using the oscilloscope. The results are shown in figure 7.15, along with the beam profile of a 3 × 3 array simulated with Field II [150, 151] for the same delay pattern, assuming a piston-like transducer for a continuous-wave excitation. Given that the 20 cycle excitation in our measurement is almost a CW excitation, we observe that the theoretical values agree quite well with the measurement results, especially with the position of the grating lobes and side lobes. There is also reasonable agreement in the level of the grating lobes between the theory and the measurement. In addition, the measured beam-width of a 3 × 3 sub-array is almost identical to the expected beam-width of an element with the same size, which indicates that the crosstalk between elements of neighboring sub-arrays is very small.

While figure 7.15 demonstrates the proper operation of the micro-beamformer, the results for the 3 × 3 element sub-array are not easily extendable to a 32 × 32 element array of a full TEE probe. In general, for a large array that is operated in pulsed mode, the radiation pattern will be concentrated more around the main beam and the grating lobes will be much lower than in the foregoing results. The beam profile of such a 32 × 32 array operating in a pulsed mode (for a 3-cycle sinusoidal at 5 MHz) for the three steering angles was simulated using Field II, results of which are shown in figure 7.16. These concur with the expectation for a large array, and the grating lobes for the extreme steering angle i.e. 37°, is about 20 dB lower than the grating lobes from the 3 × 3 array simulations.

7.4.6. Dynamic range

The dynamic range is the ratio between the maximum and the minimum pressure that can be detected with the prototype. In order to determine the overall dynamic range, an acoustic measurement was performed in which the voltage output of the AWG was swept from 0.01 V to 10 V, and, moreover, different attenuations were applied using the benchtop attenuator. Unlike in previous experiments, a 3-cycle 5 MHz sinusoidal pulse was used, to closely resemble the signals used in imaging systems. Thus, acoustic pressures ranging from 0.8 Pa to 180 kPa were generated at the surface of the prototype's central sub-array, while the corresponding micro-beamformer output was recorded for the various gain settings of the signal-conditioning circuits.

The results from this experiment are shown in figure 7.17, where the peak to peak voltage received by the central sub-array is plotted against the peak to peak acoustic pressure incident on the surface of the sub-array. Keeping in mind the bandwidth of the transmitted pulse (4 MHz to 6 MHz for a 3-cycle sinusoidal pulse), all signals recorded during the course of this experiment were filtered using a bandpass filter between 4 MHz and 6 MHz in MATLAB to filter any out-of-band noise. In order to obtain a flat passband as well as a steep roll-off beyond the cut-off frequencies, a 15th order Butterworth filter was chosen.

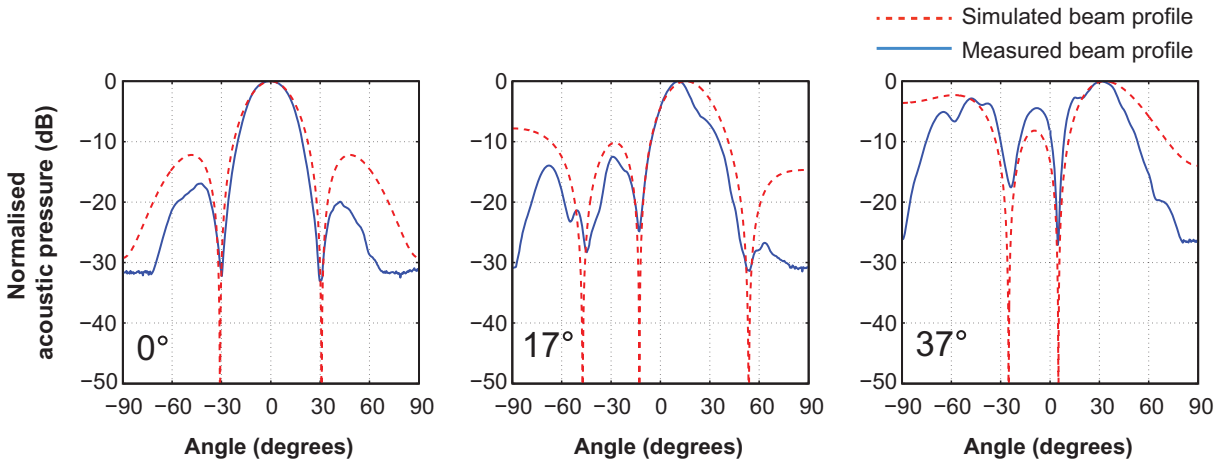

Figure 7.15. Measured and simulated beam profile of a 3 × 3 micro-beamformed sub-array excited by a 20-cycle sinusoidal pulse at 5 MHz, for steering angles of 0°, 17° and 37°.

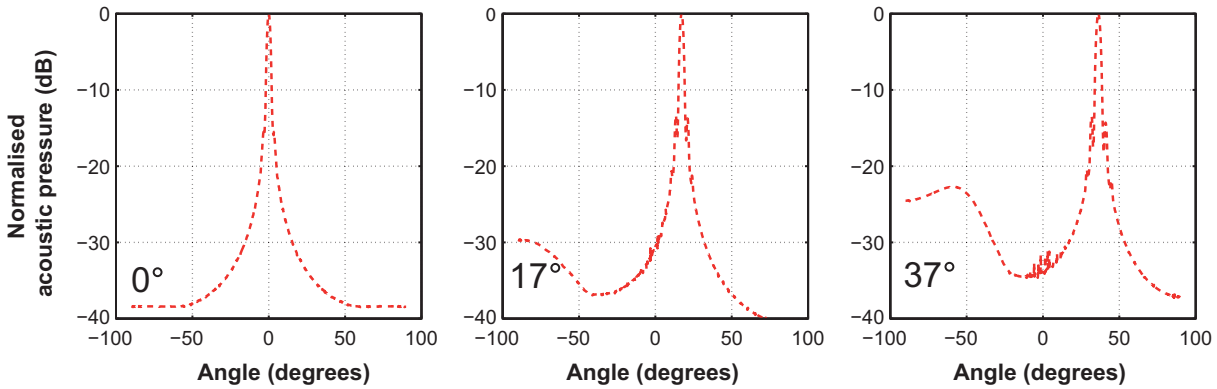

Figure 7.16. Beam profiles, simulated with Field II, for a 32× 32 array excited by a 3-cycle sinusoidal pulse at 5 MHz, for steering angles of 0°, 17° and 37°.

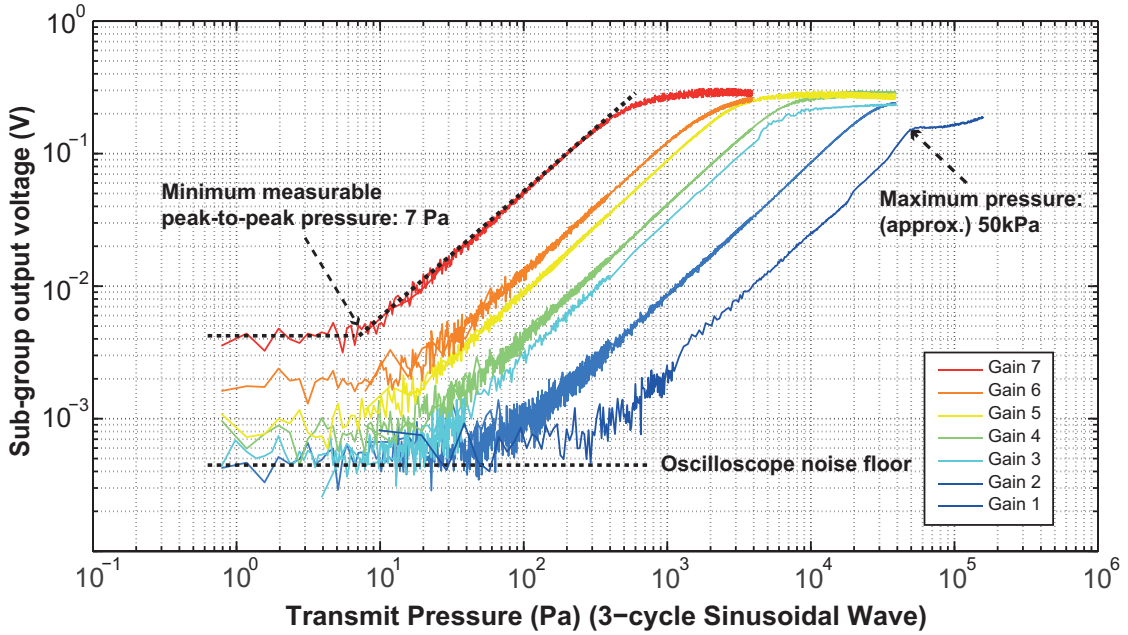

Figure 7.17. The measured output voltage (peak-to-peak) as a function of the pressure at the surface of the transducer matrix (peak-to-peak), for the different TGC gain settings, demonstrating the dynamic range of the ASIC; results obtained using a 3-cycle sinusoidal pulse at 5 MHz.

From these measurements, the sensitivity of a single transducer element is found to be about 9 μV/Pa. This is much higher than the sensitivity of 0.2 μV/Pa reported in Section IV-C, because the elements are not loaded by a cable, but only by the LNA. The measured sensitivity is in reasonable agreement with the (unloaded) sensitivity of 15 μV/Pa simulated using PZFlex.

The minimum detectable pressure is limited by noise. As shown in figure 7.17, its peak-to-peak value is approximately 7 Pa. A more accurate value is obtained by determining the rms output noise level at the highest gain setting, which, when pressure noise referred to the input of a single element using the measured sensitivity, corresponds to approximately 2.4 Pa. This is in reasonable agreement with the value expected based on the measured input-referred voltage noise of the ASIC and the Johnson-Nyquist noise associated with the resistive part of the transducer's impedance, which together corresponds to 2.1 Pa.

The maximum pressure that can be detected is about 50 kPa and is limited by the saturation of the signal in the ASIC, which occurs approximately when the peak-to-peak output voltage of the micro-beamformer reaches 200 mV. The dynamic range thus found is around 77 dB.

7.5. Summary

A prototype PZT matrix with an integrated receive ASIC that is targeted for real-time 3D TEE imaging has been presented in this paper. The 9 × 12 matrix transducer employs sub-array beamforming and pre-steering techniques to significantly reduce the number of external signal channels. Through the experimental evaluation of this prototype, we have delivered a proof of the effectiveness of the proposed techniques, including the array fabrication, the signal processing method, the integration approach and the circuit implementation. The proposed architecture may be scaled up to realize a full TEE transducer capable of making real-time 3D images.

The receive ASIC, which integrates both front-end signal conditioning circuits and micro-beamformers, has been fabricated in a 0.18 μm CMOS process. The signal conditioning circuit for each transducer element includes a single-ended LNA, which can be bypassed, and a quad-level TGC amplifier, the combination of which provides a programmable gain range of 45 dB. A micro-beamformer circuit utilizing pipeline operated sample/hold delay lines and the charge-domain summation is implemented in each sub-array. It is capable of providing a delay resolution of 40 ns and a delay depth of 280 ns to steer the beam in azimuthal and elevational directions over ±37°. The power-efficiency of all circuit blocks have been carefully optimized, leading to an average power consumption of 0.44 mW/channel.

The acoustic characteristics of a single transducer element, which has the silicon-based ASIC and the interconnection materials as the backing layer, has been evaluated with both simulations and experimental measurements. The measured response of the single element deviate quite significantly from the simulation, especially it's sensitivity, due to the capacitive loading of the single element by the measurement equipment. This effect is not observed in the case of the micro-beamformed sub-arrays, which indicates the positive effect of PZT-on-CMOS integration on the system performance.

A water-tank measurement has been performed to verify the functionality of the prototype

and evaluate its performance. Measurement results confirm the effectiveness of the micro-beamforming and the PZT-on-CMOS integration approach. The results also show more than an order of magnitude increase in sensitivity between the single element and the subgroup, indicating that the ASIC prevents the signal attenuation that would occur if the transducer elements were directly loaded by the micro-coaxial cables. This allows the prototype to achieve a measured dynamic range of 77 dB.

The promising measurement results obtained from the evaluation of the prototype PZT matrix encourage the further up-scaling of both the transducer matrix and the ASIC. Based on these results, a fully-populated matrix involving more than 1000 elements and an improved co-integrated ASIC will be implemented in our future work [152].

CHAPTER 8

Acoustic Characterization of a Miniature Matrix Transducer for Pediatric 3D Transesophageal Echocardiography[1]

Abstract

This paper presents the design, fabrication and characterization of a miniature PZT-on-CMOS matrix transducer for real-time pediatric 3-dimensional (3D) transesophageal echocardiography (TEE). This 3D TEE probe consists of a 32 × 32 array of PZT elements integrated on top of an Application Specific Integrated Circuit (ASIC). We propose a partitioned transmit/receive array architecture wherein the 8 × 8 transmitter elements, located at the center of the array, are directly wired out and the remaining receive elements are grouped into 96 sub-arrays of 3 × 3 elements. The echoes received by these sub-groups are locally processed by micro-beamformer circuits in the ASIC that allows pre-steering up to ±37º. The PZT-on-CMOS matrix transducer has been characterized acoustically and has a center frequency of 5.8 MHz, -6 dB bandwidth of 67%, a transmit efficiency of 6 kPa/V at 30 mm, and a receive dynamic range of 85 dB with minimum and maximum detectable pressures of 5 Pa and 84 kPa respectively. The properties are very suitable for a miniature pediatric real-time 3D TEE probe.

[1] This chapter is accepted for publication as:
Verya Daeichin, Deep Bera, Shreyas Raghunathan, Maysam Shabanimotlagh, Zhao Chen, Chao Chen, Emile Noothout, Hendrik J. Vos, Michiel Pertijs, Johannes Bosch, Nico de Jong, Martin Verweij; Acoustic characterization of a miniature matrix transducer for pediatric 3D transesophageal echocardiography, Ultrasound in Medicine and Biology, 2018.

8.1. Introduction

Transesophageal echocardiography (TEE) concerns ultrasound imaging of the heart from the esophagus with an ultrasound transducer mounted on the tip of a gastroscopic tube [153]. Since the introduction of TEE transducers in the 1980s [154, 155], this imaging modality has been widely used for diagnosis and real-time intra-operative imaging of the heart to guide minimally invasive cardiac procedures [156]. Often, 2-dimensional (2D) TEE is used for monitoring and the final check at the end of the operation. However, such 2D cross-sectional visualization of the heart is insufficient in the case of complicated reconstructions since the imaged targets (cardiac and valve anatomy, motion, blood flow etc.) are all 3-dimensional (3D) phenomena and hard to be interpreted from only 2D cross-sections. Recent advances in 2D matrix array technology [157, 158] have allowed the real-time 3D reconstruction of the cardiac anatomy by TEE. Various publications have shown the advantages of 3D echocardiography over 2D, both for TEE and transthoracic imaging (TTE) [159-165].

Implementation of imaging sequences for 3D imaging ideally requires access to every individual element of the 2D array so that transmit and receive timing and apodization can be controlled for each element. However, given the desired aperture of a 2D array, the need for keeping the pitch between the elements less than half the wavelength results in thousands of elements. Directly connecting every individual element to an ultrasound unit (with up to a few hundred channels) is impractical if not impossible. As an example, a TEE probe with an aperture size of 9×9 mm^2 and a central frequency of 5 MHz (wavelength of about 300 μm) requires a 60×60=3600 element array. The data transfer rate for all individual elements would amount to terabits per second.

Several solutions have been proposed to solve this problem. To reduce the cable and channel counts, some have proposed to group the elements of a 2D array into column and row configurations [39, 157, 166] or to use multiplexing techniques [44, 167]. Both methods have the limitation of not allowing continuous access to the full array during transmission and reception since only part of the elements is connected to the scanner at a given time. A more direct solution for reducing the cable or channel counts is based on sparsity: only a sparse subset of the elements are connected, instead of the full array [161, 168-171]. Although this is a promising technique, it requires more complex sequences and beamforming algorithms and the element configuration in a sparse array must be optimized to achieve acceptable image quality in terms of resolution and contrast to noise ratio.

Perhaps the most elegant way to achieve data reduction is the micro-beamforming (or sub-array beamforming) technique, which greatly reduces the number of required cables and the data transfer rate for such an array [35, 36, 39, 41, 45, 172, 173]. This technique performs the first step of the beamforming already in the probe tip using an application specific integrated circuit (ASIC). Per sub-array, partial beamforming is performed by applying micro-delays to the signal of each element and summing all signals.

Several TEE probes with matrix array transducers have been developed. Currently, there are three commercially available 3D TEE probes: X7-2t (Philips Ultrasound, Bothell, WA), Vivid E9 BT12 (General Electric Healthcare, Amersham, U.K.), and Siemens Acuson SC200 Z6M (Siemens Healthcare GmbH, Munich, Germany). However, there is no published report on

characterization and technology of either of these TEE probes. The big size of these probes (2-3 cm3) is limiting the use of such a 3D TEE technology on pediatric patients as well as for long intra-operative monitoring in adult patients. To overcome this, a significant reduction in the size of the probe head is required. We have developed a matrix transducer using micro-beamforming and ASIC technologies for TEE application which can be accommodated in a head smaller than 1 cm3. In this paper we discuss the design, technical aspects, acoustic characterization and performance of our miniaturized matrix transducer for a TEE probe. To the best of our knowledge this is the first report to discuss the details of such a probe.

8.2. Materials and methods

8.2.1. Requirements and initial design choice

The requirements for a miniature TEE probe are more challenging than those for its adult [174] and have been described in an earlier publication [36, 45]. The physical constraints include a head volume of not more than 1 cm3, and less than 200 individual cables in the shaft of 5 mm in diameter. The head volume limits the aperture area of the transducer array to 5 mm × 5 mm. The intended penetration depth is up to 12 cm and the central frequency around 5 MHz. Thus for this central frequency of 5 MHz, the pitch of the 2D PZT array is chosen as λ/2 (150 μm) in both directions to minimize grating lobes [11]. Thus, within the 5 mm × 5 mm aperture area we fabricate 32 × 32 = 1024 individual PZT elements. The dicing kerf between the elements is 20 μm.

Within the available aperture of 25 mm^2, and the 1024 total number of squared elements, different partitioned designs with separated transmitters and receivers have been evaluated numerically. In our design, we chose to partition the aperture into a small set of transmitting elements and sub-arrays of receive elements that are connected to the ASIC for micro-beamforming. The transmit elements are electrically fully separated from the receive electronics and directly wired out to the ultrasound system, allowing full freedom of choice of transmitting signals (AWG pulse shapes, delays, voltages, coding, and etc.). This still leaves us the choice of the location of the transmit elements. We considered three different designs with a cross-shaped transmitter, a central transmitter and staggered transmitter elements. These three architectures are evaluated by simulations based on multiple quality parameters such as the width of the transmit beam, lateral and elevational resolution of the receiver and grating lobe and side lobe levels. Simulations for the transmit and receive beam profiles were carried out using Field II [175] using the transducer element transfer function obtained from PZ-Flex simulations. A three cycle Gaussian modulated pulse was used as the excitation function for the array. In all the designs, a transducer element designated as a transmitter is incapable of acting as a receiver and vice versa. Therefore, the transmitter elements appear as a missing element in the receive aperture.

8.2.2. Pre-beamforming and ASIC design

The 32 × 32 array elements are directly connected to a matrix of spatially coaligned contacts on the ASIC using an interconnect layer [36, 45]. The ASIC (thickness 300 μm) has

been fabricated in low-voltage CMOS technology, which is only possible because of the partitioned design where high voltage transmit elements are wired out directly to the mainframe, while only the signals from receive elements are routed into the ASIC for pre-processing. As said, to reduce the number of output signal channels, the sub-array beamforming method, also referred to as "micro-beamforming" or "pre-steering", is adopted in this work [176]. In this case, the transducer matrix is divided into sub-arrays of 3 × 3 elements, the receive signals of which are delayed and summed by the local micro-beamformer circuit in the ASIC, reducing the number of channels by a factor of 9. In the micro-beamformer, fine delays are applied to the individual elements, so that the sub-array is acting as a large element pre-steered roughly into a predefined direction. The micro-beamforming circuit is based on a sample-and-hold delay line and charge-domain summation providing a delay resolution of 30 ns and a delay depth of 180 ns to steer the beam in both azimuthal and elevation directions over ±37°. The signals of all sub-arrays are further beamformed in the imaging system that applies larger delays to perform the full-aperture beamforming, steering and focusing. All components in the ASIC (LNAs, micro-beamformers, line drivers, logic etc) are designed for minimal power consumption to avoid overheating of the probe tip. The expected power consumption for 96 receiver subgroups is about 230 mW (270 μW/element). The front-end signal conditioning in each channel is performed by the LNA and a time-gain-compensation (TGC) amplifier. The LNA provides 3 gain settings (-12 dB, 6 dB and 24 dB) followed by the 4-step TGC gain settings (0 dB, 6 dB, 12 dB and 18 dB). Combining the gain settings of the LNA and TGC results in a gain range of -12 to 42 dB assuring a large dynamic range for receiving the echo signals.

8.2.3. Design of single element transducer

A single acoustic transducer was simulated and optimized using PZFlex, a finite difference analysis software package [177]. Commercially available CTS 3203HD is used as the piezoceramic material with a matching layer (conductive glue) mounted on top of a CMOS chip and connected via an interconnect backlayer. The material properties of different materials used in this scheme are given in Table 1. For the intended center frequency for this 3D TEE probe of 5 MHz, a piezoceramic thickness of 225 μm was chosen. In order to optimize thicknesses of the layers, simulations were performed for all different matching and backing layer thicknesses from 40 μm to 140 μm in steps of 10 μm. Thus, 11 × 11=121 corresponding FDM simulations were performed using PZFlex and hence the performance of 121 different acoustic stacks was compared in terms of electrical impedance and acoustic pressure at the surface of the transducer.

Table 8.1. Material properties used in FEM simulation

Material	Properties
Conductive Glue	$\rho = 3350$ kg/m^3, $c_p = 2000$ m/s, $c_s = 1050$ m/s
CTS 3203 HD	$c_{11} = c_{22} = 137$, $c_{12} = 88$, $c_{13} = c_{23} = 92$ MPa, $c_{33} = 126$, $c_{44} = c_{55} = 22$, $c_{66} = 25$ MPa $e_{15} = e_{24} = 16$, $e_{31} = e_{32} = 9$, $e_{33} = 22$ C/m^2 $\varepsilon_{11} = \varepsilon_{22} = 1306$, $\varepsilon_{33} = 1200$ CV/m.
Epoxy	$\rho = 2975$ kg/m^3, $c_p = 1960$ m/s, $c_s = 1047$ m/s
Silicon	$\rho = 2330$ kg/m^3, $c_p = 7526$ m/s, $c_s = 4346$ m/s

8.2.4. Fabrication of the matrix TEE prototype

Given the specification and the initial design choices, a 32 × 32 array was fabricated. In this work, we have extended the PZT-on-CMOS integration scheme that was used in our previous work [45]. Gold balls are applied on top of the ASIC's transducer bond-pads, arranged as a 32 × 32 matrix with a pitch of 150 μm at the surface of the ASIC's metallic interconnect layers. A non-conductive epoxy is deposited between the balls to electrically isolate them, and is ground down to expose the gold, forming electrical contact points for the PZT matrix. Besides functioning as electrical isolation, the non-conductive epoxy also acts as a mechanical dicing buffer (buffer layer, 30 μm thickness). On top of the epoxy, we mount the acoustic stack, which consists of an electrically conductive epoxy glue of 60 μm thickness on both sides of the 225 μm thick CTS 3203HD piezoceramic. The electrically conductive glue provides the electrical connection between the PZT and the exposed metal interconnects on the ASIC and together with the buffer layer act as a backing layer. The acoustic stack is then diced using a 20 μm dicing saw to create 32 × 32 individual PZT transducers. For the purpose of electrical separation, the dicing kerfs extend into the buffer layer for about 10 μm. An aluminum ground foil (8 μm) is glued to the matching layer, on top of the PZT. The total thickness of the assembled transducer is 683 μm.

8.2.5. Acoustic characterization

The 32 × 32 PZT-on-CMOS array was mounted on a PCB daughter-board which was connected to a motherboard that interfaces to a Verasonics (Vantage System, Verasonics Inc. Kirkland, Washington, USA) data acquisition system. The motherboard is designed such that it can be mounted on the Verasonics machine using two Cannon connectors (LLC DLM5-260PW6A, ITT Corporation, NY, USA). Commercially available micro-coaxial cables (Samtec, New Albany, IN, USA) are used to transfer the TX (64) and RX (96) data between the daughterboard and the motherboard. The signals from the receiving part of the system are recorded using one of the two connectors of the Verasonics system, while the high-voltage transmit signals are provided to the transmit array via the other. The 8 × 8 transmit array elements are directly wired out of the ASIC (via the metallic interconnect top layers of the ASIC, without connection to the electronics) and connected via the motherboard to the Verasonics or other pulsers for acoustical tests. The receive elements are connected to the electronic circuitry in the ASIC via the metal interconnects. The signals from 3 × 3 elements

are micro-beamformed, amplified and passed to the cable drivers in the PCB and recorded using the Verasonics. In this paper, the results from the acoustical performance are discussed in detail. The detailed evaluation of the electronics can be found in [36]. The prototype was immersed in a water tank for acoustic characterization and the 8 × 8 transmitters and the 96 sub-groups of the receiver were evaluated separately.

To measure the variation in sensitivity between the individual elements (transmitters) and individual sub-groups (receivers) the entire array was used in receive mode and was exposed to a pseudo-planar wave (see figure 8.9 in the appendix) emitted by an external 5 MHz 0.5-inch single-element transmit transducer (V309, Olympus Scientific Solutions, Waltham, MA, USA) at a distance of 32 cm transmitting a 3-cycle burst with an input peak-to-peak voltage of 10 V. The variation in sensitivity of the individual 64 elements of the transmit array was then measured by using them in receive mode and calculating the variation of the amplitude of the received signals. The same approach was used for determining the sensitivity variation of the 96 receive sub-groups.

In order to evaluate the frequency response of a single element of the array, three single elements of the transmit array were chosen randomly and excited by a short (10 ns) pulse with an input peak-to-peak voltage of 20 V using an arbitrary waveform generator (33250A, Keysight Technologies, Santa Clara, CA, USA). The generated acoustic signal was recorded at 15 mm away from the transducer surface with a 0.2 mm needle hydrophone (Precision Acoustics, Dorchester, U.K.). The signals were compensated for the excitation pulse and the hydrophone transfer function before determining the transfer function of the three single elements.

The efficiency of the transmit elements was measured by exciting the entire transmit sub-array (64 elements) with a 3-cycle 5 MHz pulse from the Verasonics and varying the excitation voltage from 10 V to 40 V. The generated pressure waves were recorded using the needle hydrophone on axis in the far field (30 mm from the transducer surface). Peak-to-peak pressures generated by the transmit array as a function of peak-to-peak input voltages were recorded and the signals were corrected for the attenuation in water.

The pulse-echo measurements were carried out by coupling the prototype with acoustic gel to a quartz plate at a distance of 5 mm from the transducer surface. All the transmitters were excited simultaneously with a 3-cycle 5 MHz burst of 2 V using the Verasonics. The LNA and TGC gains of the receive groups in the ASIC were both set to the moderate gain of 6 dB, amplifying the echo signals by a total gain of 12 dB before recording by the Verasonics input channels. A constant Verasonics TGC setting of 500 was used to avoid saturation and clipping of the receive signals.

The dynamic range of the receiver, i.e. the largest range of pressures which can be detected by the transducer, was measured as follows. The external 5 MHz single-element transducer was excited with a 3-cycle burst of varying voltage to generate a pressure range of 0.2 Pa to 300 kPa at the surface of the prototype placed 32 cm away from the source. The corresponding micro-beamformer output was recorded by the Verasonics for three different gain settings of the ASIC signal conditioning circuit. The highest LNA and TGC gain settings of 24 dB and 18 dB (42 dB in total) were used for recording the lower range of the pressures. For the middle range, the gain settings were 6 dB and 6 dB (12 dB in total). For the higher

range, LNA gain of -12 dB and TGC gain of 0 dB (-12 dB in total) were used. The signals recorded by the Verasonics were bandpass filtered (cut-off frequencies of 4 and 6 MHz) using a 5th order Butterworth filter in MATLAB. Then, the peak-to-peak amplitudes of the received signals (no averaging) were plotted against the input pressure at the transducer surface. To calculate the minimum and maximum detectable pressures from the plot, linear curves were fit to three different parts of the dataset: the noise part (input pressures up to 2 Pa), the linear part (input pressures from 10 Pa to 10 kPa), and the saturated part (above 200 kPa). The intersection of the linear part with the noise part and the saturated part were chosen as the minimum and the maximum detectable pressures respectively.

Furthermore, the transmit-receive beam profile at three different steering angles ((0°,0°), (17°,17°), and (37°,37°)) was evaluated. The beam profile of the transmit array was determined by mounting the hydrophone on the X-Y stage of the water tank and performing a linear scan in the lateral and elevation directions for each steering settings at 15 mm from the surface of the transducer. The different elements of the transmitter were driven by a 3-cycle 5 MHz pulse from the Verasonics with different time delays, in order to achieve a transmit steering of (0°,0°), (17°,17°), and (37°,37°). The peak-to-peak pressure recorded by the hydrophone was then recorded for different hydrophone positions for all steering angles and corrected for the hydrophone directivity (see supplementary material and figure 8.10 in the appendix). For the receive beam-profile the prototype was mounted on a rotational arm in the water-tank, in front of the single-element 5 MHz transducer driven by a 3-cycle 5 MHz burst. In order to construct echoes from different angles, the prototype was rotated from -50° to +50° in steps of 2° laterally with respect to the source. The acoustic signal from the 96 sub-arrays was captured at every angle using the Verasonics and the beam-profile of the individual sub-groups was computed. Using the appropriate delays with respect to the center of the sub-groups, the beam-profile of the entire receive array was calculated from the data acquired by all the sub-groups at all the angles. The elevation beam-profile of the sub-groups and the receive array was measured by re-positioning the prototype 90 degrees rotated with respect to the previous configuration such that the rotational arm of the water-tank now records the elevation beam-profile. The receive ASIC is capable of providing delays from 30 ns to 210 ns in steps of 30 ns to each receive element within the sub-group. Thus, in line with the findings in [176], we can steer the individual sub-groups to angles 0º, ±17º, and ±37º along the lateral and elevation directions. The net transmit-receive beam profile is described by the product of the transmit and receive angular responses. Therefore, after calculating the transmit and receive beam profile at these three different angles, the beams were combined using the product of transmit and receive beams in both lateral and elevation directions at each angle to acquire the overall transmit-receive beam profiles for steering angles of (0°,0°), (17°,17°), and (37°,37°).

8.2.6. 3D imaging

To demonstrate the 3D imaging capability of the prototype, a pattern of five-point scatterers (steel balls on needles), forming a rotated letter “T”, was placed at a distance of approximately 40 mm in front of the transducer array. The sub-arrays were pre-steered in each

of the 25 possible directions. Diverging waves were transmitted from the transmit sub-array in matching directions, using pulses of 18 Vpp (Volt peak-to-peak), generated by the Verasonics system. A 3D volume image was reconstructed by combining the sub-group output signals recorded using the Verasonics system from multiple of such transmit-receive events and rendered to get a frontal view of the point scatterers. The details of the transmit-receive configuration as well as the 3D beamforming algorithm can be found in [178]. The 3D image reconstruction has been done offline and 169 transmit-receive events were used to generate one volume.

8.3. Results

In the previous sections, we described the design optimization and manufacturing processes of the acoustic stack for optimal transmission and receive properties of a single transducer element. In this section, we present the result of our simulated model and the experimental results acquired with our prototype matrix TEE transducer for a transmit-receive architecture capable of attaining 3D ultrasound images.

8.3.1. Design choice

From the numerical study, we found that an optimized transducer would have a backing layer thickness of around 90 μm and matching layer thickness of around 70 μm. Given these parameters, we obtain a center frequency of around 5.5 MHz, a bandwidth of 70% and a transmit efficiency of 8.4 kPa/V at 30 mm for 64 transmit elements and a Johnson-Nyquist noise voltage equivalent of around 8 $\mathrm{nV}/\sqrt{\mathrm{Hz}}$ for an operating temperature of 37º C and 70% bandwidth.

Three different transmitter architectures were simulated in Field II and their beam profiles were analyzed. The different designs and their corresponding beam profiles are shown in figure 8.1. The green blocks in the figures denote the receiver elements of the array and the white spaces denote the transmitter positions.

To generate sufficient acoustic power the entire transmit array should be excited. Accordingly, the design with the central transmitter (figure 8.1c) benefits from a larger opening angle of 13.2 degrees (-3 dB points) in comparison to 3.2 degrees with the other two designs (figure 8.1a and 8.1b). A symmetric broad beam with reasonable power generated by the central transmitters can illuminate a larger area with a single excitation, allowing to increase the frame rate. Moreover, the staggered pattern (figure 8.1b) results in large transmit grating lobes. Side lobes appear in the receiver's beam profile in all the three designs at +5 and -5 degrees, with levels around -10 dB. The large hole in the receive aperture of figure 8.1c results in larger side lobes, which can be analyzed by plotting the point-spread-function (PSF). The PSF of the current receiver was compared with the PSF of a fully populated 32 x 32 receiver, as shown in supplementary figure 8.3. The transfer function of the individual elements was obtained from the PZ-Flex simulations. The comparison of the two PSFs shows only a small difference in the way a single point is imaged by the receiver. We have chosen the design with central transmitter (figure 8.1c) because of its lower level of grating lobes and

excellent lateral resolution resulting in a PSF almost as good as a fully populated receiver array of the same size (supplementary figure 8.3).

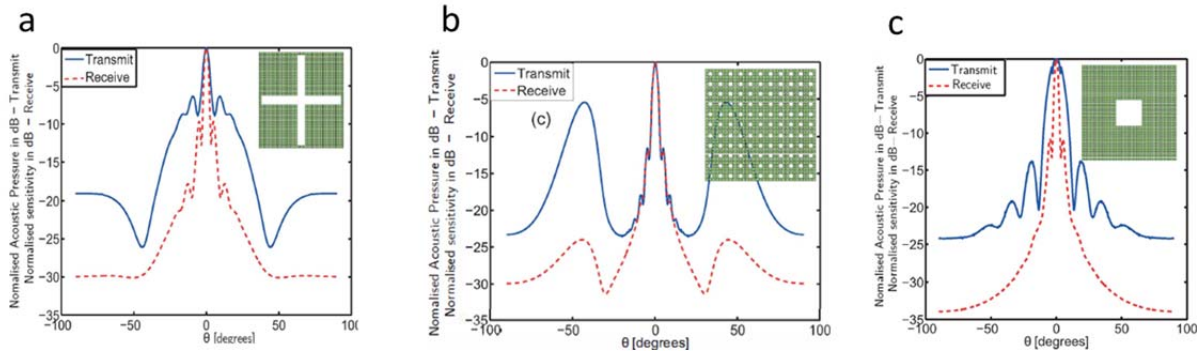

Figure 8.1. Architecture and transmit and receive beam profiles for **(a)** a cross-shaped transmitter; **(b)** a staggered transmitter; **(c)** a central transmitter.

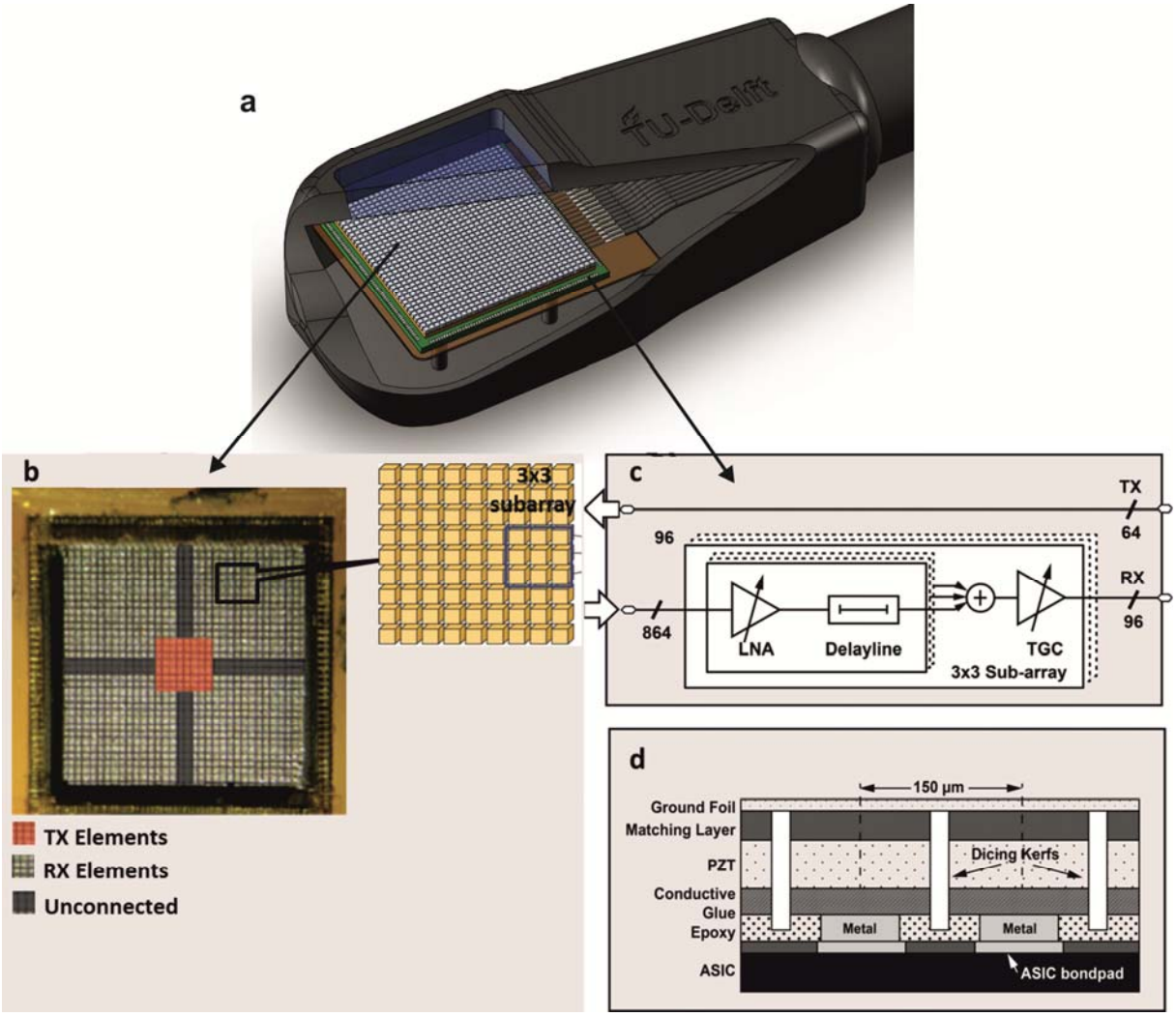

Figure 8.2. (a) A schematic of a miniature 3D TEE probe with front-end ASIC; **(b)** The layout of our prototype for pediatric 3D TEE transducer; **(c)** The concept of the micro-beamforming in the ASIC; **(d)** The detailed cross-section of various layers of the prototype transducer with total thickness of 683 µm (not to scale).

8.3.2. Prototyping

Figure 8.2 depicts the schematic of a miniature 3D TEE probe and a photograph of our matrix transducer prototype with a front-end ASIC. The layout of our central transmitter design and a schematic showing the concept of micro-beamforming in the receive sub-groups is depicted in figure 8.2b and 8.2c. Note that two rows and columns of elements in the receiving part (the dark grey 'cross') had to be sacrificed to allow for access to the 64 central transmit elements via the metal interconnect layers. Figure 8.2d is depicting the details of the various layers, described above, for manufacturing the prototype.

8.3.3. Acoustic characterization

The variation in the sensitivity of transmitters (individual elements) and receivers (individual sub-groups) of the prototype is depicted in figure 8.3. There were two sub-groups among the receivers and one single element among the transmit elements with no signals (dark blue) which were excluded from the sensitivity variation measurements. The area in the middle of figure 8.3a corresponds to the transmit part of the array. The sensitivity variation of the transmit array was measured separately and displayed in figure 8.3b. The sub-groups of the receivers show a sensitivity variation of 7.6 dB and individual elements of the transmitter have a sensitivity variation range less than 1 dB.

The transfer functions of three single elements of the transmit array of the prototype are plotted in figure 8.4. The slight time shift in the time signals correspond to the different locations of the elements with respect to the hydrophone. The Fourier transforms of the signals (figure 8.4b) show a mean center frequency of 5.8 MHz with a mean -6 dB bandwidth of 67%.

The peak-to-peak output pressure recorded by the needle hydrophone at 30 mm from the transducer surface as a function of the peak-to-peak input voltage is plotted in supplementary figure 8.4. The efficiency of the transmit array (8 × 8 elements) is calculated to be around 6 kPa/V at the distance of 30 mm.

The result of the pulse-echo measurements is shown in figure 8.5 where the received echo signals from the quartz plate of three different sub-groups are plotted in time and frequency domain. The amplitudes of the time signals in figure 8.6a are displayed in arbitrary units. The normalized Fourier transforms of these time signals are shown in figure 8.5b. The slight time shift observed in the time signals is due to the different locations of these sub-groups.

The acoustic dynamic range of the prototype is plotted in figure 8.6. The lowest detectable pressure is 5 Pa. This pressure was measured when the ASIC gain was set to 42 dB. The highest detectable pressure before saturation of the signal is 84 kPa, which was measured when the ASIC gain was set to -12 dB, resulting in an acoustic dynamic range of 85 dB (5 Pa to 84 kPa) for this prototype..

The transmit-receive beam profile for the lateral and elevation direction and three different steering angles of (0°,0°), (17°,17°), and (37°,37°) are shown in figure 8.7. In this figure, the normalized peak-to-peak received pressure is plotted as a function of angle for each steering setting. The plot shows that the -6 dB opening angle of the transmit-receive array is about 4°,

and that the transmitter and receiver sub-groups can be steered effectively to any of the three angles (0°, 17°, and 37°) in both lateral and elevation directions.

8.3.4. 3D imaging

Figure 8.8a shows the positions of the 5 point scatterers (5 steel balls on needles) of the phantom, and figure 8.8b shows the corresponding volume rendered image of this phantom placed on a c-plane at 40 mm with 40 dB dynamic range. In the rendered image, the positions of the point scatterers accurately matched with the actual positions of the scatterers. For each scatterer, one main lobe and four side lobes (in both lateral and elevation directions) are observed.

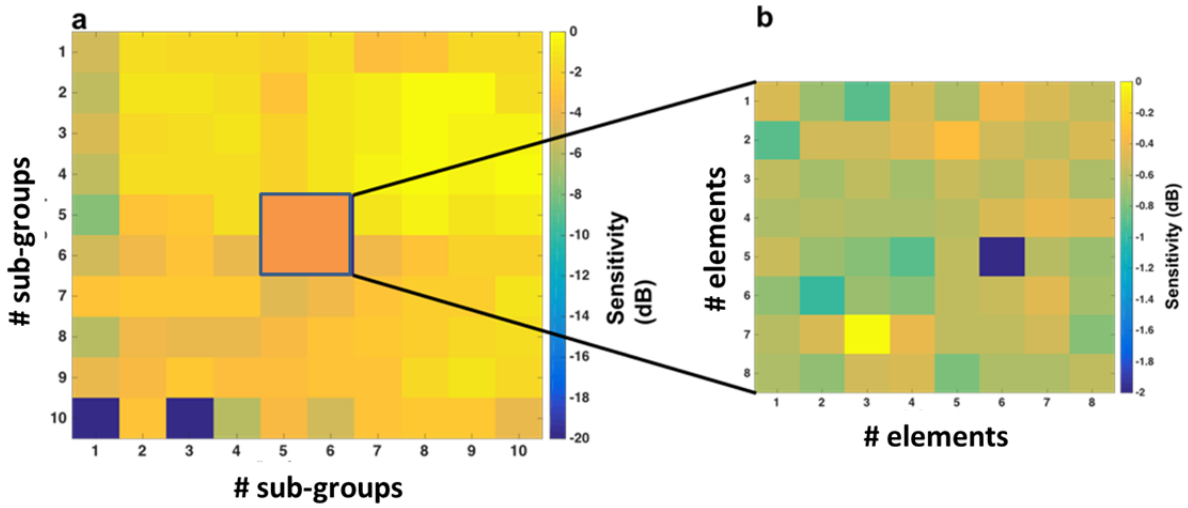

Figure 8.3. (a) Sensitivity variation of the receive sub-groups of the prototype. The dark blue square in the center shows the transmit sub-array. **(b)** Sensitivity variation of each individual element (8 × 8) of the transmit sub-array.

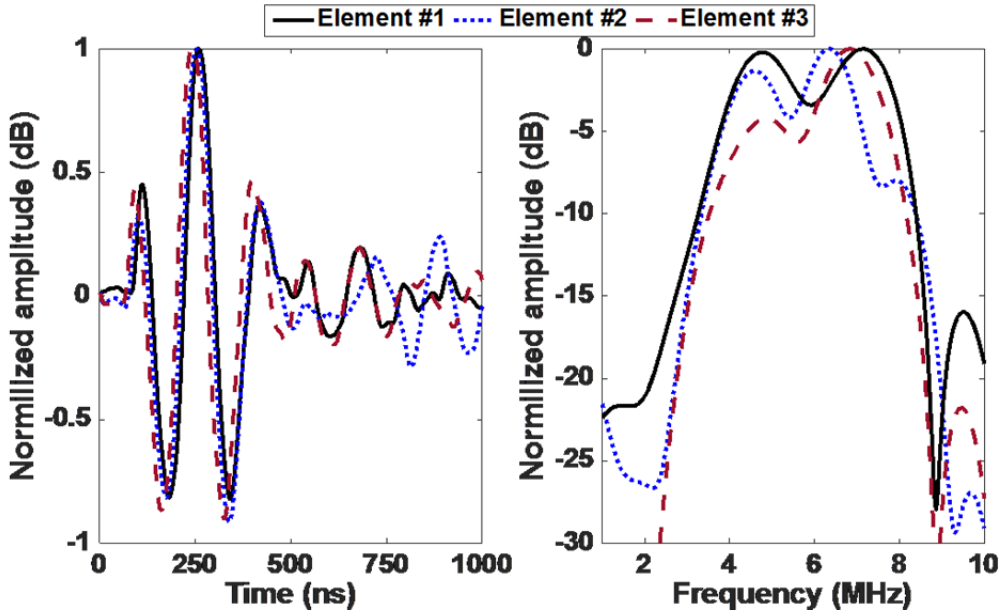

Figure 8.4. Transmit transfer function of three randomly selected single elements of the prototype transmit sub-array in **(a)** time domain and **(b)** frequency domain.

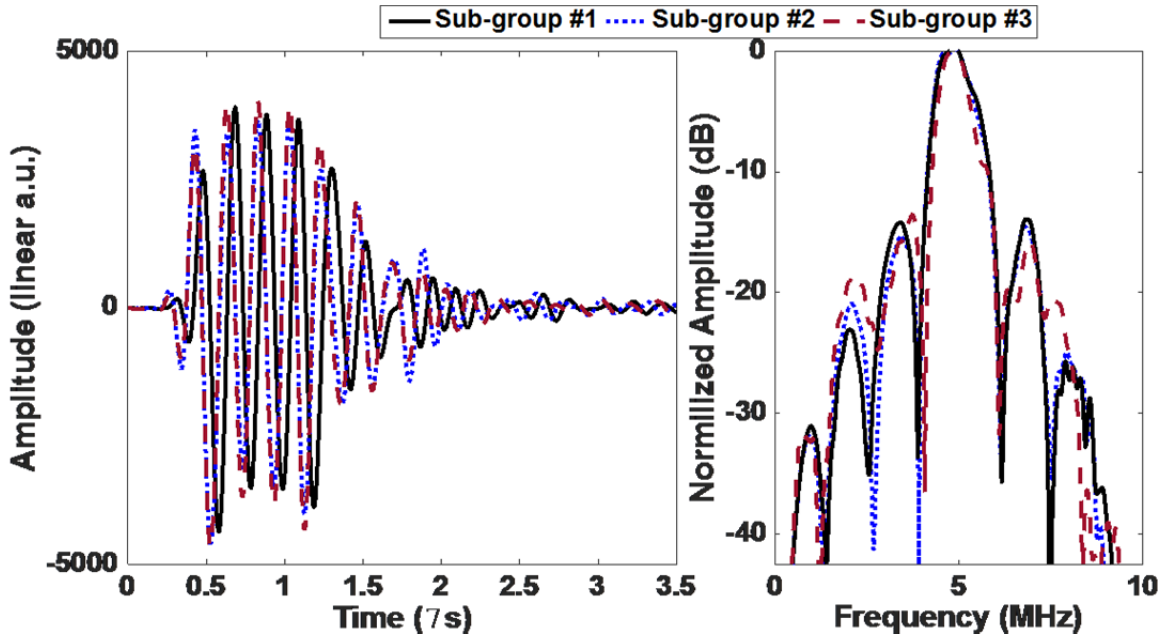

Figure 8.5. Received echo signals by three different sub-groups from a quartz plate 5 mm away from the surface of the transducer in **(a)** time domain and **(b)** frequency domain.

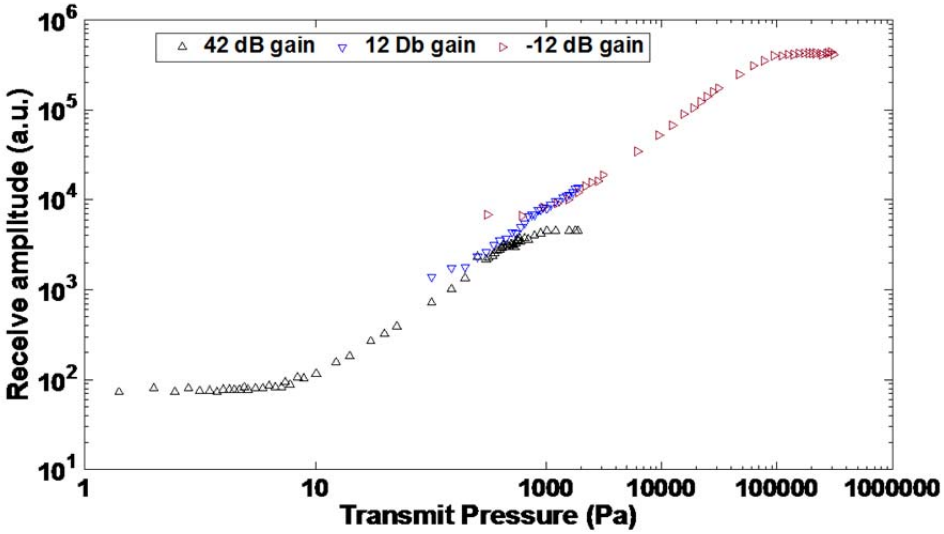

Figure 8.6. Measured peak-to-peak signal amplitude recorded by the Verasonics as a function of the peak-to-peak pressure at the surface of the transducer array for three different gain settings.

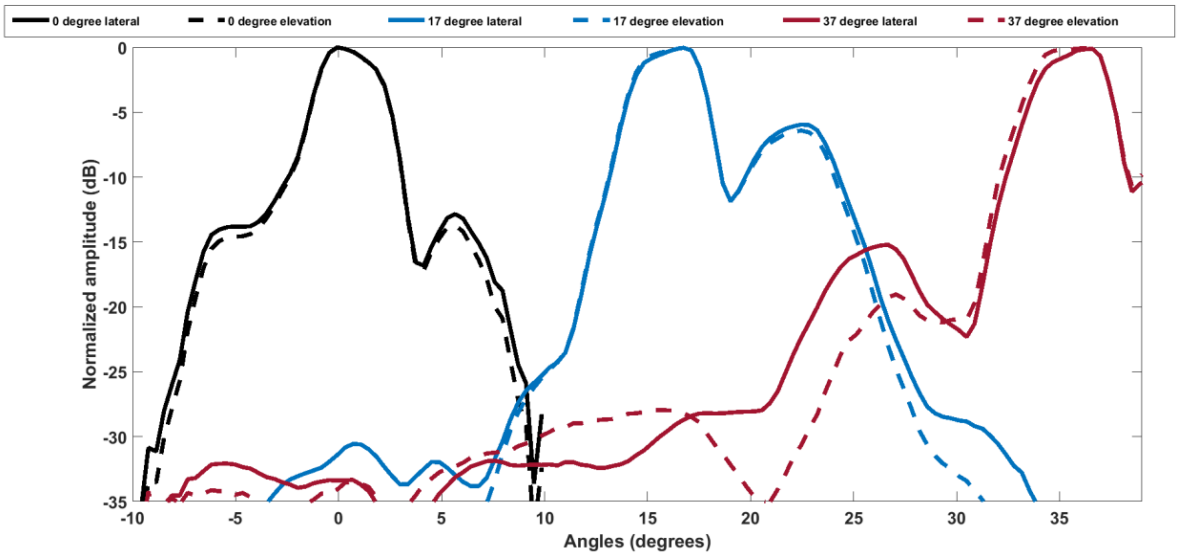

Figure 8.7. Transmit-receive beam profile of the prototype in lateral and elevation directions for three different steering angles ((0°,0°), (17°,17°), and (37°,37°)).

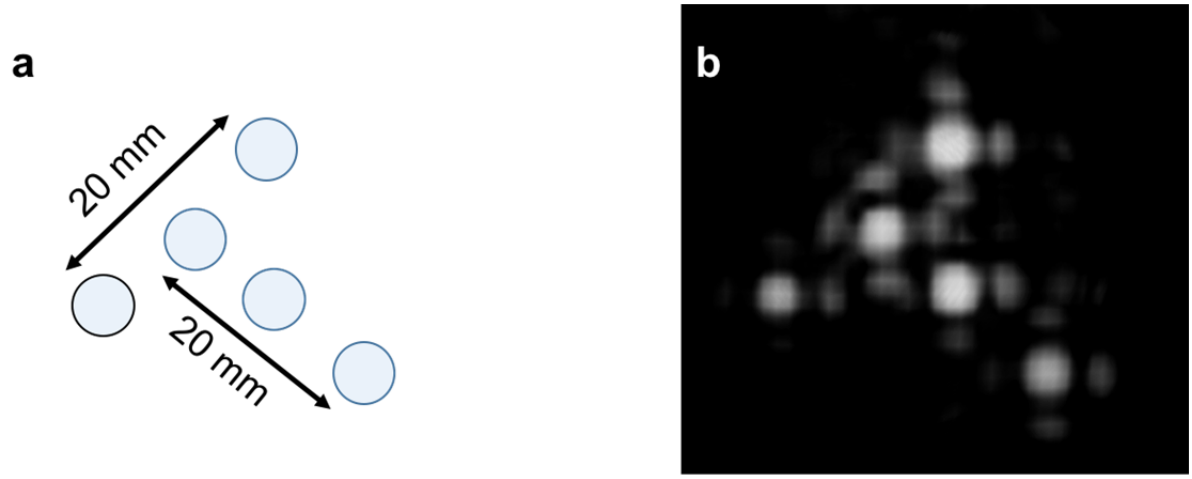

Figure 8.8. (a) The pattern of 5 point scatterers (5 steel balls on needles). **(b)** volume-rendered 3-D image with 40 dB dynamic range.

8.4. Discussions

A front-end ASIC with an integrated 32 × 32 PZT matrix transducer has been designed and fabricated to enable next-generation miniature ultrasound probes for real-time 3D TEE. The transducer array is split into a transmit sub-array and receive sub-groups. To address the critical challenge of cable count reduction, sub-array receive beamforming is realized in the ASIC with a highly compact and power-efficient circuit-level implementation, which utilizes the mismatch-scrambling technique to optimize the dynamic range. A power- and area-efficient LNA architecture is proposed to further optimize the performance. Based on these features, the ASIC demonstrates state-of-the-art power and area efficiency, and has been successfully applied in 3D ultrasound imaging.

The details of the ASIC design and its performance have been reported in our earlier publications [36]. The functionality of the ASIC was tested in a proof of concept study where

a 9 × 12 array with a larger pitch of 200 μm was fabricated on top of the ASIC for basic acoustic measurements. The receive ASIC integrates both the front-end signal conditioning circuits and the micro-beamformer. In this prototype, the signal conditioning circuit has a triple-level LNA and a quad-level TGC amplifier providing a total programmable gain range of 54 dB.

An important feature of a TEE probe which should meet the FDA regulations is low in-probe power dissipation to prevent excessive tissue temperature rise. Such requirements apply to both the largest transmit power and the self-heating associated with the in-probe electronics. According to the regulations, the maximum temperature that may be attained by the surface is restricted to 41 degrees Celsius. This limits the total power budget of the in-probe transmit and receive circuit to about 0.5 W [176]. The state-of-art of ultrasound front-end ASICs has a power consumption of a few mW per channel, adding up to several Watts for the entire array [179, 180]. In our design the 64 (8 × 8) transmitter sub-array in the center is electrically separated from the receive electronics. This configuration allows the use of dense low-voltage IC technology for the ASIC, thus saving power and area. Our ASIC design consumes only 0.27 mW per element, adding up to 230 mW for the entire array in full receive operation [45]. Our transmitter dissipates 267 mW in a worst case scenario of real-time imaging (64 elements, 5 kHz prf, 5 cycles, 3kohm real impedance, pulse amplitude 50V RMS), which make the total dissipation less than 0.5 Watt. The lack of transmit electronics and the relatively small transmit aperture also limit the transmit heat generation with respect to other devices [39]. Also, despite the missing elements in the receive aperture, our numerical study shows that the PSF limiting the resolution in the image of our probe is comparable with a fully populated receiver probe of the same dimensions. Our design, compared to [181] which uses the majority of elements to transmit and a sparse array to receive, achieves better receiving sensitivity and lower side-lobes.

The sensitivity variation range between the elements was found to be 0.97 dB for the transmit sub-array and 7.6 dB for the receive array, confirming the quality of the fabrication process. The higher sensitivity variations observed in our measurements is partly due to the incident beam of the single element transducer used as an external excitation which has about 2 dB variation over the 5 mm size of the receive aperture of the prototype. Moreover, the elements at the edges of the probe are also more prone to mechanical damages during the manufacturing process, increasing the variation range.

The transfer function of the single elements of the prototype shows a center frequency of 5.8 MHz and a fractional bandwidth of 67%. The reverberation signals that appear after the main signal in the time trace are caused by reflections from a thin foil which acts as an acoustic window to the water tank. The foil was not perfectly flat, and the transit time in the acoustic coupling gel between the probe and foil varied for different elements. This difference was observed in the different reverberation times in the time traces, and corresponding differences in dip-locations in the transfer functions. As such, this artifact is caused by the measurement setup, not by the probe itself.

The array has been mounted on top of an ASIC in order to reduce the electric signal losses that would otherwise occur between the acoustic stack and the mainframe. However, the

silicon layer of the ASIC (300 µm) has a very low acoustic attenuation, and can sustain traveling lateral waves with a shear component. By exciting an element, such waves will be generated in the silicon layer, and these will transport a portion of the acoustic energy into the neighboring elements or even into the element itself, when the wave is reflected back from the edges of the silicon layer. This mechanism effectively leads to acoustical cross-talk between the elements in the matrix array degrading the beam profile (Shabanimotlagh, et al. 2017). Similar problems have been reported in capacitive micromachined ultrasound transducers (CMUT) where the silicon substrate induces significant acoustic crosstalk between array elements [182]. Although some compensation signal processing for such crosstalk has been proposed in the CMUT field [183, 184], a more practical solution to the problem is to optimize the manufacturing process. Two methods have been proposed recently [127]: 1) Reducing the thickness of the silicon layer and adding an absorbing backing layer; 2) dicing the back side of the silicon layer underneath the ASIC. Although the effect of silicon (as an imperfect backing layer) on the acoustic stack has been partially addressed within our optimization process, we have not included any effects that lateral modes induced in the silicon layer might have on our array. We anticipate that reducing the thickness of the silicon layer and adding an absorbing backing layer will not only diminish the cross-talk but will also improve the bandwidth of the transducer.

The programmable gain settings of the LNA and the TGC signal conditioning circuit of the ASIC provide a total gain range of 54 dB, which results in the large overall acoustic dynamic receive range of 85 dB for our prototype. Thanks to this large receive dynamic range, small echo signals (as low as 5 Pa) can be detected by the receivers. Also, in our design, the separation of the transmit array from the low voltage receive electronics enables the transmit elements to be driven by high input voltages. The transmit efficiency of 6 kPa/V of the transmit array guarantees that a sufficiently large pressure (e.g. 600 kPa with an input voltage of 100 V) can be generated by the transmitters.

While the transmit sub-array of the prototype can be steered to any angle up to ±45°in both lateral and elevation directions, the receive sub-groups are designed to be pre-steered at five different angles in both lateral and elevation directions: 0°, ±17°, and ±37°; i.e., to 25 fixed angles in 3D space. The overall transmit-receive steering is successfully demonstrated for these angles and the opening angle of the overall beam profile is about 4°. The beam width of the single pre-steered receive groups is wide enough (44°) to support beamforming of many such beams within the overlap of transmit and receive. Hence, for a transmit-receive event steered to a certain angle, only a specific sub-volume around that angle was beamformed. Despite the receive grating lobes due to the sub-array pitch, the narrow opening angle of the transmit-receive beam guarantees significant reduction of the grating lobes in the final 3D image if an appropriate transmit-receive event is applied.

Our prototype with on-board micro-beamforming and a small central transmitter allows for multiline parallel beamforming at high framerate with a low number of channels within the limitations of the small aperture size of the transducer. Because of the architecture of our probe, existing 3D parallel beamforming techniques [185-188] were not suitable. Therefore, novel multiline 3D beamforming approaches were proposed that utilize the capabilities of the

prototype transducer to produce volumes at high frame rate with good image quality [189]. Results indicate that the proposed multiline 3D beamforming techniques with the prototype matrix transducer can produce volumes with good image quality at a maximum rate of 300 Hz, suitable for real-time pediatric 3D TEE. In the simulation, the width of point spread functions, lateral shift invariance and clutter level were similar to those using conventional single line acquisitions with a hypothetical, idealized matrix transducer of the same size. Our proposed method can produce volumes with -6 dB main lobe widths of ~ 4° and sidelobe levels lower than -20 dB, with a total opening angle of 90° × 90°.

Currently our prototype is mounted on a large PCB for acoustic characterization and therefore it is not suitable for (pre-)clinical use yet. In future work, a prototype of the probe will be assembled on the tip of a gastroscopic tube for (pre-)clinical validation.

8.5. Summary

In this chapter we have described the acoustic design, fabrication and characteristics of a PZT on CMOS 3D-TEE transducer capable of real-time 3D imaging. We have optimized the acoustic stack using finite element modeling (PZFlex). The 8 × 8 transmit sub-array has a transmit efficiency of 6 kPa/V at 30 mm and the single elements have a center frequency of 5.8 MHz and a –6 dB fractional bandwidth of 67%. The receive dynamic range is 85 dB with minimum and maximum detectable pressures of 5 Pa and 84 kPa. The micro-beamforming circuits within the ASIC effectively reduce the receive channel count to 96 receive lines, and the functionality of the sub-groups has been illustrated. The combined transmit-receive beams are successfully steered to the 25 pre-defined angles in 3D space to enable real-time 3D TEE with proper transmit-receive strategies.

Appendix

The beam profile of the external single element transducer was measured separately using the needle hydrophone at the similar distance (32 cm) away from the surface of the transducer and displayed in figure 8.9. The white square indicates the dimension of the matrix transducer in comparison to the incident acoustic wave. Considering the directivity of the needle hydrophone (see below) the acoustic wave received by the matrix transducer can be considered as a plane wave with amplitude variation of less than 2 dB.

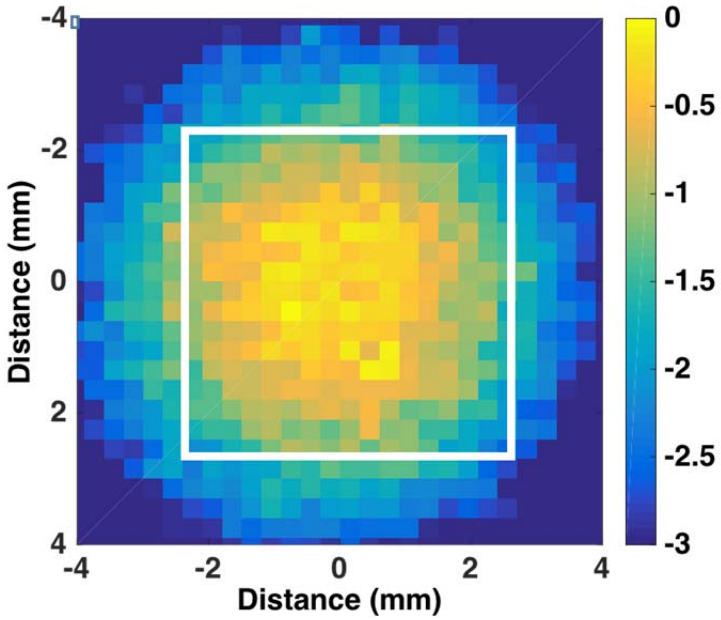

Figure 8.9. Beam profile of a single element 5 MHz transducer at the distance of 32 cm measured with a 0.2 mm needle hydrophone. The white square indicates the dimension of the matrix transducer in comparison to the incident acoustic wave.

Also, the hydrophone sensitivity decreases as it is rotated with respect to the normal position. For a needle hydrophone the directivity (D) as a function of the angle relative to the normal (θ) and the frequency of the incoming wave (f) can be estimated as follow (ONDA 2017):

$$D[\theta, f] = \frac{\left(1 + \cos\frac{\theta}{2}\right) 2J_1[ka \sin\theta]}{ka \sin\theta} \quad (1)$$

where J_1 is the Bessel function of the first kind, k is the wave number and a is the radius of the needle hydrophone. Using the formula above the directivity function of the 0.2 mm needle hydrophone at 5 MHz is estimated (figure 8.10) to be used for correcting the measurement in this paper.

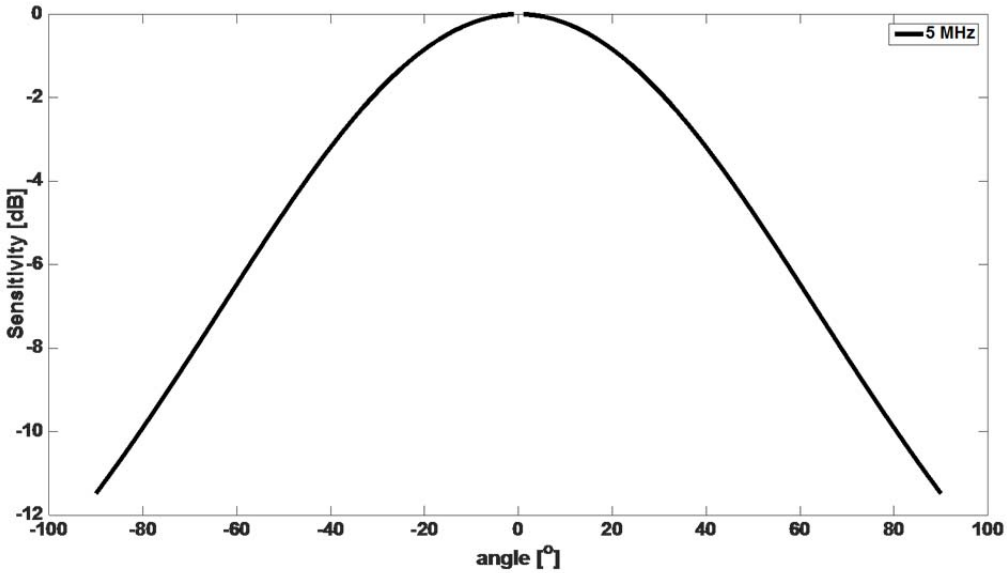

Figure 8.10. Calculated directivity pattern of the 0.2 mm needle hydrophone at 5 MHz.

The PSF of the current receiver was compared with the PSF of a fully populated 32 × 32 receiver, as shown in supplementary figure 8.11. The transfer function of the individual elements was obtained from the PZ-Flex simulations. The comparison of the two PSFs shows only a small difference in the way a single point is imaged by the receiver. The receiver is at focus at 90 mm along the axial direction.

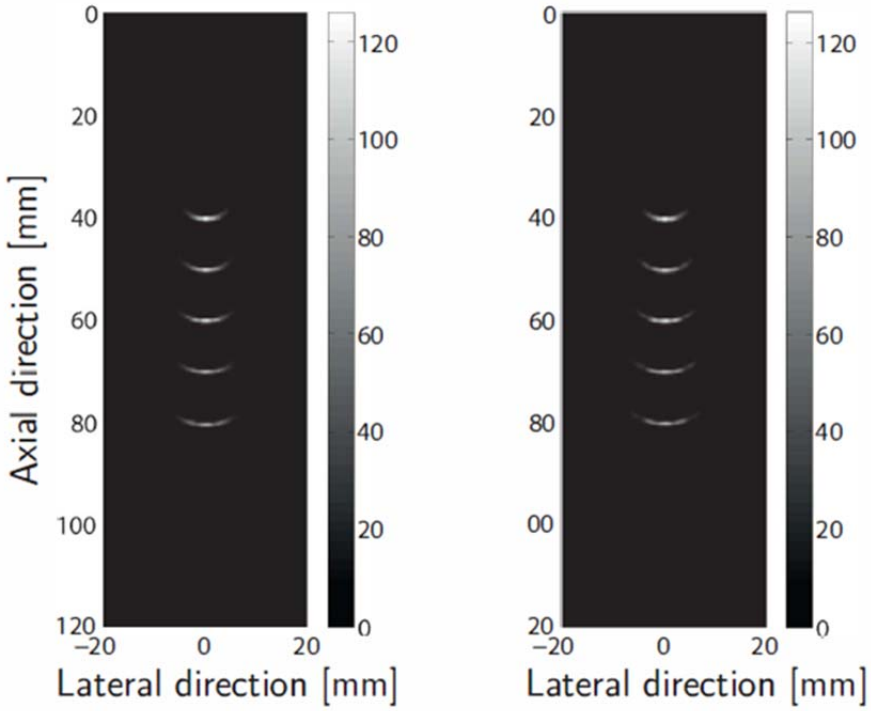

Figure 8.11. Comparison of the PSF of a fully populated receiver (left) and the current receiver (right).

The peak to peak output pressure recorded by the needle hydrophone at the distance of 30 mm as a function of the peak to peak input voltage is plotted in supplementary figure 8.12. The transmit pressure increases linearly by increasing the input pressure and the efficiency of the transmit array (8 × 8 elements) is 6 kPa/V.

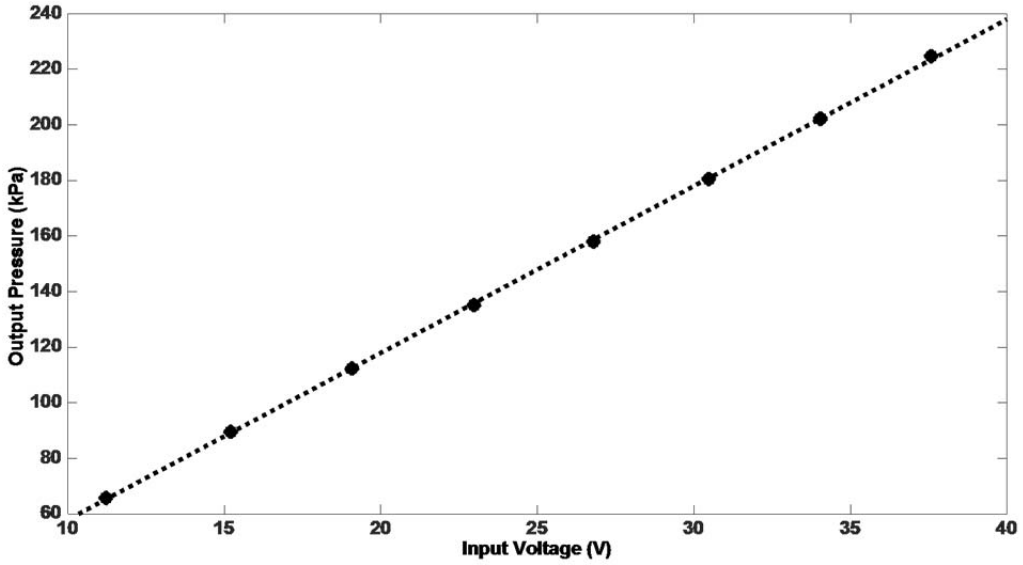

Figure 8.12. Generated peak to peak output pressure of the transmit array as a function of peak to peak input voltage.

CHAPTER 9

Discussions and Conclusions

We demonstrated ultrasound matrix transducers which could be used for real-time volumetric imaging. The probes contain >1000 transducer elements, which are directly mounted on top of an ASIC. The ASIC has the task of micro-beamforming, switching, selection of the aperture in transmit and receive, impedance matching, signal amplification, and data reduction to connect the transducer elements to the ultrasound machine. In this thesis, we demonstrated the mechanical design, fabrication, and acoustical characterization of such probes, with two specific applications in mind: carotid imaging with an external probe, and cardiac imaging with a TEE probe.

In clinics, there is a high demand for 3D ultrasound imaging, since anatomical structures, as well as all motions and blood flow under investigations, have components in all three dimensions. With conventional techniques for 3D imaging using 1D probes (mechanical sweeping, and freehand technique), the volume rate of the final 3D rendered images is not sufficient to track the motion and flow rate accurately. Another approach for 3D imaging was to select a limited number of elements in the 2D matrix to transmit and receive. Compared to other approaches, this technique has poor resolution. To overcome all of those limitations, this thesis demonstrates the integration of microelectronics and matrix transducer technology. The promising results of our work show that this approach is a suitable technology for 3D imaging in real-time.

9.1. Contributions to the physics of ultrasound transducers

The work presented in the chapters 2 to 4 in this thesis have brought new knowledge on the physics of transducer design and analysis from two specific aspects, which are discussed below:

9.1.1. Subdicing

The geometry of the ultrasound transducer element has a crucial effect on its electro-mechanical performance. The frequency of a transducer is chosen based on the depth of imaging for the organ under investigation. In general for high image quality a large aperture, and accordingly a large number of elements, is intended. On the other hand, for an efficient vibration, the width to thickness ratio of the element should be kept below 0.6 times wavelength, and this criterion limits the maximum width for the transducer element. This can be critical especially for high-frequency applications, where small elements are required. In chapter 2 of this thesis, we presented the subdicing as a solution to this limiting factor. We extensively explained the physical effect of subdicing on the mechanical vibration of an element, and explained how the optimal number of subdicing should be determined. In chapter 3 we have applied the subdicing solution to elements of a matrix transducer, and experimentally showed the improvement in the performance of the transducer obtained by subdicing.

9.1.2. Crosstalk

Crosstalk has two sources: electrical and mechanical. Mechanical crosstalk in an ultrasound transducer refers to the vibration of an element due to the excitation of the neighboring elements. Mechanical crosstalk has an important influence on the directivity pattern of a single element. In our approach, the ultrasound transducer elements are mounted directly on top of an ASIC. Since the ASIC is made of silicon, which is a hard and non-attenuating material, it can sustain traveling waves. When an element is excited, Lamb waves are generated in the ASIC and propagate through the whole chip. These waves couple to the front media through the neighboring elements, and generate extra peaks in the directivity plot. These peaks occur at angles which are related to the Lamb wave speed in the silicon. In chapter 4, we proposed two solutions to suppress this mechanical crosstalk. By reducing the thickness of the chip, the Lamb wave speeds converge to the Rayleigh wave, and this result in shifting the peaks to higher angles (i.e. to $>90^{o}$ in an ideal case). Simulation results showed that by having a proper backing material, with high attenuation, behind the ASIC the energy of the traveling wave is absorbed by the backing and the extra peaks are removed from the directivity plot. The second solution is to make subdices on the back side of the ASIC. In this way, the traveling waves inside the chip are disturbed and effectively they cancel out each other. This happens when the subdicing cuts are deep enough to avoid the Lamb wave propagation through the chip. We concluded that with a proper choice for the silicon thickness (in the first approach) or depth of cut (in the second approach), both solutions can be used to remove the extra peak from the directivity plot.

9.2. Clinical applications

9.2.1. Carotid imaging

Accurate assessment of carotid artery disease by measuring blood flow, plaque deformation and pulse wave velocity requires 3D information. The volume rates also should be high enough (> 1 kHz) to display the transient behavior along the arterial wall [77]. Building a transducer that is capable of providing 3D US imaging at such volume rates is challenging, especially when considering the large (> 20 mm) aperture and relatively high (> 5 MHz) frequency that is normally desired for carotid artery imaging. We have designed a dedicated ultrasound matrix transducer together with an ASIC for real-time 3D echography of carotid arteries. The ASIC is designed such that it can be scaled up by tiling multiple ASICs in a head-to-head and side-by-side fashion. A prototype of the PZT matrix transducer on a single ASIC was fabricated and tested in this thesis. The promising measurement results obtained from the characterization of the prototype encourage further effort on up-scaling for a larger aperture with a matrix of 2×10 ASICs containing ~20,000 transducer elements. Tiling the ASICs and manufacturing the matrix transducer on top, is challenging and needs further research and experiment. Since the PhD period has a limited time, this part is not included in this thesis. This the first time that such a probe is introduced, we foresee a lot of novel usages. We explain some of the applications below.

The blood flow in the cardiovascular system, and especially in the carotid artery is a complex 3D phenomenon. In the areas close to the bifurcation, short vortices happen within 100-200 ms. For an accurate assessment of the dynamics of the blood flow, 3D velocity data at hundreds of volumes per second is required [116, 123]. The presented matrix transducer is in principle capable of acquiring 3D data with such a high frame rate when it is programmed in plane wave imaging mode. In this thesis, we have obtained 3D images with 500 Hz volume rate. This volume rate is much higher than the state of the art approaches [19]. Still, to increase the frame rate, we can electronically step the imaging planes over two or more elements in reception. On the other hand, to improve the image quality through compounding, there is potential for steering the plane wave up-to $\pm 20°$, since the rows can be individually excited by the ultrasound machine. However, this will reduce the frame rate [124].

With the developed ASIC a variety of aperture selections could be employed for different image acquisition schemes. The probe has the potential to be programmed for imaging at different focal depths. By generating element configurations with different aperture size and combining the data, we can generate high image resolution at larger depths. This can be used in the assessment of carotid plaque growth with the high-resolution volumetric image. For this purpose, the plaque burden could be quantified by predicting the total plaque volume from the 3D ultrasound image, which is a more accurate approach than using the total plaque area from 2D ultrasound [125]. In applications where both frame rate and image quality are important, the dynamic linear array mode (electronic shifting of a specific aperture size in both transmit and receive) can be used. For example, multiple 3D images with high resolution within a heart cycle are required to track the plaque deformation and to find the mechanical forces caused by the blood flow [115]. One of the operational modes of our transducer is the

configuration of random element patterns. This mode can be utilized to generate different sparse arrays for 3D imaging. Usually, static sparse array transducers are designed to overcome the cable count limit imposed by ultrasound machines, while still having a 2D matrix array with a large aperture [19, 28, 31]. However, in our case, we can also dynamically generate a set of known sparse arrays. This yields the electronic version of a recent approach using a single element transducer with a coded mask [126]. With this technique, the number of measurements required to reconstruct a volumetric image can be drastically reduced.

This transducer is basically designed for the carotid artery imaging application. However, since it is an external probe there is no restriction on using it for other organs. For instance, our probe could be used to provide multiple volumetric images during a pulsation period to evaluate the local displacements, strain parameters, and in general the hemodynamic changes in the abdominal aortic valve, and to analyze the rupture risk on patients with an abdominal aortic aneurysm. Abdominal aortic aneurysm rupture which is caused by mechanical vascular tissue failure, are conventionally assessed with biomechanical properties of the vessel wall, through 2D cross-sectional image of the aorta, where the stiffness of the aorta is calculated based on the measurement of the change in the diameter of the aorta during the pulsation and the pulse pressure [190]. With the developments in the ultrasound techniques such as tissue Doppler imaging or 2D speckle tracking, it is possible to have a more detailed study of arterial wall motion and provide a more accurate evaluation of the strain parameters along the aorta. Such measurements might be sufficient to analyze a healthy aorta, but aneurysms are complex 3D structures and their biomechanical properties vary spatially [191]. On the other hand, for the quantitative characterization of tumors, the developed probe could be used for 3D real-time imaging and use contrast agents to increase the sensitivity and visualizing the small vessels and veins. Furthermore, with high frame rate data acquisition capability in 3D, it is possible to render complex flow patterns over an imaging view using vector imaging. All of these applications seems now possible with the developed probe.

9.2.2. Transoesophageal Echocardiography

Oldelft Ultrasound has recently introduced the microMulti TEE transducer (μTEE) primarily for neonatal and pediatric patients. The μTEE probe has a phased array including 32 transducer elements and can produce 2D images. The probe has proven to be very useful in pediatric patients mainly because of the small size and excellent images [62-64]. Furthermore, this probe has been used for monitoring adults undergoing minimally-invasive interventions [65, 66]. Additionally, the μTEE probe is useful for diagnosing hemodynamically unstable patients both in routine preoperative cases and in postoperative critical care [67].

For 3D TEE in adults, there are a number of commercially available matrix array TEE probes (X7-2t from Philips Ultrasound, Bothell, WA [68], V5M TEE from Siemens Healthcare GmbH, Erlangen, Germany [69], and 6VT-D from General Electric Healthcare, Amersham, U.K. [70]). These matrix TEE probes are capable of real-time acquisition and live 3D display. However, they are much larger than the μTEE probes and therefore cannot be used for pediatric patients. Also in adults, due to patient discomfort, they are not suitable for

long-term monitoring without full anesthesia. Whereas a transnasal insertion of the µTEE probe has shown to be tolerated by patients for up to 24 hours [71, 72].

Several studies have shown that real-time 3D imaging is more beneficial than 2D imaging in most cardiac conditions [73, 74] because of its superior visualization of different 3D structures in the heart. Even though the µTEE probe is very useful for real-time 2D imaging, it is incapable of performing real-time 3D imaging on the heart. It should be noted that it is possible to reconstruct a 3D image from 2D TEE images (also for the µTEE probe) by rotating the imaging plane and recording over many heart cycles, but that procedure requires offline processing of sequential acquisitions gated to ECG [75]. These lengthy acquisitions and the post-processing of the acquired data increase the duration of the examination and also suffer from radial artifacts [76]. Therefore, it does not meet the needs for real-time 3D imaging.

We have developed a matrix TEE transducer with the size of the µTEE probe, and imaging capabilities of 3D TEE probe. The results in chapters 7 and 8 explain the design, fabrication, and characterization of two prototypes of miniaturized matrix transducer suitable for 3D TEE in pediatric patients as well as for transnasal use in adults for long-term monitoring. The transducer consists of a receive aperture with an effective aperture area similar to the µTEE (5 × 5 mm^2) and a very small central transmitter (1.2 × 1.2 mm^2) capable of producing wide transmit beams. It is integrated on an ASIC for applying micro-beamforming to pre-steer the receive beams in 3D space. Thus, the micro-beamformers help in connecting the required elements (~1000) using a limited number of cables (~130) that can fit in the gastroscopic tube and can be connected to any ultrasound system.

9.2.3. Other potential applications

In this thesis, we aimed to develop matrix transducers for two specific clinical applications: imaging of the carotid artery, and transoesophageal echocardiography (TEE). However, the developed technology for fabrication of the transducer elements on top of an ASIC can also be employed for other applications. Some of the potential applications are described below:

- **Real-time 3D intracardiac echocardiography:** Many cardiovascular problems such as rhythm-disorder treatments or catheter-based valve replacement, can be treated using minimally invasive interventions. Accurate visualization is crucial for the success and effectiveness of these interventions. Since these procedures are complex, they could benefit from real-time 3D visualization. With a similar approach to the developed technology, a matrix transducer together with an ASIC could be designed to generate 3D images of the heart, before, during and after the intervention procedure.

- **Monitoring the brain perfusion:** Researches show that approximately 10% of the children are born prematurely. With the improvements in fetal and neonatal care, the survival rate has significantly improved. Yet, they regularly show neurodevelopmental problems, which could be the origin of diseases with lifelong burdens. The main reason for these problems is due to inappropriate brain perfusion during and after delivery.

Keeping adequate blood flow and oxygenation in the underdeveloped brain is crucial to normal brain development. Several treatments approaches could prevent or minimize the brain damage. There is a high demand for a safe and accessible monitoring system that can assess the brain perfusion and control the brain development of the baby throughout the incubation period in the hospital. Ultrasound matrix transducers could be a good candidate for 3D visualization of the blood perfusion in preterm babies. With the developed technology in this thesis for manufacturing the matrix transducers, developing a probe for such an application could be an interesting topic.

- **Ultrasonic flow meter:** Ultrasonic flow meters are used to measure flow in different industrial applications. The performance of most of these flowmeters are based on measuring the traveling time of an ultrasound pulse through the fluid. One approach is by clamping two transducers on the pipe. These type of flow meters are attractive since the installation does not need to cut the pipe or shut down the flow, however, their stability is limited, and their installation requires complex alignment of the transducers. It would be interesting to design a flow meter using the matrix transducers, which consist of many transducer elements that can be used in transmit and receive. These elements can be used for electronic steering of the ultrasound beam, which enables the automatic alignment and calibration of the measurement device. This technology could highly improve the accuracy and applicability of these sensors.

9.3. Recommendations for future research

We have developed a new technique for making ultrasound matrix transducer for 3D ultrasound imaging in real-time. While the results of this thesis have shown the applicability of the technique, several suggestions could be made to continue the current research and to further improve the technology. Some specific suggestions are given below:

- **Tiled array transducer for carotid imaging:** We have designed an ASIC suitable for 3D imaging of carotid arteries. We fabricated a prototype of the transducer on a single ASIC and characterized the performance of the chip, electronics system, and mechanical properties of the individual pillars. The characterization results are presented in chapters 5 and 6. In general, the electrical and acoustical measurement results are in accordance with designed values. The results are promising for further up-scaling to a big aperture by tiling a matrix of 2×10 ASICs including ~ 20000 transducer elements, which is appropriate for a carotid arteries imaging. The design of the transducer is such that it allows tiling of multiple ASIC next to each other in head-to-head and side-by-side fashion. However, the alignment between the ASICs is vital during the fabrication process. For upscaling the transducer a precise approach should be developed for alignment. These need further research and validation, to make this product appropriate for clinical use.

- **Miniaturizing the transducer setup for TEE:** In chapter 8 we described the acoustic design, fabrication, and characteristics of a PZT on CMOS 3D-TEE transducer capable of 3D imaging in real time. The performance of the micro-beamformers, the electromechanical properties of the transducer elements (i.e. the transmit and receive efficiency, the bandwidth, and the dynamic range), and the 3D imaging capabilities of the whole transducer was examined in different measurements. The results show a successful design and fabrication of the transducer. Currently, the transducer is made on a 10 cm × 10 cm wide daughterboard PCB, which is very larger than the requirements for the intended application. This bigger setup was basically designed to have a lot of access points to different paths/signals to verify and optimize the performance of the whole transducer. Before this probe can be tested in animals or in clinical applications the probe and the connecting cables should be accommodated in an appropriate tube.

- **Crosstalk reduction with subdicing the silicon:** In chapter 4 the physics of the acoustical crosstalk in an array of transducer elements were discussed, and two solutions were proposed to reduce the crosstalk. These solutions were tested in simulations, but an experimental validation is crucial. To follow this study, it would be interesting to apply these solutions on a real transducer. Since all of the electronics circuits are designed on <10 μm depth from the silicon surface, these solutions should not harm the electronics of the chip. However, in order to make subdices, or to reduce the thickness, mechanical dicing or grinding needs to be done. These mechanical actions may damage the ASIC. Therefore, a research needs to be designed to find optimal dicing/grinding procedure to have minimal effect on the electronics of the silicon. We expect to reduce the acoustical crosstalk with this approach, and this improvement would highly impact the final images obtained from the matrix transducer.

- **Piezoelectric ceramic material:** The technology of manufacturing the piezoelectric materials have improved in the past two decades. The performance of a transducer is highly influenced by the properties of the piezoelectric materials used in their fabrication. Selection of an appropriate material for a transducer is based on many factors, including material properties, transducer area, and frequency of operation. In general, for the transducer elements with a small aperture, a piezoelectric material with high dielectric permittivity is needed. Piezoelectric single crystals have been developed with high coupling factor, and permittivity, which makes them a good candidate for medical imaging applications. However since the Curie temperature of these materials is low, and they are more brittle than the conventional PZT ceramics, the application of them is more limited. Piezoelectric polymers, such as PVDF materials which are flexible and low cost, have been used in many applications, especially when a wideband frequency range is needed. These polymers have high sensitivity in receive but they have low transmit efficiency, and they are mostly used in single element transducer designs. Piezoelectric composite materials have superior performance compared to bulk piezoelectric materials. Compared to PZT ceramics, composite materials have a higher coupling factor in plate

mode, and lower acoustic impedance which better matches to the human body. All of these materials have their pros and cons in different applications. On the other hand, the electromechanical coupling factor of the piezoelectric material depends on the boundary conditions and therefore the geometry of the transducer element. Usually, the piezoelectric constant in the rod mode is different than in the plate mode. Since elements in ultrasound matrix transducers have small surface area it would be interesting to compare the performance of different piezoelectric materials with each other. This comparison is fair when the fabrication procedure of the matrix transducer (especially the dicing parameters) is optimized for each type of material. The results of such an analysis will have a high impact in the research field.

Bibliography

1. S.M. Leinders, *Characterization of a novel optical micro-machined ultrasound transducer*, in *ImPhys/Acoustical Wavefield Imaging*. 2017, Delft University of Technology: Delft, The Netherlands.
2. P.L.M.J. van Neer, *Ultrasonic superharmonic imaging*, in *Biomedical Engineering*. 2010, Erasmus Medical Center: Rotterdam, The Netherlands.
3. T. Szabo, "Diagnostic Ultrasound Imaging: Inside Out", 2013, *Academic Press*.
4. S. Campbell, "A Short History of Sonography in Obstetrics and Gynaecology", *Facts, Views and Vision in ObGyn*, 2013, vol. **5**, no. 3, pp. 213-229.
5. J.H.P. Groen, "Piezoelectric Materials and Applications", 2013, *The Netherlands*, *Stichting Applied Piezo*.
6. M. Ainslie, "Principles of Sonar Performance Modelling", Springer Praxis Books, 2010, *Springer-Verlag Berlin Heidelberg*.
7. K. Graff, "Historical highlights in ultrasonics", *IEEE International Frequency Control Symposium and Exposition*, 2004.
8. A. Kurjak, "Ultrasound scanning – Prof. Ian Donald (1910–1987)", *European Journal of Obstetrics & Gynecology and Reproductive Biology*, 2000, vol. **90**, no. 2, pp. 187-189.
9. J. Seo and Y.-s. Kim, "Ultrasound imaging and beyond: recent advances in medical ultrasound", *Biomedical Engineering Letters*, 2017, vol. **7**, no. 2, pp. 57-58.
10. W. Lee and Y. Roh, "Ultrasonic transducers for medical diagnostic imaging", *Biomedical Engineering Letters*, 2017, vol. **7**, no. 2, pp. 91-97.
11. R.S.C. Cobbold, "Foundations of Biomedical Ultrasound ", 2007, *Oxford University Press*.
12. C.S. Desilets, J.D. Fraser and G.S. Kino, "The design of efficient broad-band piezoelectric transducers", *IEEE Transactions on Sonics and Ultrasonics*, 1978, vol. **25**, no. 3, pp. 115-125.
13. K. Itsumi, Y. Hosono, N. Yamamoto and Y. Yamashita, "Low acoustic attenuation silicone rubber lens for medical ultrasonic array probe", *IEEE Transactions on Ultrasonics, Ferroelectrics, and Frequency Control*, 2009, vol. **56**, no. 4, pp. 870-874.
14. L. Wonseok and R. Yongrae, "New Design of the Kerfs of an Ultrasonic Two-Dimensional Array Transducer to Minimize Cross-Talk", *Japanese Journal of Applied Physics*, 2010, vol. **49**, no. 7S (07HD06), pp.
15. J. Janjic, M. Shabanimotlagh, G.v. Soest, A.F.W.v.d. Steen, N.d. Jong and M.D. Verweij, "Improving the Performance of a 1-D Ultrasound Transducer Array by Subdicing", *IEEE Transactions on Ultrasonics, Ferroelectrics, and Frequency Control*, 2016, vol. **63**, no. 8, pp. 1161-1171.
16. L. Alpinion Medical Systems Co., *E-Cube 15 Brochure*. 2015: Korea.
17. F. Aaron, B.D. Dónal and H.N. Cardinal, "Three-dimensional ultrasound imaging", *Physics in Medicine and Biology*, 2001, vol. **46**, no. 5, pp. R67.
18. R.W. Prager, U.Z. Ijaz, A.H. Gee and G.M. Treece., "Three-dimensional ultrasound imaging", *Proceedings of the Institution of Mechanical Engineers. Part H, Journal of engineering in medicine*, 2010, vol. **224**, no. 2, pp. 193-223.
19. Q. Huang and Z. Zeng, "A Review on Real-Time 3D Ultrasound Imaging Technology", *BioMed Research International*, 2017, vol. **2017**, no. 6027029, pp. 1-20.
20. P.A. Picot, D.W. Rickey, R. Mitchell, R.N. Rankin and A. Fenster, "Three-dimensional colour doppler imaging", *Ultrasound in Medicine and Biology*, 1993, vol. **19**, no. 2, pp. 95-104.
21. D.B. Downey and A. Fenster, "Vascular imaging with a three-dimensional power Doppler system", *American Journal of Roentgenology*, 1995, vol. **165**, no. 3, pp. 665-668.
22. Z. Guo and A. Fenster, "Three-dimensional power Doppler imaging: A phantom study to quantify vessel stenosis", *Ultrasound in Medicine and Biology*, 1996, vol. **22**, no. 8, pp. 1059-1069.
23. H. Gao, Q. Huang, X. Xu and X. Li, "Wireless and sensorless 3D ultrasound imaging", *Neurocomputing*, 2016, vol. **195**, no. 159-171.

24. J.N. Welch, J.A. Johnson, M.R. Bax, R. Badr and R. Shahidi, "A real-time freehand 3D ultrasound system for image-guided surgery", *IEEE Ultrasonics Symposium*, 2000.
25. R.W. Prager, A. Gee and L. Berman, "Stradx: real-time acquisition and visualization of freehand three-dimensional ultrasound", *Medical Image Analysis*, 1999, vol. **3**, no. 2, pp. 129-140.
26. E.A. Geiser, L.G. Christie, D.A. Conetta, C.R. Conti and G.S. Gossman, "A mechanical arm for spatial registration of two-dimensional echocardiographic sections", *Catheterization and Cardiovascular Diagnosis*, 1982, vol. **8**, no. 1, pp. 89-101.
27. D.L. King, D.L. King and M.Y. Shao, "Three-dimensional spatial registration and interactive display of position and orientation of real-time ultrasound images", *Journal of Ultrasound in Medicine*, 1990, vol. **9**, no. 9, pp. 525-532.
28. E. Roux, A. Ramalli, M. Robini, H. Liebgott, C. Cachard and P. Tortoli, "Spiral array inspired multi-depth cost function for 2D sparse array optimization", *IEEE International Ultrasonics Symposium*, 2015.
29. S.W. Smith, W. Lee, E.D. Light, J.T. Yen, P. Wolf and S. Idriss, "Two dimensional arrays for 3-D ultrasound imaging", *IEEE Ultrasonics Symposium*, 2002.
30. K. Erikson, A. Hairston, A. Nicoli, J. Stockwell and T. White, "A 128 x 128 (16K) Ultrasonic Transducer Hybrid Array", in Acoustical Imaging, 1997, *Springer US Boston, MA*.
31. E. Nicholas, P. Aki, S. Junho and H. Kullervo, "The utility of sparse 2D fully electronically steerable focused ultrasound phased arrays for thermal surgery: a simulation study", *Physics in Medicine and Biology*, 2011, vol. **56**, no. 15, pp. 4913-4932.
32. P. Ramaekers, M.d. Greef, R. Berriet, C.T.W. Moonen and M. Ries, "Evaluation of a novel therapeutic focused ultrasound transducer based on Fermat's spiral", *Physics in Medicine & Biology*, 2017, vol. **62**, no. 12, pp. 5021.
33. J.T. Yen, J.P. Steinberg and S.W. Smith, "Sparse 2-D array design for real time rectilinear volumetric imaging", *IEEE Transactions on Ultrasonics, Ferroelectrics, and Frequency Control*, 2000, vol. **47**, no. 1, pp. 93-110.
34. D. Wildes, W. Lee, B. Haider, S. Cogan, K. Sundaresan, D.M. Mills, C. Yetter, P.H. Hart, C.R. Haun, M. Concepcion, J. Kirkhorn and M. Bitoun, "4-D ICE: A 2-D Array Transducer With Integrated ASIC in a 10-Fr Catheter for Real-Time 3-D Intracardiac Echocardiography", *IEEE Transactions on Ultrasonics, Ferroelectrics, and Frequency Control*, 2016, vol. **63**, no. 12, pp. 2159-2173.
35. I.O. Wygant, N.S. Jamal, H.J. Lee, A. Nikoozadeh, O. Oralkan, M. Karaman and B.T. Khuri-yakub, "An integrated circuit with transmit beamforming flip-chip bonded to a 2-D CMUT array for 3-D ultrasound imaging", *IEEE Transactions on Ultrasonics, Ferroelectrics, and Frequency Control*, 2009, vol. **56**, no. 10, pp. 2145-2156.
36. C. Chen, Z. Chen, D. Bera, S.B. Raghunathan, M. Shabanimotlagh, E. Noothout, Z.Y. Chang, J. Ponte, C. Prins, H.J. Vos, J.G. Bosch, M.D. Verweij, N.d. Jong and M.A.P. Pertijs, "A Front-End ASIC With Receive Sub-array Beamforming Integrated With a 32 x 32 PZT Matrix Transducer for 3-D Transesophageal Echocardiography", *IEEE Journal of Solid-State Circuits*, 2017, vol. **52**, no. 4, pp. 994-1006.
37. H.g. Kang, S. Bae, P. Kim, J. Park, G. Lee, W. Jung, M. Park, K. Kim, W. Lee and T.K. Song, "Column-based micro-beamformer for improved 2D beamforming using a matrix array transducer", *IEEE Biomedical Circuits and Systems Conference*, 2015.
38. M.F. Rasmussen and J.A. Jensen, "3-D ultrasound imaging performance of a row-column addressed 2-D array transducer: A measurement study", *IEEE International Ultrasonics Symposium* 2013.
39. K. Chen, L. Hae-Seung and C.G. Sodini, "A Column-Row-Parallel ASIC architecture for 3D wearable / portable medical ultrasonic imaging", *Symposium on VLSI Circuits Digest of Technical Papers*, 2014.
40. M. Flesch, M. Pernot, J. Provost, G. Ferin, A. Nguyen-Dinh, M. Tanter and T. Deffieux, "4D in vivo ultrafast ultrasound imaging using a row-column addressed matrix and coherently-

compounded orthogonal plane waves", *Physics in Medicine and Biology*, 2017, vol. **62**, no. 11, pp. 4571-4588.

41. R. Fisher, K. Thomenius, R. Wodnicki, R. Thomas, S. Cogan, C. Hazard, W. Lee, D. Mills, B. Khuri-Yakub, A. Ergun and G. Yaralioglu, "Reconfigurable arrays for portable ultrasound", *IEEE Ultrasonics Symposium*, 2005.
42. S. Tamano, T. Kobayashi, S. Shuzou, H. Kenji, J. Sakano and T. Azuma, "3D ultrasound imaging system using Fresnel ring array & high voltage multiplexer IC", *IEEE Ultrasonics Symposium*, 2004.
43. C.R. Hazard, R.A. Fisher, D.M. Mills, L.S. Smith, K.E. Thomenius and R.G. Wodnicki, "Annular array beamforming for 2D arrays with reduced system channels", *IEEE Symposium on Ultrasonics*, 2003.
44. B. Savord and R. Solomon, "Fully sampled matrix transducer for real time 3D ultrasonic imaging", *IEEE Symposium on Ultrasonics*, 2003.
45. C. Chen, S.B. Raghunathan, Z. Yu, M. Shabanimotlagh, Z. Chen, Z.y. Chang, S. Blaak, C. Prins, J. Ponte, E. Noothout, H.J. Vos, J.G. Bosch, M.D. Verweij, N.d. Jong and M.A.P. Pertijs, "A Prototype PZT Matrix Transducer With Low-Power Integrated Receive ASIC for 3-D Transesophageal Echocardiography", *IEEE Transactions on Ultrasonics, Ferroelectrics, and Frequency Control*, 2016, vol. **63**, no. 1, pp. 47-59.
46. D. Mozaffarian, E.J. Benjamin, A.S. Go, D.K. Arnett, M.J. Blaha, M. Cushman, S.R. Das, S. de Ferranti, J.-P. Després, H.J. Fullerton, V.J. Howard, M.D. Huffman, C.R. Isasi, M.C. Jiménez, S.E. Judd, B.M. Kissela, J.H. Lichtman, L.D. Lisabeth, S. Liu, R.H. Mackey, D.J. Magid, D.K. McGuire, E.R. Mohler, C.S. Moy, P. Muntner, M.E. Mussolino, K. Nasir, R.W. Neumar, G. Nichol, L. Palaniappan, D.K. Pandey, M.J. Reeves, C.J. Rodriguez, W. Rosamond, P.D. Sorlie, J. Stein, A. Towfighi, T.N. Turan, S.S. Virani, D. Woo, R.W. Yeh and M.B. Turner, "Executive Summary: Heart Disease and Stroke Statistics - 2016 Update", *Circulation*, 2016, vol. **133**, no. 4, pp. 447-454.
47. J.E. Wilhjelm, "Conventional and compound scanning of the Carotid artery", in Vascular Ultrasound, 2003, *Springer Japan Tokyo*.
48. A. Pandya and A. Gupta, "Improving imaging to optimize screening strategies for carotid artery stenosis", *Clinical Imaging*, 2016, vol. **40**, no. 2, pp. 276-278.
49. G.W. Petty, R.D. Brown, J.P. Whisnant, J.D. Sicks, W.M. O'Fallon and D.O. Wiebers, "Ischemic Stroke Subtypes", *Stroke*, 1999, vol. **30**, no. 12, pp. 2513-2516.
50. B.J. Schaller, "Imaging of Carotid Artery Stenosis", 2007, *Vienna*, *Springer*.
51. H.C. Stary, A.B. Chandler, S. Glagov, J.R. Guyton, W. Insull, M.E. Rosenfeld, S.A. Schaffer, C.J. Schwartz, W.D. Wagner and R.W. Wissler, "A definition of initial, fatty streak, and intermediate lesions of atherosclerosis. A report from the Committee on Vascular Lesions of the Council on Arteriosclerosis, American Heart Association", *Circulation*, 1994, vol. **89**, no. 5, pp. 2462-2478.
52. I. Kallikazaros, C. Tsioufis, S. Sideris, C. Stefanadis and P. Toutouzas, "Carotid Artery Disease as a Marker for the Presence of Severe Coronary Artery Disease in Patients Evaluated for Chest Pain", *Stroke*, 1999, vol. **30**, no. 5, pp. 1002-1007.
53. T.E. Craven, J.E. Ryu, M.A. Espeland, F.R. Kahl, W.M. McKinney, J.F. Toole, M.R. McMahan, C.J. Thompson, G. Heiss and J.R. Crouse, "Evaluation of the associations between carotid artery atherosclerosis and coronary artery stenosis. A case-control study", *Circulation*, 1990, vol. **82**, no. 4, pp. 1230-1242.
54. T.H. Park, "Evaluation of Carotid Plaque Using Ultrasound Imaging", *Journal of Cardiovascular Ultrasound*, 2016, vol. **24**, no. 2, pp. 91-95.
55. H.A. Reinhold and M.P. West, "Chapter 6 - Nervous System", in Acute Care Handbook for Physical Therapists (Fourth Edition), 2014, *W.B. Saunders St. Louis*.
56. T. Adla and R. Adlova, "Multimodality Imaging of Carotid Stenosis", *The International Journal of Angiology: Official Publication of the International College of Angiology, Inc*, 2015, vol. **24**, no. 3, pp. 179-184.

57. R.G.P. Shah;, "Echocardiography of the aortic root", *Investigative Radiology*, 1968, vol. **3**, no. 5, pp. 356-366.
58. M.P.G.O. Helge, "Contrast-enhanced and targeted ultrasound", *World journal of gastroenterology*, 2011, vol. **17**, no. 1, pp. 28-41.
59. W.D. Hall, J.W. Hurst and H.K. Walker, "The Origins of the History and Physical Examination", 1990, *Boston: Butterworths*.
60. A.L. Klibanov, "Ultrasound Contrast Agents: Development of the Field and Current Status", in Contrast Agents II: Optical, Ultrasound, X-Ray and Radiopharmaceutical Imaging, 2002, *Springer Berlin Heidelberg Berlin, Heidelberg*.
61. S. Kaul, "Myocardial Contrast Echocardiography", *Circulation*, 2008, vol. **118**, no. 3, pp. 291-308.
62. M. Lang Roberto and V. Mor-Avi, "Clinical utility of contrast-enhanced echocardiography", *Clinical Cardiology*, 2009, vol. **29**, no. S1, pp. 15-25.
63. J. Shalhoub, D.R.J. Owen, T.D. Gauthier, C. Monaco, E. Leen and A.H. Davies, "The use of contrast enhanced ultrasound in carotid arterial disease", *European journal of vascular and endovascular surgery: the official journal of the European Society for Vascular Surgery*, 2010, vol. **39**, no. 4, pp. 381-387.
64. S.I. Jang and D.K. Lee, "Contrast-enhanced endoscopic ultrasonography: advance and current status", *Ultrasonography (Seoul, Korea)*, 2014, vol. **33**, no. 3, pp. 161-169.
65. C.V. Neciu, B. Radu, C. Liliana, A.F. Badea and I. Opincariu, "Oral and I.V. contrast enhanced ultrasonography of the digestive tract--a useful completion of the B-mode examination: a literature review and an exhaustive illustration through images", *Medical ultrasonography*, 2015, vol. **17**, no. 1, pp. 62-73.
66. K. Kooiman, H.J. Vos, M. Versluis and N. de Jong, "Acoustic behavior of microbubbles and implications for drug delivery", *Advanced Drug Delivery Reviews*, 2014, vol. **72**, no. 28-48.
67. E. Stride, "Physical principles of microbubbles for ultrasound imaging and therapy", *Cerebrovasc Dis*, 2009, vol. **27**, no. 2, pp. 1-13.
68. I. Lentacker, I. De Cock, R. Deckers, S.C. De Smedt and C.T.W. Moonen, "Understanding ultrasound induced sonoporation: Definitions and underlying mechanisms", *Advanced Drug Delivery Reviews*, 2014, vol. **72**, no. 49-64.
69. J. Wu and W.L. Nyborg, "Ultrasound, cavitation bubbles and their interaction with cells", *Advanced Drug Delivery Reviews*, 2008, vol. **60**, no. 10, pp. 1103-1116.
70. S. Hernot and A.L. Klibanov, "Microbubbles in ultrasound-triggered drug and gene delivery", *Advanced drug delivery reviews* 2008, vol. **60**, no. 10, pp. 1153-1166.
71. A.L. Klibanov, "Microbubble contrast agents: targeted ultrasound imaging and ultrasound-assisted drug-delivery applications", *Investigative Radiology*, 2006, vol. **41**, no. 3, pp. 354-362.
72. K.W. Ferrara, "Driving delivery vehicles with ultrasound", *Advanced Drug Delivery Reviews*, 2008, vol. **60**, no. 10, pp. 1097-1102.
73. J.B. Fowlkes, O.D. Kripfgans and P.L. Carson, "Microbubbles for ultrasound diagnosis and therapy", *IEEE International Symposium on Biomedical Imaging: Nano to Macro*, 2004.
74. A. Zeghimi, J.M. Escoffre and A. Bouakaz, "Role of endocytosis in sonoporation-mediated membrane permeabilization and uptake of small molecules: a electron microscopy study", *Physical Biology*, 2015, vol. **12**, no. 6, pp. 066007.
75. Y. Hu, J.M.F. Wan and A.C.H. Yu, "Membrane Perforation and Recovery Dynamics in Microbubble-Mediated Sonoporation", *Ultrasound in Medicine and Biology*, 2013, vol. **39**, no. 12, pp. 2393-2405.
76. M. Scatena and C. Giachelli, "The alpha;v;beta;3 Integrin, NF-kapa;B, Osteoprotegerin Endothelial Cell Survival Pathway", *Trends in Cardiovascular Medicine*, 2002, vol. **12**, no. 2, pp. 83-88.
77. P. Kruizinga, F. Mastik, S.C.H. van den Oord, A.F.L. Schinkel, J.G. Bosch, N. de Jong, G. van Soest and A.F.W. van der Steen, "High-Definition Imaging of Carotid Artery Wall Dynamics", *Ultrasound in Medicine and Biology*, 2014, vol. **40**, no. 10, pp. 2392-2403.

78. N. de Jong, N. Bom, J. Souquet and G. Faber, "Vibration modes, matching layers and grating lobes"*, Ultrasonics*, 1985, vol. **23**, no. 4, pp. 176-182.
79. A.D. Pierce, "Acoustics: An Introduction to Its Physical Principles and Applications", 1991, *Acoustical Society of America*.
80. J.P. Arenas, "Numerical computation of the sound radiation from a planar baffled vibrating surface"*, Journal of Computational Acoustics*, 2008, vol. **16**, no. 03, pp. 321-341.
81. M.R.J.R.J. McGough, "Using FOCUS to determine the radiation impedance for square transducers", *International Symposium on Therapeutic Ultrasound*, 2012, New York, United States, American Institute of Physics.
82. J. Janjic, M. Shabanimotlagh, M.D. Verweij, G.v. Soest, A.F.W.v.d. Steen and N.d. Jong, "Quantifying the effect of subdicing on element vibration in ultrasound transducers", *IEEE International Ultrasonics Symposium*, 2015.
83. R.E. McKeighen, *Design guidelines for medical ultrasonic arrays*, in *Medical Imaging: Ultrasonic Transducer Engineering*. 1998, Proceedings of SPIE - The International Society for Optical Engineering: San Diego, CA, United States. p. 2-18.
84. Q. Wenkang and C. Wenwu, "Finite element study on 1-D array transducer design"*, IEEE Transactions on Ultrasonics, Ferroelectrics, and Frequency Control*, 2000, vol. **47**, no. 4, pp. 949-955.
85. M.E. Frijlink and L. Spicci, "The effect of oblique sub-dicing on acoustic performance", *IEEE International Ultrasonics Symposium*, 2012.
86. W. Xia, D. Piras, J.C.G. van Hespen, S. van Veldhoven, C. Prins, T.G. van Leeuwen, W. Steenbergen and S. Manohar, "An optimized ultrasound detector for photoacoustic breast tomography"*, Medical Physics*, 2013, vol. **40**, no. 3, pp. 032901 - 13 pages.
87. J.F. Guess, C.G. Oakley, S.J. Douglas and R.D. Morgan, "Cross-talk paths in array transducers", *IEEE Ultrasonics Symposium*, 1995.
88. D.T. Blackstock, "Fundamentals of Physical Acoustics", 2000, *Hoboken, NJ, USA*, *John Wiley & Sons*.
89. K.K. Shung, "Diagnostic Ultrasound: Imaging and Blood Flow Measurements", 2006, *Boca Raton, FL, USA*, *CRC Press, Taylor & Francis Group*.
90. Y. Zhou, "Principles and Applications of Therapeutic Ultrasound in Healthcare", 2015, *CRC Press*.
91. P.L.M.J. van Neer, G. Matte, J. Sijl, J.M.G. Borsboom and N. de Jong, "Transfer functions of US transducers for harmonic imaging and bubble responses"*, Ultrasonics*, 2007, vol. **46**, no. 4, pp. 336-340.
92. E. Vicenzini, S. Pro, G. Sirimarco, P. Pulitano, O. Mecarelli, G.L. Lenzi and V. Di Piero, "Three dimensional imaging of carotid arteries: Advantages and pitfalls of ultrasound investigations"*, Perspectives in Medicine*, 2012, vol. **1**, no. 1, pp. 82-85.
93. M.W. Docter, R.H.S.H. Beurskens, G. Ferin, P.J. Brands, J.G. Bosch and N.d. Jong, "A matrix phased array system for 3D high frame-rate imaging of the carotid arteries", *IEEE International Ultrasonics Symposium*, 2010.
94. J. Sato, M. Kawabuchi and A. Fukumoto, "Dependence of the electromechanical coupling coefficient on the width-to-thickness ratio of plank-shaped piezoelectric transducers used for electronically scanned ultrasound diagnostic systems"*, The Journal of the Acoustical Society of America*, 1979, vol. **66**, no. 6, pp. 1609-1611.
95. D.H. Cortes, S.K. Datta and O.M. Mukdadi, "Elastic guided wave propagation in a periodic array of multi-layered piezoelectric plates with finite cross-sections"*, Ultrasonics*, 2010, vol. **50**, no. 3, pp. 347-356.
96. H.J. Lee and S. Zhang, "Design of low-loss 1-3 piezoelectric composites for high-power transducer applications"*, IEEE Transactions on Ultrasonics, Ferroelectrics, and Frequency Control*, 2012, vol. **59**, no. 9, pp. 1969-1975.
97. R.-F. Chang;, A. Fenster;, C. Kathuria;, F. Molinari; and J.S. Suri, "Advances in Diagnostic and Therapeutic Ultrasound Imaging", Bioinformatics and Biomedical Imaging, 2008, *Artech House*.

98. A. Landry, J.D. Spence and A. Fenster, "Measurement of Carotid Plaque Volume by 3-Dimensional Ultrasound", *Stroke*, 2004, vol. **35**, no. 4, pp. 864-869.
99. F. Aaron, L. Anthony, B.D. Donal, A.H. Robert and J.D. Spence, "3D Ultrasound Imaging of the Carotid Arteries", *Current Drug Targets - Cardiovascular & Hematological Disorders*, 2004, vol. **4**, no. 2, pp. 161-175.
100. B. Denarie, T.A. Tangen, I.K. Ekroll, N. Rolim, H. Torp, T. Bjåstad and L. Lovstakken, "Coherent Plane Wave Compounding for Very High Frame Rate Ultrasonography of Rapidly Moving Targets", *IEEE Transactions on Medical Imaging*, 2013, vol. **32**, no. 7, pp. 1265-1276.
101. N.N. Abboud;, G.L. Wojcik;, D.K. Vaughan;, J. Mould;, D.J. Powell; and L. Nikodym, "Finite element modeling for ultrasonic transducers", *Proceedings of SPIE - The International Society for Optical Engineering*, 1998, vol. **3341**, no. 19-42.
102. J.M. Cannata, J.A. Williams, L. Zhang, C.H. Hu and K.K. Shung, "A high-frequency linear ultrasonic array utilizing an interdigitally bonded 2-2 piezo-composite", *IEEE Transactions on Ultrasonics, Ferroelectrics, and Frequency Control*, 2011, vol. **58**, no. 10, pp. 2202-2212.
103. I.S. Domínguez;, P.A. Contla;, F.G. Nocetti; and M.R. López;, *Cross-talk response analysis on a piezoelectric ultrasonic matrix array*, in *International Congress on Sound and Vibration*. 2012: Vilnius; Lithuania;. p. 3112-3119.
104. D.H. Turnbull and F.S. Foster, "Fabrication and characterization of transducer elements in two-dimensional arrays for medical ultrasound imaging", *IEEE Ultrasonics Symposium*, 1991.
105. R.A. Ibrahim, "Handbook of Structural Life Assessment", 2017, *Wiley and Sons, Incorporated, John*.
106. C. Chen, Z. Chen, D. Bera, S.B. Raghunathan, M. Shabanimotlagh, E. Noothout, Z.Y. Chang, J. Ponte, C. Prins, H.J. Vos, J.G. Bosch, M.D. Verweij, N.d. Jong and M.A.P. Pertijs, "A front-end ASIC with receive sub-array beamforming integrated with a 32 x 32 PZT matrix transducer for 3-D transesophageal echocardiography", *IEEE Symposium on VLSI Circuits*, 2016.
107. *Coaxial cables*, Axon, Editor. 2015.
108. H.R. Tahmasebpour, A.R. Buckley, P.L. Cooperberg and C.H. Fix, "Sonographic Examination of the Carotid Arteries", *RadioGraphics*, 2005, vol. **25**, no. 6, pp. 1561-1575.
109. E. Kang, Q. Ding, M. Shabanimotlagh, P. Kruizinga, Z.Y. Chang, E. Noothout, H.J. Vos, J.G. Bosch, M.D. Verweij, N.d. Jong and M.A.P. Pertijs, "A Reconfigurable Ultrasound Transceiver ASIC With 24 x 40 Elements for 3-D Carotid Artery Imaging", *IEEE Journal of Solid-State Circuits*, 2018, vol. **53**, no. 7, pp. 2065-2075.
110. http://verasonics.com/. *Vantage research ultrasound*. 2018.
111. J.D. Spence, M. Eliasziw, M. DiCicco, D.G. Hackam, R. Galil and T. Lohmann, "Carotid Plaque Area", *Stroke*, 2002, vol. **33**, no. 12, pp. 2916-2922.
112. U. Schminke, L. Motsch, B. Griewing, M. Gaull and C. Kessler, "Three-dimensional power-mode ultrasound for quantification of the progression of carotid artery atherosclerosis", *Journal of Neurology*, 2000, vol. **247**, no. 2, pp. 106–111.
113. A. Delcker and C. Tegeler, "Influence of ECG-Triggered Data Acquisition on Reliability for Carotid Plaque Volume Measurements with a Magnetic Sensor Three-Dimensional Ultrasound System", *Ultrasound in Medicine and Biology*, 1998, vol. **24**, no. 4, pp. 601-605.
114. A. Delcker and H.C. Diener, "Quantification of atherosclerotic plaques in carotid arteries by three-dimensional ultrasound", *The British Journal of Radiology*, 1994, vol. **67**, no. 799, pp. 672-678.
115. A. Harloff, "Carotid Plaque Hemodynamics", *Interventional Neurology*, 2012, vol. **1**, no. 1, pp. 44-54.
116. S. Holbek, M.J. Pihl, C. Ewertsen, M.B. Nielsen and J.A. Jensen, "In vivo 3-D vector velocity estimation with continuous data", *IEEE International Ultrasonics Symposium* 2015.
117. J.N. Welch, J.A. Johnson, M.R. Bax, R. Badr and R. Shahidi, "A real-time freehand 3D ultrasound system for image-guided surgery", *IEEE Ultrasonics Symposium*, 2000.

118. P. Ramaekers, M.d. Greef, R. Berriet, C.T.W. Moonen and M. Ries, "Evaluation of a novel therapeutic focused ultrasound transducer based on Fermat's spiral", *Physics in Medicine and Biology*, 2017, vol. **62**, no. 12, pp. 5021.
119. E. Kang, Q. Ding, M. Shabanimotlagh, P. Kruizinga, Z.Y. Chang, E. Noothout, H.J. Vos, J.G. Bosch, M.D. Verweij, N. de Jong and M.A.P. Pertijs, "A Reconfigurable Ultrasound Transceiver ASIC With 24 x 40 Elements for 3-D Carotid Artery Imaging", *IEEE Journal of Solid-State Circuits*, 2018, vol. **53**, no. 7, pp. 2065-2075.
120. P. Kruizinga, E. Kang, M. Shabanimotlagh, Q. Ding, E. Noothout, Z.Y. Chang, H.J. Vos, J.G. Bosch, M.D. Verweij, M.A.P. Pertijs and N.d. Jong, "Towards 3D ultrasound imaging of the carotid artery using a programmable and tileable matrix array", *IEEE International Ultrasonics Symposium* 2017.
121. P. Tortoli, M. Lenge, D. Righi, G. Ciuti, H. Liebgott and S. Ricci, "Comparison of Carotid Artery Blood Velocity Measurements by Vector and Standard Doppler Approaches", *Ultrasound in Medicine and Biology*, 2015, vol. **41**, no. 5, pp. 1354-1362.
122. P. Kruizinga, F. Mastik, N.d. Jong, A.F.W.v.d. Steen and G.v. Soest, "High frame rate ultrasound imaging of human carotid artery dynamics", *IEEE International Ultrasonics Symposium*, 2012.
123. D.H. Evans, J.A. Jensen and M.B. Nielsen, "Ultrasonic colour Doppler imaging", *Interface Focus*, 2011, vol. **1**, no. 4, pp. 490-502.
124. S. Salles, H. Liebgott, O. Basset, C. Cachard, D. Vray and R. Lavarello, "Experimental evaluation of spectral-based quantitative ultrasound imaging using plane wave compounding", *IEEE Transactions on Ultrasonics, Ferroelectrics, and Frequency Control*, 2014, vol. **61**, no. 11, pp. 1824-1834.
125. S.S. Yee Ho, "Current status of carotid ultrasound in atherosclerosis", *Quantitative Imaging in Medicine and Surgery*, 2016, vol. **6**, no. 3, pp. 285-296.
126. P. Kruizinga, P. van der Meulen, A. Fedjajevs, F. Mastik, G. Springeling, N. de Jong, J.G. Bosch and G. Leus, "Compressive 3D ultrasound imaging using a single sensor", *Science Advances*, 2017, vol. **3**, no. 12, pp. e1701423.
127. M. Shabanimotlagh, V. Daeichin, S.B. Raghunathan, P. Kruizinga, H.J. Vos, J.G. Bosch, M. Pertijs, N.d. Jong and M. Verweij, "Optimizing the directivity of piezoelectric matrix transducer elements mounted on an ASIC", *IEEE International Ultrasonics Symposium*, 2017.
128. E.A. Fisher, J.A. Stahl, J.H. Budd and M.E. Goldman, "Transesophageal echocardiography: Procedures and clinical application", *J. Am. Coll. Cardiol*, 1991, vol. **18**, no. 5, pp. 1333–1348.
129. I.S. Salgo, "Three-Dimensional Echocardiographic Technology", *Cardiol. Clin.*, 2007, vol. **25**, no. 2, pp. 231–239.
130. W.G. Daniel, R. Erbel, W. Kasper, C.A. Visser, R. Engberding, G.R. Sutherland, E. Grube, P. Hanrath, B. Maisch, K. Dennig, M. Schartl, P. Kremer, C. Angermann, S. Iliceto, J.M. Curtius and A. Mügge, "Safety of Transesophageal Echocardiography. A multicenter survey of 10,419 examinations", *Circulation*, 1991, vol. **83**, no. 3, pp. 817-821.
131. G. Côté and A. Denault, "Transesophageal echocardiography-related complications", *Can J Anaesth*, 2008, vol. **55**, no. 9, pp. 622-647.
132. Z. Yu, S. Blaak, Z. Chang, J. Yao, J.G. Bosch, C. Prins, C.T. Lancée, N. de Jong, M.A.P. Pertijs and G.C.M. Meijer, "Front-end receiver electronics for a matrix transducer for 3D transesophageal echocardiography", *IEEE Trans. Ultrason., Ferroelectr., Freq. Control*, 2012, vol. **59**, no. 7, pp. 1500-1512.
133. M.I. Fuller, K. Ranganathan, S. Zhou, T.N. Blalock, J. Hossack and W.F. Walker, "Experimental system prototype of a portable lowcost, c-scan ultrasound imaging device", *IEEE Trans. Biomed. Eng.*, 2008, vol. **55**, no. 2, pp. 519-530.
134. U.S. Food and Drug Administration (FDA), "Guidance for Industry and FDA Staff– Information for Manufacturers Seeking Marketing Clearance of Diagnostic Ultrasound Systems and Transducers", Sept. 2008.

135. A. Bhuyan, J.W. Choe, B.C. Lee, I.O. Wygant, A. Nikoozadeh, O. Oralkan and B.T. Khuri-Yakub, "3D Volumetric Ultrasound Imaging with a 32⋄32 CMUT Array Integrated with Front-End ICs Using Flip-Chip Bonding Technology", *Proc. IEEE Int. Solid-State Circuits Conf. Dig. Tech. Papers*, 2013.
136. I.O. Wygant, X. Zhuang, D.T. Yeh, O. Oralkan, A.S. Ergun, M. Karaman and B.T. Khuri-Yakub, "Integration of 2D CMUT arrays with front-end electronics for volumetric ultrasound imaging", *IEEE Trans. Ultrason., Ferroelectr., Freq. Control*, 2008, vol. **55**, no. 2, pp. 327-342.
137. B. Savord and R. Solomon, "Fully Sampled Matrix Transducer for Real Time 3D Ultrasonic Imaging", *Proc. IEEE Ultrasonics Symp.* , 2003.
138. I.O. Wygant, N.S. Jamal, H.J. Lee, A. Nikoozadeh, O. Oralkan, M. Karaman and B.T. Khuri-Yakub, "An integrated circuit with transmit beamforming flip-chip bonded to a 2-D CMUT array for 3-D ultrasound imaging", *IEEE Trans. Ultrason., Ferroelectr., Freq. Control*, 2009, vol. **56**, no. 10, pp. 2145-2156.
139. M.A. Uddin, M.O. Alam, Y.C. Chan and H.P. Chan, "Adhesion strength and contact resistance of flip chip on flex packages—effect of curing degree of anisotropic conductive film", *Microelectronics Reliability*, 2004, vol. **44**, no. 505-514.
140. Z. Yu, *Low-Power Receive-Electronics for a Miniature 3D Ultrasound Probe*. 2012, Delft University of Technology: Delft, The Netherlands.
141. S. Blaak, Z. Yu, G.C.M. Meijer, C. Prins, C.T. Lancée, J.G. Bosch and N. de Jong, "Design of a Micro-beamformer for a 2D Piezoelectric Ultrasound Transducer", *Proc. IEEE Ultrasonics Symp.*, 2009.
142. K. Chen, H.-S. Lee, A.P. Chandrakasan and C.G. Sodini, "Ultrasonic imaging transceiver design for CMUT: a three-level 30-vpp pulse-shaping pulser with improved efficiency and a noise-optimized receiver", *IEEE J. Solid-State Circuits*, 2013, vol. **48**, no. 11, pp. 2734-2745.
143. M. Sautto, D. Leone, A. Savoia, D. Ghisu, F. Quaglia, G. Caliano and A. Mazzanti, "A CMUT transceiver front-end with 100-V TX driver and 1-mW low-noise capacitive feedback RX amplifier in BCD-SOI technology", *Proc. ESSCIRC*, 2014.
144. P.E. Allen and D.R. Holberg, "CMOS Analog Circuit Design", 2002, *Oxford University Press*.
145. J. Yao, Z. Yu, M.A.P. Pertijs, G.C.M. Meijer, C.T. Lancée, J.G. Bosch and N. de Jong, "Design of a low power time-gain-compensation amplifier for a 2D piezoelectric ultrasound transducer", *Proc. IEEE Ultrasonics Symp.*, 2010.
146. K. Kaviani, O. Oralkan, P. Khuri-Yakub and B. Wooley, "A multichannel pipeline analog-to-digital converter for an integrated 3-D ultrasound imaging system", *IEEE J. Solid-State Circuits*, 2003, vol. **38**, no. 7, pp. 1266-1270.
147. Z. Yu, M.A.P. Pertijs and G.C.M. Meijer, "An ultrasound beamformer using pipeline-operated S/H delay stages and charge-mode summation", *Electron.Lett.*, Sept. 2011, vol. **47**, no. 18, pp. 1011-1012.
148. A.J. Lopez-Martin, J. Ramirez-Angulo, R.G. Carvajal and L. Acosta, "Power-efficient class AB CMOS buffer", *Electron.Lett.*, Jan. 2009, vol. **45**, no. 2, pp. 89-90.
149. E.J.W. Merks, J.M.G. Borsboom, M.M. Voormolen, N. Bom, A.F.W.v.d. Steen and N.d. Jong, "A KLM-circuit model of a multi-layer transducer for bladder volume measurements", *Ultrasonics*, 2006, vol. **44(SUPPL. 1)**, no. e805-e710.
150. J.A. Jensen and N.B. Svendsen, "Calculation of pressure fields from arbitrarily shaped, apodized, and excited ultrasound transducers", *IEEE Trans. Ultrason., Ferroelectr., Freq. Control*, 1992, vol. **39**, no. 2, pp. 262-267.
151. J.A. Jensen, "Field: A Program for Simulating Ultrasound Systems", *10th Nordic-Baltic Conference on Biomedical Imaging*, 1996.
152. S.B. Raghunathan, D. Bera, C. Chen, S. Blaak, C. Prins, M.A.P. Pertijs, J.G. Bosch, N.d. Jong and M.D. Verweij, "Design of a miniature ultrasound probe for 3D transesophageal echocardiography", *Proc. IEEE Ultrasonics Symp.*, 2014.
153. J.B. Seward, B.K. Khandheria, J.K. Oh, M.D. Abel, R.W. Hughes, W.D. Edwards, B.A. Nichols, W.K. Freeman and A.J. Tajik, "Transesophageal Echocardiography: Technique,

Anatomic Correlations, Implementation, and Clinical Applications", *Mayo Clinic Proceedings*, 1988, vol. **63**, no. 7, pp. 649-680.
154. N.G. Pandian, T.-L. Hsu, S.L. Schwartz, A. Weintraub, Q.-L. Cao, A.T. Schneider, G. Gordon, M. England and J. Simonetti, "Multiplane Transesophageal Echocardiography", *Echocardiography*, 1992, vol. **9**, no. 6, pp. 649-666.
155. J.R.T.C. Roelandt, I.R. Thomson, W.B. Vletter, P. Brommersma, N. Bom and D.T. Linker, "Multiplane Transesophageal Echocardiography: Latest Evolution in an Imaging Revolution", *Journal of the American Society of Echocardiography*, 1992, vol. **5**, no. 4, pp. 361-367.
156. J. Kwak;, M. Andrawes;, S. Garvin; and M.N. D'Ambra, "3D transesophageal echocardiography: a review of recent literature 2007–2009", *Current Opinion in Anaesthesiology*, 2010, vol. **23**, no. 1, pp. 80-88.
157. T.L. Christiansen, M.F. Rasmussen, J.P. Bagge, L.N. Moesner, J.A. Jensen and E.V. Thomsen, "3-D imaging using row-column-addressed arrays with integrated apodization - part ii: transducer fabrication and experimental results", *IEEE Transactions on Ultrasonics, Ferroelectrics, and Frequency Control*, 2015, vol. **62**, no. 5, pp. 959-971.
158. E.D. Light, S.F. Idriss, P.D. Wolf and S.W. Smith, "Real-time three-dimensional intracardiac echocardiography", *Ultrasound in Medicine and Biology*, 2001, vol. **27**, no. 9, pp. 1177-1183.
159. A.S. Gopal, A.M. Keller, Z. Shen, P.M. Sapin, K.M. Schroeder, D.L. King and D.L. King, "Three-dimensional echocardiography: In vitro and in vivo validation of left ventricular mass and comparison with conventional echocardiographic methods", *Journal of the American College of Cardiology*, 1994, vol. **24**, no. 2, pp. 504-513.
160. M. Handke, D.M. Schäfer, G. Heinrichs, E. Magosaki and A. Geibel, "Quantitative Assessment of Aortic Stenosis by Three-Dimensional Anyplane and Three-Dimensional Volume-Rendered Echocardiography", *Echocardiography*, 2002, vol. **19**, no. 1, pp. 45-53.
161. P. Jean, P. Clement, A. Juan Esteban, I. Marion, F. Mathias, G. Jean-Luc, T. Mickael and P. Mathieu, "3D ultrafast ultrasound imaging in vivo", *Physics in Medicine & Biology*, 2014, vol. **59**, no. 19, pp. L1.
162. J.S. Raichlen, S.S. Trivedi, G.T. Herman, M.G.S. John Sutton and N. Reicher, "Dynamic three-dimensional reconstruction of the left ventricle from two-dimensional echocardiograms", *Journal of the American College of Cardiology*, 1986, vol. **8**, no. 2, pp. 364-370.
163. A. Salustri, S. Spitaels, J. McGhie, W. Vletter and J.R.T.C. Roelandt, "Transthoracic three-dimensional echocardiography in adult patients with congenital heart disease", *Journal of the American College of Cardiology*, 1995, vol. **26**, no. 3, pp. 759-767.
164. P.M. Sapin, K.D. Schroeder, M.D. Smith, A.N. DeMaria and D.L. King, "Three-dimensional echocardiographic measurement of left ventricular volume in vitro: Comparison with two-dimensional echocardiography and cineventriculography", *Journal of the American College of Cardiology*, 1993, vol. **22**, no. 5, pp. 1530-1537.
165. L. Sugeng, L. Weinert, K. Thiele and R.M. Lang, "Real-Time Three-Dimensional Echocardiography Using a Novel Matrix Array Transducer", *Echocardiography*, 2003, vol. **20**, no. 7, pp. 623-635.
166. A.S. Logan, L.L.P. Wong, A.I.H. Chen and J.T.W. Yeow, "A 32 x 32 element row-column addressed capacitive micromachined ultrasonic transducer", *IEEE Transactions on Ultrasonics, Ferroelectrics, and Frequency Control*, 2011, vol. **58**, no. 6, pp. 1266-1271.
167. R.R. Shell, *Three-dimensional imaging system for sonar system*, U.S.o. Navy, Editor. 2001.
168. A. Austeng and S. Holm, "Sparse 2-D arrays for 3-D phased array imaging - design methods", *IEEE Transactions on Ultrasonics, Ferroelectrics, and Frequency Control*, 2002, vol. **49**, no. 8, pp. 1073-1086.
169. B. Diarra, H. Liebgott, M. Robini, P. Tortoli and C. Cachard, "Novel strategies in 2D sparse arrays for 3D ultrasound imaging", *Physica Medica: European Journal of Medical Physics*, 2016, vol. **32**, no. 2, pp. 420-421.
170. E. Roux, A. Ramalli, H. Liebgott, C. Cachard, M.C. Robini and P. Tortoli, "Wideband 2-D Array Design Optimization With Fabrication Constraints for 3-D US Imaging", *IEEE*

Transactions on Ultrasonics, Ferroelectrics, and Frequency Control, 2017, vol. **64**, no. 1, pp. 108-125.

171. E. Roux, A. Ramalli, P. Tortoli, C. Cachard, M.C. Robini and H. Liebgott, "2-D Ultrasound Sparse Arrays Multidepth Radiation Optimization Using Simulated Annealing and Spiral-Array Inspired Energy Functions"*, IEEE Transactions on Ultrasonics, Ferroelectrics, and Frequency Control*, 2016, vol. **63**, no. 12, pp. 2138-2149.
172. J. Kortbek, J.A. Jensen and K.L. Gammelmark, "Sequential beamforming for synthetic aperture imaging"*, Ultrasonics*, 2013, vol. **53**, no. 1, pp. 1-16.
173. G. Matrone, A.S. Savoia, M. Terenzi, G. Caliano, F. Quaglia and G. Magenes, "A volumetric CMUT-based ultrasound imaging system simulator with integrated reception and μ-beamforming electronics models"*, IEEE Transactions on Ultrasonics, Ferroelectrics, and Frequency Control*, 2014, vol. **61**, no. 5, pp. 792-804.
174. S. Blaak, C.T. Lancée, J.G. Bosch, C. Prins, A.F.W.v.d. Steen and N.d. Jong, "A matrix transducer for 3D Transesophageal Echocardiography with a separate transmit and receive subarray", *IEEE International Ultrasonics Symposium*, 2011.
175. J.A. Jensen, *A Program for Simulating Ultrasound Systems*, in *Nordibaltic Conference on Biomedical Imaging*. 1996. p. 351-353.
176. Z. Yu, *Low-Power Receive-Electronics for a Miniature 3D Ultrasound Probe*. 2012, TU Delft.
177. N.N. Abboud;, G. Wojcik;, D.K. Vaughan;, J. Mould;, D.J. Powell; and N. Lisa;, "Electromechanical modeling using explicit time-domain finite elements", *IEEE Ultrasonics Symposium*, 1993.
178. D. Bera, H.J. Vos, S.B. Raghunathan, C. Chen, Z. Chen, M.D. Verweij, M.A.P. Pertijs, N.d. Jong and J.G. Bosch, "Three-dimensional beamforming combining micro-beamformed RF datasets", *IEEE International Ultrasonics Symposium*, 2016.
179. A. Bhuyan, J.W. Choe, B.C. Lee, I. Wygant, A. Nikoozadeh, O. Oralkan and B.T. Khuri-Yakub, "3D volumetric ultrasound imaging with a 32×32 CMUT array integrated with front-end ICs using flip-chip bonding technology", *IEEE International Solid-State Circuits Conference Digest of Technical Papers*, 2013.
180. I.O. Wygant, X. Zhuang, D.T. Yeh, O. Oralkan, A.S. Ergun, M. Karaman and B.T. Khuri-yakub, "Integration of 2D CMUT arrays with front-end electronics for volumetric ultrasound imaging"*, IEEE Transactions on Ultrasonics, Ferroelectrics, and Frequency Control*, 2008, vol. **55**, no. 2, pp. 327-342.
181. A. Bhuyan, J.W. Choe, B.C. Lee, I.O. Wygant, A. Nikoozadeh, O. Ö and B.T. Khuri-Yakub, "Integrated Circuits for Volumetric Ultrasound Imaging With 2-D CMUT Arrays"*, IEEE Transactions on Biomedical Circuits and Systems*, 2013, vol. **7**, no. 6, pp. 796-804.
182. J. Xuecheng, O. Oralkan, F.L. Degertekin and B.T. Khuri-Yakub, "Characterization of one-dimensional capacitive micromachined ultrasonic immersion transducer arrays"*, IEEE Transactions on Ultrasonics, Ferroelectrics, and Frequency Control*, 2001, vol. **48**, no. 3, pp. 750-760.
183. Z. Shiwei, G.L. Wojcik and J.A. Hossack, "An approach for reducing adjacent element crosstalk in ultrasound arrays"*, IEEE Transactions on Ultrasonics, Ferroelectrics, and Frequency Control*, 2003, vol. **50**, no. 12, pp. 1752-1761.
184. S. Zhou and J.A. Hossack, "Reducing inter-element acoustic crosstalk in capacitive micromachined ultrasound transducers"*, IEEE Transactions on Ultrasonics, Ferroelectrics, and Frequency Control*, 2007, vol. **54**, no. 6, pp. 1217-1228.
185. D. Shattuck, M.D. Weinshenker, S.W. Smith and O.T.v. Ramm, "Explososcan: a parallel processing technique for high speed ultrasound imaging with linear phased arrays"*, The Journal of the Acoustical Society of America*, 1984, vol. **75**, no. 4, pp. 1273-1282.
186. T. Hergum, T. Bjastad, K. Kristoffersen and H. Torp, "Parallel beamforming using synthetic transmit beams"*, IEEE Transactions on Ultrasonics, Ferroelectrics, and Frequency Control*, 2007, vol. **54**, no. 2, pp. 271-280.

187. L. Tong, A. Ramalli, R. Jasaityte, P. Tortoli and J.D. hooge, "Multi-Transmit Beam Forming for Fast Cardiac Imaging—Experimental Validation and In Vivo Application"*, IEEE Transactions on Medical Imaging*, 2014, vol. **33**, no. 6, pp. 1205-1219.
188. H. Hasegawa and H. Kanai, "High frame rate echocardiography using diverging beams", *IEEE International Ultrasonics Symposium*, 2011.
189. D. Bera, S.B. Raghunathan, C. Chen, Z. Chen, M.A.P. Pertijs, M.D. Verweij, V. Daeichin, H.J. Vos, A.F.W.v.d. Steen, N.d. Jong and J.G. Bosch, "Multiline 3D beamforming using micro-beamformed datasets for pediatric transesophageal echocardiography"*, Physics in Medicine and Biology*, 2018, vol. **63**, no. 7, pp. 075015.
190. M.F.S. O'Rourke, Jan A, C. Vlachopoulos, D.A. Duprez and G.E. Plante, "Clinical applications of arterial stiffness; definitions and reference values"*, American journal of hypertension*, 2002, vol. **15**, no. 5, pp. 426-444.
191. P. Bihari, A. Shelke, T.H. Nwe, M. Mularczyk, K. Nelson, T. Schmandra, P. Knez and T. Schmitz-Rixen, "Strain Measurement of Abdominal Aortic Aneurysm with Real-time 3D Ultrasound Speckle Tracking"*, European Journal of Vascular and Endovascular Surgery*, 2013, vol. **45**, no. 4, pp. 315-323.

Propositions[1]
Related to the thesis

Ultrasound Matrix Transducers for High Frame Rate 3D Medical Imaging

Maysam Shabanimotlagh

1. Acoustic characterization of a transducer is not only about the sound waves. (This thesis)

2. Making extra cuts and removing material improve the performance of a transducer. (This thesis)

3. "Geographical determinism" is always the source of illogical judgments.

4. A strong dictatorship is better than a weak democracy.

5. If you want to love people, you have to stop judging them.

6. When people ask your opinion, in fact, they are looking for your confirmation.

7. A creative mind looks at the environment in a way different than what they are designed for.

8. We should optimize our lives, taking into account our conditions and requirements, and not based on the successes or failure of the others.

9. To discover life, work hard, sport hard, party hard, rest hard, … hard.

[1] These propositions are regarded as opposable and defendable, and have been approved as such by the promotors Nico de Jong and Martin Verweij.

Acknowledgments

And now I am at the end of my PhD journey. I was really looking forward to writing these words, to thank all people who have supported me in this journey. The past four years were the most fruitful, challenging, and interesting years in my life. A new country, the language, culture, weather, family, friends, sports, and of course the science. This thesis is an outcome of the work by a group of researchers at three different departments: Acoustical Wavefield Imaging at TUDelft, Electronic Instrumentation Laboratory at TUDelft, and Biomedical Engineering department at Thoraxcenter in ErasmusMC. The following lines are devoted to the individuals whose work have some traces in this research, and to the great people who helped me to do my research while enjoying the life.

First of all, I would like to express my gratitude to Martin Verweij and Nico de Jong, my promotors. Thank you for offering me a PhD position at Acoustic Wavefield Imaging. It was a great pleasure to work in such an environment with a lot of knowledge, skills and expertise, and nice colleagues. During all the meetings we had, I was trained on how to approach the problems to find applicable solutions, and little by little become a physicist. I really appreciate your guidance in the past four years and for all of that, I want to thank you. Martin, your critical thinking in scientific problems brought a lot of new ideas to understand different physical phenomena, and to find solutions for the challenges during the project. Nico, your experimental viewpoint, and your pragmatic attitude pushed us forward to reach the final goals of the projects. In my opinion, you two are a perfect company for a PhD student. It was fantastic to work with you and be a part of your team in the past years.

This multidisciplinary project could not come to an end without the supervisory team from Electronic Instrumentation Lab, and Biomedical Engineering department. Special thanks to Michiel Pertijs and Hans Bosch for your support. I learned a lot from you during our regular biweekly MICA / PUMA meetings and other meetings. I want to thank Rik Vos for the useful discussions we had, especially in my first two years of PhD. You were always patient and welcome to share your knowledge and your previous experiences with me.

I would like to thank Eunchul Kang and Pieter Kruizinga, my colleagues in the PUMA project. Troubleshooting the PUMA samples was not possible without your involvements. It was really nice to have a collaboration with you. Eunchul I learned a lot of electronics from you, and I am so happy to have you in the team. I really like your organized approach in doing measurements. My best wishes for the rest of your PhD. Pieter, it was interesting to work on your special phantoms with chocolate milk. I wish you the best of luck in your new position. By the way, next time you travel to Iran, don't forget to bring kilos of saffron with your luggage!

Deep Bera, Zhao Chen, and Chao Chen, collaboration with you on the MICA project was a nice experience for me. I remember our endless discussions in the lab to debug the problems of the samples. Fortunately, we managed to solve all the issues and make the MICA samples work. Deep, you were a motivator to play tennis at the lunchtime when the weather was nice, and I am still amazed that you were so happy to have hot cola after sport!

Special thanks to Shreyas Raghunathan. You were always supporting me during my PhD. I learned a lot from and with you, especially in the first three years of my work. We experienced so many things together: learning PZFlex, doing measurements, preparing reports, going to conferences, organizing courses and workshop, playing darts, etc. I never forget the Taiwan trip and the waitress who thought we come from a poor country!

Verya Daeichin, finalizing this thesis could not finish on time without your comments and suggestions. I would like to thank you for your support in wrapping up the final results of my PhD and preparing the article. 'Damet garm!'[1]

Paul van Neer, thanks for your friendly advice, and thank you for the time you put on discussing my project and sharing your experiences with enthusiasm. You could point out all the critical issues until you fully understand all the details. In my opinion, if someone could answer all of your questions, he should not be worried about any other question.

Emile Noothout, because of your expertise and hard work, it has been possible to fabricate the transducers and the measurement setups. Many critical issues were clarified after our conversations, and I greatly appreciate that. I would also like to thank Zu-yao Cheng, for his effort in preparing the electronics of the transducers.

I want to express my gratitude to Margret van Fessem and Angela van der Sande who always facilitate all the official works. In addition to your administrative assistant, I highly appreciate your organization of all group activities, such as the Christmas drinks, international dinners, the happy hours, the day out events and all other activities. Margaret, I appreciate your advice and your support to deal with the new situation, at the beginning of my work, when I moved to the Netherland. Angela, it was very interesting to experience the ice skating with you for the first time in my life.

Henry den Bok and Edo Bergsma, with your help all my software and hardware problems, were quickly solved. Besides your technical advices, I have always been happy to discuss with you about different topics during the coffee times. Henry, I really enjoyed to have collaboration with you for designing the PCBs, and I learned a lot from and with you.

[1] Greetings in Fenglish (Farsi with English alphabet!).

I would like to thank everyone in Acoustic Wavefield Imaging group, in particular, to all the PhDs and PostDoc's of the medical acoustics: Suzanne Leinders, Shreyas Raghunathan, Verya Daeichin, Jack Massaad, Fabian Fool, Alberico Sabbadini, Elango Selvam, Ulas Taskin, Mikhail Davydenko and Boudewine Ossenkoppele. All discussions, and especially all the nonsense discussions and crazy ideas, darts and basketball games in the room, sjoelen, table football and table tennis, make it difficult for me to leave this nice group. With all of these activities, I was able to do my research with great pleasure. Thank you all for bringing the positive atmosphere in the whole department.

I want to thank my colleagues at the biomedical department at Thoraxcenter of Erasmus MC. Jovana Janjic, I really enjoyed our collaboration to understand the physics of subdicing and the discussions on PZFlex simulations. Robert Beurskens, I appreciate your calm character in explaining all the details of the electronic measurements. Discussions with you were very insightful. Reza Pakdaman, Mehdi Soozande, Sophinese Iskander-Rizk, and Jason Voorneveld, it was fun to be with you at different occasions, meetings, conferences, etc. and discuss on different random topics.

Special thanks to Hamed Ahmadpanahi, Maryam Khodadadian, Farnaz Eghbal, and Mojde Taherian for all the lunch meetings and all the funny stories and discussions we had. Those hours really charged me for a whole day of work. I cannot forget that Mostafa Zahmatkesh was most of the times invisibly available. Hassan HosseinNia and Davood Farhadi, the planning meetings on Fridays was really important and promising for a nice weekend.

I want to give my deepest gratitude to my family. Maman and Baba, thank you for all you have done for me in the past thirty years. Thanks for providing a good education for me. Without the inspiration and support you gave me, I might not be the person I am today. I have the greatest feeling when I see the smile on your faces. Special thanks to my mother in law, for the continuous moral and emotional support from a distance. You have always brought kindness to our life. Sara, my little sister, I want to thank you for taking care of everything and all the works, while we are out of the country. Dear Maryam and Naser, thanks for bringing happiness to the whole family with Masiha. Sanaz jan, thanks for everything you have done in the past years. I want to thank all of you for your interest and your nice visits to the Netherland, which we have always enjoyed.

Finally and the most importantly Farnaz, my dear wife. In the past years, we have overcome all the obstacles together. Thank you so much for your unlimited support, understanding, and love. We have had so many wonderful moments, and I am looking for more in the future. At this moment, we are expecting a new baby to our family, which will make the life more beautiful than the previous years. We are so enthusiastic to hear his first words, to see him walk on the first steps, and to celebrate his development to overcome every milestone.

Maysam Shabanimotlagh
1st August 2018

List of Publications

Journal papers:

- **Maysam Shabanimotlagh**, Eunchul Kang, Pieter Kruizinga, Qing Ding, Emile Noothout, Zu-Yao Chang, Hans Bosch, Michiel Pertijs, Nico de Jong, Martin Verweij; A new PZT matrix transducer with integrated electronics for carotid imaging; Physics in Medicine and Biology; Submitted.

- **Maysam Shabanimotlagh**, Shreyas B. Raghunathan, Jovana Janjic, Verya Daeichin, Emile Noothout, Michiel A.P. Pertijs, Johan G. Bosch, Nico de Jong, Martin D. Verweij; Effect of subdicing on performance of an ultrasound matrix transducer for carotid imaging: numerical and experimental study; IEEE Transactions on Ultrasonics, Ferroelectrics, and Frequency Control; Submitted.

- Eunchul Kang, Qing Ding, **Maysam Shabanimotlagh**, Pieter Kruizinga, Zu-yao Chang, Emile Noothout, Hendrik J. Vos, Johan G. Bosch, Martin D. Verweij, Nico de Jong, and Michiel A. P. Pertijs; A reconfigurable ultrasound transceiver ASIC with 24 × 40 elements for 3D carotid artery imaging; IEEE Journal of Solid-State Circuits; 2018; Accepted.

- Verya Daeichin, Deep Bera, Shreyas Raghunathan, **Maysam Shabanimotlagh**, Zhao Chen, Chao Chen, Emile Noothout, Hendrik J. Vos, Michiel Pertijs, Johannes Bosch, Nico de Jong, Martin Verweij; Acoustic characterization of a miniature matrix transducer for pediatric 3D transesophageal echocardiography, Ultrasound in Medicine and Biology; 2018; In Press.

- Chao Chen, Zhao Chen, Deep Bera, Shreyas B. Raghunathan, **Maysam Shabanimotlagh**, Emile Noothout, Zu-Yao Chang, Jacco Ponte, Christian Prins, Hendrik J. Vos, Johan G. Bosch, Martin D. Verweij, Nico de Jong, and Michiel A. P. Pertijs; A Front-End ASIC with Receive Sub-array Beamforming Integrated with a 32 × 32 PZT Matrix Transducer for 3-D Transesophageal Echocardiography; IEEE Journal of Solid-State Circuits; 2017; 52(4),7807320, pp. 994-1006.

- Chao Chen, Shreyas B. Raghunathan, Zili Yu, **Maysam Shabanimotlagh**, Zhao Chen, Zu-yao Chang, Sandra Blaak, Christian Prins, Jacco Ponte, Emile Noothout, Hendrik J.

Vos, Johan G. Bosch, Martin D. Verweij, Nico de Jong, and Michiel A. P. Pertijs; A prototype PZT matrix transducer with low-power integrated receive ASIC for 3D transesophageal echocardiography; IEEE Transactions on Ultrasonics, Ferroelectrics, and Frequency Control; 2016; 63(1),7313028, pp. 47-59.

- Jovana Janjic, **Maysam Shabanimotlagh**[1], Gijs van Soest, Antonius F. W. van der Steen, Nico de Jong, and Martin D. Verweij; Improving the performance of a 1-D ultrasound transducer array by subdicing; IEEE Transactions on Ultrasonics, Ferroelectrics, and Frequency Control; 2016; 63(8),7464369, pp. 1161-1171.

- Seyyed M Hasheminejad, **Maysam Shabanimotlagh**; Magnetic-field-dependent sound transmission properties of magnetorheological elastomer-based adaptive panels; Smart Materials and Structures; 2010; 19(3),035006.

- Seyyed M Hasheminejad, **Maysam Shabanimotlagh**; Sound insulation characteristics of functionally graded panels; Acta Acustica united with Acustica; 2008; 94(2), pp. 290-300.

Conference papers:

- **Maysam Shabanimotlagh**, Verya Daeichin, Shreyas B. Raghunathan, Pieter Kruizinga, Hendrik J. Vos, Johannes G. Bosch, Michiel Pertijs, Nico de Jong, Martin Verweij; Optimizing the directivity of piezoelectric matrix transducer elements mounted on an ASIC; IEEE International Ultrasonics Symposium (IUS), 8091752, Washington, USA; Oct. 2017.

- Pieter Kruizinga, Eunchul Kang, **Maysam Shabanimotlagh**, Qing Ding, Emile Noothout, Zu Yao Chang, Hendrik J. Vos, Johannes G. Bosch, Martin D. Verweij, Michiel A.P. Pertijs and Nico de Jong; Towards 3D ultrasound imaging of the carotid artery using a programmable and tileable matrix array; IEEE International Ultrasonics Symposium (IUS), Washington, USA; Oct. 2017.

- Eunchul Kang, Qing Ding, **Maysam Shabanimotlagh**, Pieter Kruizinga, Zu-Yao Chang, Emile Noothout, Hendrik J. Vos, Johannes G. Bosch, Martin D. Verweij, Nico de Jong, Michiel A.P. Pertijs; A reconfigurable 24 × 40 element transceiver ASIC for compact 3D medical ultrasound probes; ESSCIRC 2017 - 43rd IEEE European Solid-State Circuits Conference. Sept. 2017.

- **Maysam Shabanimotlagh**, Shreyas Raghunathan, Deep Bera, Zhao Chen, Chao Chen, Verya Daeichin, Michiel Pertijs, Hans Gosch, Nico de Jong, Martin Verweij; Acoustic characterization of a 32 × 32 element PZT on ASIC matrix transducer for 3D transesophageal echocardiography; 6th Dutch Bio-medical Engineering Conference, Egmond aan Zee, The Netherlands, Jan. 2017.

- **Maysam Shabanimotlagh**, Jovana Janjic, Shreyas Raghunathan, Michiel A.P. Pertijs, Nico de Jong, Martin Verweij; The role of sub-dicing in the acoustical design of an

[1] The first and second authors equally contributed to this work.

ultrasound matrix transducer for carotid arteries imaging; IEEE International Ultrasonics Symposium (IUS),7728470, Tours, France; Oct. 2016. (invited for publications)

- Chao Chen, Zhao Chen, Deep Bera, Shreyas Raghunathan, **Maysam Shabanimotlagh**, Emile Noothout, Zu-yao Chang, Jacob Ponte, Christian Prins, Rik Vos, Hanse Bosch, Martin Verweij, Nico de Jong, Michiel Pertijs; A front-end ASIC with receive sub-array beamforming integrated with a 32 × 32 PZT matrix transducer for 3-D transesophageal echocardiography; IEEE Symposium on VLSI Circuits, Digest of Technical Papers; 7573470, Tours, France; Oct. 2016.

- **Maysam Shabanimotlagh**, Shreyas Raghunathan, Nico de Jong, Martin D. Verweij; The acoustical performance of an ultrasound matrix transducer directly stacked on a silicon chip; The Journal of the Acoustical Society of America 140, 3033; Nov. 2016; https://doi.org/10.1121/1.4969411.

- Jovana Janjic, **Maysam Shabanimotlagh**, Martin D. Verweij, Gijs van Soest, Anonius F.W. van der Steen, Nico de Jong; Quantifying the effect of subdicing on element vibration in ultrasound transducers; 2015 IEEE International Ultrasonics Symposium (IUS); 7329410, Taipei, Taiwan; Oct. 2015.

- Michiel Pertijs, Chao Chen, Shreyas Raghunathan, Zili Yu, **Maysam Shabanimotlagh**, Zhao Chen, Zu-yao Chang, Emile Noothout, Sandra Blaak, Jacco Ponte, Christian Prins, Hans Bosch, Martin Verweij, Nico de Jong; Low-power receive electronics for a miniature real-time 3D ultrasound probe; Proceedings, 6th IEEE International Workshop on Advances in Sensors and Interfaces (IWASI); 7184963, pp. 235-238, Gallipoli, Italy; 2015.

About the Author

Maysam Shabanimotlagh was born on 26th July 1985 in Tehran, Iran. He received his Bachelor and Masters degree in Mechanical Engineering from Iran University of Science and Technology, respectively in 2008 and 2010. During Sep. 2006 and Aug. 2010, as a part-time researcher he worked at Acoustics research Laboratory of Iran University of Science and Technology. His research was on acoustical properties of functionally graded materials, and magnetorheological elastomers. After finishing the Master's program, he joined to the Mechatronics Laboratory of Tarbiat Modares University in Tehran, Iran. For three years he was a part-time researcher where his main focus was on material properties of magnetorheological fluids and their potential applications for making new sensors and actuators for rehabilitation application. However, he spent the rest of his time to gain experience in different academic and industrial positions. In 2014 he joined to Acoustic Wavefield Imaging department at the Technical University of Delft, The Netherlands. His research was about design, fabrication, and characterization of ultrasonic transducers for medical imaging applications. This thesis is the outcome of his four years of research as a PhD candidate.

Sponsored by: